Mathematical modelling and optimisation of Venturi-enhanced hydropower

Graham Patrick Benham

St Anne's College

University of Oxford

A thesis submitted for the degree of

Doctor of Philosophy

Trinity 2018

Contents

List of Figures

List of Tables

Abstract

In this thesis we study a novel type of hydropower generation which uses a Venturi contraction to amplify the pressure drop across a turbine, allowing for cost-effective hydropower generation in situations where the head drop is small, such as in rivers and weirs. The efficiency is sensitive to how the secondary flow, which passes through the turbine, mixes with the accelerated primary flow, which is diverted around the turbine, within the confines of a closed geometry. In particular, it is important to understand the behaviour of the turbulent shear layers between the primary and secondary flows, which grow downstream, mixing the flows together. The behaviour of the shear layers in the expanding part of the Venturi contraction is strongly dependent on the shape of the channel. An important consequence of the channel shape, and hence the flow behaviour, is the degree of pressure amplification across the turbine, which determines the amount of generated power.

We focus on mathematically modelling the mixing of the flows in turbulent shear layers, and we investigate two different ways to increase pressure amplification: optimising the shape of the channel, and using swirl to enhance mixing. The channel shape optimisation reveals an interesting balance between the effects of mixing and wall drag. Wide channel expansion tends to accentuate non-uniform flow, causing poor pressure amplification, whilst shallow expansion creates enhanced wall drag, which is also detrimental to pressure amplification. We show how the maximum power is generated with a channel shape that strikes a balance between these two effects. We find that swirl enhances mixing by increasing shear layer growth rates, but it produces large pressure losses in doing so, and for large amounts of swirl a slowly recirculating region can form along the channel centreline. Whilst swirl does not improve efficiency, there may be some inevitable swirl present in the flow, and we show how this affects the optimum channel shape. We also establish the criteria for the existence of such a recirculation region so that it may be avoided.

Acknowledgements

I would like to give thanks to the following people, who have helped make this thesis possible:

My academic supervisors, Ian Hewitt and Colin Please, who have inspired me with their approach to applied mathematics. I am grateful for all their guidance, encouragement and advice. They have been tremendously generous with their time, and I have thoroughly enjoyed working with them.

My industrial supervisor, Paul Bird, who has been supportive throughout the project, and who has helped me keep a close link to the industrial application.

Alfonso Castrejon-Pita, for his time and patience in teaching a mathematician how to be an experimentalist.

Rob Style, who helped with the early stages of the project.

John Ockendon, who has taught me a great deal and who has contributed many interesting ideas to the project.

The EPSRC and VerdErg Renewable Energy for their financial support.

My girlfriend, Paola Castañeda, who has been a great source of support, through all the highs and lows.

My family and friends, who have been at my side, always encouraging me.

St Anne's College, for providing me with a fantastic social environment, and through which I have come to know many wonderful people.

Chapter 1

Introduction

1.1 Venturi-enhanced hydropower

This thesis is concerned with the flow in a Venturi contraction which is used to amplify the pressure drop across a hydropower turbine. The work is motivated by a novel technology developed by VerdErg Renewable Energy Limited, called Venturi-Enhanced Turbine Technology (VETT), which is used for generating hydropower electricity in situations where the drop in head is small (e.g. rivers, weirs and tides). We study the flow behaviour in the Venturi and investigate ways of optimising the geometry, with the aim of generating as much power as possible.

In Figure 1.1 we compare conventional hydropower to Venturi-enhanced hydropower. In conventional hydropower (a) a pressure drop[1] Δp_{total} drives a flow rate Q_{total} across a turbine. The total available power is

$$P_{total} = \Delta p_{total} \times Q_{total}. \tag{1.1}$$

In low head[2] situations, where Δp_{total} is small (a few metres, perhaps), the conventional approach may not be cost-effective, since the power generated may not be sufficient to pay back the capital costs.

One way of reducing these costs is by scaling down the size and capacity of the turbine by using a Venturi contraction. In Venturi-enhanced hydropower (b) a reduced portion of the total flow (secondary) with flow rate Q_s passes through a pipe with constant cross-section containing the turbine, whilst the majority of the flow (primary) is diverted around the turbine and accelerated through a contraction. According to

[1]Note that Δp_{total} here refers to the overall drop in static pressure, rather than the drop in 'total pressure', which is sometimes used in the literature to refer to the sum of the static pressure and the dynamic pressure (kinetic energy per unit volume).

[2]The head drop is equal to the pressure drop divided by ρg, where ρ is the density and g is the gravitational acceleration.

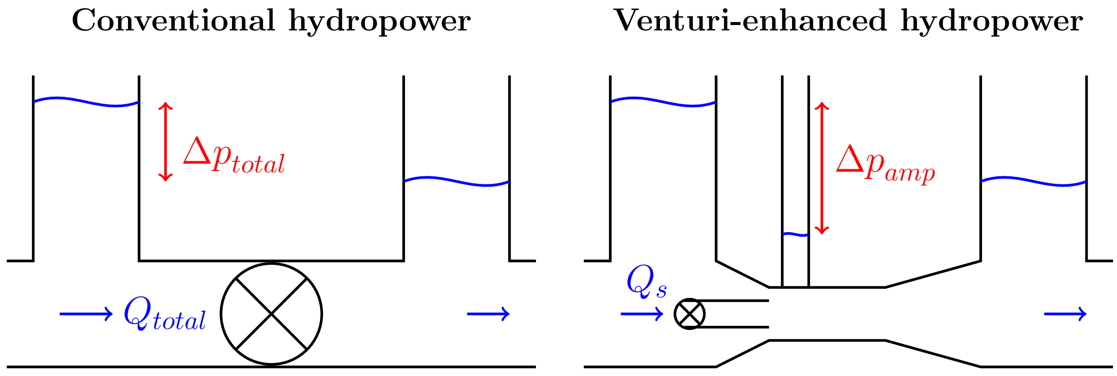

Figure 1.1: Comparison between conventional and Venturi-enhanced hydropower. In conventional hydropower a pressure drop Δp_{total} drives a flow rate Q_{total} across a turbine. In Venturi-enhanced hydropower a reduced flow rate Q_s passes through the turbine, whilst the remaining flow is accelerated through a contraction, amplifying the pressure drop across the turbine to Δp_{amp}.

the Bernoulli principle, the static pressure drops as the flow accelerates, such that the Venturi contraction amplifies the pressure drop across the turbine to Δp_{amp}. The use of the Venturi effect here is similar to a mechanical gearing system. Instead of a turbine dealing with the full flow and a low head, it deals with a reduced flow and an amplified head, thereby allowing for cheaper electricity production. In this way, Venturi-enhanced hydropower becomes cost-effective for many low head sites where conventional hydropower would not be cost-effective. This opens up many opportunities for hydropower generation in flatter countries such as the UK. In addition, Venturi-enhanced hydropower is attractive for its low environmental impact due to the fact that aquatic life can pass through the turbine-free primary flow unharmed.

Similarly to (1.1), the total power generated by Venturi-enhanced hydropower is

$$P_V = \Delta p_{amp} \times Q_s. \tag{1.2}$$

It is important to note that (1.1) and (1.2) are not necessarily equal. In particular, by separating the flow into two parts, accelerating one part, and mixing them back together again, there is a fundamental energy loss (resulting in a loss of power). This is due to viscous dissipation associated with shear stress between the flows as they mix together, which we will discuss later. The ratio between (1.2) and (1.1), which we call the hydrodynamic efficiency, is given by

$$\eta = \frac{\Delta p_{amp} Q_s}{\Delta p_{total} Q_{total}}. \tag{1.3}$$

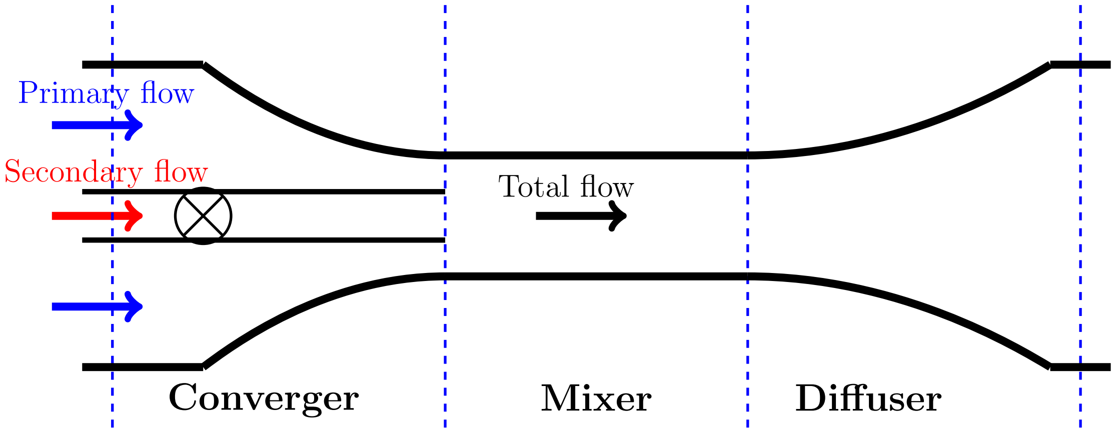

Figure 1.2: Schematic diagram showing a cylindrical cross-section of Venturi-enhanced hydropower. The primary flow is accelerated through a Venturi contraction (converger), amplifying the pressure drop across the secondary flow, which flows through the turbine. Both flows combine in the mixer to form the total flow, before expanding and decelerating in the diffuser.

Equation (1.3) can be rewritten in terms of two key parameters, the flow rate fraction $\mathcal{F} = Q_s/Q_{total}$, and the pressure ratio $R_p = \Delta p_{amp}/\Delta p_{total}$, such that

$$\eta = \mathcal{F} \times R_p. \tag{1.4}$$

In order to improve the cost-effectiveness of Venturi-enhanced hydropower, we balance keeping $\mathcal{F}$ small, reducing the cost of the turbine, whilst keeping R_p as large as possible, increasing the generated power. However, R_p itself, and hence the efficiency η, depend on $\mathcal{F}$ as well as other factors (such as the shape of the Venturi), and this dependence is unknown. Therefore, the work in this thesis focuses on understanding how the efficiency depends on the hydrodynamics in the Venturi, and in turn how to design the Venturi to maximise efficiency.

1.1.1 The converger, mixer and diffuser

In Figure 1.2 we illustrate the geometry of Venturi-enhanced hydropower, as is representative of VerdErg's VETT. In the current design, the geometry is axisymmetric and is divided into a converger, a mixer and a diffuser. Other designs could have a two-dimensional Venturi contraction, instead of axisymmetric, and therefore throughout this thesis we consider both axisymmetric and two-dimensional geometries. Furthermore, we later discuss how the mixer and the diffuser may be combined into the same section. However, for the purpose of illustrating the operating principles, here we keep the current design. The function of each of the three sections is as follows:

- **Converger**: A contracting annular section of pipe which accelerates the primary flow. The secondary flow, including the turbine, is kept in a straight pipe of constant cross-section running along the same axis as the primary flow. By the Bernoulli principle, the pressure decreases as the primary flow is accelerated, such that the turbine feels an amplified pressure drop.

- **Mixer**: A straight section of pipe in which the primary and secondary flows mix together. Although there is significant mixing, the flow is not expected to be uniform or fully developed by the end of the mixer.

- **Diffuser**: A widening section in which the flow decelerates and the pressure increases.

The primary function of the converger is to amplify the pressure drop across the turbine. In order for this to work, the low pressure induced by the acceleration of the primary flow must be felt by the secondary flow where they meet, at the end of the converger section. In other words, the pressure must be uniform across the end of the converger section. It is not immediately obvious whether this is indeed physically true. However, it becomes clear by noting the Kutta condition [53], which states that the streamlines must leave a sharp trailing edge straight. Regardless of whether the pressure is uniform at the trailing edge of the converger, it is expected to be uniform across the cross section of the mixer, a short distance downstream. This is due to boundary layer theory [87], which states that pressure variations in the transverse direction are small because the aspect ratio of the mixer is long and thin. Hence, if the pressure is non-uniform at the trailing edge of the converger, then according to inviscid theory the primary and secondary flows must undergo acceleration/deceleration as they enter the mixer, where the pressure becomes uniform (a change in pressure results in a change in velocity). However, this would result in an expansion/contraction of the streamlines near the trailing edge, which violates the Kutta condition. Therefore, we conclude that pressure is uniform across the trailing edge of the converger, such that the streamlines leave the trailing edge straight.

This phenomenon is illustrated in Figure 1.3, where we consider flow in a channel with an off-centre dividing wall. There is stronger drag, and therefore a stronger pressure gradient, on one side of the dividing wall than the other. Hence, the pressure cannot be uniform across both the leading and trailing edges of the dividing wall. If the pressure is uniform across the leading edge (a), then the streamlines must be distorted downstream of the trailing edge, and vice versa. However, from the

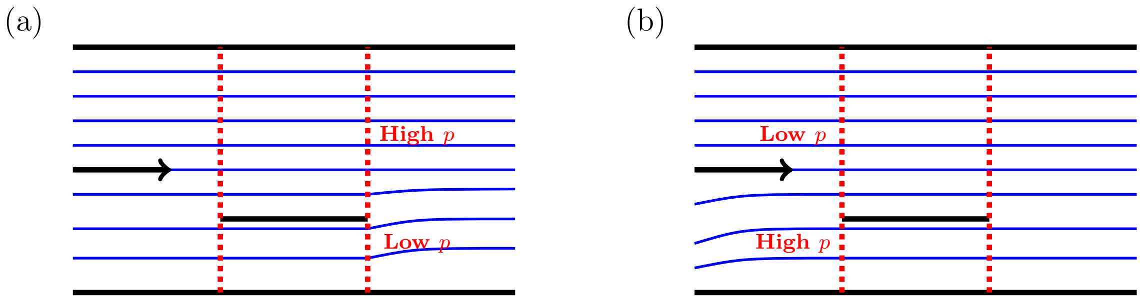

Figure 1.3: Flow through a channel with an off-centre dividing wall cannot have uniform pressure both at the leading and trailing edges of the wall, due to larger drag on one side of the wall than the other. Uniform pressure across the trailing edge (b) is correct, since uniform pressure across the leading edge (a) violates the Kutta condition.

Kutta condition, we know that the streamlines must leave the trailing edge straight. Therefore, we conclude that the pressure must be uniform across the trailing edge (b).

The inflow of the mixer is composed of the slower secondary flow in the centre and the faster primary flow on the outside. The primary function of the mixer is to enable the two flows to exchange momentum (and energy), producing a combined flow which is as uniform as possible. Of the whole geometry, the mixer has the narrowest cross-section, producing the strongest wall drag. Therefore, the length of the mixer must be chosen carefully, such that it is long enough that the primary and secondary flows mix well, but not so long that wall drag causes undue energy losses. Besides energy losses due to wall drag, there is also an inevitable energy loss due to viscous dissipation associated with shear stress between the flows as they mix together[3]. This is similar to the phenomenon in classical mechanics where two moving particles of different speeds must lose energy to friction as they combine to form the same particle. Unlike wall drag losses, which we try to minimise, this fundamental energy loss is unavoidable. That being said, it is not obvious why an entire section ought to be devoted entirely to the purpose of mixing the flows. In fact, the main reason why the primary and secondary flows need to mix well within the mixer is because the diffuser section, after the mixer section, has the tendency to perform poorly if the inflow has strongly non-uniform velocity [106]. Therefore, the mixer section can be thought of as a pre-requisite to the diffuser, where the performance of the diffuser depends strongly on the performance of the mixer. Although we illustrate a mixer

[3] In reality energy is dissipated by small scale eddies, which we discuss later in Chapter 2.

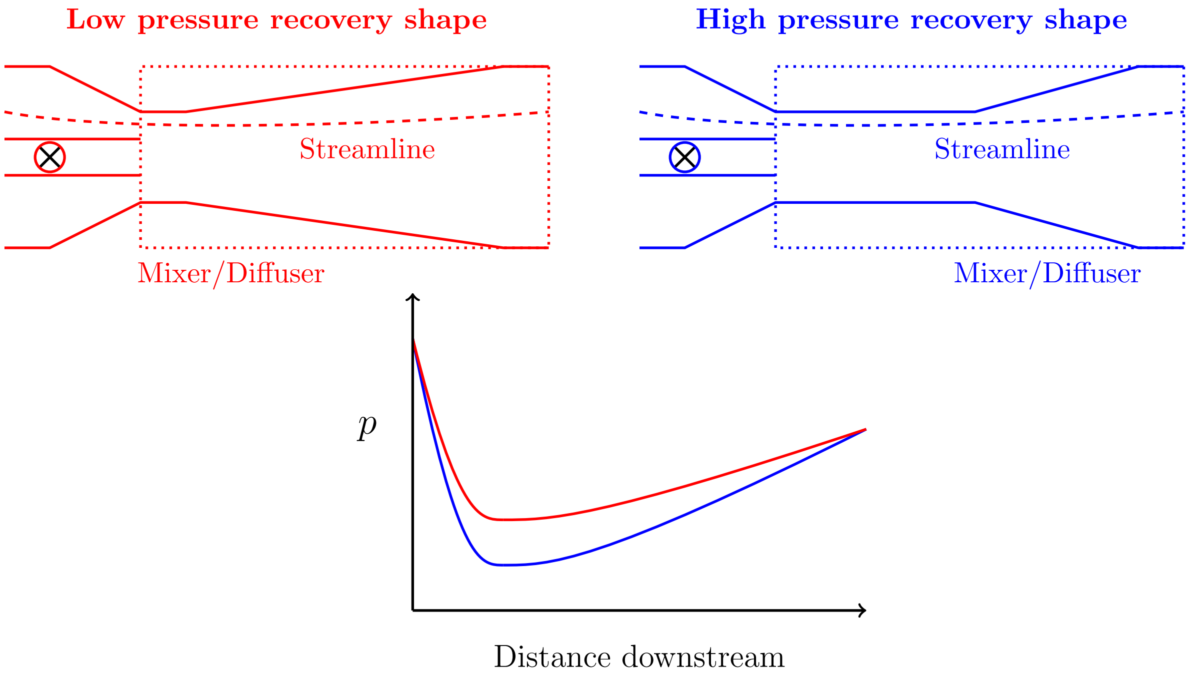

Figure 1.4: Example pressure curves along a streamline which passes through the primary flow and through the Venturi contraction (mixer/diffuser shapes are figurative). If the pressure recovery in the mixer/diffuser is high then the pressure amplification is larger, resulting in more generated power. Conversely, low pressure recovery results in less generated power.

section with constant cross-section in Figure 1.2, it is also possible for the mixer to contract or expand.

The diffuser section has the function of converting high speed low pressure flow to low speed high pressure flow. Diffuser performance is characterised by pressure recovery, which is a measure of the pressure gained between the inflow and the outflow, relative to the kinetic energy at the inflow. Since the pressure at the diffuser outflow is fixed (determined by the hydrostatic pressure of the river/weir), the pressure recovery of the diffuser affects the inflow pressure only. Therefore, a diffuser with large pressure recovery has a relatively low inflow pressure. Since pressure is continuous between the mixer and diffuser, a low pressure at the diffuser inflow contributes to the pressure amplification across the turbine. Therefore, increasing diffuser pressure recovery causes a direct increase in the power generated by the turbine, which is illustrated in Figure 1.4.

Since the inflow of the diffuser is not fully mixed, the diffuser is partly responsible for mixing the flow, similarly to the mixer. Therefore, although the current design distinguishes the mixer and the diffuser as separate sections, we find it useful to consider the mixer and the diffuser as the same section, where the combined function is to mix the primary and secondary flows together, whilst simultaneously recovering as much pressure as possible. Following on from this, we consider dividing the geometry into two parts: a converger and a mixer/diffuser. We propose to optimise the design of each part to generate as much power from the turbine as possible. From an engineering perspective, the design of the converger is relatively straightforward. Convergers and nozzles are well studied in the literature [12], and the optimum shape has a curved profile that strikes a balance between not being too long, which is detrimental for wall drag, and not being to short, which can cause undesirable backflow. Conversely, the mixer/diffuser is much more difficult to design. Although diffuser design is well studied in the case of uniform flow [12], there is very little literature in the case of non-uniform flow. Furthermore, instead of the simple diffuser shapes that are considered in the literature, such as straight sided expansions, we consider a combined mixer/diffuser with a potentially complex shape composed of multiple sections or a continuous curved profile.

Therefore, this thesis focuses on the mathematical modelling and optimisation of the flow inside the mixer/diffuser, rather than the converger. To describe the flow in the mixer/diffuser, it is necessary to understand how the primary and secondary flows mix together. In the next section we discuss how a preliminary mixing model allows us to gain some insight.

1.1.2 A preliminary model for mixing

As described earlier, the main region of interest for the work in this thesis is the mixer/diffuser. Within this region, the primary and secondary flows mix together and expand. Due to the fact that the flows have different speeds, there is a fundamental energy loss associated with their mixing, corresponding to viscous dissipation.

To illustrate this, we calculate the energy loss using a very simple model for the flow. In this model we assume that the primary and secondary flows are fully mixed by the end of the mixer. Let the primary flow have speed U_p and an annular cross-section with area A_p. Similarly, let the secondary flow have speed U_s and a circular cross-section with area A_s, where $A_t = A_p + A_s$ is the total cross-sectional area of both flows. By conservation of mass, after the flows mix together they form a combined flow with uniform velocity

$$\bar{U} = \mathcal{A} U_s + (1 - \mathcal{A})\, U_p, \tag{1.5}$$

where $\mathcal{A} = A_s/A_t \in (0, 1)$ is the area ratio between the secondary flow and the total flow. A momentum balance between the inlet and outlet of the mixer indicates that there must be a change in the pressure. We denote p_{in} and p_{out} as the pressures at the inlet and outlet of the mixer, respectively, which are assumed to be uniform across the cross-section, as described earlier. If we neglect the effect of drag at the walls, then conservation of momentum gives

$$\rho(A_s U_s^2 + A_p U_p^2) + p_{in} = \rho A_t \bar{U}^2 + p_{out}. \tag{1.6}$$

By rearranging (1.6), we find a simplified expression for the change in pressure, given in non-dimensional terms as

$$\frac{p_{out} - p_{in}}{\rho U_p^2} = \mathcal{A}(1 - \mathcal{A})(1 - \beta)^2, \tag{1.7}$$

where $\beta = U_s/U_p \in (0, 1)$ is the velocity ratio between secondary and primary flows. Clearly, (1.7) is a positive quantity. Therefore, one of the consequences of the flows mixing together is an inevitable rise in pressure. Next, let us consider the change in the flux of energy between the inlet and outlet of the mixer, which is

$$\begin{aligned} E_{out} - E_{in} =& \bar{U} A_t \left(p_{out} + \frac{1}{2}\rho\bar{U}^2 \right) \\ &- \left(U_s A_s \left(p_{in} + \frac{1}{2}\rho U_s^2 \right) + U_p A_p \left(p_{in} + \frac{1}{2}\rho U_p^2 \right) \right). \end{aligned} \tag{1.8}$$

After simplification, (1.8) is rewritten in non-dimensional terms as

$$\frac{E_{out} - E_{in}}{\rho U_p^3 A_t} = -\frac{1}{2}\mathcal{A}(1 - \mathcal{A})(1 - \beta)^2(\beta(1 - \mathcal{A}) + \mathcal{A}), \tag{1.9}$$

which is clearly a negative quantity. Therefore, a second consequence of the mixing of the flows is a fundamental loss of energy, due to viscous dissipation.

In Figure 1.5 (a) we plot (1.7) and (1.9) for different values of $\mathcal{A}$ and β. The pressure change is monotone decreasing in β and is symmetric about $\mathcal{A} = 1/2$. Energy loss is largest for small values of β (though not strictly monotone), and attains its maximum (absolute) value at $\beta = 0$, $\mathcal{A} = 2/3$. On the other hand, the energy loss is zero for $\beta = 1$ or $\mathcal{A} = 0$, 1, which corresponds to uniform flow. Therefore, flows which are more non-uniform will suffer from a larger fundamental energy loss due to mixing. Hence, a strong Venturi contraction, which results in a very non-uniform inflow at the mixer, produces a large energy loss. Likewise, the least energy is lost if there is no Venturi contraction (i.e. conventional hydropower). Consequently, whilst

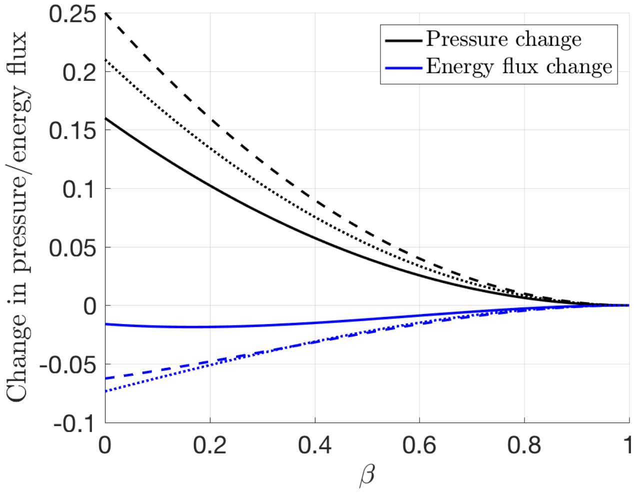

Figure 1.5: Change in non-dimensional pressure and energy flux, as defined in Equations (1.7) and (1.9), where a non-uniform velocity profile, consisting of primary and secondary flows, becomes uniform in the mixer section. Solid, dashed and dotted lines correspond to $\mathcal{A} = 0.2$, $\mathcal{A} = 0.5$ and $\mathcal{A} = 0.7$, respectively.

the Venturi reduces the cost of the turbine, it also reduces the hydropower efficiency (1.4).

Although useful for these preliminary calculations, there are several major limitations of a simple model such as this. Firstly, we have ignored wall drag, which is an important contribution to the total energy loss in the mixer/diffuser. Secondly, we have restricted our attention to a straight sided mixer which mixes the primary and secondary flows perfectly. As soon as we consider the combined mixer/diffuser with contracting or expanding walls, where the diffuser receives a partially mixed flow, rather than a perfectly mixed flow, then the analysis becomes more difficult. To begin with, a simple conservation of momentum argument like (1.6) is not possible for non-uniform flow in an expanding/contracting channel. For such an analysis we would require knowledge of the resultant force on the fluid due to the walls. Unfortunately, the resultant force from the walls depends on the momentum of the flow itself, which varies spatially. Therefore, in order to use conservation of momentum arguments similar to (1.6), it is necessary to create a model for how the flow develops spatially. In particular, the primary and secondary flows mix together within *turbulent shear layers*, which are regions of fluid with large velocity gradients, and which grow downstream, entraining both the primary and secondary flows.

The work in this thesis focuses on understanding this mixing process, and how to improve mixing by optimising the channel geometry and/or introducing swirl.

1.2 Diffuser design literature review

In this thesis, we give a specific literature review for the work in each chapter at the beginning of that chapter. We have chosen this approach instead of a complete literature review at the beginning of the thesis because the topics of each chapter require literature from fairly different fields that do not flow together well. However, common to each chapter is the concept of a diffuser. Therefore, we include a literature review of diffusers here for the purpose of familiarising the reader with how diffusers are typically designed and how performance is measured.

A diffuser is an expanding duct with the purpose of reducing flow velocity, whilst recovering static pressure. As the flow decelerates, the kinetic energy is converted into potential energy, in the form of static pressure. The more pressure recovered from kinetic energy, the better the performance of a diffuser. There is a large literature on the design of diffusers in the case where the inflow is uniform [12], but a limited literature for non-uniform inlet flows.

In the case where the inflow is uniform, there are two main factors which affect diffuser performance. Firstly, there is drag from the walls. The narrower and longer the diffuser, the greater the wall drag. In addition, wall drag is also affected by the surface roughness of the walls. Secondly, there is *diffuser stall*, or *boundary layer separation*. Since the flow decelerates as it expands, there are strong pressure gradients that produce a force opposing the direction of the flow. If this force is sufficiently strong, due to a wide expansion of the walls, the boundary layers near the diffuser walls can decelerate and grow rapidly [87]. This is illustrated in Figure 1.6. If the boundary layers separate (b), the majority of the flow does not decelerate significantly, producing a jet-like peaked velocity profile at the outlet. Since the flow is not significantly decelerated, very little kinetic energy is converted to pressure. Hence, optimum diffuser shapes strike a balance between not expanding too fast, which results in diffuser stall, and not expanding too slowly, which is detrimental for wall drag.

In the case where the inflow is non-uniform, such as in Venturi-enhanced hydropower, there are other factors, in addition to wall drag and boundary layer separation, which affect diffuser performance. In particular, non-uniform flows have the tendency to become more non-uniform as they expand and decelerate [106], and this can have a detrimental effect on diffuser performance. This is discussed in more detail in Chapter 5.

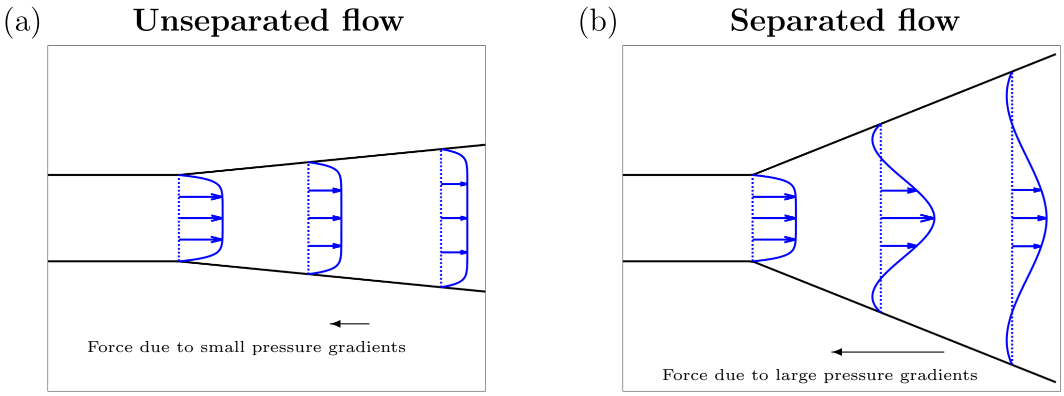

Figure 1.6: Schematic diagram illustrating the difference between unseparated and separated flow in a diffuser, showing velocity profiles at three locations. For unseparated flow the velocity decreases uniformly, maintaining its profile. For separated flow the boundary layers thicken and there is some reverse flow. This creates a peaked velocity profile where the flow near the walls remains slow, whilst the flow in the centre remains fast.

One useful parameter which characterises diffuser performance is the pressure recovery coefficient C_p [12]. The pressure recovery coefficient is a measure of the amount of kinetic energy in a flow which is converted into static pressure. There are various ways to define C_p, but we use the so-called mass-averaged pressure recovery [32], which is defined as

$$C_p = \frac{\int_A up\, dA\big|_{out} - \int_A up\, dA\big|_{in}}{\int_A \frac{1}{2}\rho u^3\, dA\big|_{in}}, \tag{1.10}$$

where A indicates a cross-sectional area. The value of C_p takes values between $-\infty$ and 1, where $C_p = 1$ if all the inlet kinetic energy is converted into static pressure. If a diffuser has inlet and outlet cross-sectional areas A_{in} and A_{out}, respectively, then for a fixed finite area ratio A_{out}/A_{in} and inlet flow profile, there is a maximum possible pressure recovery, which is less than 1 [12]. In the case of uniform inviscid flow this ideal limit is $C_{p_I} = 1-(A_{in}/A_{out})^2$ but for non-uniform flow, it is not known what the corresponding limit is (although we derive a rough estimate in Chapter 7). Another definition of C_p, which is often used in the literature is

$$C_p = \frac{p_{out} - p_{in}}{\frac{1}{2}\rho U_{in}^2}, \tag{1.11}$$

where $U_{in} = 1/A \int_A u\, dA\big|_{in}$ is the average velocity at the inlet. Note that (1.11) is equivalent to (1.10) in the case of uniform flow. This definition of C_p (1.11) makes use of the fact that the diffuser shape is long and thin and, due to boundary layer theory [87], pressure is approximately uniform across the inlet and outlet. From an experimental point of view (1.11) is much easier to measure than (1.10), since it only requires pressure measurements at two locations and a measurement of the total flow rate, whereas (1.10) requires measurements of velocity and pressure across both the inlet and outlet cross-sections. However, for non-uniform inflows (1.11) is not an appropriate measure of pressure recovery, since it is not normalised properly. To see this, we calculate (1.11) for the non-uniform flow in the example in Section 1.1.2. The result is

$$C_p = \frac{2\mathcal{A}(1-\mathcal{A})(1-\beta)^2}{(1-\mathcal{A}+\mathcal{A}\beta)^2}. \tag{1.12}$$

Clearly, (1.12) attains values larger than unity (e.g. $C_p = 1.34$ for $\mathcal{A} = 0.5$, $\beta = 0.1$), which is misleading. Using the mass-averaged definition (1.10), we perform the same calculation, finding

$$C_p = \frac{2\mathcal{A}(1-\mathcal{A})(1-\beta)^2(1-\mathcal{A}+\mathcal{A}\beta)}{1-\mathcal{A}+\mathcal{A}\beta^3}. \tag{1.13}$$

The expression (1.13) is always less than unity and, in fact, it achieves its maximum of $C_p = 1/2$ when $\beta = 0$ and $\mathcal{A} = 1/2$. Therefore, we confirm that (1.10) is a better definition for non-uniform flow.

There are many experimental studies which calculate pressure recovery for a variety of diffuser shapes. Detailed pressure recovery calculations are given by Reneau et al. [81] for two-dimensional diffusers, and McDonald et al. [65] for conical diffusers. We display these results in the case of a straight-sided conical diffuser in Figure 1.7, where C_p is calculated according to (1.11). The straight-sided conical diffuser shapes are characterised by the total diffuser angle[4] 2θ and length ratio L/R_1, where L and R_1 are the dimensional length and inlet radius, respectively (see diagram in Figure 1.7). Level set contours of C_p are shown for different values of 2θ and L/R_1. Also shown is the locus of points, C_p^* that corresponds to the maximum value of C_p for a given value of L/R_1. Above the line given by C_p^*, the diffuser angle is wide enough that the effects of boundary layer separation begin to dominate. For length ratios between 3 and 40, the optimum total angle varies slightly between $2\theta = 10°$ and $2\theta = 6°$. However, diffusers are often designed conservatively, with a diffuser angle slightly smaller than the theoretical optimum. This is because the optimum pressure recovery C_p^* lies in a region of marginal stability [12]. That is to say, the flow exhibits

[4]Note that θ is related to the notation α for the diffuser angle which we use later in the thesis, by the relation $\alpha = \tan\theta$.

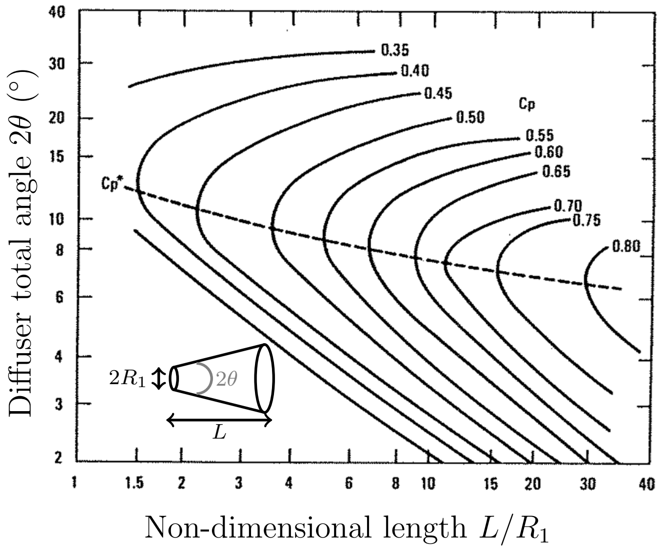

Figure 1.7: Contours of pressure recovery C_p defined according to (1.11), measured experimentally for straight sided conical diffusers of different shapes. This image is taken from Blevins [12] but the experiments were performed by McDonald et al. [65].

erratic behaviour, a thickening of the boundary layers, and small regions of separation. Conical diffusers are often designed with total angle $2\theta = 7°$, because, for a large range of length ratios, this value is close to optimum, whilst being in a region of stability. In the case of two-dimensional diffusers, the optimum pressure recovery curve C_p^* occurs for larger expansion angles. Similarly to conical diffusers, two-dimensional diffusers are often designed with total angle $2\theta = 14°$ as a conservatively stable value that is close to optimum.

For the work in this thesis, we do not focus on modelling boundary layer separation. Instead, we use the values of $\theta = 3.5°$, for conical diffusers, and $\theta = 7°$, for two-dimensional diffusers, as standard values for the expansion (half) angle, and we assume that above these values the effects of boundary layer separation become important. In reality, there is no hard border that divides situations where boundary layers separate and situations where they do not. The border is much softer, with the early stages of boundary layer separation involving a gradual thickening of the boundary layers, and increasingly erratic flow behaviour, and later stages involving sizeable regions of separated flow. Full details of the different regimes of diffuser stall are discussed by Reneau et al. [81], Carlson et al. [16] and Fox et al. [33]. However, for the purposes of this research, we find the standard values $\theta = 3.5°$, $7°$ useful to approximate the onset of the early stage effects of boundary layer separation, and we restrict our attention to diffuser angles smaller than these values. In this way, we focus on understanding the mixing between the primary and secondary flows within the mixer/diffuser at small diffuser angles, rather than the effects of boundary layer separation that occur at larger diffuser angles.

In the case where the diffuser inflow is non-uniform, there is a limited literature. However, there are some experimental studies which investigate diffuser performance for specific non-uniform inflow profiles (see [106] for example). A comprehensive literature review for diffusers with non-uniform inflow is given at the beginning of Chapter 5.

1.3 Overview

The work in this thesis focuses on the mixing of the primary and secondary flows inside the mixer/diffuser section of Venturi-enhanced hydropower. As discussed earlier, the recovery of pressure between the inlet and the outlet of the mixer/diffuser is crucial to the hydropower efficiency (1.4). The more pressure recovery, the greater the pressure amplification across the turbine, resulting in more generated power. Therefore, we focus on understanding how the flows mix together, and how to design the geometry to maximise pressure recovery.

The approach we follow is to use simple models to describe the time-averaged behaviour of the flow. These models are intuitive and have a low computational cost, allowing us to easily search the design parameter space to improve pressure recovery. In order to validate these models, we use two approaches. Firstly, we make comparisons with particle image velocimetry (PIV) measurements from a hydrodynamics experiment, using several different channel geometries. Secondly, for situations where we have not performed experiments, we compare the results of our models to the results of computational fluid dynamics (CFD), with several widely used Reynolds-averaged Navier-Stokes (RANS) models. The RANS models are more computationally expensive and less intuitive than our simple models, and they are difficult to use for optimisation purposes. Therefore, we use our simple models for optimisation whilst we use the RANS models for validation, and to search for optima locally near those found using the simple models.

In Chapter 2 we introduce the background mathematics which will be applied throughout this thesis. We derive the RANS equations for the time-averaged behaviour of turbulent flow. We discuss several turbulence closure assumptions, including the classic Prandtl mixing length model, and the k-ε two-equation model. The former is used as the basis for our simple models for the mixing of the primary and secondary flows. The latter is a popular turbulence model which we use throughout this thesis, solving numerically, as a means of validating the results of our simple models.

Following from the RANS equations, we describe the basic framework for the derivation of our simple models. We exploit the fact that the domain is long and thin, such that the boundary layer approximation is appropriate [87]. The turbulent boundary layer equations are a simplification of the RANS equations, which we integrate across the cross-section of the flow, deriving several ordinary differential equations that form the basis of our simple models.

Next we discuss how the primary and secondary flows mix within shear layers, which are thin turbulent regions of the flow with large velocity gradients, and which grow downstream, entraining fluid as they do. For unconfined flows, shear layers can be described using a simple analytical model, which we derive from the turbulent boundary layer equations and Prandtl mixing length theory [87, 48]. For situations where the flow is confined within walls we show how to derive a similar model using an entrainment argument. This forms part of the simple models we later use to describe how the primary and secondary flows mix together within the confining walls of the mixer/diffuser.

In Chapter 3 we describe our experimental work which investigates the development of turbulent shear layers in confining channels. We use two different experimental techniques to visualise the flow in a hydrodynamics tank: ink tracer visualisation and PIV. The results from these experiments give us an insight into the relationship between the shape of the channel and the flow development. Furthermore, the velocity and pressure data generated by the PIV analysis will be used in Chapter 4 to validate our simple model and compare with CFD calculations.

In Chapter 4 we present a simple model for the development of shear layers between parallel flows in confining channels, such as the primary and secondary flows in the mixer/diffuser. The model approximates the flow in the shear layer as a linear profile separating uniform-velocity streams. Both the channel geometry and wall drag affect the development of the flow. We compare the predictions of the model with PIV experiments and computational fluid dynamics, finding good agreement. We use the model to investigate the effect of the inflow conditions on the growth of the shear layer. We show that if the inflow is very non-uniform, or if the channel expansion angle is too large, an undesirable stagnation region may form inside the channel. Finally, we show how our model can be improved by incorporating additional features, such as a boundary layer near the channel wall.

In Chapter 5 we use the simple model of Chapter 4 to identify the diffuser shape that maximises pressure recovery for several classes of non-uniform inflow. Since we consider the inflow to be non-uniform, the diffuser is equivalent to a mixer/diffuser. We find that wide diffuser angles tend to accentuate non-uniform flow, causing poor pressure recovery, whilst shallow diffuser angles create enhanced wall drag, which is also detrimental to pressure recovery. Optimal diffuser shapes strike a balance between these two effects, and the optimal shape depends on the structure of the non-uniform inflow.

Three classes of non-uniform inflow are considered, with the streamwise velocity varying across the width of the diffuser entrance. The first case is a typical inflow from Venturi-enhanced hydropower, consisting of primary and secondary flows with a shear layer in between. The second case is a limiting case where the primary and secondary flows are of similar speed. The third case is a pure shear profile with linear velocity variation between the centre and outer edge of the diffuser. This case corresponds to the downstream limit of the first case, where the shear layer has spread across the width of the diffuser.

We describe the evolution of the flow profile using the simple model from Chapter 4. The governing equations of this model form the dynamics of an optimal control problem where the control is the diffuser shape. A numerical optimisation approach is used to solve the optimal control problem and Pontryagin's Maximum Principle [78] is used to find analytical solutions in the second and third cases. We show that some of the optimal diffuser shapes can be well approximated by piecewise linear sections. This suggests a low-dimensional parameterisation of the shapes, providing a structure in which more detailed and computationally expensive turbulence models can be used to find optimal shapes for more realistic flow behaviour.

For several of the classes of non-uniform inflow which are considered in Chapter 5, the optimal diffuser shape has an initial straight section which is necessary for mixing the flows well before expansion. This indicates that for these cases the original distinction between the mixer and the diffuser in Venturi-enhanced hydropower is indeed appropriate. However, the straight narrow mixer section, though necessary, has the strongest wall drag of the entire geometry. Hence, we next consider a mechanism to mix the flows over a shorter length scale, with the aim of shortening the mixer, thereby reducing losses and increasing pressure recovery.

Previous studies show that shear layer growth rates, and hence mixing, can be increased with the introduction of swirl [71, 38]. However, the effect of swirl on pressure recovery in a confined flow is uncertain. Whilst it would be relatively easy to introduce swirl to the secondary flow, using helical vanes inside the secondary pipe, it is very likely that a small amount of swirl is present in the secondary flow already, due to the presence of the turbine upstream, and it is important to understand its effect.

Therefore, in Chapter 6 we study the problem of mixing between core and annular flows in a pipe (corresponding to secondary and primary flows), examining the effect of a swirling core flow. We develop a simple model that approximates the axial flow profile as a linear shear layer separating uniform-velocity core and annular streams. The azimuthal flow profile is approximated as a solid body rotation within the core region, and a parabolic mixing profile within the shear layer. Using this model, which shows good agreement with CFD calculations, we confirm that a swirling core is useful for increasing shear layer growth rates, but find that it is detrimental to pressure recovery, and for large amounts of swirl a stagnation region can form along the pipe axis. This indicates that swirl should be avoided for Venturi-enhanced hydropower. However, should there be some swirl present in the flow, we show how this affects the optimum shape. We also establish the criteria for the development of the stagnation region in terms of the pipe expansion angle and inflow velocity profile, so that it may be avoided.

As a partly conclusive addition, Chapter 7 relates the results from the previous chapters to a real-world application. In this chapter, we incorporate the whole geometry of Venturi-enhanced hydropower into a mathematical model, including the intake from the river, the turbine itself, and the outlet which flows back into the river. This relates the pressure recovery of the mixer/diffuser to the actual amount of power generated. Using realistic values for the pressure drop and flow rate, we optimise the geometry using the simple model of Chapter 4 and the optimisation techniques of Chapter 5. Since the results of Chapter 6 indicate that swirl is not suitable for improving pressure recovery, and hence generated power, we do not discuss swirl in great detail for this analysis. However, should a small amount of swirl be present in the flow, we discuss how this may affect our optimisation.

Finally, in Chapter 8 we discuss the conclusions and implications from the work in this thesis. We also outline further related work which could be pursued.

Chapter 2

Background mathematics

This chapter presents the mathematical derivation of all the necessary concepts for this research. We start by discussing the Navier-Stokes equations, high Reynolds number flows and the nature of turbulence. Then we derive the Reynolds-averaged Navier-Stokes equations for the time-averaged behaviour of turbulent flows. We discuss different possible closure assumptions, including Prandtl mixing length theory and the k-ε model. We then derive the turbulent boundary layer equations, for modelling flows in long-thin domains, and we integrate these equations, forming simplified equations of mass and momentum. These equations will be used throughout the thesis as the basis for our simple models for describing flow situations. Finally, we derive the classic model for shear layers between unconfined parallel flows, and we show how it is possible to extend this model to the case where the flows are confined.

We attempt to go into as little detail as necessary for understanding the concepts presented here. For further details, we direct the reader to standard textbooks in this field. Boundary Layer Theory by Schlichting et al. [87] is without doubt the most informative and thorough. Turbulent Flows by Pope [79] and the 'Turbulence' review article by Jimenez [6] are also helpful.

2.1 Turbulence modelling

The flows we consider are incompressible Newtonian fluid flows, for which the Navier-Stokes equations apply. The Navier-Stokes equations are

$$\nabla \cdot \mathbf{u} = 0, \tag{2.1}$$

$$\rho \frac{\partial \mathbf{u}}{\partial t} + \rho \left(\mathbf{u} \cdot \nabla \right) \mathbf{u} = -\nabla p + \mu \nabla^2 \mathbf{u}, \tag{2.2}$$

where μ is the viscosity, ρ is the density, p is the pressure and $\mathbf{u} = (u, v, w)$ is the velocity in three dimensions. Let us assign the following scalings to each variable

$$\mathbf{u} = U_0\hat{\mathbf{u}}, \quad p = \rho U_0^2 \hat{p}, \quad (x, y, z) = L\left(\hat{x}, \hat{y}, \hat{z}\right), \quad t = \frac{L}{U_0}\hat{t}. \tag{2.3}$$

In terms of these scaled variables, we rewrite (2.1)-(2.2) as

$$\hat{\nabla} \cdot \hat{\mathbf{u}} = 0, \tag{2.4}$$

$$\frac{\partial \hat{\mathbf{u}}}{\partial \hat{t}} + \left(\hat{\mathbf{u}} \cdot \hat{\nabla}\right)\hat{\mathbf{u}} = -\hat{\nabla}\hat{p} + \frac{1}{Re}\hat{\nabla}^2\hat{\mathbf{u}}, \tag{2.5}$$

where

$$Re = \frac{\rho U_0 L}{\mu}, \tag{2.6}$$

is the Reynolds number, which measures the ratio of inertial to viscous forces. We consider high Reynolds number flows $Re \gg 1$, where inertia is important. In particular, for these flows, the non-linear inertial terms on the left hand side of the Navier-Stokes equations (2.2) are responsible for complex flow behaviour, also known as turbulence, which is characteristic of the high Reynolds number regime.

One of the characteristic features of turbulent flows is the mechanism through which energy is transferred between eddies. Although, at high Reynolds number, viscous terms appear to be negligible (see (2.5)), turbulence is in fact dissipative. It does not, however, dissipate energy at the large scale, like laminar flows. Instead, energy is exchanged in an inviscid way between eddies of diminishing size. Energy is only dissipated due to eddies which are so small that viscous effects become important. This critical size is called the Kolmogorov length scale [6] and is given by

$$\eta = \left(\frac{\nu^3}{\varepsilon}\right)^{1/4}, \tag{2.7}$$

where ε is the turbulent energy dissipation and ν is the kinematic viscosity $\nu = \mu/\rho$. When modelling turbulence, it is necessary to account for many different length scales, from the Kolmogorov scale η up to the dominant length scale of the problem L. This can be problematic for computations.

In order to solve (2.1)-(2.2) numerically, which is known as Direct Numerical Simulation (DNS), the domain is discretised spatially, with step size Δx. Let us assume that there are N elements along each dimension of the domain, such that

$$N\Delta x = L. \tag{2.8}$$

Re	Spatial steps		Time steps	Total	
	2D	3D		2D	3D
10^3	3.2×10^4	5.6×10^6	1.8×10^2	5.6×10^6	1.0×10^9
10^4	1.0×10^6	1.0×10^9	1.0×10^3	1.0×10^9	1.0×10^{12}
10^5	3.2×10^7	1.8×10^{11}	5.6×10^3	1.8×10^{11}	1.0×10^{15}
10^6	1.0×10^9	3.2×10^{13}	3.2×10^4	3.2×10^{13}	1.0×10^{18}

Table 2.1: Minimum number of spatial and time steps for DNS in two and three-dimensional flows at different Reynolds numbers.

Making sure that the smallest eddies are resolved, we must choose $\Delta x \leq \eta$. According to a simple scaling law [79], the energy dissipation is approximately

$$\varepsilon \approx \frac{\tilde{u}^3}{L}, \tag{2.9}$$

where $\tilde{u}$ is the root mean squared velocity. Therefore, if we redefine the Reynolds number (2.6) in terms of $\tilde{u}$, then the number of spatial steps must be

$$N \geq Re^{3/4}. \tag{2.10}$$

Therefore, the number of steps for a two dimensional domain scales like $N^2 \sim Re^{3/2}$, and like $N^3 \sim Re^{9/4}$ for a three-dimensional domain. To make things worse, we must also consider the number of discretisation points in time. Since memory storage requirements (due to spatial discretisation) are very large at high Reynolds numbers, integration of the solution in time is usually performed using an explicit method [51]. For explicit methods with time step Δt, the Courant-Friedrichs-Lewy (CFL) condition

$$C = \frac{\tilde{u}\Delta t}{\Delta x} < 1, \tag{2.11}$$

must hold in order to achieve stability. If we take $\tau = L/\tilde{u}$ as the appropriate timescale of the problem, similarly to the scaling in (2.3), then the number of time steps N_t is given by

$$N_t \Delta t = \frac{L}{\tilde{u}}. \tag{2.12}$$

Hence, the CFL condition (2.11) implies

$$N_t \geq \frac{1}{C} Re^{3/4}. \tag{2.13}$$

In Table 2.1 we display the minimum number of spatial and time steps necessary to perform DNS at Reynolds numbers between $Re = 10^3$ and $Re = 10^6$. It is clear that DNS becomes incredibly computationally intensive at even moderately

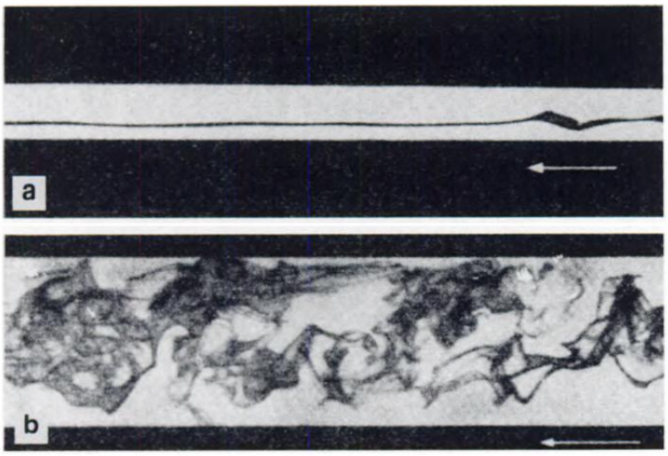

Figure 2.1: Illustration of the difference between laminar flow (a) at Reynolds number $Re = 1150$ and turbulent flow (b) at Reynolds number $Re = 2520$. This image is taken from [26], which describes the coloured filament experiments of Reynolds [82].

high Reynolds numbers for both two and three-dimensional problems, though three-dimensional problems are much worse. For example, if we cap the number of degrees of freedom at 10^{10}, which is still a very computationally demanding procedure, then $Re > 2.8 \times 10^4$ becomes intractable for two-dimensional flows and $Re > 2.2 \times 10^3$ for three-dimensional flows. To put this in perspective, the Reynolds number for a typical flow through Venturi-enhanced hydropower is $Re \sim 10^6$. Hence, DNS cannot be applied to model the flow in our case.

Reynolds exhibited the disruptive and chaotic qualities of turbulence in 1883 [82] with a coloured dye experiment (see Figure 2.1). He concluded that it would be almost impossible to model flow characteristics exactly and introduced the idea of averaging the Navier-Stokes equations over time. Such approaches are known as Reynolds-averaged Navier-Stokes (RANS) modelling. Let us define the time-averaging of a function f as

$$\bar{f} = \lim_{T \to \infty} \frac{1}{T} \int_0^T f(t)\, dt. \tag{2.14}$$

We split all variables into a time-dependant part, which corresponds to turbulent fluctuations, and a time-averaged part, such that

$$u_i = U_i(x, y, z) + u_i'(x, y, z, t), \quad i = 1, 2, 3, \tag{2.15}$$

$$p = P(x, y, z) + p'(x, y, z, t), \tag{2.16}$$

where subscripts $1, 2, 3$ correspond to coordinate directions x, y, z. We define the fluctuating parts to have zero mean, such that

$$\overline{u_i'} = 0, \quad i = 1, 2, 3, \tag{2.17}$$

$$\overline{p_i'} = 0. \tag{2.18}$$

This decomposition into mean and fluctuating parts is known as the Reynolds decomposition.

By inserting (2.15)-(2.16) into (2.1) and averaging, we see that the continuity equation is preserved for both the mean and fluctuating parts of the velocity

$$\frac{\partial U_i}{\partial x_i} = 0, \tag{2.19}$$

$$\frac{\partial u_i'}{\partial x_i} = 0, \tag{2.20}$$

where we sum over the indices using Einstein notation. Similarly, by inserting (2.15)-(2.16) into (2.2) and averaging, we get

$$\rho U_j \frac{\partial U_i}{\partial x_j} = -\frac{\partial P}{\partial x_i} + \mu \frac{\partial^2 U_i}{\partial x_j \partial x_j} - \overline{\rho u_j' \frac{\partial u_i'}{\partial x_j}}, \tag{2.21}$$

where the final term on the right hand side is an inertial term due to the turbulent fluctuations. We keep it on the right hand side, together with the viscous stress term, because it represents a stress contribution due to the turbulent fluctuations. Hence, it is known as the Reynolds stress term. It is typically written in terms of an 'eddy viscosity' μ_t, which we will not yet explicitly define, but gives the relation

$$-\overline{\rho u_j' \frac{\partial u_i'}{\partial x_j}} = \frac{\partial}{\partial x_j}\left(\mu_t \left(\frac{\partial U_i}{\partial x_j} + \frac{\partial U_j}{\partial x_i}\right)\right). \tag{2.22}$$

Considering (2.22), the momentum equation (2.21) can be rewritten as

$$\rho U_j \frac{\partial U_i}{\partial x_j} = -\frac{\partial P}{\partial x_i} + \frac{\partial}{\partial x_j}\left((\mu + \mu_t)\left(\frac{\partial U_i}{\partial x_j} + \frac{\partial U_j}{\partial x_i}\right)\right). \tag{2.23}$$

The eddy viscosity plays an important role in turbulence modelling. Whilst in laminar flows, viscous stresses are responsible for the diffusion of momentum, in turbulent flows, it is the eddies and the turbulent fluctuations which are responsible. Therefore, we represent the Reynolds stress as a diffusive term on the right hand side of (2.23), where the diffusion coefficient is the non-linear eddy viscosity.

Another important feature of the turbulent fluctuations is their associated kinetic energy k, which is defined as

$$k = \frac{1}{2}\overline{u_i' u_i'}. \tag{2.24}$$

We derive an equation for k by subtracting equation (2.23) from (2.2), which gives

$$\rho U_j \frac{\partial u_i'}{\partial x_j} + \rho u_j' \frac{\partial U_i}{\partial x_j} = -\frac{\partial p'}{\partial x_i} - \rho u_j' \frac{\partial u_i'}{\partial x_j} + \frac{\partial}{\partial x_j}\left(\mu\left(\frac{\partial u_i'}{\partial x_j} + \frac{\partial u_j'}{\partial x_i}\right) - \mu_t\left(\frac{\partial U_i}{\partial x_j} + \frac{\partial U_j}{\partial x_i}\right)\right), \quad (2.25)$$

followed by multiplying with u_i', dividing by ρ, and averaging over time, such that we get

$$U_i \frac{\partial k}{\partial x_i} = -\frac{\partial T_i}{\partial x_i} + \mathcal{P} - \varepsilon. \quad (2.26)$$

Here, we define the turbulent energy flux T_i, the turbulent energy production $\mathcal{P}$ and the turbulent energy dissipation ε as follows:

$$T_i = \overline{\left(\frac{1}{2}u_i' u_j' u_j' + \frac{1}{\rho}u_i' p' - \nu u_j'\left(\frac{\partial u_i'}{\partial x_j} + \frac{\partial u_j'}{\partial x_i}\right)\right)}, \quad (2.27)$$

$$\mathcal{P} = \frac{\nu_t}{2}\left(\frac{\partial U_i}{\partial x_j} + \frac{\partial U_j}{\partial x_i}\right)\left(\frac{\partial U_i}{\partial x_j} + \frac{\partial U_j}{\partial x_i}\right), \quad (2.28)$$

$$\varepsilon = \frac{\nu}{2}\overline{\left(\frac{\partial u_i'}{\partial x_j} + \frac{\partial u_j'}{\partial x_i}\right)\left(\frac{\partial u_i'}{\partial x_j} + \frac{\partial u_j'}{\partial x_i}\right)}, \quad (2.29)$$

where $\nu_t = \mu_t/\rho$ is the kinematic eddy viscosity. Equations (2.19), (2.23) and (2.26) together are by no means complete. The non-uniqueness of the Reynolds decomposition results in a so-called 'closure problem', where we are left with too few equations for too many unknowns. Typically, turbulence models make an empirical hypothesis for μ_t, T_i and ε to close the system. In the next section we discuss several such turbulence closure assumptions.

It should be noted that there is another method for modelling turbulence, which is a blend between the RANS approach and DNS. This method, known as Large Eddy Simulation (LES), resolves all the features of the turbulence downs to a certain length scale, like DNS, but uses a 'subgrid-scale' model to account for the features which are smaller than that length scale [79]. This approach is generally more accurate than RANS modelling, whilst maintaining a relatively low computational cost. However, for the work in this thesis we have not explored the use of LES.

2.2 Turbulence closure assumptions

There are a vast number of different turbulence closure models that have been proposed in the literature [79]. These models are largely classified into three different types. The first and most basic type, known as algebraic models, do not model the turbulent kinetic energy k, but instead use an eddy viscosity μ_t, which is a function of the mean velocity U_i and its gradients alone. In these models, (2.19) and (2.23) form a complete system of equations. The second type of closure models are known as one-equation models, which in addition to (2.19) and (2.23), have another governing equation. If the eddy viscosity depends on k, the additional governing equation is (2.26) (which requires further modelling assumptions for T_i and ε), or alternatively the governing equation (which is empirical) may be for the eddy viscosity μ_t itself [91]. The third type, known as two-equation models, include two additional governing equations. For example, if the eddy viscosity depends on k and the turbulent energy dissipation ε, these governing equations would be for k (2.26) and ε (an empirical equation). For the majority of this thesis we make use of only two different closure models: an algebraic Prandtl mixing length model [87], and a two-equation k-ε model [55]. Next we summarise the assumptions of these models.

2.2.1 Prandtl mixing length theory

In the early 20$^{\text{th}}$ century Ludwig Prandtl suggested a very simple algebraic model for the eddy viscosity which is based on simple scaling laws [80]. Prandtl mixing length theory states that the kinematic eddy viscosity is proportional to a velocity scale via a mixing length ℓ, such that

$$\nu_t = \ell\, U_0, \tag{2.30}$$

where, in simple shear flow, the velocity scale is locally determined by the mean velocity gradient

$$U_0 = \ell \left| \frac{\partial U}{\partial y} \right|. \tag{2.31}$$

Therefore, the eddy viscosity is written as

$$\nu_t = \ell^2 \left| \frac{\partial U}{\partial y} \right|. \tag{2.32}$$

The mixing length ℓ can be interpreted as the approximate distance it takes for a parcel of fluid to move before it becomes blended into its surroundings due to turbulent mixing [87]. The mixing length is considered as a variable and it is modelled differently depending on the problem. For example, in wall bounded flows the mixing length may be taken as the distance to the wall [35]. For flow in a shear layer, the mixing length may be taken as proportional to the width of the shear layer [79].

Since (2.32) is independent of k, the Prandtl mixing length model consists of only Equations (2.19) and (2.23), which form a complete system. This model provides a good approximation for simple turbulent flows, such as a boundary layer on a flat plate, or a free shear layer [87]. However, this eddy viscosity model is very simple and does not accurately capture the behaviour of more complicated turbulent flows. Nevertheless, it is one of the few turbulence models which yields simple and useful analytical results. Later in this chapter we use Prandtl mixing length theory to derive a model for the growth of a turbulent shear layer.

2.2.2 The k-ε model

Probably the most widely used turbulence model, the k-ε model uses an eddy viscosity which depends on both the turbulent kinetic energy k and the turbulent energy dissipation ε. Though we give a brief summary of the model here, full details are given by Launder & Spalding [55]. If we assume that the kinematic eddy viscosity depends on k and ε alone, then dimensional analysis indicates that

$$\nu_t = C_\mu \frac{k^2}{\varepsilon}, \tag{2.33}$$

where C_μ is an empirical constant of proportionality which has been determined from experiments, finding $C_\mu \approx 0.09$ [79].

In the k-ε model, as with many one and two-equation models, the turbulent energy flux (2.27) is modelled using a gradient-diffusion hypothesis [79] of the form

$$T_i = -\frac{\nu_t}{\sigma_k}\frac{\partial k}{\partial x_i}, \tag{2.34}$$

where σ_k is an empirical constant which is usually taken to be $\sigma_k = 1$. The physical interpretation of equation (2.34) is that the turbulent fluctuations are responsible for the diffusion of the turbulent kinetic energy k.

Considering (2.33) and (2.34), the governing equation for k (2.26) becomes

$$\frac{\partial}{\partial x_i}\left(kU_i - \frac{\nu_t}{\sigma_k}\frac{\partial k}{\partial x_i}\right) = \mathcal{P} - \varepsilon. \tag{2.35}$$

In addition to an equation for k, the k-ε model introduces a governing equation for the turbulent energy dissipation ε. This equation, which we can think of as entirely empirical, is

$$\frac{\partial}{\partial x_i}\left(\varepsilon U_i - \frac{\nu_t}{\sigma_\varepsilon}\frac{\partial \varepsilon}{\partial x_i}\right) = \frac{\varepsilon}{k}\left(C_1\mathcal{P} - C_2\varepsilon\right), \tag{2.36}$$

where C_1, C_2 and σ_ε are empirical constants which have been determined experimentally. A full list of the turbulence parameters of the k-ε model and their default

Parameter	C_μ	C_1	C_2	σ_k	σ_ε
Value	0.09	1.44	1.92	1.0	1.3

Table 2.2: List of turbulence parameters for the k-ε model and their default values.

values are given in Table 2.2. These default values show good comparison with experiments for a range of problems. However, they are not considered universal, and better comparison can be achieved for specific problems using different values for the parameters [79].

In summary, the complete system of equations for the k-ε model are the mass and momentum equations, (2.19) and (2.23), the k equation (2.35), and the ε equation (2.36). A discussion of the appropriate boundary conditions for k and ε is given by [55].

2.3 Turbulent boundary layer equations

The geometry of Ventruri-enhanced hydropower has a long and thin aspect ratio. For example, if we consider the mixer/diffuser section, a typical value for the total length is 20 m, whilst a typical value for the diameter is 0.5 m, giving a typical aspect ratio of 0.025. Therefore, the boundary layer approximation applies to the RANS equations (2.19) and (2.23).

We assign the following scalings to each variable

$$
\begin{gathered}
x = L\hat{x}, \quad y = \frac{L}{\sqrt{Re}}\hat{y}, \quad z = \frac{L}{\sqrt{Re}}\hat{z}, \quad U = U_0\hat{U}, \quad V = \frac{U_0}{\sqrt{Re}}\hat{V}, \\
W = \frac{U_0}{\sqrt{Re}}\hat{W}, \quad P = \rho U_0^2\hat{P}, \quad \mu_t = \mu\hat{\mu}_t.
\end{gathered}
\tag{2.37}
$$

In terms of these scaled variables, we rewrite Equations (2.19)-(2.23), highlighting the leading order terms, such that

$$\frac{\partial \hat{U}}{\partial \hat{x}} + \frac{\partial \hat{V}}{\partial \hat{y}} + \frac{\partial \hat{W}}{\partial \hat{z}} = 0, \tag{2.38}$$

$$\begin{aligned} \hat{U}\frac{\partial \hat{U}}{\partial \hat{x}} + \hat{V}\frac{\partial \hat{U}}{\partial \hat{y}} + \hat{W}\frac{\partial \hat{U}}{\partial \hat{z}} &= -\frac{\partial \hat{P}}{\partial \hat{x}} + \frac{1}{Re}\frac{\partial}{\partial \hat{x}}\left((1+\hat{\mu}_t)\, 2\frac{\partial \hat{U}}{\partial \hat{x}}\right) \\ &+ \frac{\partial}{\partial \hat{y}}\left((1+\hat{\mu}_t)\left(\frac{\partial \hat{U}}{\partial \hat{y}} + \frac{1}{Re}\frac{\partial \hat{V}}{\partial \hat{x}}\right)\right) + \frac{\partial}{\partial \hat{z}}\left((1+\hat{\mu}_t)\left(\frac{\partial \hat{U}}{\partial \hat{z}} + \frac{1}{Re}\frac{\partial \hat{W}}{\partial \hat{x}}\right)\right), \end{aligned} \tag{2.39}$$

$$\begin{aligned} \hat{U}\frac{\partial \hat{V}}{\partial \hat{x}} + \hat{V}\frac{\partial \hat{V}}{\partial \hat{y}} + \hat{W}\frac{\partial \hat{V}}{\partial \hat{z}} &= -Re\frac{\partial \hat{P}}{\partial \hat{y}} + \frac{1}{Re}\frac{\partial}{\partial \hat{x}}\left((1+\hat{\mu}_t)\left(\frac{\partial \hat{V}}{\partial \hat{x}} + Re\frac{\partial \hat{U}}{\partial \hat{y}}\right)\right) \\ &+ \frac{\partial}{\partial \hat{y}}\left((1+\hat{\mu}_t)\, 2\frac{\partial \hat{V}}{\partial \hat{y}}\right) + \frac{\partial}{\partial \hat{z}}\left((1+\hat{\mu}_t)\left(\frac{\partial \hat{V}}{\partial \hat{z}} + \frac{\partial \hat{W}}{\partial \hat{y}}\right)\right), \end{aligned} \tag{2.40}$$

$$\begin{aligned} \hat{U}\frac{\partial \hat{W}}{\partial \hat{x}} + \hat{V}\frac{\partial \hat{W}}{\partial \hat{y}} + \hat{W}\frac{\partial \hat{W}}{\partial \hat{z}} &= -Re\frac{\partial \hat{P}}{\partial \hat{z}} + \frac{1}{Re}\frac{\partial}{\partial \hat{x}}\left((1+\hat{\mu}_t)\left(\frac{\partial \hat{W}}{\partial \hat{x}} + Re\frac{\partial \hat{U}}{\partial \hat{z}}\right)\right) \\ &+ \frac{\partial}{\partial \hat{y}}\left((1+\hat{\mu}_t)\left(\frac{\partial \hat{W}}{\partial \hat{y}} + \frac{\partial \hat{V}}{\partial \hat{z}}\right)\right) + \frac{\partial}{\partial \hat{z}}\left((1+\hat{\mu}_t)\, 2\frac{\partial \hat{W}}{\partial \hat{z}}\right). \end{aligned} \tag{2.41}$$

Therefore, to leading order, the non-dimensional turbulent boundary layer equations are

$$\frac{\partial \hat{U}}{\partial \hat{x}} + \frac{\partial \hat{V}}{\partial \hat{y}} + \frac{\partial \hat{W}}{\partial \hat{z}} = 0, \tag{2.42}$$

$$\hat{U}\frac{\partial \hat{U}}{\partial \hat{x}} + \hat{V}\frac{\partial \hat{U}}{\partial \hat{y}} + \hat{W}\frac{\partial \hat{U}}{\partial \hat{z}} = -\frac{\partial \hat{P}}{\partial \hat{x}} + \frac{\partial}{\partial \hat{y}}\left((1+\hat{\mu}_t)\frac{\partial \hat{U}}{\partial \hat{y}}\right) + \frac{\partial}{\partial \hat{z}}\left((1+\hat{\mu}_t)\frac{\partial \hat{U}}{\partial \hat{z}}\right), \tag{2.43}$$

$$0 = -\frac{\partial \hat{P}}{\partial \hat{y}}, \tag{2.44}$$

$$0 = -\frac{\partial \hat{P}}{\partial \hat{z}}. \tag{2.45}$$

Rewriting (2.42)-(2.45) in dimensional form, and reverting the variables back to lower case for convenience, we get

$$\frac{\partial u}{\partial x}+\frac{\partial v}{\partial y}+\frac{\partial w}{\partial z}=0, \tag{2.46}$$

$$\begin{aligned}u\frac{\partial u}{\partial x}+v\frac{\partial u}{\partial y}+w\frac{\partial u}{\partial z}&=-\frac{1}{\rho}\frac{\partial p}{\partial x}+\frac{\partial}{\partial y}\left(\left(\nu+\nu_t\right)\frac{\partial u}{\partial y}\right)\\&\quad+\frac{\partial}{\partial z}\left(\left(\nu+\nu_t\right)\frac{\partial u}{\partial z}\right),\end{aligned} \tag{2.47}$$

$$0=-\frac{\partial p}{\partial y}, \tag{2.48}$$

$$0=-\frac{\partial p}{\partial z}. \tag{2.49}$$

For two-dimensional flows with coordinates (x, y), the corresponding turbulent boundary layer equations are

$$\frac{\partial u}{\partial x}+\frac{\partial v}{\partial y}=0, \tag{2.50}$$

$$u\frac{\partial u}{\partial x}+v\frac{\partial u}{\partial y}=-\frac{1}{\rho}\frac{\partial p}{\partial x}+\frac{\partial}{\partial y}\left(\left(\nu+\nu_t\right)\frac{\partial u}{\partial y}\right), \tag{2.51}$$

$$0=-\frac{\partial p}{\partial y}. \tag{2.52}$$

For axisymmetric flows, we follow the above steps, except starting with the Navier-Stokes equations in cylindrical coordinates (x, r, θ). The corresponding the time-averaged velocities are (U_x, U_r, U_θ). Since the flow is axisymmetric, we ignore all derivatives in θ. Furthermore, the corresponding scalings for the variables are

$$\begin{gathered}x=L\hat{x},\quad r=\frac{L}{\sqrt{Re}}\hat{r},\quad \theta=\hat{\theta},\quad U_x=U_0\hat{U},\quad U_r=\frac{U_0}{\sqrt{Re}}\hat{U}_r,\\ U_\theta=U_0\hat{U}_\theta,\quad P=\rho U_0^2\hat{P},\quad \mu_t=\mu\hat{\mu}_t.\end{gathered} \tag{2.53}$$

Therefore, in dimensional form and reverting the variables back to lower case for convenience, the cylindrical turbulent boundary layer equations are

$$\frac{\partial u_x}{\partial x}+\frac{1}{r}\frac{\partial}{\partial r}\left(ru_r\right)=0, \tag{2.54}$$

$$u_x\frac{\partial u_x}{\partial x}+u_r\frac{\partial u_x}{\partial r}=-\frac{1}{\rho}\frac{\partial p}{\partial x}+\frac{1}{r}\frac{\partial}{\partial r}\left(\left(\nu+\nu_t\right)r\frac{\partial u_x}{\partial r}\right), \tag{2.55}$$

$$-\frac{u_\theta^2}{r}=-\frac{1}{\rho}\frac{\partial p}{\partial r}, \tag{2.56}$$

$$u_x\frac{\partial u_\theta}{\partial x}+\frac{u_r}{r}\frac{\partial}{\partial r}\left(ru_\theta\right)=\frac{1}{r^2}\frac{\partial}{\partial r}\left(\left(\nu+\nu_t\right)r^2\left(\frac{\partial u_\theta}{\partial r}-\frac{u_\theta}{r}\right)\right). \tag{2.57}$$

If there is no azimuthal velocity component, $u_\theta = 0$, then Equations (2.54)-(2.57) reduce to

$$\frac{\partial u_x}{\partial x} + \frac{1}{r}\frac{\partial}{\partial r}(r u_r) = 0, \tag{2.58}$$

$$u_x \frac{\partial u_x}{\partial x} + u_r \frac{\partial u_x}{\partial r} = -\frac{1}{\rho}\frac{\partial p}{\partial x} + \frac{1}{r}\frac{\partial}{\partial r}\left((\nu + \nu_t)\, r \frac{\partial u_x}{\partial r} \right), \tag{2.59}$$

$$0 = -\frac{1}{\rho}\frac{\partial p}{\partial r}. \tag{2.60}$$

2.4 Integral equations of mass and momentum

Having derived the turbulent boundary layer equations, we now use them to formulate integral equations of mass and momentum which we use later in the thesis. These equations are derived by integrating the turbulent boundary layer equations across a region of flow. This approach enables us to model the flow behaviour using ordinary differential equations (ODEs), instead of the RANS partial differential equations (2.19) and (2.23). These ODEs are computationally cheap and attractive for their simplicity. We derive the equations in three different flow scenarios: a two-dimensional fluid layer, a three-dimensional rectangular channel, and a cylindrical pipe.

2.4.1 Two-dimensional fluid layer

We start by considering incompressible flow in a two-dimensional fluid layer defined by $0 \leq x \leq L$, $a(x) \leq y \leq b(x)$, where a, $b \ll L$ (see Figure 2.2). Because the domain is long and thin, the two-dimensional boundary layer approximation to the Navier-Stokes equations (2.50)-(2.52) is appropriate for modelling the flow in the whole domain. Firstly note that because of (2.52) the pressure varies in the x direction alone $p = p(x)$. We integrate conservation of mass (2.50) across the fluid layer, from $y = a$ to $y = b$, giving

$$\frac{\mathrm{d}}{\mathrm{d}x}\int_a^b u \,\mathrm{d}y + \left(v - u\frac{\mathrm{d}b}{\mathrm{d}x} \right)\bigg|_{y=b} - \left(v - u\frac{\mathrm{d}a}{\mathrm{d}x} \right)\bigg|_{y=a} = 0. \tag{2.61}$$

Next we integrate conservation of momentum (2.51) across the fluid layer, from $y = a$ to $y = b$, giving

$$\begin{aligned} \rho\frac{\mathrm{d}}{\mathrm{d}x}\int_a^b u^2 \,\mathrm{d}y + \rho\left(uv - u^2\frac{\mathrm{d}b}{\mathrm{d}x} \right)\bigg|_{y=b} - \rho\left(uv - u^2\frac{\mathrm{d}a}{\mathrm{d}x} \right)\bigg|_{y=a} & \\ = -(b-a)\frac{\mathrm{d}p}{\mathrm{d}x} + \tau_b - \tau_a&, \end{aligned} \tag{2.62}$$

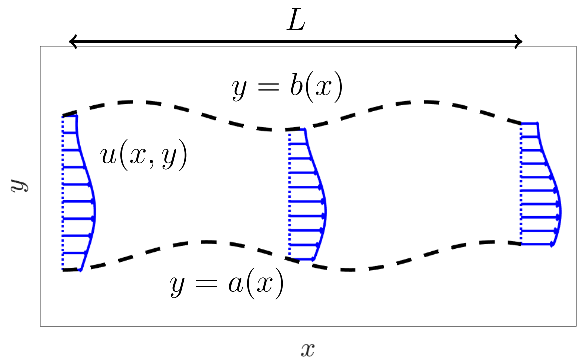

Figure 2.2: Schematic diagram of a two-dimensional fluid layer.

where the shear stress terms τ_a and τ_b are given by

$$\tau_a = \left[\rho\left(\nu + \nu_t\right)\frac{\partial u}{\partial y}\right]_{y=a}, \tag{2.63}$$

$$\tau_b = \left[\rho\left(\nu + \nu_t\right)\frac{\partial u}{\partial y}\right]_{y=b}. \tag{2.64}$$

Equations (2.61)-(2.64) do not form a complete system of equations since there are more than 2 unknown variables and there are only 2 governing equations. In particular, the integrated the boundary layer equations are ordinary differential equations, which do not tell us how u varies with y. However, if we prescribe the functional form of u, such that u is given in terms of y and n coefficients which depend on x, $U_1(x)$, $U_2(x)$, $\ldots, U_n(x)$, then we can insert u into (2.61) and (2.62), giving governing equations for the coefficients. We need to be careful in choosing the other unknowns of the problem, such that the total number of variables sums to 2.

In total, there are $7 + n$ variables, $a(x)$, $b(x)$, $v|_{y=a}$, $v|_{y=b}$, τ_a, τ_b, $p(x)$, $U_1(x)$, $U_2(x)$, $\ldots, U_n(x)$, so we need to prescribe $5+n$ of these variables to make the system complete. For example, we could choose $n = 1$ and prescribe all the variables except $p(x)$, thereby solving for the velocity and pressure in a layer of prescribed width. Another option would be to choose $n = 0$ (i.e. coefficients independent of x), and prescribe all the variables except $b(x)$ and $p(x)$, thereby solving a free boundary problem for the width of the layer, together with the pressure. For the purpose of illustration we choose two simple examples: a plane shear flow with entrainment, and a flow in a two-dimensional channel.

2.4.1.1 Plane shear flow with entrainment

In this example, we consider plane shear flow between an impermeable wall and an infinite free stream, as illustrated in Figure 2.3. The impermeable wall is at

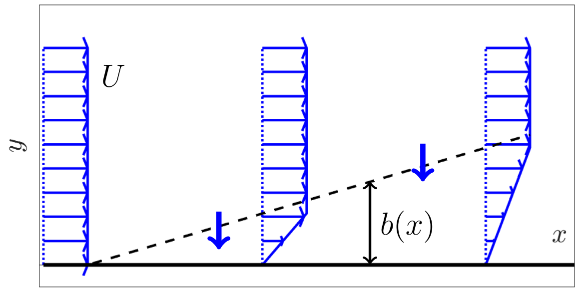

Figure 2.3: Schematic diagram of a plane shear flow with entrainment.

$y = a = 0$, such that $v|_{y=0} = 0$, whereas the infinite free stream, with constant velocity U, is defined for $y > b(x)$. We assume that the flow in the fluid layer, defined for $0 \leq y \leq b(x)$, has a shear profile in which the velocity varies linearly with y, such that

$$u = \frac{Uy}{b(x)}. \tag{2.65}$$

For this case, $n = 0$, since U is a constant. Similarly to the model of Morton et al. for jets [70], we assume that the plane shear flow layer entrains fluid from the free stream at a rate proportional to the free stream velocity, such that

$$\left.\left(v - u\frac{\mathrm{d}b}{\mathrm{d}x}\right)\right|_{y=b} = -EU, \tag{2.66}$$

where E is an entrainment coefficient. Finally, in order to determine the stress terms, (2.63) and (2.64), we require a closure assumption for the eddy viscosity ν_t. For this we use a Prandtl mixing length model (2.32) with a mixing length taken as the width of the layer $\ell = b$, such that

$$\nu_t = bU. \tag{2.67}$$

Furthermore, we expect $\nu \ll \nu_t$ within the layer such that the stress terms are approximated as

$$\tau_0 = \tau_b = \rho U^2. \tag{2.68}$$

With these assumptions, (2.61) and (2.62) become

$$\frac{1}{2}U\frac{\mathrm{d}b}{\mathrm{d}x} - EU = 0, \tag{2.69}$$

$$\frac{1}{3}\rho U^2\frac{\mathrm{d}b}{\mathrm{d}x} - \rho EU^2 = -b\frac{\mathrm{d}p}{\mathrm{d}x}, \tag{2.70}$$

which is a complete system of ordinary differential equations for $b(x)$ and $p(x)$. The solutions is

$$b = b(0) + 2Ex, \tag{2.71}$$
$$p = p(0) + \frac{1}{6}\rho U^2 \log\left(1 + \frac{2Ex}{b(0)}\right). \tag{2.72}$$

Hence, the width of the layer grows linearly, whilst the pressure grows logarithmically.

2.4.1.2 Two-dimensional channel

In this example, we consider flow in a two dimensional channel defined by $-h(x) \leq y \leq h(x)$. We assume that the flow is symmetric about the channel centreline $y = 0$ and hence, we only consider the region defined by $0 \leq y \leq h(x)$. Therefore, we take $a = 0$ and $b = h$. We impose the no-slip condition on the wall at $y = h(x)$, such that

$$u = v = 0, \quad \text{on} \quad y = h(x), \tag{2.73}$$

whereas on the channel centreline, we have the symmetry condition

$$\frac{\partial u}{\partial y} = v = 0, \quad \text{on} \quad y = 0. \tag{2.74}$$

Therefore, both the transverse velocities, $v|_{y=0}$ and $v_{y=h}$, and the stress at the centreline (2.63) vanish.

Next, we decompose the flow into an 'outer flow', with velocity $u = U(x)$ (i.e. $n = 1$), and narrow boundary layers adjacent to the walls that allow the no-slip conditions to be satisfied. We adopt two different approaches to modelling the boundary layers at the wall. In the first and most simple case, the boundary layers are not resolved explicitly but their effect is parameterised by writing the wall stress term (2.64) in terms of the outer velocity near the wall and a friction factor, such that

$$\tau_h = -\frac{1}{8} f \rho U^2, \tag{2.75}$$

where f is an empirical friction factor. Therefore, the governing equations for the flow are

$$\frac{\mathrm{d}}{\mathrm{d}x}\int_0^h u \,\mathrm{d}y = 0, \tag{2.76}$$
$$\rho\frac{\mathrm{d}}{\mathrm{d}x}\int_0^h u^2 \,\mathrm{d}y = -h\frac{\mathrm{d}p}{\mathrm{d}x} - \frac{1}{8} f \rho U^2, \tag{2.77}$$

which simplify to

$$\frac{\mathrm{d}U}{\mathrm{d}x} = -\frac{U}{h}\frac{\mathrm{d}h}{\mathrm{d}x}, \tag{2.78}$$

$$\frac{\mathrm{d}p}{\mathrm{d}x} = \rho\frac{U^2}{h}\left(\frac{\mathrm{d}h}{\mathrm{d}x} - \frac{f}{8}\right). \tag{2.79}$$

For certain channel shapes (e.g. linearly expanding walls), it is possible to find an analytical solution to (2.78)-(2.79) for the velocity U and pressure p.

In the second approach, we resolve the boundary layer by introducing a region in between the wall and the bulk flow profile, in which we assume a 1/7 power law velocity profile. This is motivated by experimental studies [87] which show that such a velocity profile within the boundary layer exhibits good comparison with the data for a range of Reynolds numbers ($4 \times 10^3 < Re < 3.2 \times 10^6$).

Therefore, near the wall at $y = h$, we introduce a boundary layer of width $h_b(x)$, such that the velocity profile takes the form

$$u = \begin{cases} U\left(\frac{h-y}{h_b}\right)^{1/7} & : \quad h - h_b < y < h, \\ U & : \quad 0 < y < h - h_b. \end{cases} \tag{2.80}$$

Equation (2.80) satisfies the no-slip condition (2.73) and matches with the velocity in the plug region. In reality, within the turbulent boundary layer there is a viscous sub-layer, a log-law layer and a matching region in between [87], but for the purposes of this study we neglect these details and assume that (2.80) applies all the way to the channel wall. Hence, we model the stress term (2.64) using the same friction factor parameterisation as the first approach, resulting in Equation (2.75).

However, in the second approach, we have introduced a new unknown variable h_b, the boundary layer thickness. This is determined by applying the same width-averaging methodology as above to a fluid layer with $a = h - h_b$ and $b = h$. In this way, (2.61) and (2.62) become

$$\frac{\mathrm{d}}{\mathrm{d}x}\int_{h-h_b}^{h} u\,\mathrm{d}y - v|_{y=h-h_b} + U\frac{\mathrm{d}}{\mathrm{d}x}(h - h_b) = 0, \tag{2.81}$$

$$\rho\frac{\mathrm{d}}{\mathrm{d}x}\int_{h-h_b}^{h} u^2\,\mathrm{d}y - \rho U v|_{y=h-h_b} + \rho U^2\frac{\mathrm{d}}{\mathrm{d}x}(h - h_b) = -h_b\frac{\mathrm{d}p}{\mathrm{d}x} - \frac{1}{8}f\rho U^2 - \tau_{h-h_b}. \tag{2.82}$$

We ignore the shear stress between the edge of the boundary layer and the plug region, such that $\tau_{h-h_b} = 0$, since we expect it to be small. By substituting $v|_{y=h-h_b}$ from (2.81) into (2.82), we get

$$\rho\frac{\mathrm{d}}{\mathrm{d}x}\int_{h-h_b}^{h} u^2\,\mathrm{d}y - \rho U\frac{\mathrm{d}}{\mathrm{d}x}\int_{h-h_b}^{h} u\,\mathrm{d}y = -h_b\frac{\mathrm{d}p}{\mathrm{d}x} - \frac{1}{8}f\rho U^2. \tag{2.83}$$

The system of equations (2.76), (2.77) and (2.83) (where u is given by (2.80)) govern the unknowns $U(x)$, $p(x)$ and $h_b(x)$, given a channel shape $h(x)$. Note that it is straightforward to show that (2.77) and (2.83) imply that Bernoulli's equation holds in the region $0 < y < h - h_b$, such that

$$p + \frac{1}{2}\rho U^2 = \text{const.} \tag{2.84}$$

Therefore, the above system describes an inviscid plug region with no energy loss, and a boundary layer region which accounts for wall drag.

These very simple examples are illustrative of the methodology used throughout the chapters in the thesis. We use integral equations of mass and momentum of the same form as (2.61) and (2.62), together with certain assumptions about the form of the flow profile, the entrainment, and stress terms, which simplify the problem to solving a set of ordinary differential equations for a reduced number of variables.

2.4.2 Three-dimensional rectangular channel

Next we consider incompressible flow in a three dimensional channel defined by $0 \leq x \leq L$, $-h(x) \leq y \leq h(x)$, $-D \leq z \leq D$, where $h \ll L$ and $D \ll L$. This example is motivated by our experimental work where we investigate flow in a rectangular channel, as discussed later in Chapter 3. We assume that the flow is symmetric about the xy and xz planes and hence, we only consider the region defined by $0 \leq x \leq L$, $0 \leq y \leq h(x)$ and $0 \leq z \leq D$. Because the domain is long and thin, we model the flow with the three-dimensional turbulent boundary layer equations (2.46)-(2.49). Similarly to before, the pressure varies in the x direction alone $p = p(x)$. We impose the no-slip condition on the walls at $y = h(x)$ and $z = D$

$$u = v = w = 0, \quad \text{on} \quad y = h(x), \tag{2.85}$$

$$u = v = w = 0, \quad \text{on} \quad z = D, \tag{2.86}$$

whereas on the xz and xy planes we impose the symmetry conditions

$$\frac{\partial u}{\partial y} = \frac{\partial w}{\partial y} = v = 0, \quad \text{on} \quad y = 0, \tag{2.87}$$

$$\frac{\partial u}{\partial z} = \frac{\partial v}{\partial z} = w = 0, \quad \text{on} \quad z = 0. \tag{2.88}$$

Now we integrate Equations (2.46) and (2.47) across the channel in the y and z directions, using boundary conditions (2.85)-(2.88), to give

$$\frac{\mathrm{d}}{\mathrm{d}x}\int_0^D\int_0^h u\,\mathrm{d}y\,\mathrm{d}z = 0, \tag{2.89}$$

$$\rho\frac{\mathrm{d}}{\mathrm{d}x}\int_0^D\int_0^h u^2\,\mathrm{d}y\,\mathrm{d}z = -Dh\frac{\mathrm{d}p}{\mathrm{d}x} + D\tau_h + h\tau_D, \tag{2.90}$$

where the wall stress terms are

$$\tau_h = \frac{1}{D}\int_0^D \left[\rho\left(\nu+\nu_t\right)\frac{\partial u}{\partial y}\right]_{y=h}\mathrm{d}z, \tag{2.91}$$

$$\tau_D = \frac{1}{h}\int_0^h \left[\rho\left(\nu+\nu_t\right)\frac{\partial u}{\partial z}\right]_{z=D}\mathrm{d}y. \tag{2.92}$$

Similarly to the two-dimensional channel, we approximate the stress terms by decomposing the flow into an 'outer flow' and narrow boundary layers adjacent to the walls that allow the no-slip conditions to be satisfied. Therefore, we approximate (2.91)-(2.92) in terms of the outer velocity near the wall and a friction factor. Let us assume that the bulk velocity within the channel is independent of z (except for narrow boundary layers near the top and bottom walls), such that $u = u(x, y)$ in the bulk, where the velocity near the wall at $y = h$ is $u = U(x)$. Therefore, in this case the wall stress terms on the right hand side of (2.90) are replaced with

$$D\tau_h + h\tau_D = -\frac{1}{8}Df\rho U^2 + \int_0^h -\frac{1}{8}f\rho u^2\,\mathrm{d}y, \tag{2.93}$$

where f is an empirical friction factor. With these approximations, Equations (2.89) and (2.90) rearrange to give

$$\frac{\mathrm{d}}{\mathrm{d}x}\int_0^h u\,\mathrm{d}y = 0, \tag{2.94}$$

$$\rho\frac{\mathrm{d}}{\mathrm{d}x}\int_0^h u^2\,\mathrm{d}y = -h\frac{\mathrm{d}p}{\mathrm{d}x} - \frac{1}{8}f\rho U^2 + \frac{1}{D}\int_0^h -\frac{1}{8}f\rho u^2\,\mathrm{d}y. \tag{2.95}$$

Equations (2.94)-(2.95) do not form a closed system since we have not prescribed the y-dependence of u. However, we do so later in Chapter 4.

It should be noted that if we remove the z dimension (let $D \to \infty$), the final term in (2.95) vanishes and we are left with the two-dimensional form of the equations (2.76)-(2.77), as expected.

Note that, for plug flow which is independent of y everywhere, and independent of z everywhere except in narrow boundary layers near the top and bottom walls, it is possible to derive an equation which is similar to Bernoulli's equation (2.84) with an added wall drag contribution. If the bulk flow is taken as $u = U(x)$, then by integrating (2.47) over the depth of the channel, we get

$$\frac{\mathrm{d}}{\mathrm{d}x}\left(p + \frac{1}{2}\rho U^2\right) D = \left[\rho\left(\nu + \nu_t\right)\frac{\partial u}{\partial z}\right]_0^D = -\frac{1}{8} f \rho U^2, \tag{2.96}$$

where we have made use of the same friction factor parameterisation of the wall stress as above. If the right hand side of Equation (2.96) is zero, then it is identical to (2.84). Therefore, (2.96) can be interpreted as an analogue for Bernoulli's equation in situations where there is wall drag only on the top and bottom walls.

2.4.3 Cylindrical pipe

We start by outlining the analogue equations to (2.61) and (2.62) for axisymmetric flow in an annulus defined for $a(x) \leq r \leq b(x)$. This is useful to help follow the cylindrical pipe example which follows. We integrate conservation of mass (2.54) across the fluid layer, from $r = a$ to $r = b$, giving

$$\frac{\mathrm{d}}{\mathrm{d}x}\int_a^b r u_x \,\mathrm{d}r + \left.\left(r u_r - r u_x \frac{\mathrm{d}b}{\mathrm{d}x}\right)\right|_{r=b} - \left.\left(r u_r - r u_x \frac{\mathrm{d}a}{\mathrm{d}x}\right)\right|_{r=a} = 0. \tag{2.97}$$

Next we integrate conservation of axial and azimuthal momentum (2.55)-(2.56) across the fluid layer, from $r = a$ to $r = b$, giving

$$\begin{aligned}\rho\frac{\mathrm{d}}{\mathrm{d}x}\int_a^b r u_x^2 \,\mathrm{d}r &+ \rho\left.\left(r u_x u_r - r u_x^2 \frac{\mathrm{d}b}{\mathrm{d}x}\right)\right|_{r=b} \\ &- \rho\left.\left(r u_x u_r - u_x^2 \frac{\mathrm{d}a}{\mathrm{d}x}\right)\right|_{r=a} = -\int_a^b r\frac{\partial p}{\partial x}\,\mathrm{d}r + b\tau_{b_r} - a\tau_{a_r},\end{aligned} \tag{2.98}$$

$$\begin{aligned}\rho\frac{\mathrm{d}}{\mathrm{d}x}\int_a^b r^2 u_x u_\theta \,\mathrm{d}r &+ \rho\left.\left(r^2 u_\theta u_r - r^2 u_x u_\theta \frac{\mathrm{d}b}{\mathrm{d}x}\right)\right|_{r=b} \\ &- \rho\left.\left(r^2 u_\theta u_r - r^2 u_x u_\theta \frac{\mathrm{d}a}{\mathrm{d}x}\right)\right|_{r=a} = b^2\tau_{b_\theta} - a^2\tau_{a_\theta},\end{aligned} \tag{2.99}$$

where the shear stress terms are given by

$$\tau_{a_r} = \left[\rho\left(\nu + \nu_t\right)\frac{\partial u_x}{\partial r}\right]_{r=a}, \tag{2.100}$$

$$\tau_{b_r} = \left[\rho\left(\nu + \nu_t\right)\frac{\partial u_x}{\partial r}\right]_{r=b}, \tag{2.101}$$

$$\tau_{a_\theta} = \left[\rho\left(\nu + \nu_t\right)\left(\frac{\partial u_\theta}{\partial r} - \frac{u_\theta}{r}\right)\right]_{r=a}, \tag{2.102}$$

$$\tau_{b_\theta} = \left[\rho\left(\nu + \nu_t\right)\left(\frac{\partial u_\theta}{\partial r} - \frac{u_\theta}{r}\right)\right]_{r=b}. \tag{2.103}$$

Next we consider axisymmetric flow in a cylindrical pipe defined by $0 \leq x \leq L$ and $0 \leq r \leq h(x)$, where $h \ll L$. Because the domain is long and thin, we model the flow in the whole domain using the cylindrical turbulent boundary layer equations (2.54)-(2.57). Hence, we follow the fluid layer example above with $a = 0$ and $b = h$. We impose the no-slip condition on the pipe wall $r = h(x)$, and the symmetry condition on the pipe axis $r = 0$, such that

$$u_x = u_r = u_\theta = 0, \quad \text{on} \quad r = h(x), \tag{2.104}$$

$$\frac{\partial u_x}{\partial r} = 0, \quad \text{and} \quad u_r,\, u_\theta = \text{finite}, \quad \text{on} \quad r = 0. \tag{2.105}$$

Therefore, both the radial velocities, $u_r|_{r=0}$ and $u_r|_{r=h}$, and the stress on the centreline (2.100) vanish. In this way, (2.97)-(2.99) become

$$\frac{\mathrm{d}}{\mathrm{d}x}\int_0^h r u_x \,\mathrm{d}r = 0, \tag{2.106}$$

$$\rho\frac{\mathrm{d}}{\mathrm{d}x}\int_0^h r u_x^2 \,\mathrm{d}r = -\int_0^h r\frac{\partial p}{\partial x}\,\mathrm{d}r + h\tau_{h_r}, \tag{2.107}$$

$$\rho\frac{\mathrm{d}}{\mathrm{d}x}\int_0^h r^2 u_\theta u_x \,\mathrm{d}r = h^2\tau_{h_\theta}. \tag{2.108}$$

Similarly to the two-dimensional channel, we approximate the stress terms, (2.101) and (2.103), in terms of the outer velocity near the wall and a friction factor. Therefore, if the bulk flow profile is taken to be a solid body rotating plug flow, with velocity $\mathbf{u} = (U_x(x), 0, U_\theta(x)r/h)$, then following Bourget & Marichal [13], the wall stress terms on the right hand side of (2.107) and (2.108) are replaced with

$$h\tau_{h_r} = -\frac{1}{8}f\rho U_x h\sqrt{U_x^2 + U_\theta^2}, \tag{2.109}$$

$$h^2\tau_{h_\theta} = -\frac{1}{8}f\rho U_\theta h^2\sqrt{U_x^2 + U_\theta^2}. \tag{2.110}$$

Then, (2.56) and (2.106)-(2.107) form a complete system of equations for the variables $U_x(x)$, $U_\theta(x)$ and $p(x,r)$, given a pipe shape $h(x)$.

It should be noted that in the non-swirling case (2.108) is redundant, and (2.56) indicates that $p = p(x)$, such that the remaining equations become

$$\frac{\mathrm{d}}{\mathrm{d}x}\int_0^h r u_x \,\mathrm{d}r = 0, \tag{2.111}$$

$$\rho\frac{\mathrm{d}}{\mathrm{d}x}\int_0^h r u_x^2 \,\mathrm{d}r = -\frac{1}{2}h^2\frac{\mathrm{d}p}{\mathrm{d}x} - \frac{1}{8}f\rho U_x^2 h. \tag{2.112}$$

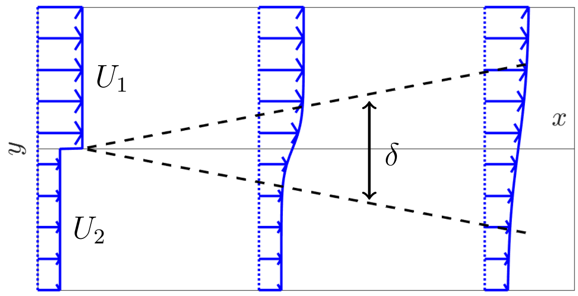

Figure 2.4: Schematic diagram of a shear layer between parallel flows.

2.5 A shear layer model for unconfined parallel flows

Shear layers, where two parallel flows undergo turbulent mixing, are a common feature of the work in this thesis. For laterally unconfined flows, shear layers can be described using a simple analytical model, which is derived from the turbulent boundary layer equations and Prandtl mixing length theory. In this section we derive this simple model, which we will later modify to account for situations with confining walls.

The flow situation we consider is illustrated in Figure 2.4, in which we illustrate our chosen coordinate system (x, y). A flow with velocity U_1 in the x direction meets a second, parallel flow with velocity $U_2 < U_1$. Due to the Kelvin-Helmholtz instability [100], the flow profile is unstable to perturbations. The discontinuous jump in velocity between U_2 and U_1 generates a vortex sheet which rolls up downstream into discrete vortical structures. These structures pair and merge forming larger vortical structures [105]. In this way a region of flow forms between the parallel flows which undergoes intense mixing, and which grows downstream, entraining fluid from either side. The time-averaged velocity in the layer is a smoothed quasi-linear profile which increases from U_2 to U_1 over an approximate width $\delta(x)$ [48]. The layer is known as a *shear layer* due to these large velocity gradients, or a *mixing layer*, due to the intense mixing.

The shear layer region is long and thin, such that the two-dimensional boundary layer approximation applies (2.50)-(2.52). However, since the flow is unconfined, it is expected that pressure gradients in the x direction are negligible [48]. Furthermore, we ignore the viscous stress term in (2.51) since we expect $\nu \ll \nu_t$ within the shear layer. Therefore, the governing equations, defined for $0 \leq x < \infty$ and $-\infty < y < \infty$, are

$$\frac{\partial u}{\partial x} + \frac{\partial v}{\partial y} = 0, \tag{2.113}$$

$$u\frac{\partial u}{\partial x} + v\frac{\partial u}{\partial y} = \frac{\partial}{\partial y}\left(\nu_t \frac{\partial u}{\partial y}\right). \tag{2.114}$$

The boundary conditions for the streamwise velocity u correspond to matching with the free stream velocities

$$u(x, \infty) = U_1, \tag{2.115}$$

$$u(x, -\infty) = U_2, \tag{2.116}$$

and the inflow condition

$$u(0, y) = U_c + \frac{\Delta U}{2}\mathrm{sgn}(y), \tag{2.117}$$

where $U_c = (U_1 + U_2)/2$ is the average velocity and $\Delta U = U_1 - U_2$ is the velocity difference. From [87, 96] there is also the boundary condition

$$v(x, \infty) = -\frac{U_2}{U_1} v(x, -\infty). \tag{2.118}$$

The condition (2.118) indicates that there is greater entrainment from the slower stream than the faster stream. Hence the dividing streamline, along which $v = 0$, is inclined downwards from the x-axis. This is in accordance with experimental observations [79].

We rewrite the velocity u in terms of a similarity variable $\zeta = y/\delta(x)$ that depends on the width of the shear layer, such that

$$u = U_c + \Delta U \frac{\mathrm{d}\mathcal{U}}{\mathrm{d}\zeta}, \tag{2.119}$$

where $\mathcal{U} = \mathcal{U}(\zeta)$ is an unknown function. From (2.113) the transverse velocity v must take the form

$$v = \Delta U \frac{\mathrm{d}\delta}{\mathrm{d}x}\left(\zeta \frac{\mathrm{d}\mathcal{U}}{\mathrm{d}\zeta} - \mathcal{U}\right). \tag{2.120}$$

We use the Prandtl mixing length model (2.32) for the eddy viscosity, where we approximate the velocity gradient by

$$\left|\frac{\partial u}{\partial y}\right| \approx \frac{\Delta U}{\delta}, \tag{2.121}$$

and we use a mixing length proportional to the width of the shear layer $\ell = C\delta$, such that

$$\nu_t = C^2 \delta \Delta U. \tag{2.122}$$

Inserting (2.119), (2.120) and (2.122) into the momentum equation (2.114), we get

$$\frac{\mathrm{d}\delta}{\mathrm{d}x}\frac{U_c}{\Delta U}\left(\frac{\Delta U}{U_c}\mathcal{U}+\zeta\right)\frac{\mathrm{d}^2\mathcal{U}}{\mathrm{d}\zeta^2}+C^2\frac{\mathrm{d}^3\mathcal{U}}{\mathrm{d}\zeta^3}=0. \tag{2.123}$$

Similarity solutions to (2.123) are only possible if

$$\frac{\mathrm{d}\delta}{\mathrm{d}x}\frac{U_c}{\Delta U}=S, \tag{2.124}$$

where S is a constant known as the spreading parameter, and whose value has been determined by experiments, finding $S = 0.06 - 0.11$ [79]. Equation (2.124) is often written in terms of the free stream velocities U_1 and U_2, such that

$$\frac{\mathrm{d}\delta}{\mathrm{d}x}=2S\frac{U_1-U_2}{U_1+U_2}. \tag{2.125}$$

The shear layer growth rate (2.125) increases with velocity difference, indicating that more non-uniform shear layers entrain fluid faster.

We simplify (2.123) by introducing rescaled variables

$$\xi=\frac{\sqrt{S}}{C}\zeta, \quad F(\xi)=\frac{\Delta U\sqrt{S}}{U_c C}\mathcal{U}\left(\frac{C\xi}{\sqrt{S}}\right). \tag{2.126}$$

In terms of these new variables (2.123) becomes

$$(\xi+F)\frac{\mathrm{d}^2F}{\mathrm{d}\xi^2}+\frac{\mathrm{d}^3F}{\mathrm{d}\xi^3}=0, \tag{2.127}$$

and the boundary conditions (2.115)-(2.118) become

$$\frac{\mathrm{d}F}{\mathrm{d}\xi}(\pm\infty)=\pm\frac{U_1-U_2}{U_1+U_2}, \tag{2.128}$$

$$\lim_{\xi\to\infty}\left(\xi\frac{\mathrm{d}F}{\mathrm{d}\xi}-F\right)=-\left(\frac{U_2}{U_1}\right)\lim_{\xi\to-\infty}\left(\xi\frac{\mathrm{d}F}{\mathrm{d}\xi}-F\right). \tag{2.129}$$

Given a value for U_2/U_1, or equivalently $\Delta U/U_c$, we can solve Equation (2.127), with boundary conditions (2.128)-(2.129), for the function $F(\xi)$.

In Figure 2.5 we plot the solution to (2.127)-(2.129), using three different values of $U_2/U_1 = 0.3,\ 0.5,\ 0.7$ (corresponding to $\Delta U/U_c = 1.08,\ 0.67,\ 0.35$). We solve (2.127) numerically on a finite domain defined by $-10 \leq \xi \leq 10$, applying the boundary conditions (2.128)-(2.129) at $\xi = \pm 10$ instead of $\pm\infty$. We can see that the streamwise velocity (a) within the shear layer is approximately linear. We will revisit this observation in Chapter 4, where we approximate the velocity profile in a shear layer using a piecewise linear function. The transverse velocity (b) indicates that there is greater

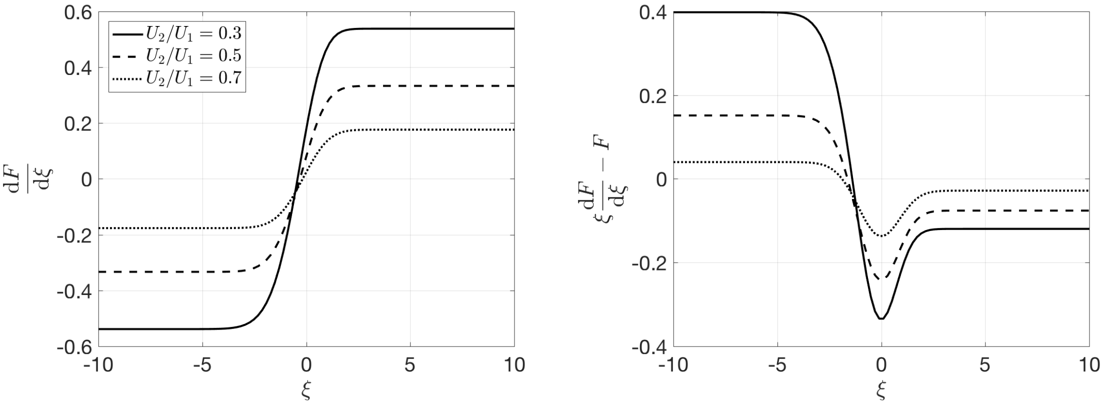

Figure 2.5: Solution to (2.127) for different values of U_2/U_1. (a) Streamwise velocity (2.119) (rescaled). (b) Transverse velocity (2.120) (rescaled).

entrainment when the velocity difference is larger, which is consistent with (2.125). However, entrainment is always greater (in magnitude) from the slower stream.

Whilst the above analysis is useful as a simple model for shear layers which are laterally unconfined, it cannot be applied to situations with confining walls. This is because the entire analysis rests on the assumption that the free stream velocities U_1, U_2 are constant. In the next section we show how to extend the model to the case where the shear layer is confined.

2.6 A shear layer model for confined parallel flows

Consider the flow in Figure 2.4, except with walls at $y = \pm h(x)$. Due to the confining walls, conservation of mass indicates that as the shear layer grows the velocities U_1 and U_2 cannot remain constant. Instead, we propose that they vary with x. It is not obvious how the shear layer should behave in such situations, or whether the growth can be described according to (2.125). In this section, we show how to describe the behaviour using a simple entrainment model.

We assume that the flow regions on either side of the shear layer, with velocity $U_1(x)$ and $U_2(x)$, are inviscid plug regions of width $h_1(x)$ and $h_2(x)$, respectively. Within the shear layer we assume that the average velocity is $\bar{u} = (U_1 + U_2)/2$. We hypothesise that the shear layer entrains fluid from both plug regions. Similarly to a Morton-Taylor-Turner jet [70], we assume that the total rate of entrainment into the shear layer is proportional to the difference in speeds between the two plug regions $E = S_c(U_1 - U_2)$, where S_c is an entrainment constant. It is not yet clear whether more fluid is entrained from the slower plug region, as for the unconfined case, or vice versa. Thus, the conservation of mass equations (2.61) for each of the plug regions and the shear layer, are

$$\frac{\mathrm{d}}{\mathrm{d}x}(U_1 h_1) = -\sigma S_c (U_1 - U_2), \tag{2.130}$$

$$\frac{\mathrm{d}}{\mathrm{d}x}(U_2 h_2) = -(1-\sigma) S_c (U_1 - U_2), \tag{2.131}$$

$$\frac{\mathrm{d}}{\mathrm{d}x}\left(\frac{1}{2}(U_1 + U_2)\,\delta\right) = S_c (U_1 - U_2), \tag{2.132}$$

where $0 \leq \sigma \leq 1$ is an unknown quantity which determines the proportion of the entrainment from each plug region. Note that in the case of an unconfined shear layer, where U_1 and U_2 are constant, Equation (2.132) is equivalent to the unconfined shear layer growth equation (2.125), as expected. The constant S_c is therefore an analogue of the spreading parameter for confined flows.

As we will discuss in Chapter 4, it is often useful to describe how the shear in the layer behaves rather than how the width develops. Therefore, using the definition of the shear rate within the shear layer, $\varepsilon_y = (U_1 - U_2)/\delta$, and Equation (2.132), we find that

$$\frac{U_1 + U_2}{2}\frac{\mathrm{d}\varepsilon_y}{\mathrm{d}x} = -S_c \varepsilon_y^2 + \frac{1}{\delta}\left(U_1 \frac{\mathrm{d}U_1}{\mathrm{d}x} - U_2 \frac{\mathrm{d}U_2}{\mathrm{d}x}\right). \tag{2.133}$$

If we assume that Bernoulli's equation holds in each plug region

$$\frac{\mathrm{d}}{\mathrm{d}x}\left(p + \frac{1}{2}\rho U_i^2\right) = 0, \quad i = 1, 2, \tag{2.134}$$

then it follows that

$$\frac{\mathrm{d}}{\mathrm{d}x}\left(\frac{1}{2}U_1^2 - \frac{1}{2}U_2^2\right) = 0. \tag{2.135}$$

Considering (2.135), Equation (2.133) becomes

$$\frac{U_1 + U_2}{2}\frac{\mathrm{d}\varepsilon_y}{\mathrm{d}x} = -S_c \varepsilon_y^2, \tag{2.136}$$

which is the governing equation for the shear ε_y. Equation (2.136) can be considered an alternative equation to describe the growth of the shear layer, instead of (2.125).

Chapter 3

Experimental work

3.1 Introduction

In this chapter we describe our experimental work which is used to investigate the development of turbulent shear layers in confining channels. We use two different experimental techniques to visualise the flow in a hydrodynamics tank: ink tracer visualisation and particle image velocimetry (PIV). The flow scenario we consider is illustrated in Figure 3.1. We consider turbulent flow in a long, thin channel, where a slower inner flow mixes with two faster outer flows. These flows correspond to the secondary and primary flows in Venturi-enhanced hydropower, respectively.

Firstly, we record the transport of ink tracer using a high-speed camera, thereby attaining qualitative information about the flow, such as the approximate boundary of the shear layers. Secondly, we use a combination of PIV and pressure tappings to capture velocity and pressure data, providing quantitative information about the flow. We investigate three different flow geometries: a straight channel where the average velocity remains constant, a widening channel with walls that expand at 5°, where the average velocity decreases, and a channel which has a combination of a straight section and a widening section, as representative of the design of Venturi-enhanced hydropower (see Figure 1.2). The third example is investigated with ink tracer, whereas the first two examples are analysed with PIV.

The experimental results from this chapter give us an insight into the relationship between the shape of the channel and the flow development. Furthermore, the velocity and pressure data generated by the PIV analysis will be used in Chapter 4 to validate our simple model and compare with computational fluid dynamics.

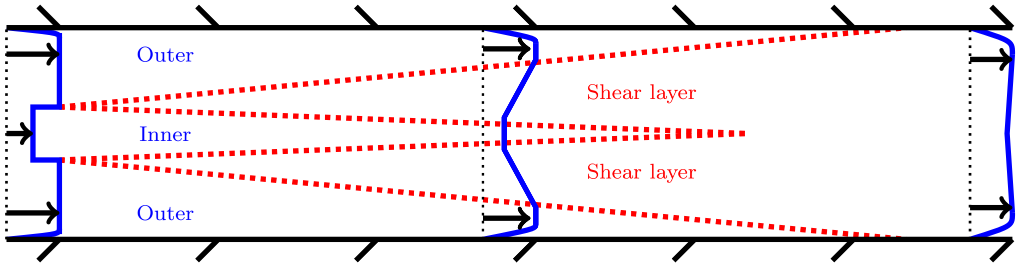

Figure 3.1: Schematic diagram of the flow we investigate experimentally, consisting of a slower inner flow (secondary) and a pair of faster outer flows (primary) in a confining channel. Here we depict a straight channel, but we also consider a widening channel, and a channel which has a combination of a straight and a widening section.

3.2 Experimental setup

We display a schematic diagram of our experimental setup in Figure 3.2. In the experiments, water flows through an acrylic closed channel of rectangular cross-section at constant flow rate (1 l/s), driven by an impeller pump. The impeller pump draws water from the drainage tank and feeds it into the first header tank, from which it enters a flow straightener, followed by a second header tank, before passing through a closed channel of rectangular cross-section. The flow straightener consists of an array of straws, 12 cm in length and 0.5 cm in diameter. The purpose of the flow straightener is to break up the large vortical structures which are present when the flow leaves the impeller pump. In this way, as the flow enters the secondary header tank, the pressure head is approximately constant (with a 3 cm head drop across the channel), and there are no flow structures which are unnaturally large compared with the cross-section of the rectangular channel.

At the inlet of the rectangular channel, three inflows merge: two fast, outer flows, and a slow inner flow along the channel centre. The inner flow is made slower than the outer flows by means of a perforated blockage. The perforation density is varied to achieve (empirically) the desired velocity ratio between inner and outer flows. For all the examples discussed here we choose a perforation density that results in a velocity ratio as close to 0.5 as experimentally possible.

The dimensions of the rectangular channel are 35 cm $\times$ 7.5 cm $\times$ 2 cm. The initial 10 cm of the channel is split into the three inflows separated by thin dividing walls. Of the three inflows, the two outer flows have dimensions 10 cm $\times$ 2.62 cm $\times$ 2 cm and the inner flow has dimensions 10 cm $\times$ 2.25 cm $\times$ 2 cm, such that the ratio of the cross-sections of the inner and outer flows combined is 0.43. Therefore, the dimensions of the

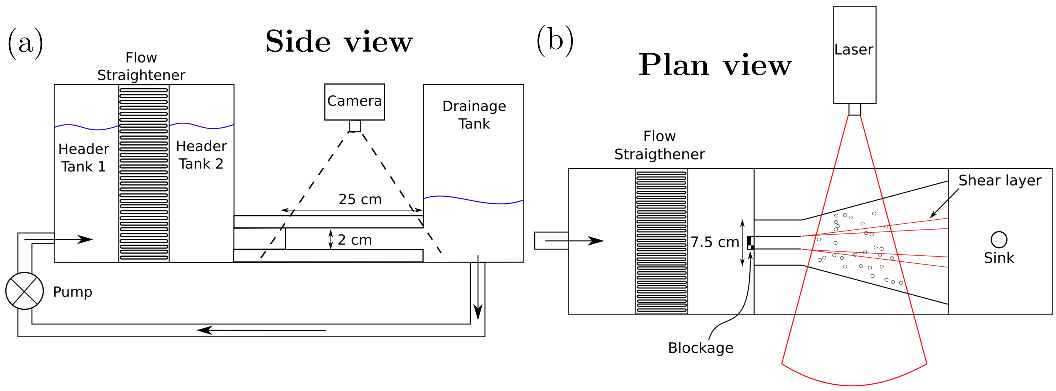

Figure 3.2: Experimental setup, showing the configuration for a widening rectangular channel. A recirculating pump provides a constant flow rate and pressure drop.

remaining part of the channel, excluding the three inflows, are $25\,\text{cm} \times 7.5\,\text{cm} \times 2\,\text{cm}$, as indicated in Figure 3.2.

If we take a typical length scale as the hydraulic diameter of the channel $2 \times \text{width} \times \text{depth}/(\text{width} + \text{depth}) = 3.2\,\text{cm}$, and a typical velocity scale as the average speed of the fast outer flow measured by PIV ($50\,\text{cm/s}$), then the Reynolds number is $Re = 1.6 \times 10^4$. At the inlet the flow is observed to be turbulent, indicated by significant turbulent fluctuations which are made visible by injected ink tracer (discussed later). Furthermore, using particle image velocimetry (PIV), we measure a turbulent intensity [87] at the inlet of

$$I = \sqrt{\frac{2k}{3\left(u^2 + v^2\right)}} \approx 10\%. \tag{3.1}$$

The entire channel is made of transparent acrylic so that it is possible to visualise the injected ink tracer and perform PIV. In the case of the ink tracer, we use black food colouring, which is injected into the inner stream via a hypodermic needle. Simultaneously, a high-speed ($1000\,\text{fs}^{-1}$) camera records the transport of the ink within the flow. The injection of ink is purely for qualitative observations of the flow, so we do not process the recorded images further.

In the case of PIV, we visualise the flow by adding a dilute suspension of neutrally-buoyant, pliolite tracer particles [93, 23], and shining a pulsed *Nd:YAG* laser sheet through the channel side wall at its halfway height. The horizontal sheet enters the tank, illuminates all particles in the plane and exits at the other side into a beam dump. We assume that the typical vertical velocities (i.e. out of the plane) are small compared to the typical streamwise velocities. This assumption is based on the fact that the rectangular channel has a long and thin aspect ratio.

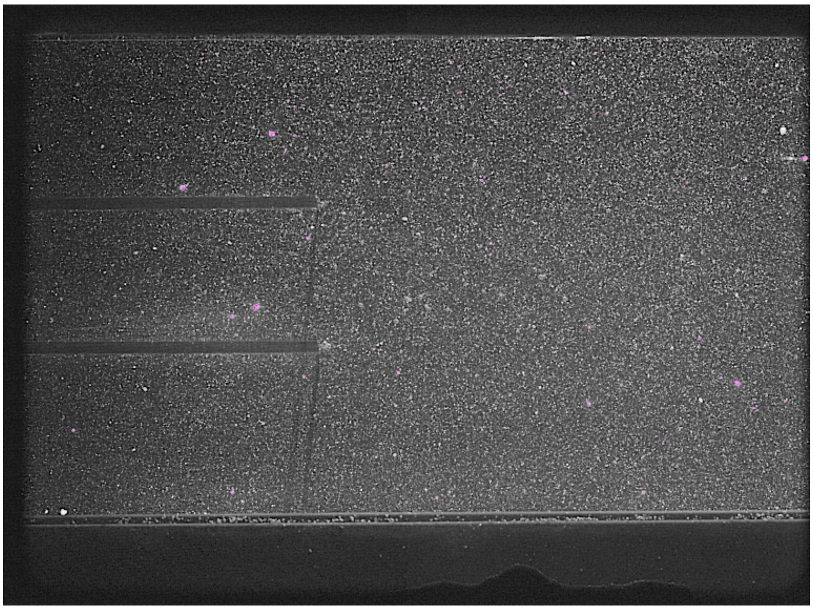

Figure 3.3: Particles in the flow illuminated by a laser sheet. The displayed region covers the first third of the channel length, including the three channel inflows separated by dividing walls (at the left), and the initial part of the straight channel section. The dimensions of the photo are 12 cm $\times$ 9 cm.

A synchronised high-speed camera takes pairs of images at 1 ms intervals, 15 times a second, controlled with the *TSI Insight 4G* computer package [98]. The camera is positioned above the channel and pointed downwards in the direction of the normal to the laser sheet plane. We are not interested in resolving the turbulence in time but, instead, we capture many pairs of images and study its time-averaged properties (we find $50 - 100$ pairs of images are sufficient).

The laser sheet is created by passing the laser through a cylindrical lens, which expands the region of illumination but reduces the laser power. In order to maintain brightly illuminated images, we restrict the expansion of the laser sheer to cover a third of the channel length. Consequently, both the laser and the camera are moved between three different positions, equally spaced along the channel. In each position, many PIV images are captured before moving to the next position. By averaging the measured flow behaviour at each of these three positions, it is possible to 'stitch' them together to study the time-averaged behaviour of the flow in the entire channel. In order to smooth the stitching process, we keep small overlap regions between the sections and use a linear weighted average within the overlap. Finally, due to restrictions on the field of vision of the camera in the case of the widening channel, it is not possible to capture the entire width of the channel in a single image. However, it is sufficient to perform PIV on one half of the widening channel, since the geometry

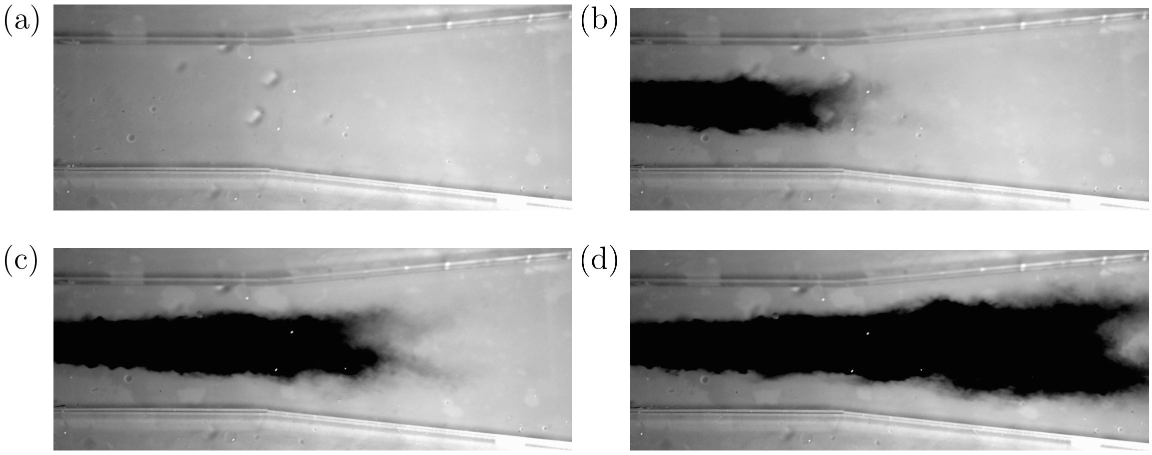

Figure 3.4: Snapshots of a high-speed video of the flow, where ink is injected into the slower inner flow. Snapshots taken at (a) $t = 0$ s, (b) $t = 0.48$ s, (c) $t = 0.70$ s, (d) $t = 1.0$ s.

is symmetric about the channel centreline, and PIV measurements from the straight channel indicate that the flow is also symmetric.

A single image of one third of the straight channel is displayed in Figure 3.3. We can see a brightly illuminated distribution of particles, as well as the three channel inflows separated by dividing walls. We use *Matlab*'s package *PIVlab* [63, 95] to extract time-averaged properties of the flow such as the streamwise and transverse velocities (u, v) and the two-dimensional turbulent kinetic energy k [87, 79]. After stitching the images together, there is a PIV resolution of 77×274 pixels for the entire channel.

In addition to velocity measurements, we also measure time-averaged pressures along the channel using open-tube-manometer pressure tappings. The channel is fitted with a removable transparent top plate, which can be replaced by another plate with a series of pressure tappings at evenly spaced locations. The tappings block the view of the flow, inhibiting PIV measurements, and so the experiments are always performed twice: one PIV experiment using the first plate and one pressure measurement experiment using the second. To calculate the pressure, we measure the water height in the tube tappings and use the linear relation between pressure and water height $p = \rho g \times$ height. The measurements correspond to static pressure, rather than total pressure, since the tapping holes are drilled perpendicular to the flow direction. These measurements are taken with callipers and we anticipate a human eye accuracy of around 0.5 cm, particularly due to difficulties in measuring the meniscus position. Changes to the height due to turbulent fluctuations are small, however measurements were repeated several times for accuracy.

3.3 Results

3.3.1 Injected ink tracer

In Figure 3.4 we display four snapshots of a high speed video recording of the injected ink tracer in a channel with a straight and a widening section. We can see that the ink, which is injected into the inner flow, mixes with the outer flows in turbulent shear layers. The Kelvin-Helmholtz instability [100], which is the mechanism for shear layer entrainment, is visible at the interface between inner and outer flows. As the shear layers grow downstream, mixing together fluid from the inner and outer flows, the region of coloured fluid expands. The outer edges of the coloured flow region correspond to the outer edges of the shear layers.

In the final two snapshots (c, d), it is possible to see the profile of the front of the coloured region more clearly. The profile is more advanced towards the outer edges of the region, and less advanced in the centre. We can therefore conclude that the velocity of the coloured region is not uniform across its cross-section. There are two possible reasons why the central portion of the coloured region is moving more slowly: Either the inner edges of the shear layer have not reached this region, such that it contains no fluid from the outer regions; Or the inner edges of shear layer have reached this region, but there is still significant shear across it. However, it is not possible to conclude which of these possibilities is correct from these results. In order to gain more detailed information about the velocity in the shear layer, we proceed to PIV techniques.

3.3.2 Particle image velocimetry

As described before, the two channel geometries which are chosen for PIV analysis are a straight channel and a widening channel. The results from the PIV analysis are shown in Figure 3.5, in the case of the straight channel, and Figure 3.6, in the case of the widening channel. We plot colour maps of the local, time-averaged flow velocities u and v and the turbulent kinetic energy k (a, b, c). In addition, we plot streamlines (d), which are calculated from u and v. Profiles of the streamwise velocity u are displayed at evenly spaced locations along the channel (e) and pressure data (f), measured with respect to the first data point, are plotted with error bars of 0.5 cm, corresponding to human eye measurement inaccuracy.

In the straight channel case, the colour plots of u and the velocity profiles clearly show the flow mixing over the whole channel length, with the faster streams slowing down and the slower stream speeding up. This can also be observed in the streamlines,

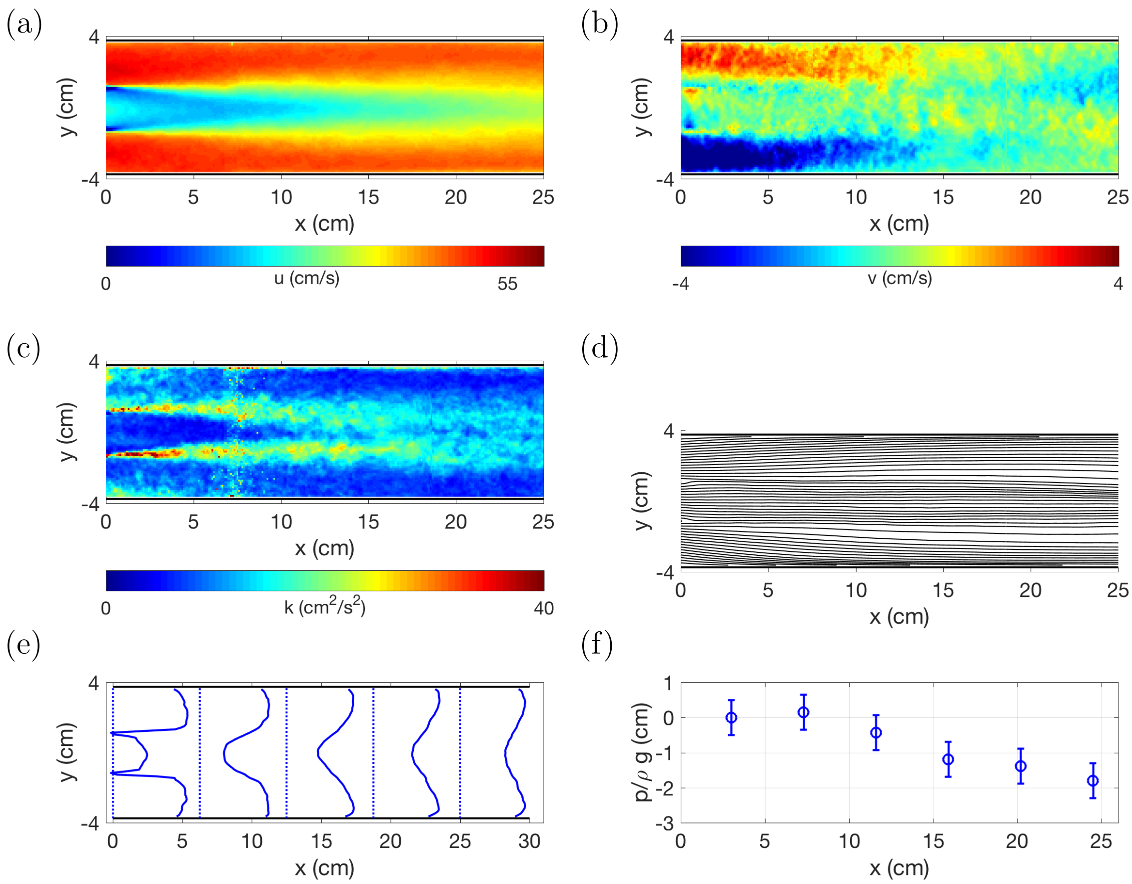

Figure 3.5: Experimental results for the straight channel, showing colour maps of the time-averaged velocities (a, b) u, v and (c) turbulent kinetic energy k, (d) streamlines, (e) velocity profiles of u at evenly spaced locations, and (f) pressure tapping measurements. Flow is from left to right.

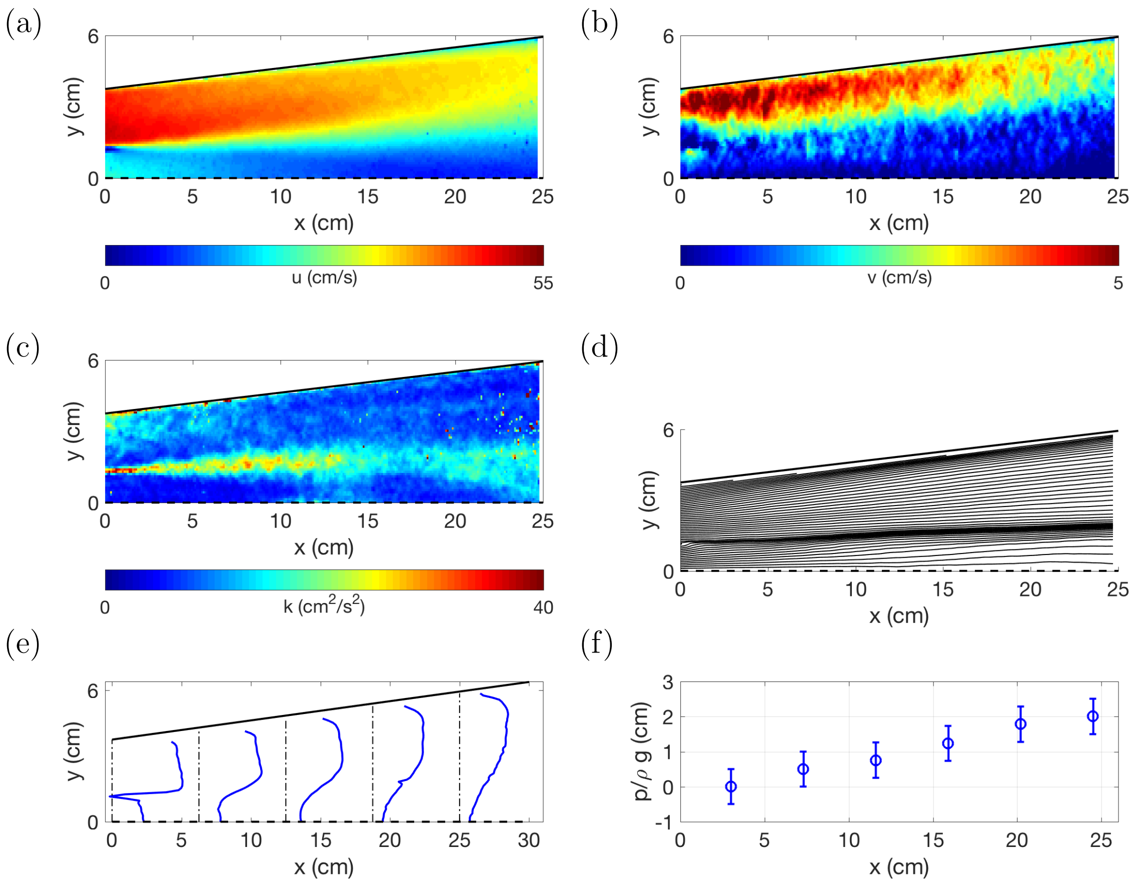

Figure 3.6: Corresponding experimental results for the widening channel. Flow is symmetric about the channel centreline so we only display half of the channel.

which show a slight contraction in the inner flow, and a slight expansion in the outer flows. In the first displayed velocity profile, the ratio between the maximum velocity of the inner and outer flows is 0.46. Boundary layers of significant width can be seen at the dividing walls of the inner flow, and at the dividing walls and the outer walls of the outer flows. At the second displayed velocity profile, no evidence of the boundary layers at the dividing walls remain, indicating that they have been absorbed by the shear layer.

From the velocity plots we see that the flow is nearly symmetric about the channel centreline, though slightly veering to one side. This is indicated both by the streamlines, and by an inlet transverse velocity v which is slightly larger in magnitude near $y = -4\,\mathrm{cm}$ compared with $y = 4\,\mathrm{cm}$ (note that the colour is saturated below $v = -4\,\mathrm{cm/s}$). However, this slight asymmetry is considered insignificant and, hence, an analysis of half the channel is taken to be acceptable. The magnitude of the transverse velocity v at the inflow is slightly larger than expected for the two outer streams. This is possibly explained by the blockage to the inner flow upstream, which may deflect some flow outwards. However, since the magnitude of the transverse velocity is a factor of 10 smaller than the streamwise velocity u, the effect is considered insignificant. The location of the shear layer is more clearly shown by the plots of turbulent kinetic energy k, where we see the expansion of the layer, as well as some evidence of wall friction at the channel's side walls. It also appears that the growth of the shear layer is slightly inclined towards the channel centre. The pressure measurements show an overall decrease in pressure, which is attributed to wall drag.

In the case of the widening channel, there is an overall flow deceleration, as seen in the colour plot of u and in the dilation of the streamlines. However, the channel expansion causes the flows to slow down at different rates, accentuating the non-uniform flow profile. At $x = 25\,\mathrm{cm}$ the slower central stream almost stops entirely. This can also be observed in the different amounts of expansion within the inner and outer flow streamlines. The first displayed velocity profile is similar to that in the straight channel example, and the ratio between the maximum velocity of the inner and outer flows is 0.45. Again, at the second displayed velocity profile, there is no evidence of the dividing wall boundary layers, indicating that they have been absorbed by the shear layer. Similarly to the straight channel case, the magnitude of the transverse velocity v in the outer inflow is slightly larger than expected, though still a factor of 10 smaller than the streamwise velocity u. Therefore, we do not consider its effect significant. The position and expansion of the shear layer can be observed in the plot of the turbulent kinetic energy k, and we see that the shear layer growth is slightly inclined away from the centreline. Finally, we see a monotone increase in pressure from the tapping measurements, which is explained by the overall deceleration of the flow.

3.4 Discussion

In addition to collecting velocity and pressure data which we can compare quantitatively to our simple model in the next chapter, we have established several qualitative properties of the flow dynamics in the channel. Firstly, by injecting ink tracer into the flow we observed that the flow was turbulent and that the inner and outer streams mixed together in shear layers generated by the Kelvin-Helmholtz instability [100]. The front profile of the ink-coloured region indicated that the two streams may not have fully mixed by the end of the channel. Secondly, the PIV analysis revealed that the shape of the channel has a significant effect on the development of the flow profile. Whilst in the case of the straight channel, a nearly uniform velocity profile was recovered by the end of the channel, in the case of the widening channel, which had nominally the same inflow, the velocity profile at the end of the channel was very non-uniform. In fact, the centre velocity near the end of the channel was almost zero. This indicates that widening channels have a tendency to accentuate non-uniform flows.

These qualitative properties have provided a preliminary insight into the problem of improving the efficiency of Venturi-enhanced hydropower. As we have discussed earlier in Chapter 1, it is often useful to consider the Venturi geometry divided into a straight 'mixing' section and a widening 'diffuser' section. Our ink tracer experiments indicated that a mixing section which is too short can produce a flow profile which is significantly non-uniform. Furthermore, the PIV results suggested that if the flow at the beginning of the diffuser section is non-uniform, the expansion may produce an even more non-uniform flow. This is likely to result in a low efficiency because a non-uniform flow has more kinetic energy flux than a uniform flow, and this discrepancy in kinetic energy flux corresponds to un-extracted energy from the flow, hidden in the pressure (see Chapter 1, Section 1.2). Therefore, in order to have a high efficiency, the diffuser must receive a relatively uniform flow profile, which is achieved by a sufficiently long mixer section.

In the chapter that follows, we create a simple model which describes turbulent shear layers in confining channels, allowing us to predict how the shape of the channel affects the flow development. We use the velocity and pressure data generated by our PIV analysis to compare quantitatively against our simple model, as well as calculations from computational fluid dynamics. Hence, the experimental work acts as a valuable reference point to validate our models, before proceeding to use those models for further predictions.

Chapter 4

Turbulent shear layers in confining channels

4.1 Introduction

Shear layers, where two parallel flows undergo turbulent mixing, are found in a wide variety of situations. For laterally unconfined flows, shear layers can be described using a simple analytical model - derived from the turbulent boundary layer equations and Prandtl mixing length theory [87, 48] (see Chapter 2, Section 2.5). However, this model is often not practicable in many situations where the flows are confined in a channel. Examples of such flows include blockages and cavities in pipes [42, 4, 92], air flow in urban environments [86, 1], environmental flows [69, 99, 3], engine and aerodynamic design [89, 19, 50], and mixing flows in diffusers, nozzles and pumps [61, 107, 88]. In such cases, it is important to account for the confining effect of the channel walls. In addition to the large literature on unconfined shear layers, as detailed in the review articles by Brown and Roshko [15] or Huerre [6], there are some numerical and experimental studies of confined shear layers. For example, Gathmann et al. [36] used numerical simulations to investigate the transition to turbulence in a confined shear layer. Furthermore, the criteria for absolute and convective instabilities in a confined compressible shear layer were studied by Robinet et al. [85]. Further numerical studies of confined shear layers are discussed in [94, 86, 56]. In the context of experimental investigations of confined shear layers, Bradshaw et al. [14] studied the behaviour of a shear layer near a backward-facing step. In addition, Castro et al. [17] calculated the shear layer structure in a separation region near a wall. The use of confined shear layers for vector thrusting was investigated by Alvi et al. [2]. Other examples of experimental investigations of confined shear layers are given by [54, 1, 92, 22]. However, while there are a limited number of experimental and numerical studies, there is no simple model for confined shear layers.

In this chapter we show that a simple model, comprising two uniform streams separated by a linear shear layer and incorporating parameterisation of wall drag, can be used to model confined shear layers and good agreement is attained with both experiments and detailed k-ε turbulence modelling. The decomposition of the flow profile into uniform streams and a linear shear layer is similar to that discussed by Jimenez [48], except that we account for confinement effects, since the velocities of the plug regions are non-constant. Furthermore, our model accounts for the interaction between the shear layer and the channel walls. The evolution of the shear profile is governed by an equation which we derive from an entrainment argument (see Chapter 2, Section 2.6), and which is also analogous to the classic analytical model for the growth of unconfined shear layers [87, 48].

The simplicity of our model means it both gives good physical intuition into the flow, and is computationally much cheaper than computational fluid dynamics (CFD) models. Furthermore, it can be applied to shear layers in a channel of arbitrary shape. Thus it can be used to quickly find optimal parameters in a wide range of engineering design problems [88]. It also avoids the need for high levels of expertise that are typically required with CFD when choosing turbulence models and selecting boundary conditions [87, 79].

First we present the model and compare the results with CFD and experiments. Then we use the model to investigate the effect of the inflow conditions on the growth of the shear layer. We show that if the inflow is very non-uniform, or if the channel expansion angle is too large, a stagnation region may form inside the channel. As an example application, we use our simple model to find the optimum design of a flow diffuser with a confined shear layer, where the objective is to maximise the pressure recovery, as is representative of Venturi-enhanced hydropower. The results of the optimisation show that the optimum diffuser shape strikes a balance between not widening to soon, which would accentuate the non-uniform flow, and not being narrow for too long, which is detrimental for drag. Finally, we present some extensions to the model, including accounting for a turbulent boundary layer at the wall, which allow for more detailed and realistic predictions of the flow.

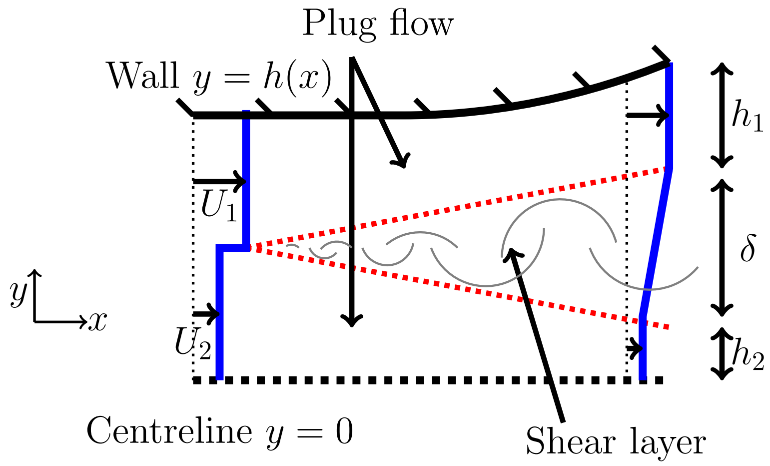

Figure 4.1: Schematic diagram of the symmetric velocity profile in half a channel. The flow can be divided into three regions: Two plug flow regions of different speeds (in which Bernoulli's equation holds) and a turbulent shear layer between them. We do not resolve boundary layers at the walls, but instead we parameterise their effect using a friction factor f. The aspect ratio here is greatly reduced for illustration purposes.

4.2 Mathematical model

The flow geometry we consider is shown in Figure 4.1, in which we illustrate our chosen coordinate system (x, y). We consider two-dimensional turbulent flow in a long, thin channel where the rate of change of the channel width is small. We assume that flow is symmetric about the channel centreline and therefore consider only half of the channel. To model this, we generalise the classical model for a shear layer between unconfined flows [87, 48], where a flow with velocity U_1 in the x direction meets a second, parallel flow with velocity $U_2 < U_1$ (as in Venturi-enhanced hydropower). As described in Chapter 2, Section 2.6, a shear layer forms at the point the flows meet and grows with a width $\delta(x)$. To good approximation, the average velocity in the shear layer increases linearly from U_2 to U_1 across its width [48]. Furthermore from the turbulent boundary layer equations and Prandtl's mixing length theory [87, 48], it can be shown that

$$\frac{\mathrm{d}\delta}{\mathrm{d}x} = 2S\frac{U_1 - U_2}{U_1 + U_2}, \tag{4.1}$$

where S is a spreading parameter, which is a non-dimensional number that has been determined by numerous unconfined shear layer experiments giving $S = 0.06 - 0.11$ [79].

It is not clear that unconfined shear layer theory should apply to confined situations, nor whether we expect the same value of the spreading parameter S. However, we incorporate a modified version of (4.1) in our model and find that it shows good comparison with both experimental and CFD calculations. In particular, when the flow is confined, the shear layer may reach the channel walls, so that its width can no longer evolve according to (4.1). To accommodate this, we derive an alternative equation to (4.1) which describes how the shear rate in the layer $\varepsilon_y = (U_1 - U_2)/\delta$ behaves, using an entrainment argument, as described in Chapter 2, Section 2.6. Hence, we continue to assume the velocity in the shear layer is linear with distance across the channel, and the shear rate evolves according to

$$\frac{U_1 + U_2}{2} \frac{\mathrm{d}\varepsilon_y}{\mathrm{d}x} = -S_c \varepsilon_y^2, \tag{4.2}$$

where we denote S_c as the spreading coefficient associated with confined shear layers. We make the key assumption that the evolution of the shear rate continues according to (4.2) even when the shear layer is adjacent to the wall. A useful interpretation of this equation is that, moving along the channel at the average velocity in the shear layer $(U_1 + U_2)/2$, the shear rate decays at a rate proportional to the square of itself. The parameter S_c, like S, must be determined from experiments or by comparison with CFD.

For the case of a confined flow we combine this description of the shear layer with conservation equations to describe the plug-like flows on either side, whose speeds U_1 and U_2 now vary with x. Note that such equations are not necessary for a unconfined shear layer when U_1 and U_2 are constant. We consider the case of symmetric flow in a half channel $0 < y < h(x)$, as shown schematically in Figure 4.1. Co-flowing inner and outer streams (corresponding to the secondary and primary flows) mix inside the channel. Following the earlier discussion, the velocity profile is approximated as

$$u = \begin{cases} U_2 & : 0 < y < h_2, \\ U_2 + \varepsilon_y (y - h_2) & : h_2 < y < h - h_1, \\ U_1 & : h - h_1 < y < h, \end{cases} \tag{4.3}$$

where $h_1(x)$ and $h_2(x)$ vary with distance along the channel. The width of the shear layer is $\delta = h - h_1 - h_2$ and is related to the shear rate ε_y by definition $\delta = (U_1 - U_2)/\varepsilon_y$. In this model we do not resolve the boundary layers at the wall, but instead we parameterise their effect using a friction factor. Later in Section 4.7 we discuss a more complex model which includes boundary layer growth, but we find that the current approach compares well with experiments and CFD, and is attractive for its simplicity. Additionally, assuming that the channel is much longer than it is wide, from boundary layer theory [87], the pressure is approximately uniform across the

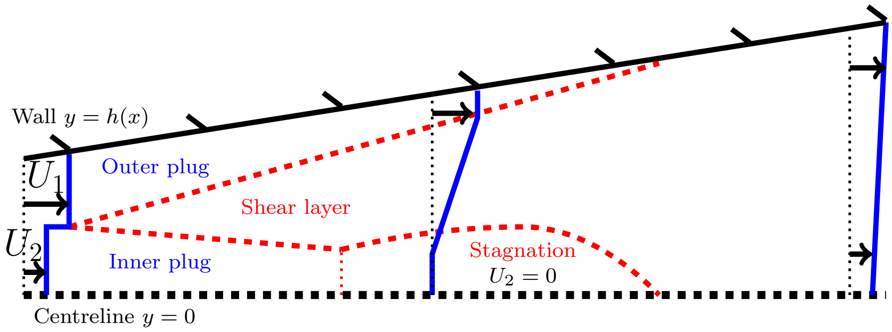

Figure 4.2: Schematic diagram of a region of stagnation within a channel. If the flow is sufficiently non-uniform, or if the channel expansion angle is sufficiently large, the slower inner flow can slow down and reach zero velocity. Velocity profiles are illustrated at three locations.

channel width, such that $p = p(x)$. By invoking conservation of mass and momentum (see Chapter 2, Section 2.4.1.2), we can now predict how U_1, U_2, h_1, h_2 and p evolve. Averaged across the whole channel, the mass and momentum equations are

$$\frac{\mathrm{d}}{\mathrm{d}x}\int_0^h u\,\mathrm{d}y = 0, \tag{4.4}$$

$$\rho\frac{\mathrm{d}}{\mathrm{d}x}\int_0^h u^2\,\mathrm{d}y = -h\frac{\mathrm{d}p}{\mathrm{d}x} + \tau_h, \tag{4.5}$$

where ρ is the density and τ_h is the wall stress. We parameterise the wall stress with a friction factor f, such that

$$\tau_h = -\frac{1}{8}f\rho U_1^2. \tag{4.6}$$

Note that f is sometimes referred to as the Darcy friction factor, which is four times larger than the often used Fanning friction factor. To estimate f we use the empirical Blasius relationship [11, 66] for flow in smooth pipes

$$f = 0.316Re^{-1/4}. \tag{4.7}$$

Although this expression was derived for fully-developed pipe flow, we use it here for partially developed flows throughout the geometries we consider because we find good comparison with CFD and experiments.

We assume that the main contributions to energy dissipation come from the wall drag and turbulent fluctuations in the shear layer. We ignore the energy dissipation in the plug flow regions since it is small by comparison [87]. Thus, in the plug regions we assume Bernoulli's equation holds [5].

In certain cases, especially when the channel expansion angle is large, the speed of the slower plug region U_2 may decrease and reach zero. This has been observed in

CFD simulations, which we display in Section 4.5. In such cases a portion of slowly recirculating flow forms inside the channel. We do not resolve the recirculation in these regions, but since velocities are small, as observed in CFD, we treat the regions as stagnant zones with zero velocity (see Figure 4.2).

Bernoulli's equation in each plug region holds along streamlines, ignoring transverse velocity components since they are small, and is implemented in a complementarity format for convenience

$$h_1\left(p+\frac{1}{2}\rho(U_1^2-U_1(0)^2)\right)=0, \quad \text{and} \quad h_1\geq 0, \tag{4.8}$$

$$U_2h_2\left(p+\frac{1}{2}\rho(U_2^2-U_2(0)^2)\right)=0, \quad \text{and} \quad h_2\geq 0, \quad U_2\geq 0, \tag{4.9}$$

where we take $p(0)=0$ as the reference pressure. The complementarity format of (4.8) and (4.9) ensures that when either of the plug regions disappears, or if the slower plug region stagnates, Bernoulli's equation ceases to hold in that region. We find good comparison between our model predictions of the stagnant region and CFD calculations, which we discuss in Section 4.5. Now, for a given channel shape $h(x)$, and inlet conditions $U_1(0)$, $U_2(0)$, $h_1(0)$ and $h_2(0)$, we can solve the system of differential algebraic equations (4.2)-(4.9) and then use (4.3) to find $u(x,y)$ and $p(x)$[1].

Note that we can extend the model to account for axisymmetric flows simply. For axisymmetric flow in a cylindrical channel $0\leq r\leq h$, we assume that that the velocity profile is identical to (4.3), except with y replaced by r. Following Chapter 2, Section 2.4.3, in the axisymmetric version of the model, (4.2), and (4.6)-(4.9) remain unchanged, but (4.4) and (4.5) are altered to account for radial symmetry

$$\frac{\mathrm{d}}{\mathrm{d}x}\int_0^h ru\,\mathrm{d}r=0, \tag{4.10}$$

$$\rho\frac{\mathrm{d}}{\mathrm{d}x}\int_0^h ru^2\,\mathrm{d}r=-\frac{1}{2}h^2\frac{\mathrm{d}p}{\mathrm{d}x}+h\tau_h. \tag{4.11}$$

4.3 Comparison with k-ε model and experiments

We now compare our model predictions with CFD calculations and our experimental data. Firstly, we consider a two-dimensional channel example where we compare our model to a steady k-ε turbulence model [55], using all standard parameter values (see

[1]Note there are 7 unknown variables U_1, U_2, h_1, h_2, δ, ε_y, p, which are all functions of x. In total there are 7 governing equations for these variables, which are (4.2), (4.4), (4.5), (4.8), (4.9), and the relations $h_1+h_2+\delta=h$ and $\varepsilon_y=(U_1-U_2)/\delta$.

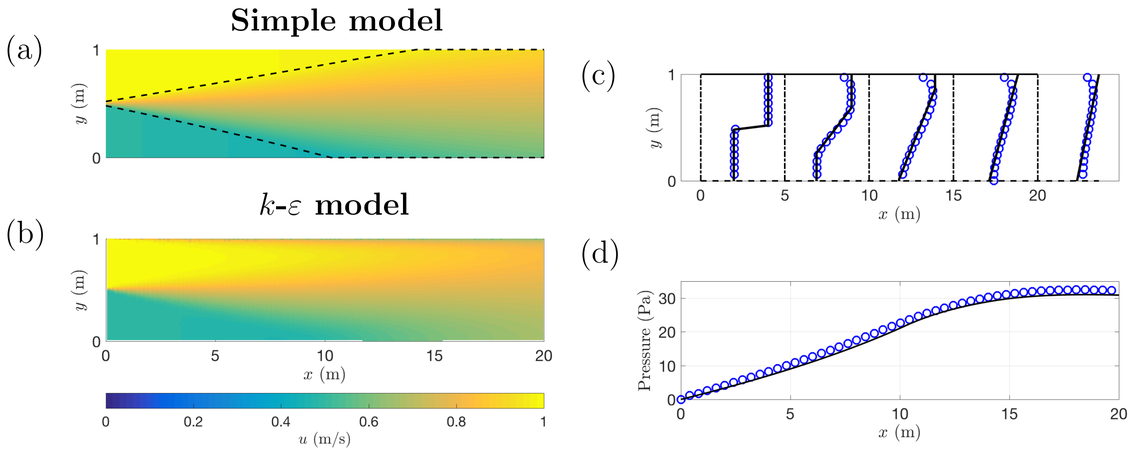

Figure 4.3: Comparison of the simple model and the k-ε model for symmetric shear flow in a two-dimensional channel, where flow is from left to right. (a, b) Time-averaged velocity in the x direction, u, where in the case of the simple model, (a), we also overlay dashed lines indicating the width of the shear layer. (c, d) Comparison of time-averaged velocity and pressure profiles calculated using the k-ε model, in blue circles, and the simple model, in solid black (the simple model does not resolve the velocity profile in the wall boundary layers). The inlet profile is given by $U_2(0)/U_1(0) = 0.5$, $h_2(0)/h(0) = 0.5$, and the Reynolds number is $Re = 10^6$.

Chapter 2, Section 2.2.2). Then we consider a three-dimensional channel example where we compare our model to experimental data as well as calculations from a k-ε model. In this case, our simple model is modified to account for drag from the top and bottom walls of the channel by including an additional drag term in (4.5). The k-ε model under-predicts shear layer growth with standard parameter values, but shows greater accuracy for an increased value of C_μ, the magnitude of the eddy viscosity. Similarly, in our model the value of the spreading parameter S_c, which controls shear layer growth, is larger than for the two-dimensional example.

In our first example we compare our model to a steady k-ε model [55] using the open-source software package *OpenFoam* [104]. We choose a straight two-dimensional symmetric geometry of length 20 m and half-width $h = 1$ m. The two-dimensional geometry has a mesh of 20000 elements, with 100 elements in the y direction and 200 in the x direction. Many other grid resolutions have been tested, and we find that solution for this grid resolution is sufficient to resolve all the details of the flow. We choose an inlet flow profile with $h_1(0) = h_2(0)$, $\delta(0) = 0$ and $U_2(0)/U_1(0) = 0.5$, where the speed of the faster plug region is $U_1(0) = 1$ m/s. Inlet conditions[2] for the turbulence variables k and ε are given by the free-stream boundary conditions

[2]See [55] for a discussion of the other boundary conditions for k and ε, such as on the walls and at the outflow.

[87] $k = I^2 \times 3/2\,(u^2 + v^2)$ and $\varepsilon = 0.09k^{3/2}/\ell$, with turbulence intensity $I = 10\%$ (motivated by PIV calculations, which are discussed later) and mixing length $\ell = 0.1h$. No-slip boundary conditions are applied to the channel walls. We use all the standard values for the k-ε turbulence parameters, which are given in Chapter 2. If we use the channel half-width h as a typical length scale, the faster plug region inlet speed $U_1(0)$ as a typical speed and choose the viscosity of water $\nu = 10^{-6}\,\mathrm{m}^2/\mathrm{s}$, then the Reynolds number is $Re = 10^6$. For comparison with the simple model, we use the Blasius relationship (4.7) to estimate the friction factor, giving a value of $f = 0.01$. For the spreading parameter S_c, we find that $S_c = 0.11$ fits best with the CFD calculations, which is within the range of reported values of S for unconfined shear layers ($S = 0.06 - 0.11$) [79].

In Figure 4.3 we display colour plots of the streamwise velocity u generated with both the simple model and the k-ε model. We also compare velocity profiles across the channel at equally spaced locations down the channel and the pressure profile, averaged across the width of the channel. We see that the shear layer grows across the channel, causing a rise in pressure due to the diffusion of momentum. In our model, the growth of the shear layer is controlled by S_c and the pressure is controlled by both f and S_c. There is a strong correlation for both velocity and pressure (with an average error of $\sim 5\%$). Near the wall the velocity comparison is less accurate due to the fact that the model does not explicitly resolve the development of boundary layers. However, it is apparent that the friction factor accurately represents the effect of the boundary layers on the pressure (wall drag) since there is a close comparison in Figure 4.3 (d). We have also made comparisons with other CFD models on the same geometry, such as the k-ω Shear Stress Transport model (SST) [67], and the results are similar. Furthermore, we have investigated longer channels and find that the simple model continues to show good comparison, eventually recovering a fully developed profile, though we do not display these results here.

Next we validate our model by comparison with Particle Image Velocimetry (PIV) experiments in a three-dimensional rectangular geometry. The experimental setup is described in detail in Chapter 3, where we give the dimensions of the geometry and a discussion of the PIV analysis. The Reynolds number for this flow (as defined in Chapter 3) is $Re = 1.6 \times 10^4$. The experimental results are shown in Figure 4.4 (c, f) for nominally the same inflow velocities in both straight and widening channels. We plot colour maps of the local, time-averaged flow speed u. These clearly show the flow mixing and, in the second case, the overall flow deceleration in the widening channel. In the straight channel case, mixing occurs over the whole channel length,

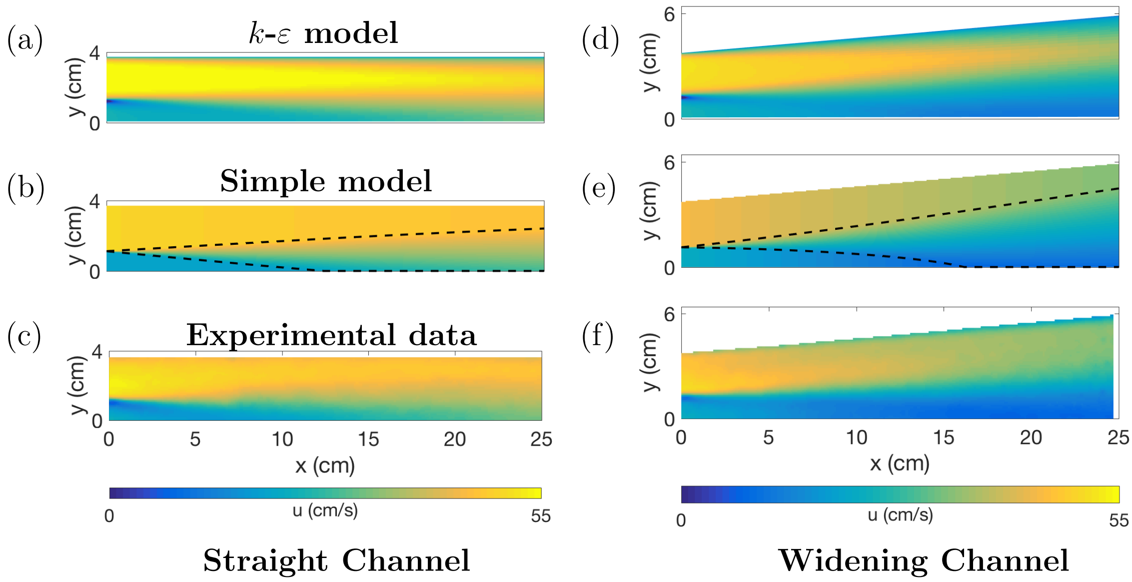

Figure 4.4: Comparison of the k-ε model, simple model and experimental data for the straight channel (a, b, c), and the widening channel (d, e, f). Flow is from left to right and is symmetric about the channel centreline so we only show half of the channel. Colour plots show the time-averaged velocity in the x direction, u. In the case of the simple model, we also overlay dashed lines representing the width of the shear layer. The inlet profile is given by $U_2(0)/U_1(0) \approx 0.5$, $h_2(0)/h(0) = 0.3$, and the Reynolds number is $Re = 1.6 \times 10^4$.

with the faster streams slowing down and the slower stream speeding up. In the case of the widening channel, the expansion causes the flows to slow down at different rates, accentuating the non-uniform flow profile. At $x = 25\,\text{cm}$ the slower central stream almost stops entirely. The location of the shear layer is more clearly shown by the plots of turbulent kinetic energy in Figure 4.5 (c, f) where we see the expansion of the layer, as well as some evidence of wall friction at the channel's side walls.

CFD modelling was performed on the three-dimensional geometry of the experiment, again using a steady k-ε model [55]. Inlet conditions were modelled slightly further upstream, at the three inflows which are separated by dividing walls (see the experimental setup in Figure 3.2). Plug flow profiles are used for modelling each of the three inflows such that the mass flux is consistent with PIV measurements. The three-dimensional geometry has a mesh of 65000 elements, with 100 elements in the x direction, 65 in the y direction and 10 in the z direction. As before, we have tested for convergence and we find that this grid resolution is sufficient to resolve all the details of the flow. Inlet conditions for the turbulence variables k and ε are given by the free-stream boundary conditions, as before, with turbulence intensity $I = 10\%$ and mixing length $\ell = 1\,\text{cm}$ (same order of magnitude of the width of each of the

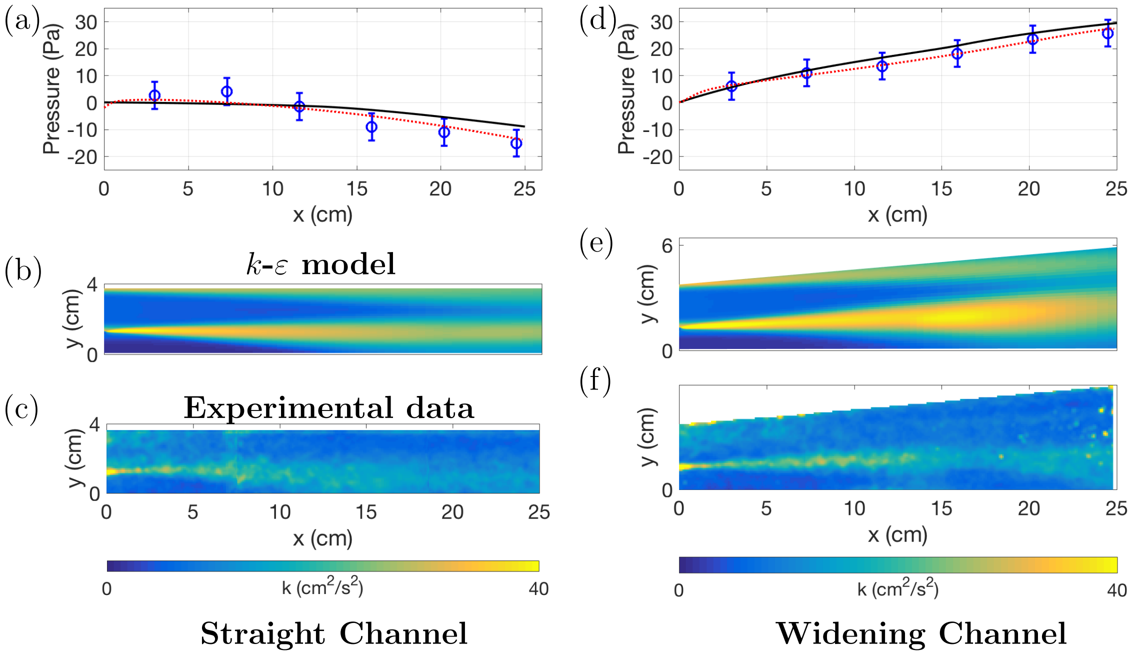

Figure 4.5: Comparison of the k-ε model, simple model and experimental data, continued from Figure 4.4. In (a, d) streamwise pressure profiles are shown, with blue data points representing experimental data and red and black lines representing calculations from the k-ε model and the simple model, respectively. Error margins correspond to an accuracy of 0.5 cm in human eye measurements. In (b, c, e, f) the time-averaged turbulent kinetic energy k is shown, calculated using the k-ε model and PIV measurements.

inlet flows). No-slip boundary conditions are applied to the channel walls. Using all the standard values for the turbulence parameters, which are given in Chapter 2, we find relatively poor agreement between the k-ε model and the experimental results. In particular, the shear layer growth rate is under-predicted. Good agreement is achieved if we double the value of the parameter C_μ, which represents the magnitude of the eddy viscosity, from its standard value of 0.09 to 0.18. The eddy viscosity, and hence the parameter C_μ, is associated with momentum diffusion and therefore controls the shear layer growth rate. We have also compared the experimental results to other RANS turbulence models, such as k-ω shear stress transport (SST) [67], using all standard parameter values, finding a similar under-prediction of the shear layer growth rate. This appears to be an issue with our three-dimensional computations, not seen in the two-dimensional comparison, and we have used this larger C_μ value in all three-dimensional comparisons.

Next, in order to compare with our simple model, we make a slight modification to account for drag from the top and bottom walls of the channel in addition to drag from the side walls. We do so by adding an extra stress term to (4.5) of the form

$$\tau_d = \frac{2}{d}\int_0^h -\frac{1}{8} f \rho u^2 \, \mathrm{d}y, \tag{4.12}$$

where d is the depth of the channel in the third dimension (see Figure 3.2). The drag from the top and bottom walls also requires a modification of Bernoulli's equations (4.8)-(4.9) that apply in the two plug regions, which now become

$$\frac{\mathrm{d}}{\mathrm{d}x}\left(p + \frac{1}{2}\rho U_i^2\right) = -\frac{2}{d}\left(\frac{1}{8} f \rho U_i^2\right), \quad i = 1, 2. \tag{4.13}$$

In Chapter 2, Section 2.4.2, we show how (4.12) and (4.13) can be derived from the turbulent boundary layer equations (note $D = d/2$). For this comparison we use the PIV-measured speeds of the streams at the inlet $x = 0$ as initial conditions for U_1 and U_2. We use the Blasius relationship (4.7) to estimate the friction factor, giving a value of $f = 0.03$. The value of the spreading parameter S_c that fits best with our data is $S_c = 0.18$, which is larger than the two-dimensional example ($S_c = 0.11$). Using a larger value of S_c is consistent with using a larger value of C_μ, since both parameters are associated with momentum diffusion. Thus, it appears that one of the effects of the top and bottom walls is to accelerate mixing.

Using these values for C_μ and S_c, the simple model, k-ε model and experiments show good agreement. For example, the streamwise velocities u are compared in Figure 4.4. Figure 4.5 also shows a comparison of the pressure change (relative to the inlet pressure) along the channel centreline. Dominant features of the flow, such as maximum and minimum velocities and pressure variation, are captured accurately by the simple model and in some cases more accurately than the k-ε model. For example, the k-ε model over-predicts the maximum velocity in both the straight and widening channel cases.

In Appendix A we compare our simple model to calculations from a k-ε model and a k-ω SST model [67] in a variety of other two-dimensional geometries with different inflow profiles and at Reynolds numbers between $Re = 10^4$ and $Re = 10^6$. Later in Section 4.7 we also compare the results of the axisymmetric version of our model (4.10)-(4.11) to those of a k-ε model in the case of a cylindrical channel. In addition, in Chapter 5 we compare our simple model to a k-ε model and a k-ω SST model for a variety of two-dimensional and axisymmetric diffuser shapes. In all the two-dimensional and axisymmetric cases above, we find that if we use default values for the turbulence parameters (which are given by [55] and [67]), $S_c = 0.11$ is an appropriate value for a good fit. However, as we have seen from our experimental results, RANS models are not always capable of predicting shear layer growth accurately. Indeed, Pope [79] discusses how the turbulence parameters in RANS models are not universal. Therefore, whilst we find that the value of the spreading parameter $S_c = 0.11$ is consistent with these two-dimensional and axisymmetric RANS models, this value is not considered universal. Similarly, the spreading parameter for unconfined shear layers has been reported in the literature to take a wide range of values between $S = 0.06$ and $S = 0.11$ [79]. Hence, we propose that $S_c = 0.11$ be used as a standard value for our simple model in two-dimensional and axisymmetric channels, just like $C_\mu = 0.09$ is proposed as a standard value for the k-ε model, but we acknowledge that it may be necessary to compare with experiments to verify that this value is appropriate for the particular application.

After comparison with both CFD and experimental data in several geometries and at different Reynolds numbers, we have shown that the simple model presented here has good capability in predicting the dominant features of the flow and pressure, provided that an appropriate value for the spreading parameter S_c is used. It can therefore serve as a useful, low-computational-cost[3] tool in modelling and optimising processes that involve confined shear layers, such as diffusers and nozzles.

4.4 The effect of inflow conditions on shear layer growth

Having established that our simple model shows good predictive capabilities, we now use it to estimate the effect of the inflow conditions on the growth of the shear layer. For this analysis, we consider both two-dimensional flow in a straight-sided channel, and axisymmetric flow in a straight-sided pipe. Widening geometries are not considered here, as the general behaviour of straight geometries exhibits many of the salient features. We maintain all variables in non-dimensional form with reference to typical length scales and velocity scales. We use the initial channel half-width as a typical length scale $h(0)$, and the speed of the faster plug region at the inlet as a typical velocity scale $U_1(0)$. Note that in this case, $h(0) = h$, since the geometries do not expand. The inflow velocity profile is defined by two non-dimensional parameters which play an important role in shear layer growth: the *velocity ratio* $U_2(0)/U_1(0)$ and the inner plug region *width ratio* $h_2(0)/h$, which both can take values between 0 and 1.

[3]For example, using finite differences with 500 discretisation points, computation time is of the order of 1 s on a laptop computer

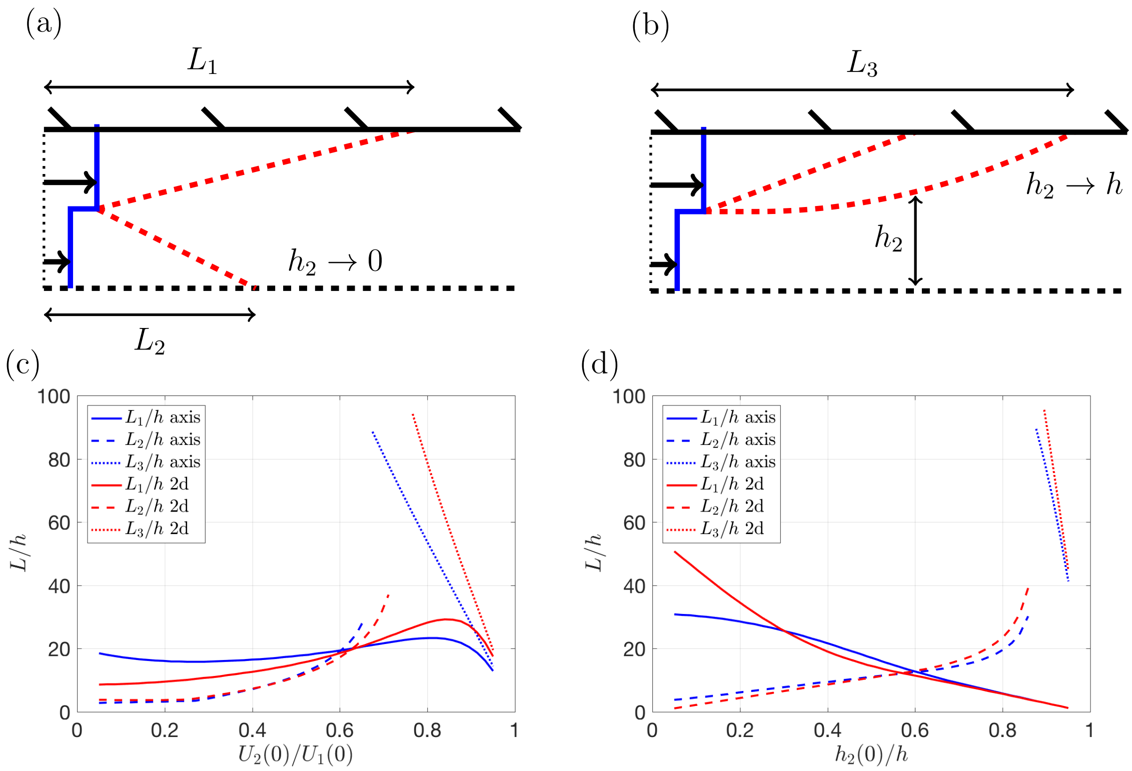

Figure 4.6: The effect of inflow conditions on shear layer growth. (a) Schematic diagram of the distances L_1 and L_2, at which the outer and inner edges of the shear layer meet the centreline and wall, respectively. (b) In some cases the shear layer is deflected away from the centre, such that its inner edge never reaches the centreline but, instead, it reaches the wall at a distance L_3. (c) The dependence of the non-dimensional distances L_1/h, L_2/h and L_3/h on the velocity ratio $U_2(0)/U_1(0)$, for a fixed value of the inner plug region width ratio $h_2(0)/h = 0.5$, in both the two-dimensional and axisymmetric cases. (d) Similarly, the value of $h_2(0)/h$ is varied whilst $U_2(0)/U_1(0) = 0.5$ is fixed.

In the case of unconfined flow, the growth rate of the shear layer is given by (4.1), which is a decreasing function of the velocity ratio. The shear layer growth rate $\mathrm{d}\delta/\mathrm{d}x$ does not depend on x, since the velocities U_1 and U_2 are constants. For confined flow, U_1 and U_2 are both functions of x, so the shear layer grows at a non-constant rate, which we model using Equation (4.2). Furthermore, there has been little exploration of how the shear layer growth rate depends on the inflow velocity ratio $U_2(0)/U_1(0)$, and the width ratio $h_2(0)/h$.

Although the shear layer growth rate is not constant, we can estimate $\mathrm{d}\delta/\mathrm{d}x$ by taking an average over a particular length scale L_δ, such that

$$\frac{\mathrm{d}\delta}{\mathrm{d}x} \approx \frac{\delta(L_\delta) - \delta(0)}{L_\delta}, \tag{4.14}$$

as is done by Gilchrist et al. [38]. However, the choice of L_δ is arbitrary and will have a significant effect on the averaged value of the growth rate. In situations where the flow is confined, there is a more natural way to characterise the shear layer growth rate, which is the distance it takes for the shear layer to reach across the channel. Since the shear layer has an inner and an outer edge, which are not necessarily symmetric about $y = h_2(0)/h$ (in the two-dimensional case), or $r = h_2(0)/h$ (in the axisymmetric case), it is useful to consider where each of these edges reaches their respective boundaries (see Figure 4.6 (a)). The outer edge of the shear layer reaches the channel wall $y = h$ (in the two-dimensional case), or the pipe wall $r = h$ (in the axisymmetric case), such that $h_1 = 0$ at some distance $x = L_1$. Similarly, the inner edge of the shear layer reaches the channel centreline $y = 0$, or the pipe axis $r = 0$, such that $h_2 = 0$ at some distance $x = L_2$. For example, see the straight channel experimental results in Figures 3.5 and 4.5, where the plots of the turbulent kinetic energy k clearly show that the shear layer is directed towards the channel centreline ($L_2 < L_1$).

Using our simple model (with $S_c = 0.11$ and $f = 0.01$), the values of L_1 and L_2 are calculated for all possible values of the inflow parameters $U_2(0)/U_1(0)$ and $h_2(0)/h$ between 0 and 1. Firstly, we vary the velocity ratio $U_2(0)/U_1(0)$, whilst holding a fixed value for the inner plug region width ratio $h_2(0)/h = 0.5$. The results are displayed in Figure 4.6 (c), for both the two-dimensional and axisymmetric cases. For velocity ratios close to 0, we find that $L_2 < L_1$, indicating that the shear layer is inclined towards the centre of the flow. However, when the velocity ratio exceeds $U_2(0)/U_1(0) \approx 0.6$, the shear layer is inclined away from the centre of the flow, such that $L_2 > L_1$. For velocity ratios close to unity, the inclination becomes so strong that the shear layer is directed away from the centre altogether, such that its inner

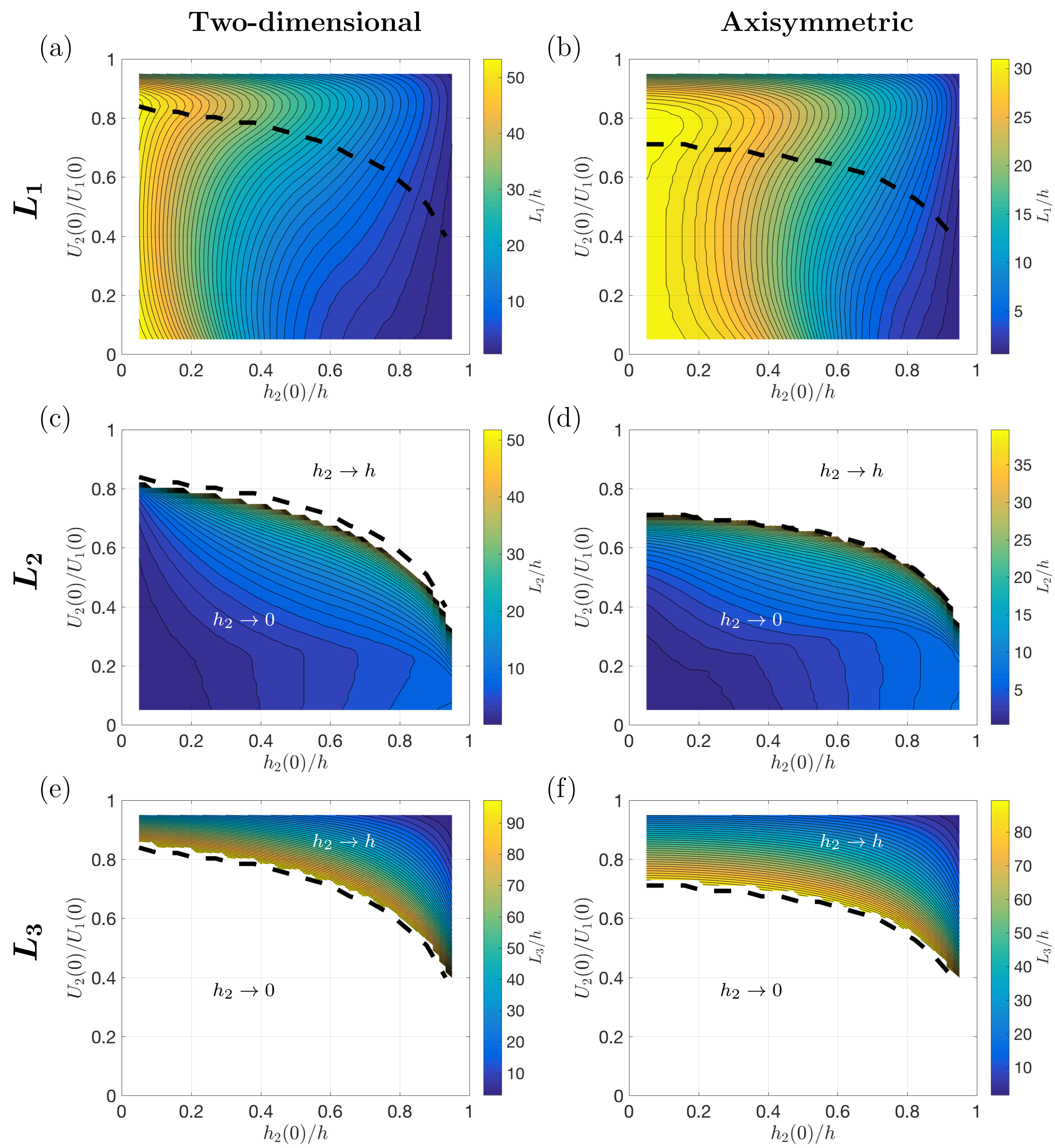

Figure 4.7: Contour plots of the non-dimensional distances L_1/h, L_2/h and L_3/h, calculated for all possible values of the inflow velocity ratio $U_2(0)/U_1(0)$ and the inner plug region width ratio $h_2(0)/h$, for both the two-dimensional case and the axisymmetric case. The boundary between regions of the parameter space where the inner edge of the shear layer reaches the centreline, $h_2 \to 0$, and regions where it reaches the wall, $h_2 \to h$, are indicated by a dashed black line.

edge never reaches the centreline. Instead, the inner edge of the shear layer curves outwards, eventually meeting the wall, $h_2 \to h$, at a distance which we denote $x = L_3$ (see Figure 4.6 (b)). As the inflow becomes uniform, $U_2(0)/U_1(0) \to 1$, the shear layer is directed further and further towards the wall, such that L_1, $L_3 \to 0$.

Next we vary the inner plug region width ratio $h_2(0)/h$, whilst holding a fixed value for the velocity ratio $U_2(0)/U_1(0) = 0.5$. The results are displayed in Figure 4.6 (d). When the inner plug region width is small, the position of the shear layer is closer to the centreline and therefore its inner edge reaches the centreline before the outer edge reaches the wall, such that $L_2 < L_1$. If the inner plug region width ratio exceeds a value of $h_2(0)/h \approx 0.6$, the shear layer is close enough to the wall that $L_2 > L_1$. However, for values of $h_2(0)/h$ close to unity, the inner edge of the shear layer is deflected towards the wall, similarly to when the velocity ratio is close to unity. Likewise, both L_1 and $L_3 \to 0$ as $h_2(0)/h \to 1$. In Figure 4.7 we display contour plots of L_1, L_2 and L_3 over all possible values of $h_2(0)/h$ and $U_2(0)/U_1(0)$ between 0 and 1. These plots show the full dependency of the shear layer growth on the inflow conditions. For example, the boundary between regions of the parameter space for which the inner edge of the shear layer reaches the centreline ($h_2 \to 0$) and regions where it is deflected to the wall ($h_2 \to h$) is indicated by a black dashed line in the contour plots.

4.5 Stagnation region

We have already seen that expanding channels have the tendency to accentuate non-uniform flow. The three-dimensional example in Figure 4.4 (d, e, f) shows that an expansion of the channel causes the inner flow to slow at a greater rate than the faster outer flow. In fact, we find that, for very large expansion angles, or for very non-uniform flow, the inner flow may slow down and stop entirely, creating a region of slowly recirculating flow inside the channel (see Figure 4.2). This has been observed both from the results of our simple model and from CFD calculations. In this section, we use our simple model to characterise the onset of this region, by approximating it as a stagnant zone with zero velocity, as described in Section 4.2.

In Figure 4.8 an example of a stagnation region is shown for a two-dimensional expanding channel with expansion angle $\alpha = \tan 5.7°$ and non-dimensional length $L/h(0) = 20$. The inlet profile is given by $U_2(0)/U_1(0) = 0.3$, $h_2(0)/h(0) = 0.5$. Velocity colour plots and streamlines are displayed, calculated using both the simple model and the same k-ε model as developed in the example in Figure 4.3 (using

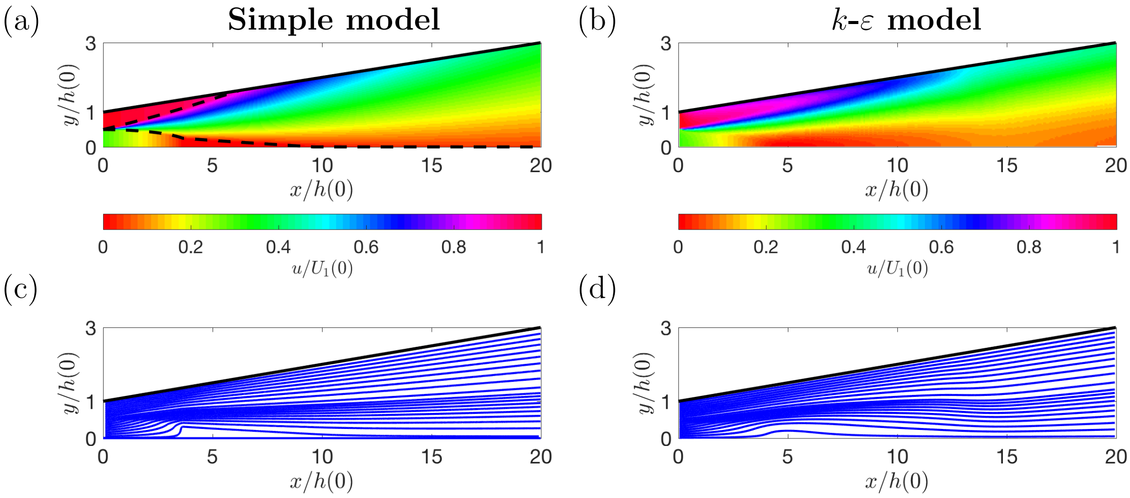

Figure 4.8: Comparison of the stagnation region in an expanding two-dimensional channel with expansion angle $\alpha = \tan 5.7°$, displaying velocity colour plots and streamlines. The inlet profile is given by $U_2(0)/U_1(0) = 0.3$, $h_2(0)/h(0) = 0.5$.

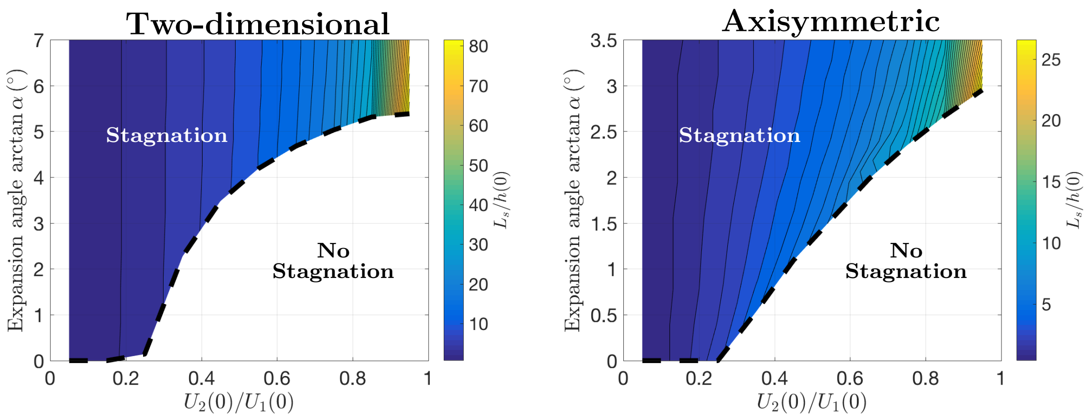

Figure 4.9: Phase diagram indicating the expansion angle and the inlet velocity ratio $U_2(0)/U_1(0)$ at which flow in a geometry (two-dimensional and axisymmetric) with linearly expanding walls stagnates. The non-dimensional distance downstream at which stagnation first occurs $L_s/h(0)$ is indicated by the contours. The inlet plug region width ratio is $h_2(0)/h(0) = 0.5$.

default values for the turbulence parameters). For comparison with the simple model we use the same values of the spreading parameter $S_c = 0.11$ and the friction factor $f = 0.01$ as in Figure 4.3. In the case of the streamlines, the transverse velocity v is calculated in terms of the streamwise velocity u (given by (4.3)), such that

$$v = -\int_0^y \frac{\partial u}{\partial x}\,\mathrm{d}y. \tag{4.15}$$

The stagnation region is made visible by a deformation of the streamlines near the channel centreline at $x \approx 5$, and a corresponding concentrated red region in the velocity colour plots. The simple model and the k-ε model show close agreement between the size and position of the stagnation region, indicating that our model has good capabilities for predicting stagnation.

From a design perspective, it is useful to establish the parameter regimes for which stagnation occurs, since avoiding such behaviour is usually necessary. In Figure 4.9 we display plots indicating the criteria for flow stagnation, calculated by the simple model, in terms of the inflow velocity ratio and the expansion angle, in both a two-dimensional channel (a) and an axisymmetric pipe (b). For the purpose of this study, we keep the inner plug region width ratio constant $h_2(0)/h(0) = 0.5$. Regions of the parameter space where a stagnation region appears are indicated. Furthermore, the non-dimensional distance downstream at which the stagnation region forms, which we denote $L_s/h(0)$, is indicated by the contours.

We can see that a stagnation region forms for large expansion angles and small velocity ratios. Both the critical expansion angle at which stagnation occurs (indicated by the dashed line) and the critical non-dimensional distance $L_s/h(0)$ increase with the velocity ratio, indicating that flows which are more uniform are less prone to stagnation. In the axisymmetric case, stagnation occurs at smaller expansion angles than the two-dimensional case, suggesting that cylindrical pipes are more susceptible to stagnation. Note that, from the discussion in Chapter 1, the typical expansion angles at which boundary layer separation occurs (which is not captured by the simple model), are $\alpha = \tan 3.5°$ in the axisymmetric case and $\alpha = \tan 7°$ in the two-dimensional case [12]. We can see that stagnation occurs at smaller expansion angles than separation, especially for velocity ratios close to 0. This indicates that stagnation is more critical than separation in channel design for non-uniform flow.

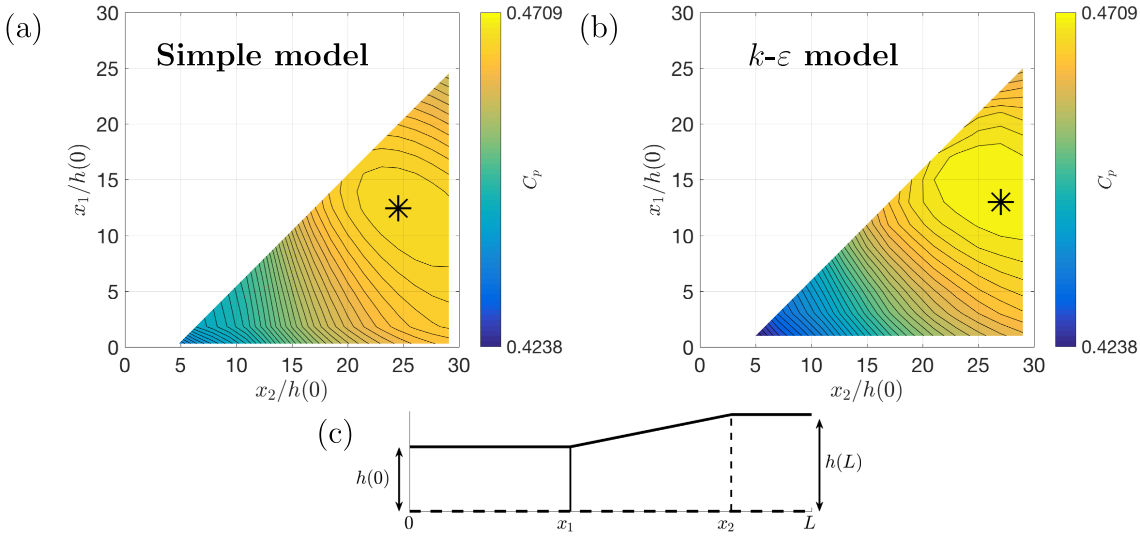

Figure 4.10: Optimum design of a diffuser with a non-uniform inlet flow profile. The diffuser, composed of two straight sections and a widening section, is 30 half-widths long $L/h(0) = 30$, and has area ratio $h(L)/h(0) = 1.5$. The inlet profile is given by $U_2(0)/U_1(0) = 0.5$, $h_2(0)/h(0) = 0.5$. The two parameters x_1 and x_2 define the split between straight and widening sections. In (a, b) contour plots of the pressure recovery coefficient (4.16) are computed using the simple model and the k-ε model, respectively, using the same colour scale.

4.6 Diffuser shape optimisation

As an application of the simple model, we study the optimal design of a two-dimensional diffuser with a non-uniform inlet flow profile. The diffuser is representative of the mixer/diffuser section in Venturi-enhanced hydropower, since the inflow is non-uniform. We restrict our attention to a particular class of shapes that are characterised by three linear sections: a straight section for $0 \leq x \leq x_1$, followed by a widening section of constant opening angle for $x_1 < x \leq x_2$, followed by another straight section for $x_2 < x \leq L$, where L is the total length of the channel (see Figure 4.10). This class of diffuser shapes is both realistic and has the advantage that it can be defined by a very small number of parameters. We measure diffuser performance by its mass-averaged pressure recovery coefficient – a measure of the pressure gained in the diffuser, relative to the kinetic energy flux at the inlet (see Chapter 1, Section 1.2),

$$C_p = \frac{\int_0^h up \,\mathrm{d}y|_{x=L} - \int_0^h up \,\mathrm{d}y|_{x=0}}{\int_0^h \frac{1}{2}\rho u^3 \,\mathrm{d}y|_{x=0}}. \tag{4.16}$$

As discussed in Chapter 1, the pressure recovery coefficient takes values $C_p \in (-\infty, 1]$, with $C_p = 1$ when all the dynamic pressure of the inlet flow is converted into static pressure. For a fixed finite area ratio $h(L)/h(0)$ and inlet flow profile, there is a maximum possible pressure recovery which is less than 1 [12]. In the case of uniform inviscid flow this ideal limit is $C_{p_I} = 1 - (h(0)/h(L))^2$ but for non-uniform flow, it is not known what the corresponding limit is [12] (although in Chapter 7 we derive a rough estimate).

For the purpose of this optimisation, we consider a two-dimensional symmetric diffuser which is 30 half-widths long $L/h(0) = 30$ and has area ratio $h(L)/h(0) = 1.5$. The inlet profile is taken to be symmetric, as in the previous examples, except with $U_2(0)/U_1(0) = 0.5$ and $h_2(0)/h(0) = 0.5$. In the context of Venturi-enhanced hydropower, the central slower stream represents the secondary flow (from the turbine) and the faster outer stream represents the primary flow. In Figure 4.10 we show a contour plot of C_p over all the possible diffuser shapes considered, calculated using both the simple model and the k-ε model. In our simple model, we use the same value of the spreading parameter $S_c = 0.11$ and the friction factor $f = 0.01$, as in Figure 4.3. We restrict the parameter space such that the opening angle of the widening section is less than the boundary layer separation limit, $\alpha = \tan 7°$, as described in Section 4.5, since our simple model is incapable of accounting for separation effects. Hence, the plots are only shown in a triangular region.

According to the simple model, there is an optimum at $x_1/h(0) = 12.4$ and $x_2/h(0) = 24.5$, giving an optimal pressure recovery of $C_p = 0.4677$. Note that this is 84% of the ideal inviscid value for uniform flow $C_{p_I} = 0.5556$. According to the k-ε model, the optimum is almost identical, with $x_1/h(0) = 13$ and $x_2/h(0) = 27$, and an optimal pressure recovery of $C_p = 0.4709$. The optimum is striking a balance between not widening too soon, which would exacerbate the non-uniform flow, and not staying narrow for too long, which would increase wall friction losses.

By comparing with Figure 4.6 (c), we see that the optimum value of x_1 coincides closely with the value of L_2 for these inflow conditions, indicating that the initial straight section must be no longer than necessary for the shear layer to reach the channel centreline. In Chapter 5 we discuss this result in greater detail and consider diffuser shape optimisation for more general classes of shapes.

4.7 Inclusion of a boundary layer and a symmetry layer

We have already compared our simple model to a k-ε model in Section 4.2 and found good agreement. However, the agreement was less good near the walls (see the two-dimensional example in Figure 4.3), due to the fact that our model does not account for boundary layer development. Furthermore, when the slower plug region is entrained by the shear layer (i.e. $h_2 = 0$), we also see less good agreement due to the fact that the velocity profile, given by (4.3), does not satisfy the symmetry condition $\partial u/\partial y = 0$ at $y = 0$. In this section we propose two extensions to our model, in the two-dimensional and axisymmetric cases, which address these discrepancies. These extensions, although they are not necessary to draw the conclusions we have made previously, are especially useful for more detailed flow predictions. By including these extensions we introduce several new variables, which we model using integral equations of mass and momentum.

Firstly, we incorporate into our two-dimensional model a turbulent boundary layer near the channel wall, by making use of the 1/7 power law, as is discussed by Schlichting et al. [87]. As discussed in Chapter 2, Section 2.4.1.2, it was shown experimentally that a velocity profile within the turbulent boundary layer, of width $h_b(x)$, which takes the form

$$u = U_1 \left(\frac{h - y}{h_b} \right)^{1/7}, \tag{4.17}$$

exhibits good comparison with experimental data for a range of Reynolds numbers ($4 \times 10^3 < Re < 3.2 \times 10^6$ [87]). Therefore, we introduce an additional layer to our velocity profile (4.3) and use (4.17) for $h - h_b < y < h$ (see Figure 4.11). Note that, in reality, there is a viscous sub-layer (and a log-law layer) within the turbulent boundary layer but, for the purposes of this study, we neglect this detail and assume that (4.17) applies all the way to the channel wall. In order to determine h_b, following Chapter 2, Section 2.4.1.2, we invoke conservation of momentum, integrated across the boundary layer width, such that

$$\rho \frac{\mathrm{d}}{\mathrm{d}x} \int_{h-h_b}^{h} u^2 \,\mathrm{d}y - \rho U_1 \frac{\mathrm{d}}{\mathrm{d}x} \int_{h-h_b}^{h} u \,\mathrm{d}y = -h_b \frac{\mathrm{d}p}{\mathrm{d}x} + \tau_h. \tag{4.18}$$

Next we incorporate a turbulent 'symmetry layer' into our model. If the slower plug region is entrained by the shear layer (i.e. $h_2 = 0$), then the velocity profile (4.3) is not symmetric about the channel centreline, $y = 0$, which is unphysical. Therefore, we posit that there is a turbulent layer along the centreline of width h_s, which satisfies the symmetry condition, $\partial u/\partial y = 0$ at $y = 0$. Motivated by comparison with CFD calculations, we propose a parabolic velocity profile within the symmetry layer. The parabola function

$$u = U_2 + \frac{(U_1 - U_2)}{2h_s\delta} \left(y^2 - h_s^2 \right), \tag{4.19}$$

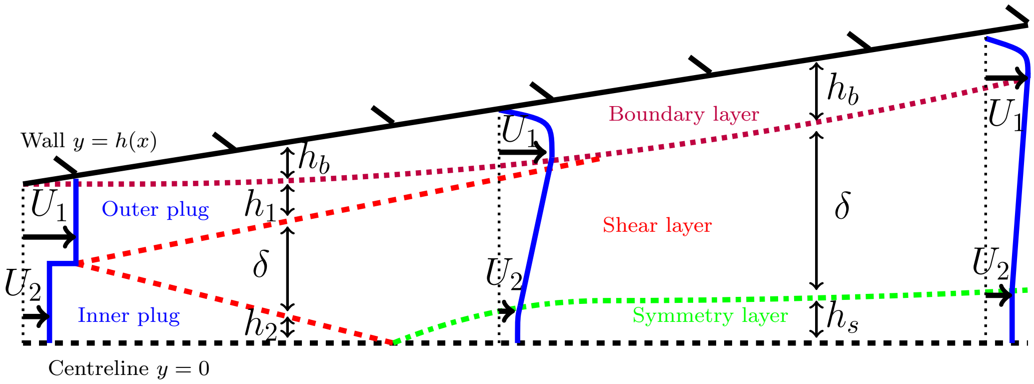

Figure 4.11: Schematic diagram illustrating the layer structure of the extended model, which includes a boundary layer near the channel wall and a symmetry layer near the channel centreline. Velocity profiles are illustrated at three locations.

is suitable, since it is both continuous and has continuous derivative $(\partial u/\partial y)$ at $y = h_s$. Therefore, we introduce the symmetry layer to our velocity profile (4.3) and use (4.19) for $0 < y < h_s$ (see Figure 4.11). The width of the symmetry layer h_s is determined by invoking conservation of momentum, integrated across the width of the layer, such that

$$\rho \frac{\mathrm{d}}{\mathrm{d}x} \int_0^{h_s} u^2 \,\mathrm{d}y - \rho U_2 \frac{\mathrm{d}}{\mathrm{d}x} \int_0^{h_s} u \,\mathrm{d}y = -h_s \frac{\mathrm{d}p}{\mathrm{d}x} + \tau_{h_s}, \tag{4.20}$$

where τ_{h_s} is the shear stress from the shear layer on the symmetry layer. Equation (4.20) is derived by following Chapter 2, Section 2.4.1, with $a = 0$ and $b = h_s$, where we impose the symmetry condition $v = \partial u/\partial y = 0$ at $y = 0$. We model τ_{h_s} with a Prandtl mixing length model [87], similarly to Chapter 2, Section 2.4.1.1, using a mixing length proportional to the shear layer width, $\ell = C\delta$, and approximating the velocity gradient $\partial u/\partial y \approx (U_1 - U_2)/\delta$, such that

$$\tau_{h_s} = \rho C^2 (U_1 - U_2)^2. \tag{4.21}$$

The constant C is related to the turbulent Reynolds number, and must be determined by fitting to experimental data or CFD calculations.

To summarise, we have incorporated two additional layers into our simple model: a turbulent boundary layer near the channel wall satisfying the no-slip condition, and a turbulent symmetry layer near the channel centreline satisfying the symmetry condition. We have introduced two new variables h_b and h_s, which are both functions of x, and are governed by Equations (4.18) and (4.20).

Note that we can easily alter the extended model to account for axisymmetric flows. For axisymmetric flow in a cylindrical channel $0 \le r \le h$, we assume that that the velocity profile in the boundary layer and the symmetry layer are identical to (4.17) and (4.19), except with y replaced by r. Following Chapter 2, we modify (4.18) and (4.20) to account for radial symmetry, such that

$$\rho \frac{\mathrm{d}}{\mathrm{d}x} \int_{h-h_b}^{h} r u^2 \,\mathrm{d}r - \rho U_1 \frac{\mathrm{d}}{\mathrm{d}x} \int_{h-h_b}^{h} r u \,\mathrm{d}r = -\frac{1}{2}\left(h^2 - (h-h_b)^2\right) \frac{\mathrm{d}p}{\mathrm{d}x} + h\tau_h, \tag{4.22}$$

$$\rho \frac{\mathrm{d}}{\mathrm{d}x} \int_{0}^{h_s} r u^2 \,\mathrm{d}r - \rho U_2 \frac{\mathrm{d}}{\mathrm{d}x} \int_{0}^{h_s} r u \,\mathrm{d}r = -\frac{1}{2} h_s^2 \frac{\mathrm{d}p}{\mathrm{d}x} + h_s \tau_{h_s}. \tag{4.23}$$

Next we compare the results of our extended model to those of our original simple model, and a k-ε model, in the case of a two-dimensional channel and an axisymmetric pipe. We consider both a straight sided geometry with no expansion, and an expanding geometry with expansion angle $\alpha = \tan 1.4°$. The geometries are 20 m long and have radius/half-width 1 m. We choose an inlet flow profile with $h_2(0)/h(0) = 0.5$ and $U_2(0)/U_1(0) = 0.5$, where the speed of the faster plug region is $U_1(0) = 1\,\mathrm{m/s}$. The Reynolds number for this flow, defined in the same way as the example in Figure 4.3, is $Re = 10^6$. For comparison with our simple model and our extended model, we use the same values for the spreading parameter $S_c = 0.11$ and the friction factor $f = 0.01$ as in Figure 4.3. For the mixing length constant C in (4.21), we find that $C = 0.13$ gives the best fit with the data.

In Figure 4.12 we compare velocity profiles across the channel at evenly spaced locations down the channel and the pressure profile, averaged across the width of the channel. The development of the boundary layer, which is not included in the simple model, is captured accurately by the extended model, which is shown by the close agreement with the k-ε model in the velocity near the walls. Furthermore, the development of the symmetry layer in the extended model results in better agreement with the k-ε model in the velocity near the centreline. The pressure profiles for both the extended model and the simple model are very similar, and both agree well with the k-ε model.

The extended model has nominally the same computational cost as the original simple model, though it contains more variables and equations, and it is perhaps more difficult to implement. Therefore, the original model serves as a convenient tool for benchmark predictions, whilst the extended model is appropriate for more detailed and accurate calculations of flow development, but it takes longer to implement.

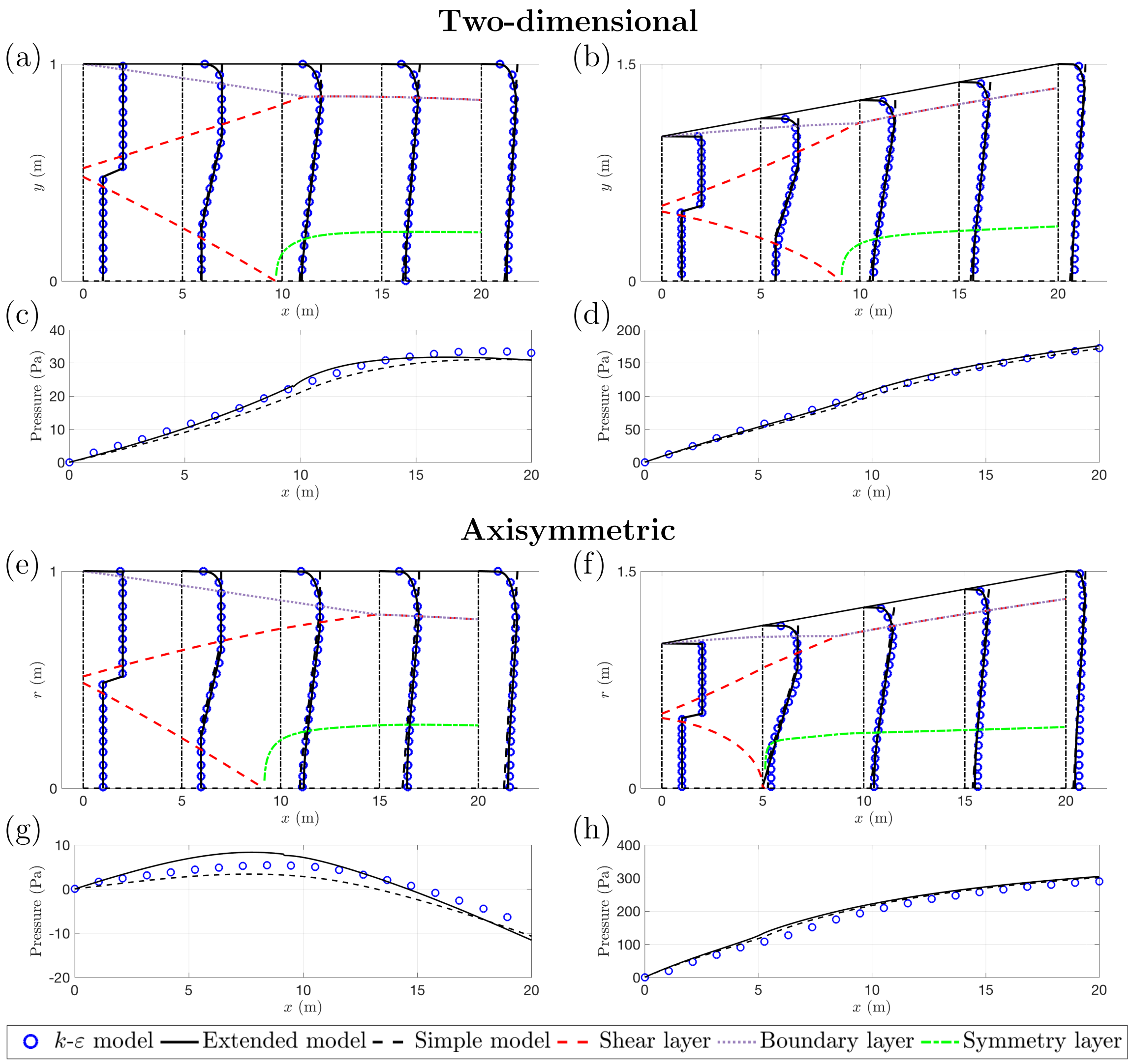

Figure 4.12: Comparison of the extended model, the simple model and the k-ε model for symmetric shear flow in a straight geometry and a widening geometry, in both the two-dimensional and axisymmetric cases. (a, b, e, f) Velocity profiles at evenly spaced locations. (c, d, g, h) Pressure, averaged across the channel width. The position of the shear layer, the boundary layer, and the symmetry layer are illustrated, as in the schematic diagram in Figure 4.11. In each case, the inlet profile is given by $U_2(0)/U_1(0) = 0.5$, $h_2(0)/h(0) = 0.5$, and the Reynolds number is $Re = 10^6$.

It should be noted, however, that whilst the extended model accounts for the boundary layer near the channel wall, it does not account for boundary layer separation. This is because the extended model uses a self-similar power law velocity profile within the boundary layer (4.17), and separated flow is not self-similar [87]. Therefore, like the original simple model, we do not expect the extended model to be accurate for very wide expansion angles.

4.8 Summary and concluding remarks

We have developed a simple model for turbulent shear layers in confined geometries and we have compared the model predictions with PIV experiments and CFD for a variety of channel shapes, in two and three dimensions and in the axisymmetric case. The model depends on two parameters, the friction factor f, which we found was well estimated by the Blasius relationship [11], and the spreading parameter S_c which was fitted to the CFD and experimental data. By comparing the simple model to CFD simulations in a two dimensional channel and an axisymmetric pipe (see Figures 4.3 and 4.12 as well as Appendix A), using the default parameter values of several RANS models, including k-ε and k-ω SST, we found that $S_c = 0.11$ was consistently an appropriate value for a good fit. However, by comparing with our experimental data, we found that the RANS models in three dimensions, with default parameter values, and our simple model, with a spreading parameter value of $S_c = 0.11$, under-predicted the shear layer growth rate. By increasing the eddy viscosity in the k-ε model, and by choosing a spreading parameter value of $S_c = 0.18$, we found good agreement between the simple model, the three-dimensional k-ε model and the experimental results. Thus, it appears that mixing was accelerated by the three-dimensional effects of the top and bottom walls in the experiment.

We propose that $S_c = 0.11$ be used as a standard value for the spreading parameter in two-dimensional and axisymmetric flows, since it was consistently an appropriate value for a good fit with several RANS models in a variety of two-dimensional and axisymmetric geometries and at different Reynolds numbers. However, we note that S_c may take other values in situations where shear layer growth rates are magnified, such as in our three-dimensional channel example. In addition, in such situations RANS models with default parameter values may not be accurate.

For the friction factor f we used the Blasius relationship (4.7) to estimate its value in terms of the Reynolds number, which we took to be constant. We have also tried allowing f to vary with x, as the average velocity (and hence the local Reynolds number Re) in the channel changes, but we found that this makes little difference to the results. This is expected since, in expanding geometries (see Figure 4.4 (d, e, f) for example), the hydrodynamic diameter increases whilst the average velocity decreases, such that Re stays approximately constant. Furthermore, according to the Blasius relationship (4.7), f depends weakly on Re.

In the comparisons between our simple model, CFD simulations in two or three dimensions and experimental data, the comparison was less good near the channel walls and along the channel centreline. This is because our simple model doesn't account for boundary layer development at the walls, and doesn't satisfy the symmetry condition at the centreline when the inner plug region is entirely entrained. By including a boundary layer and a symmetry layer into our model, it was possible to greatly reduce these discrepancies. These features, whilst not critical for predicting the general flow behaviour, are useful for more detailed calculations. As we discussed earlier, although we included a boundary layer in our extended model, we do not expect this self-similar boundary layer profile to capture the effects of boundary layer separation (not self-similar), which occurs for wide expansion angles. For future work, we could improve our extended model by considering more generalised boundary layer profiles, which can accurately capture such effects.

Using the original simple model in the two-dimensional and axisymmetric cases (without extensions to account for the boundary and symmetry layers), we investigated the dependence of the shear layer growth on the inflow conditions and the channel shape. Both the inflow velocity ratio $U_2(0)/U_1(0)$ and the inner plug region width ratio $h_2(0)/h(0)$ played an important role in the development of the shear layer. In particular, for some choices of these parameters the shear layer was directed inwards towards the flow centre, whilst for others the shear layer was directed outwards, towards the channel wall. We showed that if the flow is sufficiently non-uniform, or if the channel expansion angle is too large, then the slower central flow may slow to zero velocity, forming a stagnated region along the channel centreline. We established the criteria for the formation of such a region, in terms of the inflow velocity ratio and the channel expansion angle.

The model's simplicity and low computational cost makes it ideal for simulation and design purposes for a range of problems. As an application, we investigated optimal pressure recovery in a diffuser composed of three piecewise linear sections. We found that the optimum shape strikes a balance between not widening too soon and not staying shallow too long. However, it is of great interest to be able to find the optimum diffuser shape without restricting our attention to a particular class of shapes with a low-dimensional parameterisation. If we want to consider more general classes of diffuser shapes, then more advanced techniques are required to find the optimum. This is the topic of the next chapter.

Chapter 5

Optimal control of diffuser shapes for non-uniform flow

5.1 Introduction

In this chapter, we consider a class of expanding channel flows in which the inflow is non-uniform, resulting in turbulent shear layers confined within the channel. Expanding channels, known as diffusers, have the function of converting high-speed low-pressure flow to low-speed high-pressure flow. Diffusers have numerous applications, from turbines in aerospace and hydropower [19, 50, 89] to automotive design [49]. There is a large literature on diffusers in the case where the inflow is uniform (see [12]), but a limited literature for non-uniform inlet flows and flows with shear layers [7].

In the case where the inflow is uniform, as is discussed in Chapter 1, diffusers are usually designed to be straight sided, and the expansion angle is critical to performance [12]. The optimal angle strikes a balance between not being too shallow, since thin channels have larger wall drag, and not being too wide, since wide expansion angles result in boundary layer separation and poor consequent pressure recovery [25]. The optimum angle varies slightly, depending on the inflow boundary layer thickness, and whether the diffuser is two-dimensional or axisymmetric (conical).

In the case where the inflow is non-uniform, there have been some experimental studies which have investigated diffuser performance for specific inflow profiles. Horlock & Lewis [47] studied an asymmetric shear flow and a symmetric wake flow in a linearly expanding two-dimensional diffuser using a simple inviscid model and experiments. They found that both of these non-uniform flow profiles became accentuated by the diffuser. The experiments of Wolf & Johnston [106] studied several non-uniform inlet flows for a two-dimensional diffuser. They considered an asymmetric flow profile with uniform shear, an asymmetric step-shear profile, a symmetric jet profile, and a symmetric wake profile. For each case they studied straight sided diffusers with linearly expanding walls, using several different expansion angles and non-dimensional lengths (see Chapter 1). They found that these non-uniform inflows resulted in poorer diffuser performance than for a uniform inflow. They attributed this to the early onset of diffuser stall observed for these non-uniform inflows due to the accentuation of the flow profile. Other experimental studies are given by [9, 32, 102, 62, 41, 76, 108].

As is shown by Wolf & Johnston [106], the development of the non-uniform flow profile is strongly affected by the shape of the diffuser. An important feature in understanding non-uniform flows is the interplay between changes in the pressure and the kinetic energy flux factor, which is a normalised measure of how non-uniform a flow is [12]. A decrease in kinetic energy flux factor corresponds to a more uniform flow, and a rise in pressure. As shown by [47, 106], diffusers with wide angles have the tendency to accentuate non-uniform flows and, in some extreme cases, create a jet-like outflow. In such cases, the outflow has a high kinetic energy flux and, hence, a low pressure recovery. On the other hand, diffusers with shallow angles have longer, narrower profiles, which create a lot of wall drag and consequently a larger drop in pressure. Optimal diffuser shapes, therefore, must strike a balance between mixing the flow in a narrow section and then widening the flow to decrease wall drag.

In this chapter, we identify the optimal diffuser shape which satisfies these criteria. Unlike the previous studies of diffusers with non-uniform inflows, we do not restrict our attention to straight-sided diffusers with linearly expanding walls. Instead, we consider all continuous diffuser shapes with bounded expansion angle. We find that, for a range of parameter values, the optimum diffuser shape is approximately divided into two straight sections separated by a widening section. The initial straight section is necessary to aid mixing the flow before expansion. The expansion angle of the widening section is approximately constant and significantly smaller than typically used for diffusers with uniform inflow. Therefore, in contrast to diffusers with uniform inflow, where the expansion angle is only restricted due to boundary layer separation, diffusers with non-uniform inflow have a shape which is also restricted due to the effect of accentuating the non-uniform flow. Hence, from a design perspective, the effect of the inflow profile cannot be ignored. In our analysis, we show how to optimise diffuser design based on the nature of the non-uniform inflow.

We investigate three different classes of non-uniform inflow, with the streamwise velocity varying across the width of the diffuser entrance. The first case has inner and outer streams of different speeds, with a velocity jump between them that evolves into a shear layer downstream, and the shear layer eventually interacts with the channel walls. The second case is the limit where the speeds of the streams are similar, creating a thin, slowly growing shear layer. In the third case, the inflow is a pure shear profile, with linear velocity variation between the centre and outer edge of the diffuser. These flow profiles are motivated by Venturi-enhanced hydropower, where the inner and outer streams are the secondary and primary flows, respectively. Since the inflows are non-uniform, the diffusers we study here are equivalent to the mixer/diffuser in Venturi-enhanced hydropower.

For these non-uniform flows which we consider, the development of the flow profile, which is fundamental to pressure recovery, can be described using a simple model for turbulent shear layers in confining channels, as described in Chapter 4. In Chapter 4 we used this model to investigate optimal pressure recovery for a simple class of diffuser shapes by exhaustively searching a restricted design space. When we widen the parameter space and treat the diffuser shape as a continuous control, it is necessary to seek more complex tools to solve the problem. In this chapter, we use the simple model as the basis for numerical optimisation of the diffuser shape, where the governing equations of the model form the optimisation constraints. Such problems, as well as PDE-constrained optimisation problems, often arise in the field of flow control. With the advancement of computational power, these problems have become more feasible to solve. There are many different approaches to solving such problems which are discussed by Gunzburger [44].

In our approach we exploit the fact that the model is one-dimensional and, upon discretisation, there are relatively few decision variables. This, in combination with the use of automatic differentiation to calculate gradients, allows us to use an interior point Newton method with relatively low computational effort [73]. In certain limiting cases, we solve the optimal control problem analytically using Pontragin's maximum principle [78] and these analytical results aid interpretation of the results from the numerical optimisation. We show that some of the optimal diffuser shapes look approximately like they are composed of piecewise linear sections. This motivates a low-dimensional parameterisation of the diffuser shapes, for which we use more detailed and computationally intensive CFD models to search for optima under more realistic flow behaviours. The two CFD models we use are a k-ε model [55] and a k-ω SST model [67]. We find that the optimal diffuser shapes for both these CFD models are very similar to those found using our simple model.

Section 5.2 outlines the model for the non-uniform flow profiles we consider and sets up the optimal control problem, discussing the choice of objective, the constraints and the number of parameters. Section 5.3 outlines a numerical method for solving the optimal control problem and, using this method, we investigate optimal diffuser shapes in three different cases. In Section 5.4 we find analytical solutions to the optimal control problem in the last two of these cases. In Section 5.5, we present some CFD calculations and compare them to the results of the optimisation. Section 5.6 summarises the results of the chapter and discusses the dependance of the optimal shapes on parameter choices.

5.2 The model and optimal control problem

5.2.1 Summary of the mathematical model

In Chapter 4 we described our simple model for turbulent shear layers in confining channels. In this section we outline the flow situations we consider and summarise the governing equations of the model.

There are three different types of non-uniform channel flow we consider, all of which are symmetric about the channel centreline. In Figure 5.1 we display each case, illustrating the streamwise velocity varying across the width of the diffuser. The first, which we call the *developing shear layer case*, is an inflow composed of inner and outer streams of different speeds, with a velocity jump in between. In this case, a shear layer forms between the streams and grows downstream, eventually interacting with the channel walls. We restrict our attention to situations where the inner stream is slower than the outer stream, as is representative of Venturi-enhanced hydropower. In other situations where the outer stream is slower than the inner stream, there is a greater risk of boundary layer separation, since the slowest region of flow is next to the wall [12]. Furthermore, it is well known that asymmetric flow instabilities, such as the Coanda effect [97], can occur in these situations, which are not included in our model. The second case, called the *small shear limit*, is similar to the first case, except the inner and outer streams have near-identical velocities, such that the shear between the flows is small and the thin shear layer grows slowly. In the third case, called the *pure shear limit*, we consider a pure shear profile with linear velocity variation between the centre and outer edge of the diffuser. This corresponds

(a) **Developing shear layer** (b) **Small shear limit** (c) **Pure shear limit**

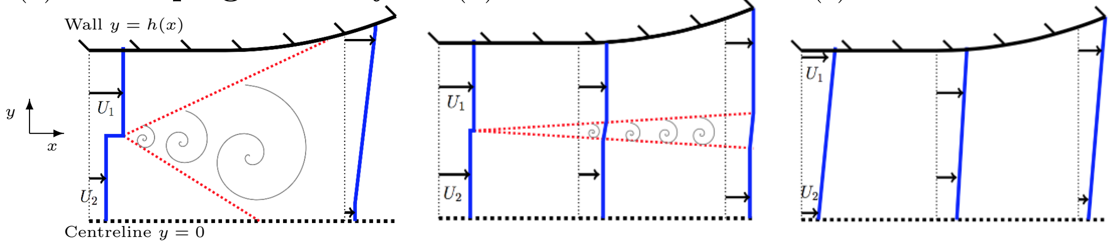

Figure 5.1: Schematic diagram of the different flow cases. a) *Developing shear layer case*, where the inflow has inner and outer streams of different speeds, with a velocity jump between them that develops into a shear layer. The channel length is sufficiently large such that the growing shear layer reaches across the channel. b) *Small shear limit* case, which is the limiting case where the speeds of the streams are similar, such that the thin, slowly growing shear layer never reaches across the channel. c) *Pure shear limit*, where the velocity varies linearly between the centre and the outer wall of the diffuser.

to the developing shear layer case far downstream, where the shear layer has reached across the entire channel.

The simple model presented in Chapter 4 is used to describe the idealised flow profiles for each of the three cases. The first two cases share the same formulation of the model, whilst the third case is slightly different. Thus, we start by describing the governing equations for the first and second cases. Initially we consider two-dimensional flow in a half channel $0 < y < h(x)$ (see Figure 5.1 (a), where we indicate our coordinate axes) and later we extend the model to axisymmetric pipes. The inflow for the first two cases is composed of a slower moving central stream with speed U_2 and a faster outer stream with speed U_1. A turbulent shear layer forms at the place where the parallel streams meet. Therefore, as in Chapter 4, we approximate the flow profile by decomposing it into two plug regions separated by a shear layer in which the velocity varies linearly between U_1 and U_2 (see Figure 4.1). The approximate velocity profile is given by (4.3). In the small shear limit, the plug flow speeds U_1 and U_2 are similar, such that the shear layer grows slowly. In the developing shear layer case the shear layer may grow and interact with the channel walls, whilst in the small shear limit the channel is chosen to be sufficiently short that the slowly growing shear layer remains thin and never reaches the channel walls.

For both the first and second cases, the simple model from Chapter 4 describes the evolution of the non-uniform velocity profile $u(x, y)$, given by (4.3), and pressure $p(x)$ in a symmetric confining channel. Equations (4.2) - (4.9) govern the variables U_1, U_2, h_1, h_2, δ, ε_y and p, which are all functions of x. These equations can be solved for all x given inflow conditions at $x = 0$. Since the shear layer forms at $x = 0$, the inflow conditions for δ and ε_y are $\delta(0) = 0$ and $\varepsilon_y(0) = \infty$[1]. Pressure is measured with reference to the value at the inlet so we can take $p(0) = 0$ without loss of generality. All other inflow conditions form part of the set of parameters which we discuss in Section 5.2.2.

In the pure shear limit the plug regions are non-existent, such that $h_1 = h_2 = 0$ and $\delta = h$. Then the velocity profile takes the form

$$u(x, y) = U_2(x) + \varepsilon_y(x)y, \tag{5.1}$$

where the shear rate is now given by $\varepsilon_y = (U_1 - U_2)/h$. In this case the governing equations of the model reduce to (4.2), (4.4) and (4.5), which govern the variables U_1, U_2, ε_y and p.

We can extend the model to account for axisymmetric flows simply. For axisymmetric flow in a cylindrical channel $0 < r < h$, we assume that that the velocity profile is identical to (4.3) in the first two cases, and (5.1) in the third case, except with y replaced by r. In the axisymmetric version of the model, (4.2) and (4.8)-(4.9) remain unchanged, but (4.4) and (4.5) are altered to account for radial symmetry, resulting in (4.10) and (4.11). The results of the axisymmetric and two-dimensional cases are compared in Section 5.3.

5.2.2 Formulation of the optimal control problem

In this section we describe the optimal control problem by choosing an optimisation objective and formulating the control variables and constraints. Starting with the objective, we note that diffuser performance can be measured in a number of different ways, for example using a pressure recovery coefficient or a loss coefficient [12]. The pressure recovery coefficient C_p is a measure of the pressure gain in the diffuser from inlet to outlet, relative to the kinetic energy flux at the inlet. The loss coefficient k_l is a measure of the total energy lost from inlet to outlet, relative to the kinetic energy flux at the inlet. For our optimal control problem, we could choose either of these coefficients as the objective. Maximising C_p, for a given inflow, would produce the diffuser that converts the greatest amount of inflow kinetic energy into static pressure at the outflow. Minimising k_l, for a given inflow, would produce the diffuser with the maximum amount of energy at the outflow.

[1] In practice it is difficult to implement $\varepsilon_y(0) = \infty$ numerically, so instead we solve for the inverse of the shear rate which satisfies $1/\varepsilon_y(0) = 0$.

For this chapter, we choose the pressure recovery coefficient as the objective since this corresponds to maximising the efficiency of Venturi-enhanced hydropower (see Chapter 1). There are several ways to define the coefficient, but motivated by the discussion in Chapter 1, we use the so-called 'mass-averaged' pressure recovery [32], which is given by (4.16) for the two-dimensional case and

$$C_p = \frac{\int_0^h upr \, \mathrm{d}r|_{x=L} - \int_0^h upr \, \mathrm{d}r|_{x=0}}{\int_0^h \frac{1}{2}\rho u^3 r \, \mathrm{d}r|_{x=0}}, \tag{5.2}$$

for the axisymmetric case. The pressure recovery coefficient can take values $C_p \in (-\infty, 1]$, where $C_p = 1$ when all the kinetic energy of the inlet flow is converted into static pressure. For a given area ratio $h(L)/h(0)$ and inflow, there is a maximum possible pressure recovery C_{p_I} which is less than 1 [12]. For two-dimensional[2] uniform inviscid flow this ideal limit is $C_{p_I} = 1 - (h(0)/h(L))^2$, but for non-uniform flow, it is not known what the limit is (although we derive a rough estimate in Chapter 7).

Now that we have chosen a suitable objective for the optimisation, we need to define a control. The diffuser shape is ultimately the control of the problem, but there are several different ways to formulate it. For example, we could use the shape function $h(x)$ as the control, or we could use its derivative, or even the second derivative. To aid our choice of control, we consider the regularity requirements of the final shape. If the minimum requirement is that the shape be continuous, it will be convenient to choose the derivative of h as the control. If we also require smoothness (i.e. existence of the first derivative of h), then it will be convenient to choose the second derivative of h as the control. However, if no such requirements exist, then it is satisfactory to use h itself as the control. For this chapter, we restrict ourselves to continuous but non-smooth shapes, and so we choose the shape derivative, or diffuser angle,

$$\alpha(x) = \frac{\mathrm{d}h}{\mathrm{d}x}, \tag{5.3}$$

as the control for optimising the diffuser shape. In reality, sudden expansions and sharp corners, if severe enough, can cause flow separation which is detrimental to pressure recovery [12]. Therefore, any such sharp corners must be rounded off with a suitable radius of curvature, upon construction. However, we neglect this concern from our mathematical analysis. An additional possible control of the problem is the channel length L. For now, we consider this fixed, but later we discuss the possibility of including L as a decision variable.

[2] For axisymmetric uniform inviscid flow the ideal limit is $C_{p_I} = 1 - (h(0)/h(L))^4$.

After defining both the objective and the control of the optimisation, we now discuss the constraints. The most obvious constraints on the variables are the governing equations and inflow conditions. In addition, we may also want some constraints on the outflow. As mentioned earlier, constraining $h(L)/h(0)$ gives us a fixed maximum value for the pressure recovery. If $h(L)/h(0)$ is unconstrained, then the pressure recovery will be maximised with $h(L)/h(0) = \infty$ [12]. However, this is impractical for construction and, due to Bernoulli's equation, we see that pressure recovery decays rapidly with h (like $\sim 1/h^2$ for two-dimensional flows and like $\sim 1/h^4$ for axisymmetric flows), so that a large majority of pressure is recovered for relatively small values of $h(L)/h(0)$. For example, in uniform inviscid axisymmetric flow, if $h(L)/h(0) = 3$ the pressure recovery is $C_{p_I} \approx 0.99$. Therefore, for practical considerations, we constrain the channel width at the outflow

$$h(L) = h_L. \tag{5.4}$$

Another important constraint we need to consider is the boundedness of the control α. In particular, we note that for large values of the diffuser angle, boundary layers at the channel walls have the tendency to separate (see discussion in Chapter 1, Section 1.2). This phenomenon, which is often called 'diffuser stall', is not something that we attempt to capture within our model. However, it is known that diffuser stall has a detrimental effect on pressure recovery (because the flow does not slow down). Considering this, we give the control α an upper bound corresponding to the smallest diffuser angle which causes stall. The first appreciable stall of a straight walled diffuser is at $\alpha \approx \tan 7^\circ$ for the two-dimensional case and $\alpha \approx \tan 3.5^\circ$ for axisymmetric diffusers (see Section 1.2). Furthermore, due to engineering constraints, it might not always be possible to construct channel shapes which contract more than a certain angle. Therefore, a lower bound on the control may also be necessary. If we denote the upper and lower bounds α_{max} and α_{min}, respectively, then α satisfies the box constraints

$$\alpha_{min} \leq \alpha \leq \alpha_{max}. \tag{5.5}$$

Whilst (5.5) applies, the optimal control might not necessarily attain these bounding values. In such cases, (5.5) may be considered irrelevant.

To summarise the formulation of the optimal control problem, we seek to maximise the pressure recovery by manipulating the control $\alpha(x)$ within its bounds:

$$\max_{\alpha_{min} \leq \alpha(x) \leq \alpha_{max}} C_p, \tag{5.6}$$

Parameter	Description
$U_2(0)/U_0$	Velocity ratio
$h_2(0)/h_0$	Plug width ratio
$h(L)/h_0$	Expansion ratio
L/h_0	Length ratio
α_{min}, α_{max}	Minimum/maximum angle
S_c	Spreading parameter
f	Friction factor

Table 5.1: List of the parameters of the optimal control problem. We treat the first 5 of these parameters as problem-specific, whereas the last 2 parameters are considered fixed. We make use of the shorthand $U_0 = U_1(0)$ and $h_0 = h(0)$.

with the constraints that Equations (4.2)-(4.9) hold, together with inlet conditions for all variables at $x = 0$, and the end constraint (5.4).

Before solving the optimal control problem, we note that there are several parameters which affect the solution. We list these parameters in Table 5.1 and discuss them in more detail in Section 5.6.

5.3 Numerical optimisation

This section, in which we solve the optimal control problem numerically for several different cases, is divided into subsections for clarity. Firstly, we describe our solution method for the numerical optimisation. Then, Section 5.3.1 studies the solution in the developing shear layer case (see Figure 5.1 (a)). In this case, we find that optimal diffuser shapes look approximately like they are composed of piecewise linear sections (as in Chapter 4, Section 4.6). This observation motivates us to introduce a low-dimensional parameterisation of the shapes that can be explored with contour plots, which is useful when comparing with CFD calculations later in Section 5.5. The small shear limit and the pure shear limit (see Figure 5.1 (b, c)) are discussed in Sections 5.3.2 and 5.3.3, respectively. Finally a description of some of the numerical details is in Section 5.3.4.

We solve the optimisation problem (5.6) numerically by discretising space into N points, introducing values of the variables U_1, U_2, h_1, h_2, δ, ε_y, p, h and α at each spatial point, and treating each discretised value as a degree of freedom. With 9 variables, the total number of degrees of freedom is $9N$. We refer to the set of all variables as $\mathbf{x} \in \mathbb{R}^{9N}$.

Of the constraints we need to impose, there are both equalities and inequalities. The equality constraints we need to impose are Equations (4.2)-(4.9), inflow conditions and the terminal condition (5.4). Some of these equality constraints are differential equations, which are imposed using a second order backward finite difference scheme. The inequality constraints consist of (5.5) and those listed in the complementarity conditions (4.8)-(4.9). We refer to the equality constraints as $c_i(x)$ and the inequality constraints as $d_i(x)$. Therefore, the optimisation problem can be written as follows:

$$\max_{\mathbf{x}\in\mathbb{R}^{9N}} C_p(\mathbf{x}), \tag{5.7}$$

such that

$$c_i(\mathbf{x}) = 0, \quad \text{for} \quad i = 1, \ldots, m_c \tag{5.8}$$

$$d_i(\mathbf{x}) \geq 0, \quad \text{for} \quad i = 1, \ldots, m_d. \tag{5.9}$$

As is often done, we impose the equality constraints using the quadratic penalty method [73], where we subtract their residual squared from the objective. Therefore, the optimisation problem (5.7)-(5.9) is rewritten as

$$\max_{\mathbf{x}\in\mathbb{R}^{9N}} \hat{C}_p(\mathbf{x}) := C_p(\mathbf{x}) - \mu_c \frac{1}{m_c} \sum_{i=1}^{m_c} c_i(\mathbf{x})^2, \tag{5.10}$$

such that

$$d_i(\mathbf{x}) \geq 0, \quad \text{for} \quad i = 1, \ldots, m_d. \tag{5.11}$$

where $\mu_c > 0$ is a penalty parameter. The quadratic penalty term is normalised by the number of constraint equations m_c so that the choice of μ_c is relatively independent of the number of discretisation points (though we later find this is not the case). We discuss how μ_c is chosen in more detail at the end of this section. Our inequality constraints d_i are simple box constraints. We treat these using the interior point method for non-linear constrained optimisation problems (with the IPOPT implementation). For the purpose of this thesis we now illustrate the basic principles of the method with a brief overview. The full details of the interior point method (including modern implementations such as IPOPT) can be found in [73, 101].

The interior point method replaces the inequality constraints d_i with logarithmic barrier functions added to the objective, similarly to the quadratic penalty method. The optimisation problem (5.10)-(5.11) is then rewritten as

$$\max_{\mathbf{x}\in\mathbb{R}^{9N}} \hat{C}_p(\mathbf{x}) + \mu_d \sum_{i=1}^{m_d} \log d_i(\mathbf{x}), \tag{5.12}$$

where $\mu_d > 0$ is a barrier parameter. The choice of μ_d is discussed by Nocedal & Wright [73]. The logarithmic barrier functions ensure that iterations always remains inside the interior of the domain, which is the reason for the name of the method. This method requires that both the objective and constraint functions are twice continuously differentiable. It is for this reason that we impose Equations (4.8) and (4.9), which have discontinuous switching behaviour, in a complementarity format. Consequently, all of the model equations satisfy the twice differentiable smoothness criterion.

The interior point method is a primal-dual method. In addition to the primal variables $\mathbf{x} \in \mathbb{R}^{9N}$, there are dual variables (or Lagrange multipliers) $\boldsymbol{\lambda} \in \mathbb{R}^{m_d}$. Optimal dual variables can be estimated by

$$d_i(\mathbf{x})\lambda_i = \mu_d, \quad \text{for} \quad i = 1, \ldots, m_d. \tag{5.13}$$

Equation (5.13) is related to complementarity slackness in the Karush-Kuhn-Tucker conditions [73]. Optimal primal variables (maximisers of (5.12)) satisfy the condition that the gradient of the objective is zero which, due to (5.13), is written

$$\boldsymbol{\nabla}\hat{C}_p + \mathbf{J}^T\boldsymbol{\lambda} = \mathbf{0}, \tag{5.14}$$

where $\mathbf{J}$ is the Jacobian matrix of the constraints d_i. The approach of the interior point method is to iteratively solve the nonlinear system of equations (5.13) and (5.14) for both the primal and dual variables using Newton's method. There is an additional constraint $\lambda_i \geq 0$, $\forall i$, which ensures (5.11), and this is imposed by choosing an appropriate step size at each iteration. Newton's method is a second order method and so requires the Hessian matrix $\mathbf{H}$ of $\hat{C}_p$. We calculate derivatives for $\mathbf{H}$ and $\mathbf{J}$, using automatic differentiation in the JuMP package [27] of the Julia programming language [8]. Computation time is fast, owing to the use of automatic differentiation to calculate gradients (as opposed to finite differencing, for example). For a discretisation $N = 100$ grid points, and therefore 900 degrees of freedom, computation time is of the order of less than 10 seconds on a laptop computer.

It is not known whether this optimisation problem is convex so there may exist multiple solutions. To have confidence about the optimal solutions that are found, we use many different initial guesses to initialise the interior point method (although we have not yet found any multiple solutions).

5.3.1 The developing shear layer case

Having discussed the optimisation routine, we use it to optimise channel shapes in several different cases, starting with the developing shear layer case. For plotting

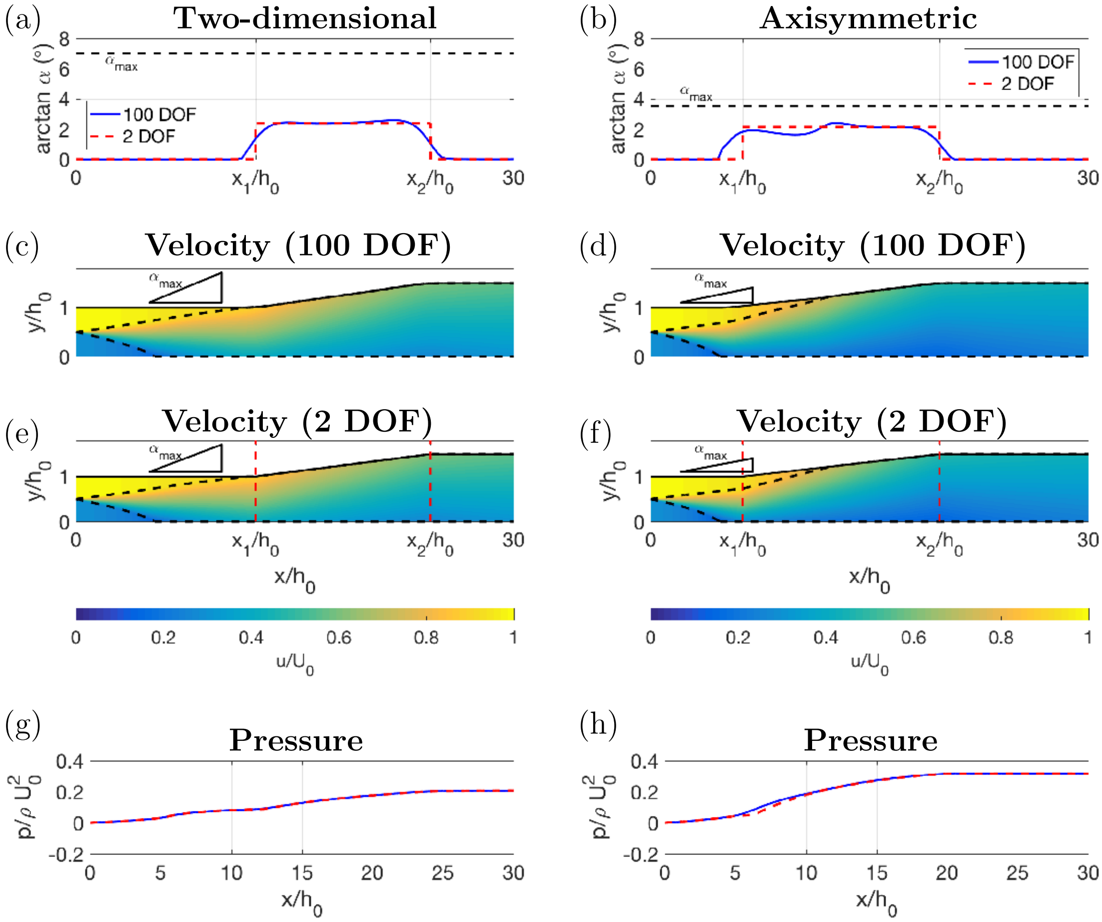

Figure 5.2: Optimal diffuser shape for the developing shear layer case, in two dimensions (a, c, e, g) and in the axisymmetric case (b, d, f, h). The optimal shapes found using 100 degrees of freedom (100 DOF) (c, d) can be well approximated by three constant-angle sections with divisions at $x = x_1$ and $x = x_2$ (2 DOF), as shown by comparisons of diffuser angle (a, b), velocity (e, f) and pressure (g, h). The inlet profile is given by $U_2(0)/U_1(0) = 0.3$, $h_2(0)/h(0) = 0.5$.

purposes, we maintain all variables in non-dimensional form with reference to typical length scales and velocity scales. We use the initial channel half-width as a typical length scale $h_0 = h(0)$ and the speed of the faster plug region at the inlet as a typical velocity scale $U_0 = U_1(0)$.

In the developing shear layer case, we start by looking at two-dimensional flow and choosing parameter values $U_2(0)/U_0 = 0.3$, $h_2(0)/h_0 = 0.5$, $h(L)/h_0 = 1.5$, $L/h_0 = 30$, $\alpha_{min} = 0°$ and $\alpha_{max} = \tan 7°$. The other parameters are taken as $S_c = 0.11$ (which we determined from comparison with CFD in Chapter 4) and $f = 0.01$ (which corresponds to a Reynolds number of $Re = 10^6$ and hydraulically smooth walls using the Blasius relationship (4.7) [11, 66]). The number of grid points for discretising the simple model is $N = 100$. Simultaneously, we also investigate axisymmetric flow with the same parameter values, except with $\alpha_{max} = \tan 3.5°$. We plot the optimal diffuser angle for the two-dimensional case in Figure 5.2 (a), the corresponding optimal diffuser shape and velocity colour map in Figure 5.2 (c), and pressure plot in Figure 5.2 (g). The axisymmetric case is plotted in Figure 5.2 (b, d, h).

In both two dimensional and axisymmetric cases, we observe that the optimal shape looks approximately like a piecewise linear function, which is divided into a straight part, followed by a widening part, followed by another straight part. In the two-dimensional case, the length of the first straight section aligns with the length it takes for the shear layer to spread completely across the channel. This suggests that mixing the flow to a more uniform profile is advantageous for the widening part to perform well. This is as expected because, as mentioned earlier, diffusers tend to accentuate non-uniform flow, producing an outflow with large kinetic energy flux (and therefore a low pressure recovery). However, as discussed earlier, long thin channels cause a large loss in pressure due to wall drag. Therefore, the optimal shape must have a straight section which is sufficiently long that the shear layer reaches across the channel, making the flow more well mixed, but no longer than that because of wall drag.

Interestingly, the widening part of the channel widens at a shallower angle than the maximum value (around $\tan 2.3°$ compared to $\tan 7°$). So the upper bound α_{max} is not needed in this case. This behaviour is unexpected since diffusers are usually designed with a widening angle as close to $\tan 7°$ as possible, regardless of the inflow (see Chapter 2). These results suggest that there is an optimum widening angle which is determined by the non-uniform inflow, rather than the risk of boundary layer separation. We discuss the axisymmetric case in more detail shortly.

Since we observe that the optimal shape in Figure 5.2 (a, c) looks approximately piecewise linear with three sections, we also try restricting the control α in this way to see if we can attain a near optimal solution with a piecewise linear shape, similarly to the example in Section 4.6. We parameterise α by splitting it into three parts: a straight part with $\alpha = 0°$ for $0 \leq x < x_1$; a widening part with constant $\alpha > 0$ for $x_1 \leq x < x_2$, and a final straight part with $\alpha = 0°$ for $x_2 \leq x \leq L$. We treat x_1 and x_2 as decision variables and the value of α in the middle section is determined by the condition

$$\alpha = \frac{h_L - h_0}{x_2 - x_1} \quad \text{for} \quad x_1 \leq x \leq x_2. \tag{5.15}$$

We optimise pressure recovery, using the same algorithm as before, but with the control $\alpha(x)$ having only 2 degrees of freedom (DOF), the two variables x_1 and x_2, instead of 100 DOF. We plot the optimal diffuser angle in Figure 5.2 (a), which is nearly identical to that obtained with 100 DOF. Moreover, the velocity colour map and pressure plot displayed in Figure 5.2 (e, g) both show a very close match. The pressure recovery coefficient for 2 DOF is $C_p = 0.5205$, which is the same as for 100 DOF (up to 4 decimal places), suggesting that piecewise linear diffuser shapes are a very good approximation in this case. In Figure 5.3 (a) we display a contour plot of C_p for all possible values of x_1 and x_2 (we cut out part of the contour plot corresponding to $\alpha > \tan 7°$ and hence the plot is only shown in a triangular region). This indicates that there is a clear unique optimum at $x_1/h_0 = 12.3$ and $x_2/h_0 = 24.3$. Note that an unoptimised shape, say with $x_1 = 0$ and $x_2 = 5$, gives a value of $C_p = 0.4254$, which is 22% worse than the optimal shape.

For the axisymmetric case, which is shown in Figure 5.2 (b, d, f, h), we find that the optimal shape has a similar structure and can also be well approximated by parameterisation with x_1 and x_2. We find that the optimal value of $x_1/h_0 = 6.3$ is shorter than the two-dimensional case. In fact, we can see in (f) that the shear layer has not reached all the way across the channel by $x = x_1$. Instead, x_1 corresponds to the point where the shear layer reaches the centre of the channel. It reaches the outer wall of the channel slightly further downstream, during the widening section. This could be explained by the fact that pressure gradients due to wall drag are stronger (per unit flux) in the axisymmetric case (e.g. Poiseuille flow [5]), and therefore the optimal shape cannot afford a longer section of straight, narrow channel.

In (b, d, f, h) we see a close comparison between the diffuser angle, velocity and pressure in the 2 DOF case and the 100 DOF case. The contour plot in Figure 5.3 (b) shows the optimum parameter values $x_1/h_0 = 6.3$ and $x_2/h_0 = 19.8$. The pressure recovery coefficient for 2 DOF is $C_p = 0.6886$ compared to $C_p = 0.7018$ for 100 DOF,

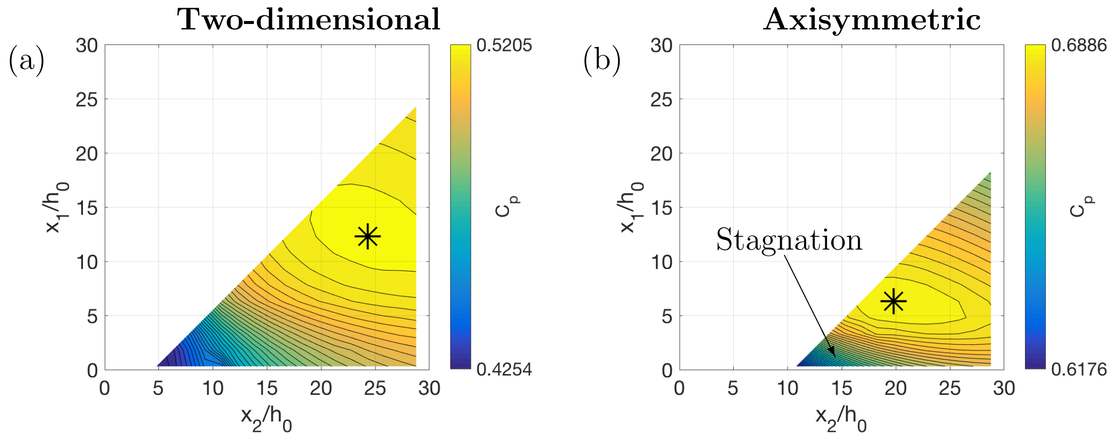

Figure 5.3: Contour plots of pressure recovery C_p (4.16), (5.2), using the low-dimensional parameterisation of the diffuser shapes, as shown in Figure 5.2 (a, b), for all permissible values of x_1 and x_2, such that $\alpha \leq \alpha_{max}$. (a) Two-dimensional case with $\alpha_{max} = \tan 7°$. (b) Axisymmetric case with $\alpha_{max} = \tan 3.5°$, indicating where the inner stream stagnates. The widening middle section has constant angle given by (5.15). The inlet profile is given by $U_2(0)/U_1(0) = 0.3$, $h_2(0)/h(0) = 0.5$.

suggesting that piecewise linear diffuser shapes are also a good approximation for the axisymmetric case, but slightly less so than for the two-dimensional case.

The contour plots in Figure 5.3 have a steep gradient for small x_1/h_0, indicating that diffuser performance is poor in this case. This corresponds to situations in which the inner stream stagnates. The phenomenon of stagnation is particularly an issue when the inner stream is slow, and this analysis shows that the way to avoid such poor performance is to have a longer straight section in which the inner stream is accelerated before diffusing. More details on the phenomenon of stagnation are in Chapter 4, Section 4.5.

5.3.2 Small shear limit

We now consider the case where the initial shear is small, for which we will later derive analytical solutions in Section 5.4 that help us understand the numerical optimisation. In the small shear limit, we consider two-dimensional flow and choose parameter values $U_2(0)/U_0 = 0.8$, $h_2(0)/h_0 = 0.5$, $h(L)/h_0 = 2.3$, $L/h_0 = 20$, $\alpha_{min} = 0$ and $\alpha_{max} = \tan 7°$. The other parameters S_c and f are taken at the same values as the previous cases. We display the optimal shape, velocity colour map and pressure plot in Figure 5.4 (a, c, e). In this case, the optimal shape widens at the maximum angle α_{max} until it reaches the exit width $h(L)$ and then stays straight. Since the shear is small and the flow is almost uniform, there is no risk of accentuating the flow

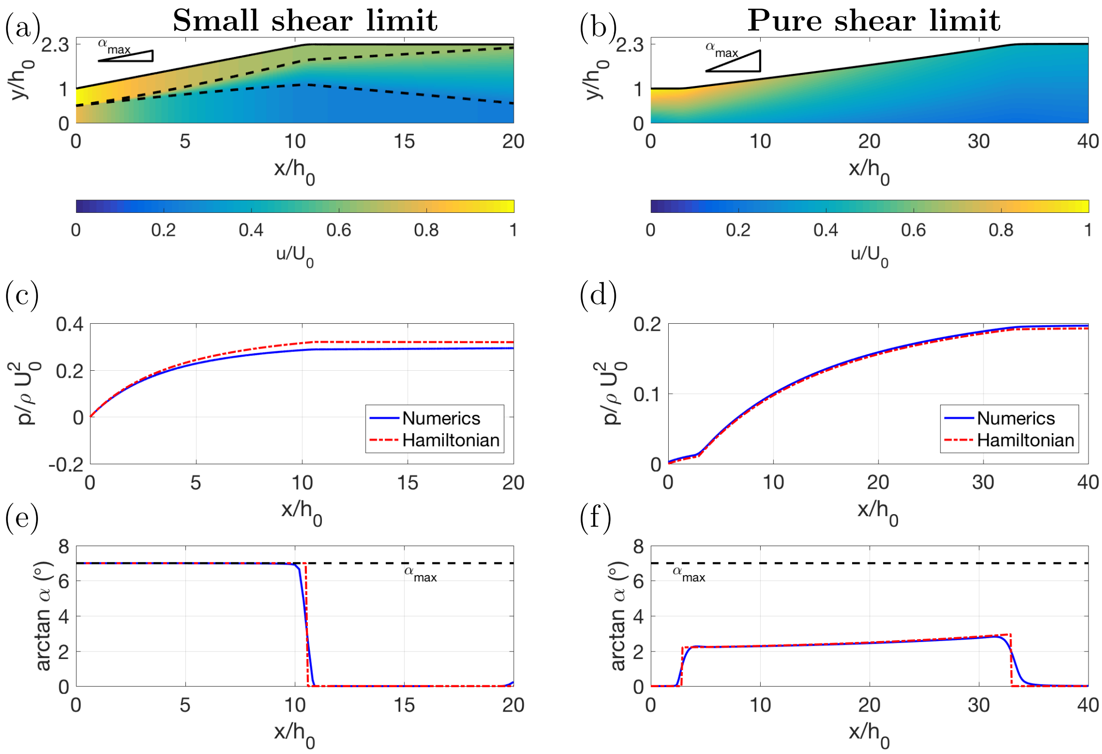

Figure 5.4: Optimal diffuser shapes, velocity colour maps, pressure plots and diffuser angle plots for the small shear limit and the pure shear limit. (a, c, e) Two-dimensional flow where the plug regions have similar speeds $U_2(0)/U_0 = 0.8$ and the channel length $L/h_0 = 20$ is sufficiently short such that the shear layer never reaches across the channel. (b, d, f) Two-dimensional flow where the shear layer has already reached across the channel at the inflow so that there are no plug regions. The inflow velocity ratio is $U_2(0)/U_0 = 0.35$ and the channel length is given by $L/h_0 = 40$.

profile drastically. Therefore, wide angles initially are not penalised much, allowing the control to take its maximum value. This design is typically what is built in the diffuser industry for a uniform inflow [12], where the maximum diffuser angle is set by the limit where boundary layer separation occurs. The optimal control only takes its extremal values, which is sometimes referred to as 'bang-bang control'. In Section 5.4.1 we discuss analytical results for this limiting case and prove that the control must be bang-bang.

5.3.3 Pure shear limit

Next we consider the case where the inflow velocity has a pure shear profile, for which we will later derive analytical solutions in Section 5.4 that help us understand the numerical optimisation, similarly to the small shear limit. For the pure shear limit, we consider two-dimensional flow and choose parameter values $U_2(0)/U_0 = 0.35$, $h(L)/h_0 = 2.3$, $L/h_0 = 40$, $\alpha_{min} = 0°$ and $\alpha_{max} = \tan 7°$. The parameters S_c and f are taken as the same as before. The optimal channel, velocity colour map, pressure and control are displayed in Figure 5.4 (b, d, f). The optimal shape is similar to those in Figure 5.2, with a natural decomposition into two straight sections separated by a widening section. The widening section has an angle that increases from $\alpha \approx \tan 2.5°$ to $\alpha \approx \tan 3°$ and is nowhere greater than $\tan 7°$, showing that the upper bound α_{max} is not needed in this case. The optimal shape, like in Figure 5.2, exhibits the balance between the necessity of a straight section that is long enough to allow some mixing, but not too long that wall drag dominates. In Section 5.4.2 we discuss analytical results for this case which describe the optimal widening angle that lies in the interval $(\alpha_{min}, \alpha_{max})$. This is of great interest because it indicates that the optimal design is unaffected by the conventional widening angle limit that exists due to boundary layer separation.

5.3.4 Numerical details

In this section we briefly discuss some of the numerical details of the optimisation, including convergence and how to choose the penalty parameter μ_c for the equality constraints in (5.10). We restrict our attention to these properties for the pure shear limit example in Figure 5.4 since, as we show in Section 5.4, an analytical solution can be found, and this is useful for the convergence analysis.

We follow a method similar to Nocedal et al. [73] for choosing μ_c. The idea is that we want to increase μ_c gradually so that the equality constraints are imposed more and more strictly, but we do not want μ_c to become so large that the problem is ill-conditioned. Therefore, we choose a maximum constraint error e_{max} for which we would like to satisfy

$$e_c := \frac{1}{m_c} \sum_{i=1}^{m_c} c_i(\mathbf{x})^2 \leq e_{max}. \tag{5.16}$$

Since our differential equations are solved using a second order finite difference scheme, an appropriate upper bound for e_{max} is the expected error of this scheme

$$e_{max} \leq \chi \Delta x^2, \tag{5.17}$$

where $\Delta x = L/N$ is the spatial step size and χ is a constant which has dimensions (m^{-2}) since the constraint equations are imposed in a non-dimensional form (which we do not discuss here). Although the pure shear limit example in Figure 5.4 was introduced in non-dimensional format, it is useful to provide dimensional values for L and χ here for the sake of reproducibility. Hence, in dimensional terms the channel length is $L = 40\,\mathrm{m}$, and we calculate $\chi = 0.0121\,\mathrm{m}^{-2}$.

We choose a convergence tolerance τ so that the solver terminates if the objective changes between iterations by less than τ. After choosing τ, we start with an initial guess for the primal variables and the penalty parameter, which we denote $\mathbf{x}^0$ and μ_c^0. We then proceed with the following algorithm:

Data: Given $\mathbf{x}^0$, μ_c^0, e_{max}, τ and a multiplicative constant $\phi > 1$
for $k = 0, 1, 2 \dots$ **do**
  Find approximate maximiser $\mathbf{x}^k$ of (5.12) using tolerance τ;
  if $e_c \leq e_{max}$ **then**
    stop with approximate solution $\mathbf{x}^k$;
  end
  Choose a new penalty parameter $\mu_c^{k+1} = \phi \mu_c^k$;
  Set the new starting guess as $\mathbf{x}_s^{k+1} = \mathbf{x}^k$;
end

The multiplicative constant ϕ needs to be sufficiently small that we don't overshoot the appropriate value of μ_c at each iteration. We find that $\phi = 1.1$ works well. Furthermore, by choosing the new starting guess at each iteration as the solution to the previous iteration, $\mathbf{x}_s^{k+1} = \mathbf{x}^k$, Newton's method converges very quickly. Note that whilst we have implemented our own code for choosing the penalty parameter μ_c, the barrier parameter μ_d is treated by the IPOPT implementation of the interior point method (which is not our code). The details of this can be found in [101].

In Figure 5.5 we plot the evolution of the objective and the constraint error e_c using this algorithm for the pure shear limit example from Figure 5.4. We can see that as we increase μ_c the difference between the objective C_p and the penalised objective

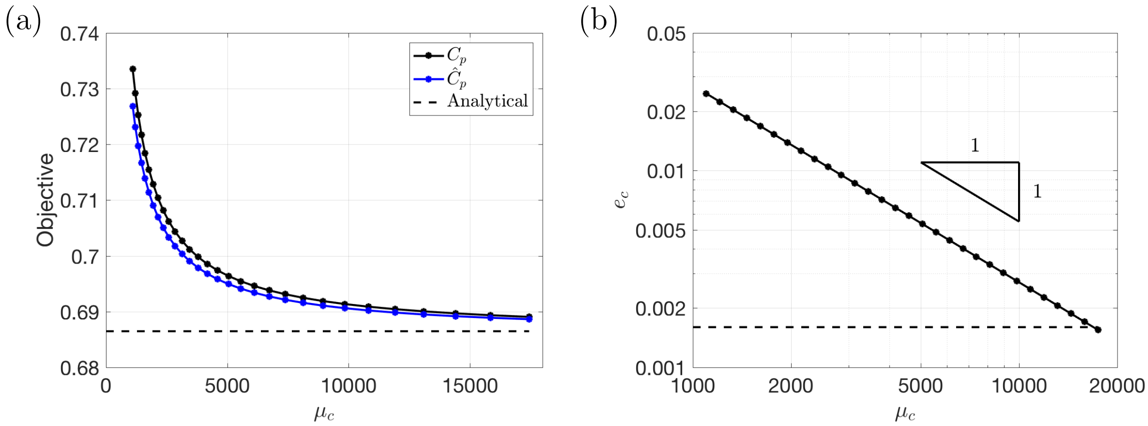

Figure 5.5: Calculating the quadratic penalty parameter μ_c using the algorithm outlined in Section 5.3.4 for the pure shear limit example in Figure 5.4. We use an initial starting value of $\mu_c^0 = 1 \times 10^3$ and a multiplicative factor of $\phi = 1.1$. The constraint error tolerance is set as $e_{max} = 1.9 \times 10^{-3}$ in accordance with (5.17) with $N = 100$, which is satisfied when $\mu_c^k = 1.74 \times 10^4$.

$\hat{C}_p$ gets smaller, and they plateau at approximately $C_p \approx \hat{C}_p \approx 0.6890$, which is very close to the analytical solution value $C_p = 0.6865$. The constraint error e_c goes like $\sim 1/\mu_c$, which is expected due to the form of (5.10).

It is also of interest to see how the solution changes as we increase the number of discretisation points N. By increasing the number of grid points, we may expect the approximate maximiser of the optimisation problem to converge. We apply the above algorithm to a sequence of optimisation problems with an increasing number of grid points N_j for $j = 1, 2, \ldots$. We use the same value of the tolerance τ for each N_j and we initialise the solution with the same initial guess $\mathbf{x}^0$ and μ_c^0. We use the pure shear limit example from Figure 5.4, for which we have an analytical solution (discussed later in Section 5.4.2). As we increase N_j, we expect the accuracy of the finite difference scheme to increase. Therefore, in accordance with (5.17), we set the maximum constraint error as

$$e_{max}(N_j) = \chi \left(L/N_j\right)^2. \tag{5.18}$$

In Figure 5.6 we analyse the convergence for N_j increasing from 50 to 250. In (a) we see that the objective C_p and the penalised objective $\hat{C}_p$ both reach a plateau at approximately $N_j = 250$ with $C_p \approx \hat{C}_p \approx 0.6865$, which corresponds to the analytical solution value (within 5 decimal places). We can see from the error plot in (c) that by choosing μ_c according to the above algorithm, the constraint error e_c maintains below the maximum constraint error e_{max} (5.18) shown in red. From (b, d) the number of

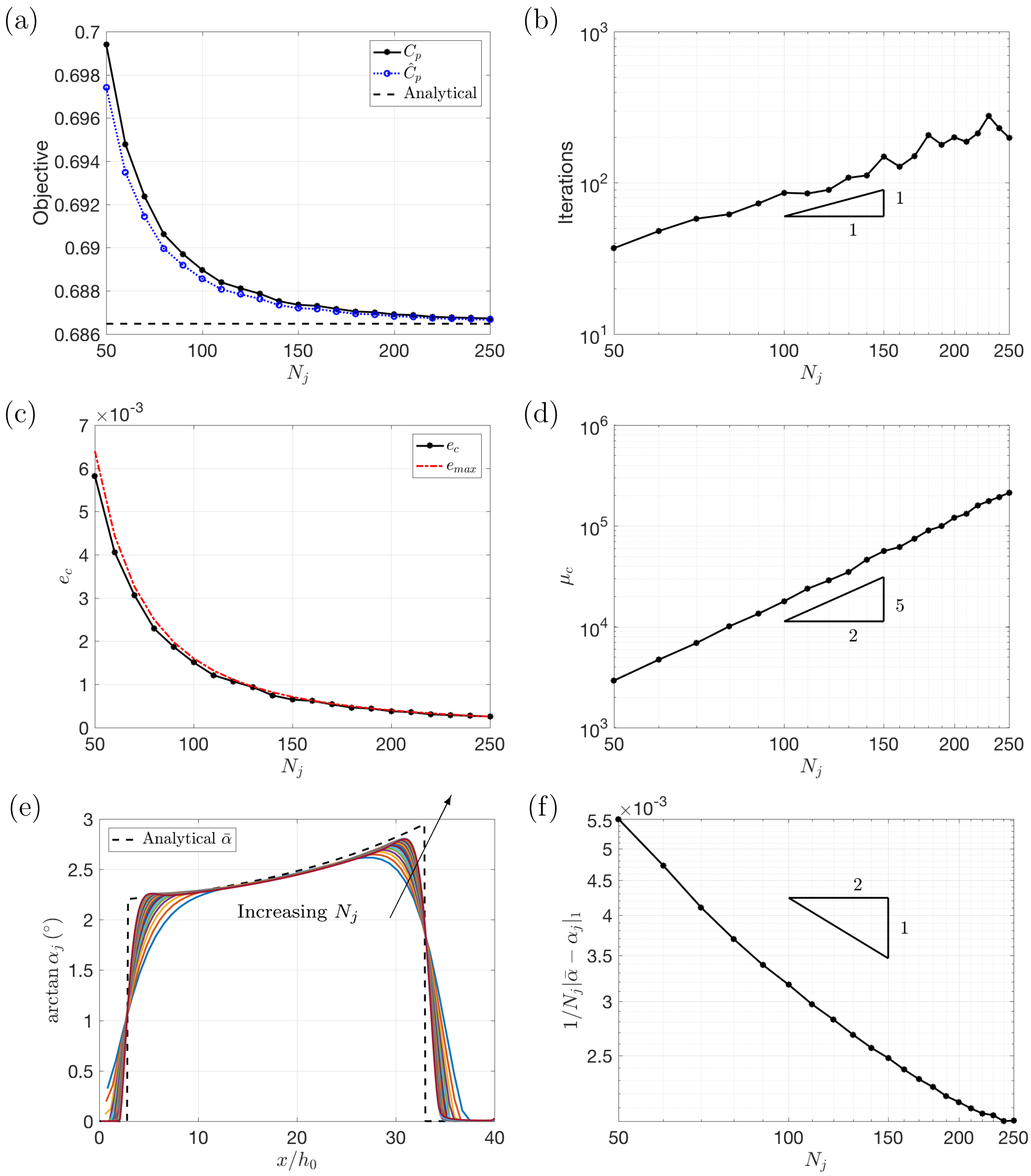

Figure 5.6: Convergence plots for numerical optimisation in the pure shear limit (see Figure 5.4) as we increase the number of grid points N. (a) Pressure recovery C_p and penalised pressure recovery $\hat{C}_p$ (5.10). (b) Number of iterations of the interior point method. (c) Constraint error e_c given by (5.16) and maximum constraint error e_{max} given by (5.18). (d) Quadratic penalty parameter μ_c which is determined by the algorithm in Section 5.3.4. (e) Numerically optimised control α_j for discretisation N_j compared to analytical solution $\bar{\alpha}$ (discussed later in Section 5.4.2). (f) Mean absolute difference between numerical and analytical solution.

iterations scales linearly with N_j, whereas the penalty parameter μ_c scales like $N_j^{5/2}$. This indicates that, whilst the iterations are relatively mesh-independent, the problem will become ill conditioned for large N. Another possible approach which avoids such ill-conditioning is the augmented Lagrangian method which we do not study here but is discussed in [73].

In (e) we compare the optimised control for each N_j to the analytical solution which we derive in Section 5.4.2. As N_j increases the corresponding optimised control α_j converges to the analytical solution, which we denote $\bar{\alpha}$. In (f) we plot the mean absolute difference between the analytical solution and α_j. We see that the mean absolute difference $1/N_j|\bar{\alpha} - \alpha_j|_1$ decreases approximately like $\sim N_j^{-1/2}$, though the exponent increases (becomes closer to 0) as N_j increases. Hence, due to ill-conditioning, we do not expect that the mean absolute difference asymptotically approaches zero as $N_j \to \infty$. However, from (e) we note that for $N_j = 250$ the numerically optimised control looks nonetheless very similar to the analytical solution. Therefore, we conclude that the convergence of our numerical optimisation routine is acceptable.

5.4 Analytical results

The numerical optimisation routine outlined in Section 5.3 can be applied to find optimal shapes for any choice of the parameters listed in Table 5.1. We have seen several examples of these in Figures 5.2 and 5.4. In this section we show that in the two limiting cases displayed in Figure 5.4, the small shear limit and the pure shear limit, it is possible to make some analytical progress which aids our understanding and interpretation of the optimal control. Furthermore, the results discussed in this section include simple relationships that may be of instructive use for the purpose of diffuser design in industry. In both cases we derive a reduced set of equations describing the flow, that is amenable to optimal control analysis using Pontryagin's maximum principle [78]. As an introduction to this section we briefly outline the mathematical background of optimal control theory, which we use later.

For the purpose of this outline, we consider a simplified optimal control problem in which a variable $y(x)$ is controlled by a control $\alpha(x)$ and the domain is defined by $0 \leq x \leq L$. Later we discuss allowing L to be an additional control but for now we treat it as fixed. We consider an objective functional

$$\max_{\alpha(x)} J(\alpha(x)) := \int_0^L F(x, y(x), \alpha(x)) \, \mathrm{d}x + \Phi(y(L)), \tag{5.19}$$

for some given functions F and Φ, subject to the ordinary differential equation

$$\frac{\mathrm{d}y}{\mathrm{d}x} = G\left(x, y(x), \alpha(x)\right), \tag{5.20}$$

and initial/terminal conditions. We assume that the control $\alpha(x)$ is piecewise continuous, $y(x)$ is absolutely continuous and F and G are of class C^2 in y and α, and piecewise continuous in x [77]. We use the adjoint variable $\lambda(x)$ to impose the ODE constraint (5.20) so that the objective functional becomes

$$J\left(\alpha(x)\right) = \int_0^L \left(F + \lambda\left(G - \frac{\mathrm{d}y}{\mathrm{d}x}\right)\right)\,\mathrm{d}x + \Phi\left(y(L)\right). \tag{5.21}$$

Consider small perturbations around the optimal control $\tilde{\alpha}(x)$ and state $\tilde{y}(x)$,

$$\alpha(x) = \tilde{\alpha}(x) + \epsilon\hat{\alpha}(x), \tag{5.22}$$

$$y(x) = \tilde{y}(x) + \epsilon\hat{y}(x), \tag{5.23}$$

where $\epsilon \ll 1$. Using integration by parts and Taylor expansions about $\epsilon = 0$, we find that the first variation (divided by ϵ) is

$$\begin{aligned}
&\frac{1}{\epsilon}\left(J\left(\tilde{\alpha}(x) + \epsilon\hat{\alpha}(x)\right) - J\left(\tilde{\alpha}(x)\right)\right) = \\
&\int_0^L \left(\left(\frac{\partial \tilde{F}}{\partial y} + \lambda\frac{\partial \tilde{G}}{\partial y} + \frac{\mathrm{d}\lambda}{\mathrm{d}x}\right)\hat{y} + \left(\frac{\partial \tilde{F}}{\partial \alpha} + \lambda\frac{\partial \tilde{G}}{\partial \alpha}\right)\hat{\alpha}\right)\,\mathrm{d}x + \lambda(0)\hat{y}(0) \\
&+ \left(\frac{\partial \Phi}{\partial y}\left(\tilde{y}(L)\right) - \lambda(L)\right)\hat{y}(L) + \mathcal{O}(\epsilon),
\end{aligned} \tag{5.24}$$

where we have introduced the shorthand notation $\tilde{F} = F(x, \tilde{y}(x), \tilde{\alpha}(x))$. To find a maximiser, we set the first variation (5.24) to zero, which is achieved by first imposing

$$\frac{\mathrm{d}\lambda}{\mathrm{d}x} + \frac{\partial \tilde{H}}{\partial y} = 0, \tag{5.25}$$

where the Hamiltonian is defined as

$$H = F + \lambda G. \tag{5.26}$$

Then, we choose boundary conditions as follows:

- If $y(0)$ is given then impose $\hat{y}(0) = 0$.
- If $y(L)$ is given then impose $\hat{y}(L) = 0$.
- If $y(0)$ is not given then impose $\lambda(0) = 0$.

- If $y(L)$ is not given then impose $\lambda(L) = \frac{\partial \Phi}{\partial y}(\tilde{y}(L))$.

After applying these boundary conditions, (5.24) becomes

$$\int_0^L \frac{\partial \tilde{H}}{\partial \alpha} \hat{\alpha} \, \mathrm{d}x + \mathcal{O}(\epsilon) = 0. \tag{5.27}$$

Since (5.27) holds for all $\hat{\alpha}$, we have

$$\frac{\partial \tilde{H}}{\partial \alpha} = 0. \tag{5.28}$$

To summarise, we have the following set of governing equations (also known as Pontryagin's Maximum Principle) to find the optimal control and state:

$$\frac{\mathrm{d}y}{\mathrm{d}x} - \frac{\partial H}{\partial \lambda} = 0, \tag{5.29}$$

$$\frac{\mathrm{d}\lambda}{\mathrm{d}x} + \frac{\partial H}{\partial y} = 0, \tag{5.30}$$

$$\frac{\partial H}{\partial \alpha} = 0, \tag{5.31}$$

and boundary conditions

$$\text{either} \quad y(0) = y_0 \quad \text{or} \quad \lambda(0) = 0, \tag{5.32}$$

$$\text{either} \quad y(L) = y_L \quad \text{or} \quad \lambda(L) = \frac{\partial \Phi}{\partial y}(y(L)). \tag{5.33}$$

If we treat L as an additional control we can repeat as above by considering perturbations $L = \tilde{L} + \epsilon$. In this case, to enforce that the first variation is zero, we need an additional constraint

$$\tilde{H}(x = \tilde{L}) = 0. \tag{5.34}$$

If the objective functional is of the form

$$J(\alpha(x)) = \int_0^L \left(F_1(x, y(x)) + F_2(x, y(x))\,\alpha(x)\right) \mathrm{d}x + \Phi(y(L)), \tag{5.35}$$

subject to the ODE constraint

$$\frac{\mathrm{d}y}{\mathrm{d}x} = G_1(x, y(x)) + G_2(x, y(x))\,\alpha(x), \tag{5.36}$$

then the problem is said to be linear in α. As described by Pitcher [77], if in addition to the problem being linear in α, the control is also bounded above and below

$$\alpha_{min} < \alpha < \alpha_{max}, \tag{5.37}$$

then (5.29) and (5.30) are exactly as before but (5.31) is replaced by

$$\tilde{\alpha}(x) = \begin{cases} \alpha_{min} & \text{if} \quad \frac{\partial H}{\partial \alpha} < 0, \\ \alpha^*(x) \in [\alpha_{min}, \alpha_{max}] & \text{if} \quad \frac{\partial H}{\partial \alpha} = 0, \\ \alpha_{max} & \text{if} \quad \frac{\partial H}{\partial \alpha} > 0. \end{cases} \tag{5.38}$$

When $\tilde{\alpha}(x)$ only takes its extreme values, then the control is said to be *bang-bang*. If $\tilde{\alpha}(x) = \alpha^*(x)$ satisfies $\partial H/\partial \alpha = 0°$ for a finite interval, then this is called a *singular arc*. Robbins [84] showed that during the singular arc, α^* is determined by solving

$$\frac{\mathrm{d}^q}{\mathrm{d}x^q}\frac{\partial H}{\partial \alpha}(x, y(x), \alpha^*(x)) = 0, \tag{5.39}$$

where q is the smallest even number for which $\mathrm{d}^q/\mathrm{d}x^q(\partial H/\partial \alpha)$ is not independent of α. For both the small shear limit and the pure shear limit, we can reduce our system to one which is linear in α. This enables us to make analytical progress using (5.38) and (5.39). In these cases, the system involves multiple state variables (instead of just $y(x)$ as discussed here). Then the analysis of this section still applies but with a Hamiltonian defined as

$$H = F + \sum_i \lambda_i G_i. \tag{5.40}$$

Furthermore, (5.29), (5.30) and boundary conditions (5.32), (5.33) apply for each state variable and corresponding adjoint variable.

5.4.1 Small shear limit

To start with, we consider a two-dimensional diffuser where the inflow, given by (4.3), is almost uniform, producing a thin, slowly growing shear layer between the plug flow regions. The channel is sufficiently short that the shear layer never reaches across the channel (see Figure 5.1 (b)). The speed of the plug regions differs by a small amount

$$U_0 - U_2(0) = \epsilon V, \tag{5.41}$$

where the constant $\epsilon \ll 1$ is redefined here, distinguishing it from the ϵ in (5.22)-(5.23). If the plug regions always exist, with positive width $h_1 > 0$, $h_2 > 0$, and we assume that the slower flow never stagnates $U_2 > 0$, then we need not consider the complementarity format for Bernoulli's equation. Therefore, we replace (4.8) and (4.9) with

$$p + \frac{1}{2}\rho U_i^2 = \frac{1}{2}\rho U_i(0)^2, \quad \text{for} \quad i = 1, 2. \tag{5.42}$$

We consider the distinguished limit where the friction factor f is small such that $f = \epsilon S_c F$, where $F = O(1)$. This is reasonable as, for example, if we consider a

Reynolds number of $Re = 10^6$ and hydraulically smooth walls, the friction factor is $f = 0.01$ (from (4.7)) and therefore, if $\epsilon = 0.1$ and $S_c = 0.11$, then $F = 0.91$. Choosing these parameter values and setting $V/U_0 = 2$, we achieve the small shear limit example in Figure 5.4 (a, c, e).

Next we expand variables in powers of the small parameter ϵ, such that

$$U_1 = U_{1_0} + \epsilon \hat{U}_1 + \dots, \tag{5.43}$$

$$U_2 = U_{2_0} + \epsilon \hat{U}_2 + \dots, \tag{5.44}$$

$$h_1 = h_{1_0} + \epsilon \hat{h}_1 + \dots, \tag{5.45}$$

$$h_2 = h_{2_0} + \epsilon \hat{h}_2 + \dots, \tag{5.46}$$

$$p = p_0 + \epsilon \hat{p} + \dots, \tag{5.47}$$

$$\delta = \delta_0 + \epsilon \hat{\delta} + \dots, \tag{5.48}$$

$$\varepsilon_y = \varepsilon_{y0} + \epsilon \hat{\varepsilon}_y + \dots. \tag{5.49}$$

In the limit $\epsilon \to 0$, (4.2)-(4.5) and (5.42) are satisfied by

$$U_{1_0} = U_{2_0} = \frac{U_0 h_0}{h}, \tag{5.50}$$

$$h_{2_0} = h - h_{1_0}, \tag{5.51}$$

$$p_0 = \frac{1}{2}\rho U_0^2 \left(1 - \frac{h_0^2}{h^2}\right), \tag{5.52}$$

$$\delta_0 = 0, \tag{5.53}$$

$$\varepsilon_{y0} = \frac{h_0 U_0}{S_c \int_0^x h(\hat{x})\, d\hat{x}}. \tag{5.54}$$

The function h_{1_0}, which represents the location of the centre of the shear layer to leading order, is determined at order $O(\epsilon)$. Bernoulli's equation (5.42) for each plug region, at order $O(\epsilon)$, is

$$\hat{p} + \rho \hat{U}_1 U_{1_0} = 0, \tag{5.55}$$

$$\hat{p} + \rho \hat{U}_2 U_{1_0} = -\rho U_0 V. \tag{5.56}$$

From the relationship $h_1 + h_2 + \delta = h$, at order $O(\epsilon)$ we find that

$$\hat{h}_1 + \hat{h}_2 + \hat{\delta} = 0. \tag{5.57}$$

Thus, using (4.3), (5.50)-(5.54) and (5.57), the conservation of mass equation (4.4) at order $O(\epsilon)$ is

$$\hat{U}_1 h_{1_0} + \hat{U}_2 (h - h_{1_0}) = -V h_2(0), \tag{5.58}$$

and the momentum equation (4.5) is

$$h\frac{\mathrm{d}\hat{p}}{\mathrm{d}x} + \rho\frac{\mathrm{d}}{\mathrm{d}x}\left(2U_{1_0}\hat{U}_1 h_{1_0} + 2U_{1_0}\hat{U}_2(h - h_{1_0})\right) = -\frac{1}{8}S_c F \rho U_{1_0}^2. \tag{5.59}$$

Next, using (5.55) - (5.57), we can simplify (5.59) to an equation purely involving h_{1_0} and h

$$Vh^2\frac{\mathrm{d}h_{1_0}}{\mathrm{d}x} - Vhh_{1_0}\frac{\mathrm{d}h}{\mathrm{d}x} = -\frac{1}{8}FS_c h_0^2 U_0, \tag{5.60}$$

which has solution

$$h_{1_0} = h\left(\frac{h_1(0)}{h_0} - \frac{S_c F h_0^2 U_0}{8V}\int_0^x \frac{1}{h(\hat{x})^3}\,d\hat{x}\right). \tag{5.61}$$

Combining (5.58) and (5.59) we obtain a differential equation for the pressure correction $\hat{p}$ in terms of the channel shape and its derivative $\alpha = h'(x)$,

$$\frac{\mathrm{d}\hat{p}}{\mathrm{d}x} = -\frac{\rho U_0^2 h_0^2}{h^3}\left(\frac{2V}{U_0}\left(1 - \frac{h_1(0)}{h_0}\right)\alpha + \frac{S_c F}{8}\right). \tag{5.62}$$

We now solve the optimal control problem outlined in Section 5.2.2. Since the inflow conditions are fixed and we take $p(0) = 0$, maximising C_p is equivalent to maximising the pressure at the outlet $p(L)$. Furthermore, the constraint equations have been reduced to (5.62). Therefore the optimal control problem, including terms up to and including order $O(\epsilon)$, and written as a system of first order differential equations, is:

$$\max_{\alpha_{min} \le \alpha(x) \le \alpha_{max}} \quad \Phi := p(L), \tag{5.63}$$

such that

$$\frac{\mathrm{d}p}{\mathrm{d}x} = \frac{\rho U_0^2 h_0^2}{h^3}\left(\left(1 - \epsilon\frac{2V}{U_0}\left(1 - \frac{h_1(0)}{h_0}\right)\right)\alpha - \epsilon\frac{SF}{8}\right), \tag{5.64}$$

$$\frac{\mathrm{d}h}{\mathrm{d}x} = \alpha, \tag{5.65}$$

$$h(0) = h_0, \tag{5.66}$$

$$p(0) = 0, \tag{5.67}$$

$$h(L) = h_L. \tag{5.68}$$

We now solve this reduced problem using Pontryagin's maximum principle [78]. The Hamiltonian for this system is

$$H = \lambda_p\frac{\mathrm{d}p}{\mathrm{d}x} + \lambda_h\frac{\mathrm{d}h}{\mathrm{d}x}, \tag{5.69}$$

where λ_p and λ_h are the adjoint variables which satisfy the adjoint equations

$$\frac{\mathrm{d}\lambda_p}{\mathrm{d}x} = -\frac{\partial H}{\partial p}, \tag{5.70}$$

$$\frac{\mathrm{d}\lambda_h}{\mathrm{d}x} = -\frac{\partial H}{\partial h}. \tag{5.71}$$

Note that the Hamiltonian (5.69) is linear in the control α due to (5.64), (5.65) and the fact that λ_p and λ_h are independent of α.

According to Pontryagin's maximum principle, variables which appear in the objective function (5.63) evaluated at $x = L$ must have natural boundary conditions which apply to their corresponding adjoint variables [78]. Since the objective function only depends on pressure at the outlet $\Phi = p(L)$, we have the natural boundary condition

$$\lambda_p(L) = \frac{\partial \Phi}{\partial p} = 1. \tag{5.72}$$

Considering (5.72) and the fact that there is no dependance of the Hamiltonian (5.69) on the pressure p, (5.70) tells us that $\lambda_p = 1$ for all values of x. There is no natural boundary condition for λ_h since we are enforcing a condition on h at the outlet $x = L$. The last condition from Pontryagin's maximum principle is the optimality condition, which usually takes the form $\partial H/\partial\alpha = 0$. However, following Pitcher [77] and McDanell & Powers [64], since the Hamiltonian is linear in the control α, the optimality condition takes the form

$$\alpha(x) = \begin{cases} \alpha_{max}, & \text{if } H_\alpha > 0, \\ \alpha^*(x) \in [\alpha_{min}, \alpha_{max}], & \text{if } H_\alpha = 0, \\ \alpha_{min}, & \text{if } H_\alpha < 0, \end{cases} \tag{5.73}$$

where we have introduced the shorthand notation $H_\alpha = \partial H/\partial\alpha$. Using (5.69) with (5.64), (5.65) and (5.71), and noting that $\lambda_p = 1$, we see that

$$\frac{\mathrm{d}H_\alpha}{\mathrm{d}x} = -\frac{3\epsilon\rho SFU_0^2h_0^2}{8h^4}, \tag{5.74}$$

which is negative for all values of x. Hence, it is impossible for singular arcs to exist in this case. Therefore the control is bang-bang, with

$$\alpha(x) = \begin{cases} \alpha_{max}, & \text{for} \quad x \in [0, \gamma], \\ \alpha_{min}, & \text{for} \quad x \in [\gamma, L], \end{cases} \tag{5.75}$$

where the switching point γ is given by

$$\gamma = \frac{h_L - h_0 - \alpha_{min}L}{\alpha_{max} - \alpha_{min}}. \tag{5.76}$$

In Figure 5.4 (c, e) we plot the solution to the optimal control problem found using the Hamiltonian approach on top of the solution found using the numerical optimisation routine outlined in Section 5.3. It is clear that the numerical optimisation routine has correctly found the bang-bang control which we have derived here, with $\gamma/h_0 = 10.59$ (the small discrepancy is probably due to the finite value of ϵ).

It should be noted that the adjoint variable λ_h is only solved for up to a constant of integration C (from integrating (5.71)) since it has no boundary condition. Instead, C is determined by the condition that

$$H_\alpha(x = \gamma) = 0. \tag{5.77}$$

In the case where we also allow the channel length L to be a control as well as α, according to Pontryagin's maximum principle [77, 78], we have the additional constraint on the Hamiltonian at the final point

$$H(x = L) = 0. \tag{5.78}$$

By calculating H (5.69), it is straightforward to show that (5.77) and (5.78) are inconsistent unless there is no switching point, such that the control is only ever equal to one of α_{min} or α_{max} and (5.77) does not apply. For the case in Figure 5.4 (a, c, e), it is clear that if $\alpha = \alpha_{min}$ for all x then the terminal constraint (5.4) is not satisfied. Instead, we conclude that $\alpha = \alpha_{max}$ for all x. Hence, including L as a control and taking $\alpha_{min} = 0°$, the optimal diffuser shape for the small shear limit is one which expands at the maximum angle until h reaches h_L, at which point the channel terminates (i.e. conventional diffuser design for uniform flow).

5.4.2 Pure shear limit

The next limiting case we investigate is the pure shear limit, in which the shear layer has already reached across the channel at the inflow, such that there are no plug regions (see Figure 5.1 (c)). The velocity profile is given by (5.1). For this velocity profile, conservation of mass and momentum equations (4.4), (4.5) reduce to

$$\frac{h}{2}(U_1 + U_2) = Q, \tag{5.79}$$

$$h\frac{\mathrm{d}p}{\mathrm{d}x} + \frac{1}{3}\rho\frac{\mathrm{d}}{\mathrm{d}x}\left(h\left(U_1^2 + U_1U_2 + U_2^2\right)\right) = -\frac{1}{8}\rho f U_1^2, \tag{5.80}$$

where Q is the constant flow rate. We now solve the optimal control problem outlined in Section 5.2.2. As in Section 5.4.1 we maximise pressure at the outlet $p(L)$. Furthermore, it is convenient to introduce a new variable, the scaled velocity difference between maximum and minimum velocities $\tilde{U} = (U_1 - U_2)/(U_1 + U_2)$. Using (5.79) and this new variable we can simplify (4.2) and (5.80), which are the reduced system of constraint equations. Therefore, the optimal control problem is as follows:

$$\max_{\alpha_{min} \leq \alpha(x) \leq \alpha_{max}} \quad \Phi := p(L), \tag{5.81}$$

such that

$$\frac{\mathrm{d}\tilde{U}}{\mathrm{d}x} = \frac{2\tilde{U}(\alpha - S_c\tilde{U})}{h}, \tag{5.82}$$

$$\frac{\mathrm{d}p}{\mathrm{d}x} = \frac{\rho Q^2 \left(32 S_c \tilde{U}^3 - 3f(1+\tilde{U})^2 + 24\alpha(1-\tilde{U}^2)\right)}{24h^3}, \tag{5.83}$$

$$\frac{\mathrm{d}h}{\mathrm{d}x} = \alpha, \tag{5.84}$$

$$\tilde{U}(0) = \tilde{U}_0, \tag{5.85}$$

$$p(0) = 0, \tag{5.86}$$

$$h(0) = h_0, \tag{5.87}$$

$$h(L) = h_L, \tag{5.88}$$

where $\tilde{U}_0 = (1 - U_2(0)/U_0)/(1 + U_2(0)/U_0)$. Similarly to Section 5.4.1, the Hamiltonian for the system is

$$H = \lambda_{\tilde{U}} \frac{\mathrm{d}\tilde{U}}{\mathrm{d}x} + \lambda_p \frac{\mathrm{d}p}{\mathrm{d}x} + \lambda_h \frac{\mathrm{d}h}{\mathrm{d}x}, \tag{5.89}$$

which is linear in the control α. The adjoint equations are

$$\frac{\mathrm{d}\lambda_{\tilde{U}}}{\mathrm{d}x} = -\frac{\partial H}{\partial \tilde{U}}, \tag{5.90}$$

$$\frac{\mathrm{d}\lambda_p}{\mathrm{d}x} = -\frac{\partial H}{\partial p}, \tag{5.91}$$

$$\frac{\mathrm{d}\lambda_h}{\mathrm{d}x} = -\frac{\partial H}{\partial h}, \tag{5.92}$$

which have the natural boundary conditions

$$\lambda_{\tilde{U}}(L) = \frac{\partial \Phi}{\partial \tilde{U}} = 0, \tag{5.93}$$

$$\lambda_p(L) = \frac{\partial \Phi}{\partial p} = 1. \tag{5.94}$$

There is no natural boundary condition for λ_h since h is already prescribed at $x = L$. Finally, as in Section 5.4.1, the optimality condition is (5.73).

Setting $H_\alpha = \mathrm{d}H_\alpha/\mathrm{d}x = 0$, and using Equation (5.39), we find that there will only be a singular arc when

$$\alpha^*(x) = \frac{2S_c\tilde{U}^2(8S_c\tilde{U}^2 - f)}{3f + f\tilde{U} + 8S_c\tilde{U}^3} \quad \text{for} \quad x \in [x_1, x_2], \tag{5.95}$$

for some $x_2 > x_1$. We can solve the coupled system (5.73), (5.82)-(5.95) numerically for the optimal control and corresponding solution. There are, however, very special cases where the singular arc value α^* is constant, when we can find analytical solutions, which we discuss at the end of this section. In practice, these solutions appear to be close to the behaviour observed in normal conditions, as can be seen in Figure 5.4 where α is approximately constant during the widening section of the diffuser.

In Figure 5.4 (d, f) we plot the solution to the optimal control problem found using the Hamiltonian approach over the solution found using the numerical optimisation routine outlined in Section 5.3. It is clear that both approaches have found the same solution, with the singular arc lying between $x_1/h_0 = 2.9$ and $x_2/h_0 = 32.9$. The singular arc represents the balance between mixing and widening effects in the diffuser. Mixing reduces the non-uniformity of the flow, whilst widening tends to accentuate the non-uniform profile, and such non-uniformity can produce a high-kinetic energy, low-pressure outlet. Therefore, the control initially takes its minimum value $\alpha = 0°$ to create good mixing. However, a straight section which is too long is detrimental to pressure recovery because of wall drag. Hence, a widening section is required after a critical length x_1.

The optimum value of α in the widening section represents a balance between mixing and widening the flow. If α is too large, then the flow profile will become too non-uniform at the outlet. Conversely, if α is too shallow, wall drag losses are enhanced. The singular arc is interesting from both a mathematical point of view, but also from an engineering point of view. It clearly shows that diffuser designs for non-uniform inflow should take into account the nature of the non-uniform inflow profile. The optimum widening angle for manufacture is given by Equation (5.95). Calculating $\alpha^*(x)$ from (5.95) is difficult in general ($\tilde{U}$ is a variable), but we find that for certain parameter values, it takes a simpler and more useful form.

In general, during the singular arc $\alpha^*(x)$ is not constant, yet in certain cases, such as Figure 5.3 (b), it doesn't vary much over the singular arc interval. This raises the question of whether it is possible to find constant α^* solutions. Noticing how the only variable in (5.95) is $\tilde{U}$, we seek solutions with constant $\tilde{U}$. Furthermore, we restrict our attention to solutions which begin on the singular arc (i.e. $x_1 = 0$). From Equation (5.82), we see that constant α^* solutions only exist if

$$\alpha^* = S_c\tilde{U}. \tag{5.96}$$

Therefore, reconciling (5.95) and (5.96), it can be shown that constant singular arc solutions exist for parameters which satisfy

$$S_c\tilde{U}(8S_c\tilde{U}^3 - 3f(1+\tilde{U})) = 0. \tag{5.97}$$

Excluding $\tilde{U} = 0$, and assuming that f and S_c are fixed, we are left with solving Equation (5.97) for $\tilde{U}$. Substituting $U_2(0)$ and U_0 back into (5.97), we rewrite the equation in terms of the inlet velocity ratio $U(0) = U_2(0)/U_0$, so that we require the parameters to satisfy

$$4S_c(U(0)-1)^3 + 3f(U(0)+1)^2 = 0. \tag{5.98}$$

Similarly, (5.96) then indicates that

$$\alpha^* = S_c\left(\frac{1-U(0)}{1+U(0)}\right). \tag{5.99}$$

For $U(0) = 0.35$, as in Figure 5.4 (b, d, f), we find $\alpha^* = \tan 2.76°$, which is very close to the solution from the numerical optimisation, indicating that (5.99) is also a good approximation for non-constant singular arcs.

Considering that in typical situations $f/S_c \approx 0.1$, and this is small, we expand (5.98) and (5.99) about f/S_c and ignore imaginary solutions, giving the approximate solution

$$U(0) = 1 - 3^{1/3}\left(\frac{f}{S_c}\right)^{1/3} + \frac{1}{3^{1/3}}\left(\frac{f}{S_c}\right)^{2/3} + \ldots, \tag{5.100}$$

$$\frac{\alpha^*}{S_c} = \frac{3^{1/3}}{2}\left(\frac{f}{S_c}\right)^{1/3} + \frac{1}{4\cdot 3^{1/3}}\left(\frac{f}{S_c}\right)^{2/3} + \ldots. \tag{5.101}$$

For the constant singular arc solution (5.99) we can solve the system (5.73), (5.82)-(5.95) exactly, which is described in Appendix B. Note, we also need to ensure that both $H_\alpha = 0$ and $\mathrm{d}H_\alpha/\mathrm{d}x = 0$ for all values of x during the singular arc. This will enforce a further constraint on the other parameters of the problem. As described in Appendix B, we formulate this constraint by writing the rescaled non-dimensional channel length $L/(S_c h_0)$ as a function of h_L/h_0 and f/S_c, and then expand the

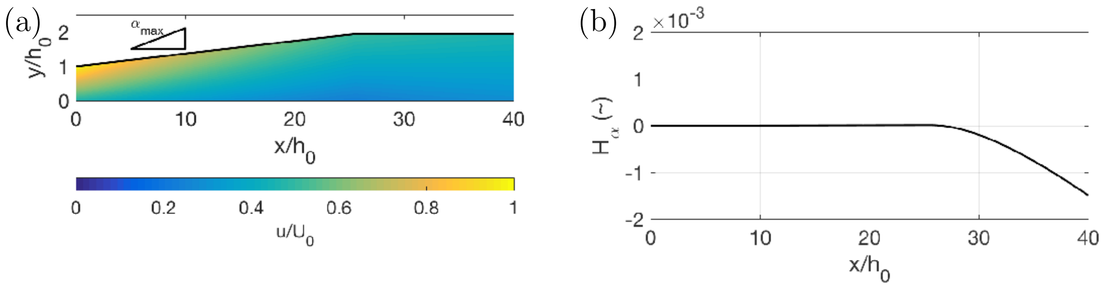

Figure 5.7: Constant singular arc solution displaying velocity colour map and a plot of $H_\alpha = \partial H/\partial \alpha$, where the Hamiltonian H is given by (5.89), for parameter values $S_c = 0.11$ and $f = 0.01$. The inflow velocity ratio $U(0) = 0.471$ is given by (5.98) and the singular arc value $\alpha^* = \tan 2.26°$ is given by (5.99).

expression in powers of f/S_c (similarly to before). Therefore, this constraint on the remaining parameters takes the approximate form

$$\frac{L}{S_c h_0} = \left(3^{-1/3}(1+2^{2/3})\frac{h_L}{h_0} - 2\cdot 3^{-1/3}\right)\left(\frac{f}{S_c}\right)^{-1/3} + \frac{1}{3} - \frac{1}{2}\frac{h_L}{h_0} + \dots. \tag{5.102}$$

As an example of such a constant singular arc solution, we choose parameter values $S_c = 0.11$ and $f = 0.01$, from which, solving Equations (5.98) and (5.99), we have an inflow velocity ratio $U(0) = 0.471$ and a singular arc value of $\alpha^* = \tan 2.26°$. Using (5.102), we find that $H_\alpha = 0$ and $\mathrm{d}H_\alpha/\mathrm{d}x = 0$ along the singular arc if we choose the remaining parameter values $\alpha_{min} = 0°$, $h_L/h_0 = 2$ and $L/h_0 = 40$. In Figure 5.7 we display the velocity colour map for this solution, together with a plot of H_α. We see that the solution starts on the singular arc until the expansion ratio $h_L/h_0 = 2$ is reached, at which point H_α becomes negative, such that the remaining length of the diffuser has angle $\alpha_{min} = 0°$.

It is of further interest to investigate how the singular arc depends on the model parameters f and S_c. We plot the relationship between the constant singular arc value α^* (5.99) and these parameters in Figure 5.8. It is clear that increasing the friction factor f results in a higher α^*. This is to be expected, since larger wall drag will penalise smaller angles more. Increasing the spreading parameter S_c also increases α^*. This is because higher spreading rates results in better mixing, and hence, wider angles are more affordable.

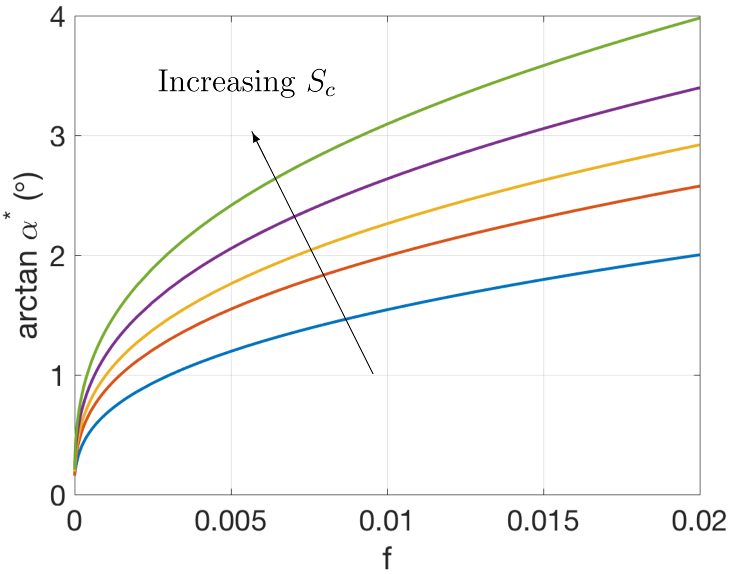

Figure 5.8: Parameter analysis for the constant α^* singular arc solution, given by (5.99), which depends on the parameters S_c and f. Here we use $S_c = 0.06$, 0.09, 0.11, 0.14 and 0.18.

5.5 Comparison with results from a k-ε model and a k-ω SST model

In this section we discuss comparisons between the flows in the optimal shapes, calculated using our simple model in Section 5.3, to calculations from CFD. We also use the (low-dimensional) piecewise linear parameterisation of the diffuser shapes that was motivated earlier to search for optima using two CFD models, and then we compare the results. In Chapter 4 we made comparisons between our simple model and a k-ε model [55], as well as experimental data generated with Particle Image Velocimetry (PIV). Here we use both a k-ε and a k-ω Shear Stress Transport (SST) model [67] to compare with some of the simple model optimisation results presented in Section 5.3. The k-ε model is one of the most popular CFD models, whilst the k-ω SST model is particularly robust in situations with strong adverse pressure gradients [67] (though for the small diffuser angles we consider in this study the adverse pressure gradients are not severe). Moreover, since a thorough comparison between the simple model and CFD has already been discussed in Chapter 4, we do not perform comparisons for all of the optimisation results of Section 5.3. Instead we look at the geometry in Figure 5.2 (e) as a single example.

Consider the example in Figure 5.2 (e), as discussed in Section 5.3. In order to compare with the simple model we use precisely the same inlet velocity profile

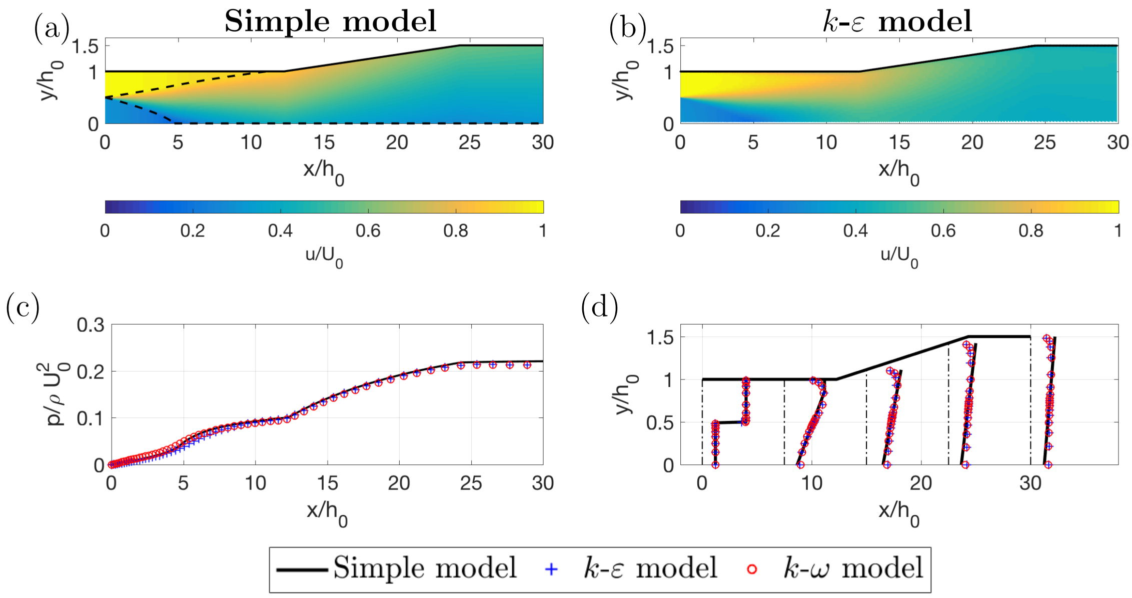

Figure 5.9: Comparison between our simple model and two CFD models (k-ε and k-ω SST) for the optimal shape in Figure 5.2 (e). The inlet profile is given by $U_2(0)/U_0 = 0.3$, $h_2(0)/h_0 = 0.5$, and the Reynolds number is $Re = 10^6$. (a) Velocity colour map calculated using our simple model, with black dashed lines indicating the shear layer. (b) Corresponding velocity colour map calculated using the k-ε model. (c) Pressure, averaged across the channel width. (d) Velocity profiles at evenly spaced locations down the channel.

as used in the simple model for the input to the CFD models. Inlet conditions for the turbulence variables k, ε and ω are taken to be the free-stream boundary conditions [87] $k = I^2 \times 3/2\,(u^2 + v^2)$, $\varepsilon = 0.09k^{3/2}/\ell$ and $\omega = \sqrt{k}/\ell$, with turbulence intensity $I = 5\%$ and mixing length $\ell = 0.1h_0$ (10% of the channel half-width). In both the CFD models, no-slip boundary conditions are applied to the channel walls. Furthermore, we use all the standard turbulence parameter values, which are given in Chapter 2 for the k-ε model and by Menter [67] for the k-ω SST model. Further details of these CFD models, including wall boundary conditions and outflow conditions, can be found in [55] and [67].

In Figure 5.9 (a, b) we display colour plots of the time-averaged streamwise velocity u generated with both the simple model and the k-ε model. Figure 5.9 (d) also compares velocity profiles at evenly spaced locations down the channel, for the simple model and both CFD models. There is good agreement between the models, with the simple model capturing the dominant features of the flow, such as maximum and minimum velocities, and the width of the shear layer. There is a slight discrepancy near the diffuser wall since our model does not resolve boundary layers, but instead

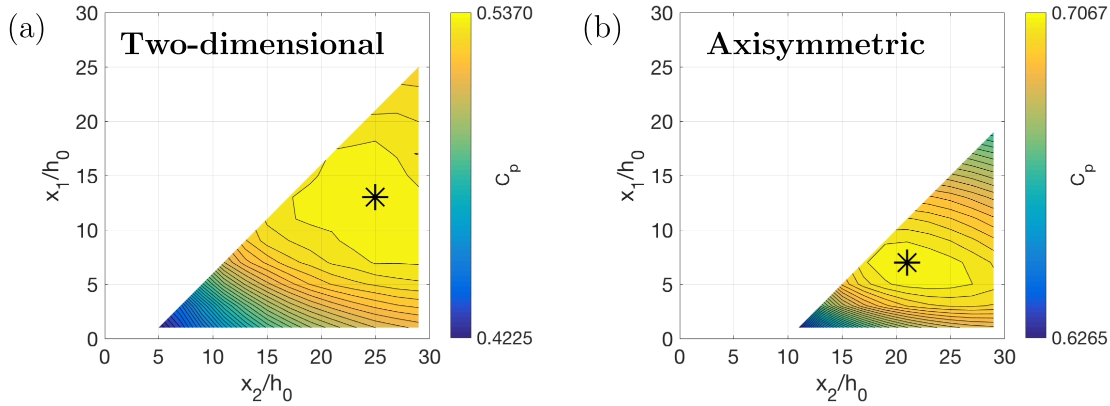

Figure 5.10: Contour plots of pressure recovery C_p, given by (4.16), (5.2), over all permissible values of x_1 and x_2, calculated using the k-ε model. Direct comparison is made with Figure 5.3, where the same contour plots are calculated using the simple model. The inlet profile is given by $U_2(0)/U_0 = 0.3$, $h_2(0)/h_0 = 0.5$.

parameterises their effect with a friction factor. However, we can see that our model accurately captures the effect of the boundary layers on the pressure by the close comparison between the models in Figure 5.9 (c).

In Section 5.3, we investigated reducing the dimension of the control α by splitting it into three piecewise constant sections divided by x_1 and x_2, which we treated as decision variables. Motivated by these piecewise linear shapes, here we make the same simplification, reducing the degrees of freedom of the control to 2. We explore the parameter space generated by x_1 and x_2, using both CFD models to calculate pressure recovery. Each calculation made by the CFD models is much more computationally expensive than that of the simple model, but because of the low dimension of the degrees of freedom, we can still feasibly explore the different possible combinations of x_1 and x_2. This would not be tractable, however, if we were to use 100 degrees of freedom, as we did with the simple model in Section 5.3. Hence, the numerical optimisation using the simple model is very useful for finding the general shape of the optimal channels, around which we can further search for optima using more realistic, yet more computationally intensive CFD models.

In Figure 5.10 we plot contours of pressure recovery C_p (4.16) as a function of the two parameters x_1 and x_2, where C_p is calculated using the k-ε model, and this should be compared with the results of the simple model, as shown in Figure 5.3. Note that in Figure 5.10, as in Figure 5.3, we exclude values of x_1 and x_2 which have a diffuser angle larger than $\tan 7°$ for the two-dimensional case and $\tan 3.5°$ for the axisymmetric case.

Comparing Figures 5.3 and 5.10, we see that the optimum diffuser shapes using both the simple model and the k-ε model, are characterised by similar values of x_1 and x_2. In the two-dimensional case, according to the k-ε model, the optimum diffuser shape has $x_1/h_0 = 13$ and $x_2/h_0 = 25$, with a pressure recovery of $C_p = 0.5370$. According to the simple model, the optimum diffuser shape has $x_1/h_0 = 12.3$ and $x_2/h_0 = 24.3$, with a pressure recovery of $C_p = 0.5205$, which is very close to that obtained with the k-ε model. Similarly, for the axisymmetric case, the k-ε model suggests an optimum diffuser shape with $x_1/h_0 = 7$ and $x_2/h_0 = 21$, giving a pressure recovery of $C_p = 0.7067$, whereas the simple model suggests $x_1/h_0 = 6.3$ and $x_2/h_0 = 19.8$, with a pressure recovery of $C_p = 0.6886$. Considering that the diffuser angle is given by (5.15), it is clear that if the optimum values of x_1 and x_2 are similar according to the simple model and the CFD, then the optimum diffuser angle is also similar. In fact, we can compare the value of C_p as a function of diffuser angle by looking at intersections of the contour plots (Figures 5.3 and 5.10) with the lines $x_1 - x_2 =$ const.

Note, as a check on accuracy, we have also generated these pressure recovery data using the k-ω SST model and we find the results are very similar. The average discrepancy between the C_p values calculated using the k-ω SST model and the k-ε model is 0.004 for the two-dimensional case, and 0.003 for the axisymmetric case.

These results indicate that the optimal shapes found using the numerical optimisation routine and the simple model are similar to the optimal shapes that would be found if we were to use either of these CFD models as a forward model. Hence, this gives us confidence that the optimal shapes generated using the simple model are close to true optimal shapes in reality.

5.6 Discussion and conclusions

5.6.1 The effect of parameter values on the optimal shape

Although we have investigated optimum diffuser shapes in a number of specific cases, we have not yet explored thoroughly the various parameters of the model, which are listed in Table 5.1. We now briefly discuss the effect that each of these parameters has on the optimal shape. However, since there are many parameters, we do not provide plots for the analysis of every single parameter.

One of the most important parameters is the velocity ratio $U_2(0)/U_0$ of the inflow. To explore this parameter, we investigate optimal diffuser shapes for a fixed inflow with $h_2(0)/h_0 = 0.5$, an expansion ratio $h_L/h_0 = 2.3$ and a length ratio $L/h_0 = 40$,

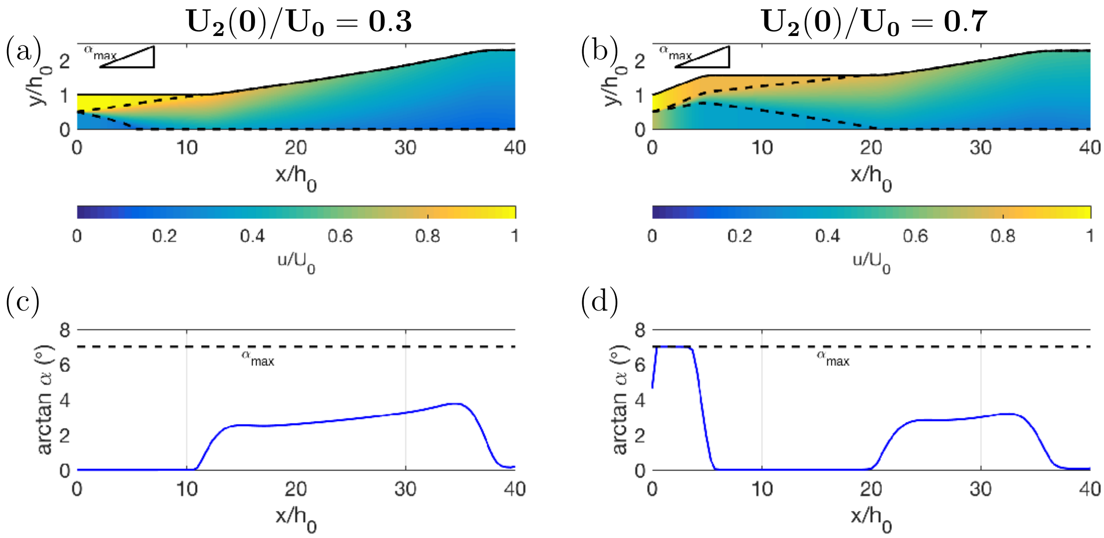

Figure 5.11: Investigation of the dependence of optimal diffuser shapes on the inflow velocity ratio in the two-dimensional case, showing velocity colour maps (a, b) and plots of the control α (c, d). In both cases we choose an inflow with $h_2(0)/h_0 = 0.5$, an expansion ratio $h_L/h_0 = 2.3$ and a length ratio $L/h_0 = 40$. The lower limit for the diffuser angle in both cases is $\alpha_{min} = 0°$. The upper limit is $\alpha_{max} = \tan 7°$.

and we vary the velocity ratio. We also use the same values for the parameters $f = 0.01$ and $S_c = 0.11$ as we have throughout this chapter. The results of the optimisation are displayed in Figure 5.11, for $U_2(0)/U_0 = 0.3$ and $U_2(0)/U_0 = 0.7$. We see that the effect of a velocity ratio which is closer to 1 is to make an initial widening section favourable. This is because when the inflow is more uniform, wider angles penalise pressure recovery less. Therefore, the balance is tipped in favour of reducing wall drag by expanding the channel a little. In the extreme case where $U_2(0)/U_0$ becomes close to unity, we have seen in Section 5.4.1 that this initial widening section dominates throughout, such that the optimal control is purely bang-bang, with no singular arc. Notice how in the case of $U_2(0)/U_0 = 0.7$ the shape can no longer be approximated well by the parameterisation using just x_1 and x_2.

The effect of increasing or decreasing the ratio of the size of the plug regions from $h_2(0)/h_0 = 0.5$ is that the distance taken for one of the plug regions to disappear becomes smaller (see Chapter 4, Section 4.4). If the velocity ratio is small then, as described earlier, this distance is critical because it marks the point where the flow is sufficiently mixed that it is acceptable to expand thereafter at a wider angle (e.g. Figure 5.2 (d)). Hence, the effect of increasing or decreasing $h_2(0)/h_0$ is that this critical distance becomes smaller.

The effects of varying the diffuser expansion ratio h_L/h_0 and length ratio L/h_0

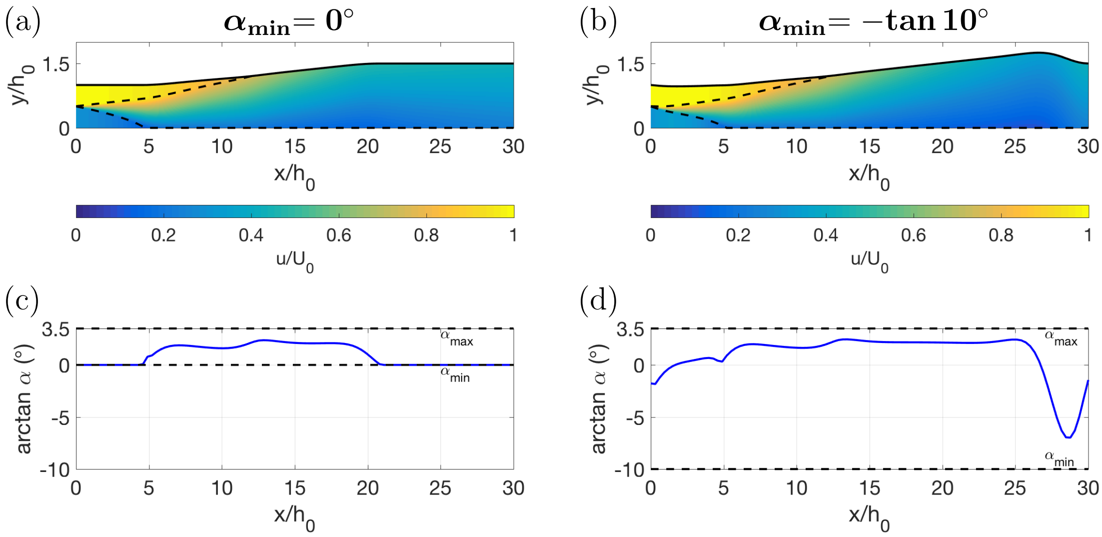

Figure 5.12: Investigation of the dependence of optimal diffuser shapes on the lower bound α_{min} for the expansion angle in the axisymmetric case, showing velocity colour maps (a, b) and plots of the control α (c, d). In both cases we choose an inflow with $U_2(0)/U_0 = 0.3$, $h_2(0)/h_0 = 0.5$, an expansion ratio $h_L/h_0 = 1.5$ and a length ratio $L/h_0 = 30$ (as in Figure 5.2 (d)). The upper limit for the diffuser angle in both cases is $\alpha_{max} = \tan 3.5°$.

are more obvious and less interesting. Neither of them affects the optimum widening angle, but instead the diffuser either expands wider and expands for longer, respectively. This is because these parameters do not affect the crucial balance between wall drag and mixing effects. However, it is useful to note the effect of including the length of the channel as a decision variable in the optimisation problem. We have already discussed this in the case of the small shear limit, but not for the developing shear layer case, nor the pure shear limit. For the developing shear layer case in Figure 5.2 the optimum channel length is slightly larger than x_2. A channel length shorter than x_2 would force the channel to widen at a sub-optimal expansion angle. A channel length much longer than x_2 causes unnecessary wall drag. The optimum length is slightly longer than x_2 because the flow at $x = x_2$ is not completely uniform, and by letting the flow profile develop a little bit more, a small amount of additional pressure recovery is achieved. The optimum widening angle for the pure shear limit in Figure 5.4 (b) is similar.

Varying the upper and lower bounds on the diffuser angle, α_{max} and α_{min}, only affects the optimal solution if the these constraints are active over an interval. For example, in Figure 5.2 (a, b) we see that α never reaches α_{max}. Therefore, in these cases, raising α_{max} would have no effect on the solutions. However, α clearly lies on the lower bound α_{min} over an interval at the beginning and near the end of the domain. Therefore, varying α_{min} here moves the optimal control along with it. To show this, in Figure 5.12 we compare the optimal diffuser shape and the optimal control α from the axisymmetric example in Figure 5.2 (b), to the same example except with the lower bound $\alpha_{min} = -\tan 10°$ instead of $\alpha_{min} = 0°$. In this case, the straight sections near the inlet and outlet in (a, c) are replaced with contracting sections in (b, d). The initial contracting section causes an increase in wall drag, but also appears to aid mixing, such that there is an overall payoff in pressure recovery. Near the end of the diffuser, the shape over-expands to reduce wall drag, and then contracts again so that $h(x)$ satisfies the terminal constraint $h(L) = h_L$. In reality, such a contraction near the end of the diffuser may not be beneficial, as it may cause recirculation zones.

Throughout this manuscript we have used a constant value of the spreading parameter $S_c = 0.11$. In Section 5.5 (as well as in Chapter 4) we showed that this parameter value is consistent with both a k-ε model and a k-ω SST model using all standard turbulence parameter values [55, 67]. However, in Chapter 4 we discussed how this value is not universal. For example, in the three-dimensional channel example in Chapter 4 the shear layer growth was magnified due to the effect from the top and bottom walls. In this case, the spreading parameter took a larger value $S_c = 0.18$. Therefore, since the value of S_c is not universal, precaution must be taken when choosing S_c for diffuser shape optimisation. In particular, S_c is associated with the shear layer growth rate, and so if S_c is larger the shear layer will entrain the plug regions over a shorter distance. In fact, S_c can be thought of as a spatial stretching factor (it can be absorbed into Equation (4.2) by rescaling x). Therefore, if S_c is 1.6 times larger (like in the three-dimensional channel example) the optimum shape will be squashed in the x direction by approximately the same factor, assuming we also shorten the length of the channel L. The value of S_c also has an effect on the optimum expansion angle of the diffuser, which is discussed in Section 5.4.2 in the case of the singular arc. Therefore, clearly the value of S_c has a significant effect on the optimum diffuser shape. Hence, it is recommended that, before running the shape optimisation, experimental measurements should be taken to determine the appropriate value of S_c for the flow scenario.

When considering values for the friction factor f, we use the Blasius relationship (4.7), finding good agreement with both CFD and experiments, as seen in Section 5.5 and in Chapter 4. For rougher channels, with a larger friction factor f, thinner channels and smaller angles will be penalised more. In such cases, the optimum widening angle is larger. Furthermore, if f is sufficiently large, it becomes more advantageous to have an initial widening section, similar to situations where the velocity ratio $U_2(0)/U_0$ is close to 1. In the extreme case where wall drag dominates, the control becomes bang-bang because the penalty of worsening the non-uniform flow is eclipsed by the effect of wall drag. For very small wall drag, the optimal diffuser shape prioritises mixing over widening the flow. In these cases, thin channels and small diffuser angles are not penalised very much, such that the critical distance after which expansion occurs is precisely the point where the shear layer has reached across the entire channel. At this point the flow is sufficiently mixed and can afford expansion.

5.6.2 Conclusions

We have developed a numerical optimisation routine to find the diffuser shape which maximises pressure recovery for a given non-uniform inflow, in both two-dimensional and axisymmetric cases. The optimisation used the simple model from Chapter 4 to describe the development of turbulent shear layers in confining channels. We found that some of the optimal diffuser shapes were well approximated by shapes which are composed of two straight sections separated by a widening section with a constant widening angle. This is in contrast to diffuser design for uniform flow, where diffusers do not typically have an initial straight section. Furthermore, we showed that the optimum widening angle was less than the angle at which boundary layer separation typically occurs, which is usually the diffuser angle chosen for uniform flow. Therefore, we have shown that the effects of non-uniform inflow are critical to diffuser performance, and should not be ignored when it comes to diffuser design.

In two limiting cases we used analytical techniques to interpret the optimal diffuser shapes found with the numerical optimisation. The first of these cases was the small shear limit, where the inflow was almost uniform, in which case the optimal control was bang-bang, such that the diffuser widens at the maximum possible angle until it reaches the desired cross-sectional area, and then remains at that area. The second case was the pure shear limit, where the inflow was a purely sheared flow with no plug regions. In this case, we showed that the optimal control may have a singular arc where, on an interval, the diffuser angle takes values between its upper and lower bounds. We showed that in certain cases the singular arc corresponds to a constant angle and this angle depends on the friction factor f and the spreading parameter S_c.

We compared some of the numerical optimisation results with CFD simulations using both a k-ε model and a k-ω SST model (using all standard turbulence parameter values), finding good agreement. In the case where we approximated the diffuser shape with piecewise linear sections, we showed that both the simple model and the CFD models share almost identical optimal shapes. This suggests that the optimal shapes found using the numerical optimisation and the simple model are indeed close to the true optimal shapes in reality.

In Chapter 4 we showed how the accuracy of the simple model could be improved by incorporating a boundary layer near the channel wall and a symmetry layer near the channel centreline. Although we have not considered these extra layers in this Chapter, we could apply the same numerical optimisation approach to the extended model. However, since the simple model without these extra layers already shows good comparison with CFD and experiments, we expect this makes little difference to the results of the optimisation. We might expect that the inclusion of the boundary layer in the extended model would render the diffuser angle upper bound α_{max} unnecessary. In this way we could search for the optimal control α in an unbounded space, without being concerned that our model does not account for boundary layer separation when the diffuser angle is very wide. However, the boundary layer incorporated into the extended model, which is a self-similar power law profile, does not represent situations where the flow separates (since separated flow is not self-similar [87]). Therefore, for future work, we could improve the extended model to account for boundary layer separation, thereby allowing our optimisation to be less restricted.

Chapter 6

The effect of swirl on confined co-axial flow

6.1 Motivation

For several of the classes of non-uniform inflow which were considered in Chapter 5 the optimal diffuser shape had an initial straight narrow section which was necessary for mixing the flows before expansion. However, this narrow section has the strongest wall drag of the entire geometry. Therefore, if it were possible to mix the flows over a shorter length scale then the narrow section could be made shorter, thereby reducing pressure losses due to drag. Hence, to further increase pressure recovery we next consider possible mechanisms for mixing enhancement.

There have been many studies which have investigated different ways to increase the growth rate of shear layers. Oster & Wygnanski [75] showed that by exciting a shear layer with an active flapping plate it was possible to enhance shear layer growth rates, if the appropriate frequency and amplitude was chosen. Greenblatt & Wygnanski [40] found similar results using acoustic excitation. Kit et al. [52] found that it was possible to use a chevron-type splitting plate at the origin of the shear layer to increase growth rates. In addition, there have been many studies [71, 38] which have shown that shear layer growth can be enhanced by introducing swirl into the flow.

Of the various approaches above, the easiest to adopt within Venturi-enhanced hydropower is the use of swirl. In particular, it would be relatively straightforward to introduce swirl into the secondary flow which passes through the turbine. One way this could be achieved is by removing/reducing the stator blades at the outflow of the turbine, such that the flow leaves the turbine with some of the swirl given to it by the entry blades. The disadvantage of this approach is a significant drop in turbine efficiency associated with not removing the swirl kinetic energy from the turbine outflow. Another more favourable approach is to carve helical vanes into the inside of the secondary pipe. These vanes would introduce a significant amount of swirl into the flow with relatively low energy losses (due to drag from the vanes).

However, even without these approaches it is quite likely that a small amount of swirl will be present in the secondary flow anyway, since the stator blades of the turbine will not operate perfectly. Therefore, it is important to understand the effects of the swirl likely to be present in the secondary flow, and whether an increase in such swirl could yield improvements to pressure recovery. This is the topic of the present chapter. In the next section we provide a literature review of swirl and outline the approach that we take in the sections that follow.

6.2 Introduction

There are many industrial applications where swirl is added to jet flows and annular flows to improve performance. Most commonly, swirl is used in combustion chambers to increase fuel mixing rates and to stabilise the flame [60, 57]. There have also been studies which indicate that swirl can be used to improve plasma jet cutting performance [39], to increase the efficiency of a jet pump [43], and to reduce flow separation in diffusers [34]. In addition, swirl is present in a variety of propulsion systems, such as in jet engines and turbomachinery, and plays an important role in the interaction between aircraft wakes [10]. Our goal in this chapter is to examine the effect of swirl on the mixing of confined co-axial flows, such as the secondary and primary flows in Venturi-enhanced hydropower.

Existing experimental studies of *unconfined* jets have shown that swirl (in the jet) can significantly increase entrainment rates and consequently the growth rate of the jet, both for compressible and incompressible fluids [71, 38]. Besides other experimental and numerical studies of unconfined jets [58, 37, 29, 31, 59, 74], there have also been some that have considered the effect of swirl on annular flows and confined flows.

In the case of annular flows, Lee et al. [57] studied the effect of swirl on the characteristics of an unconfined co-axial annular flow. In their experiments, both the core flow and the annular flow had swirl components, not necessarily in the same direction. They showed that if the swirl is sufficiently strong, a stagnation point and recirculation region can develop inside the core flow. Other studies [21, 30, 20, 72] have discussed this recirculation region and relate it to the phenomenon of vortex breakdown. In the context of combustion chambers, the recirculation region is important because it has a stabilising effect on the flame. In this region, the flame speed and flow velocity are equalised due to the relatively low velocity. Both co-swirling and counter-swirling annular flows have been investigated experimentally [83, 28, 45, 68] with the general conclusion that counter-swirl is more stabilising.

In the case of confined flows, there are a number of studies which consider the effect of swirl on the performance of a diffuser. The experiments of Fox & McDonald [34] showed that by adding a solid body rotation to the inflow of a diffuser with flow separation, it is possible to reduce separation and increase pressure recovery significantly. By contrast, for unseparated flows, it was shown that swirl makes little difference to pressure recovery. The numerical simulations of Hah [46] investigated the effects of a Rankine-type rotation and a solid-body rotation at the inlet of a diffuser, finding similar results to Fox & McDonald. Hah suggested that swirl reduces flow separation by means of the centrifugal force, which presses the boundary layer to the pipe wall. Both Fox & McDonald [34] and Hah [46] showed that performance decreases for large swirl intensities, and attribute this behaviour to the formation of a recirculation region when the swirl number is large. So [90] studied the recirculation region inside a conical diffuser in detail and presented a simple model based on integral equations of mass, axial momentum, angular momentum, and moment of axial momentum. However, there was a significant discrepancy between the model predictions and experimental results, which was attributed to the assumption of constant viscosity. The experiments of Nayeri [72] studied a shear layer between confined swirling co-axial flows. Both co-swirling and counter-swirling flows were investigated and it was found that, in both cases, the shear layer growth rates were larger than in the absence of swirl, though the counter-rotating case had the largest growth rates overall. The formation of a recirculation region was not studied. Nor was the effect of different pipe geometries.

In this chapter we present a simple model for confined co-axial flow with a swirling core, and we use the model to investigate the effect of swirl on the flow characteristics in a variety of pipe geometries. We study the effect of a swirling core on the pressure recovery in a diffuser, which is not addressed in the literature. In particular, we show that whilst a swirling core is useful for increasing shear layer growth rates and mixing the flows over a shorter length scale, it is detrimental to pressure recovery. We confirm that under certain flow conditions, a recirculation region can form along the pipe axis, and we use our model to characterise the onset and size of this region in terms of the inflow conditions and the pipe expansion angle.

The model is based on the simple model in Chapter 4 for non-swirling shear layers, and uses a similar approach to So [90], where the governing equations are integral equations of mass, axial momentum and angular momentum.

The model is described in Section 6.3, and compared to computational fluid dynamics in Section 6.4. In Section 6.5 we use the model to address the question of how swirl affects mixing and pressure loss in diffusers of different shapes. We present some extensions to the model in Section 6.6, and we close with a summary in Section 6.7.

6.3 Mathematical model

In this section we describe the flow scenario we consider and present a simple model, which is an extension of the model presented in Chapter 4 for the case of no swirl. The model in Chapter 4 considers an inflow composed of inner and outer streams of different speeds, with a velocity jump between them that evolves into a shear layer downstream. The model presented here addresses the same inflow profile for an axisymmetric pipe but with the inner (core) stream rotating. This is achieved by introducing an angular velocity component which is governed by equations derived from integrating conservation of angular momentum. Furthermore, we account for radial pressure gradients induced by the swirl as a consequence of the conservation of radial momentum. The shear layer growth equation (4.2) is modified to account for the additional effect of the azimuthal shear stress induced by the swirl.

The flow scenario we consider is shown in Figure 6.1, in which we illustrate our chosen coordinate system (x, r). We consider axisymmetric flow in a long thin cylindrical pipe $0 < r < h(x)$, where the rate of change of the pipe radius is small. The inflow is composed of a core swirling flow, with axial velocity $U_2(0)$ and solid body rotation at angular velocity $\Omega(0)$, and an annular non-swirling flow with axial velocity $U_1(0)$. A shear layer forms between the flows and grows downstream, as illustrated by red dashed lines in Figure 6.1. Throughout this study, we restrict our attention to the case where the axial velocity of the core flow is smaller than that of the annular flow $U_2 < U_1$, as is representative of Venturi-enhanced hydropower. The opposite case is prone to asymmetric instabilities, such as the Coanda effect [97], which are not included in our model.

We approximate the axial flow profile u_x by decomposing it into two uniform-velocity plug regions separated by a shear layer in which the velocity varies linearly

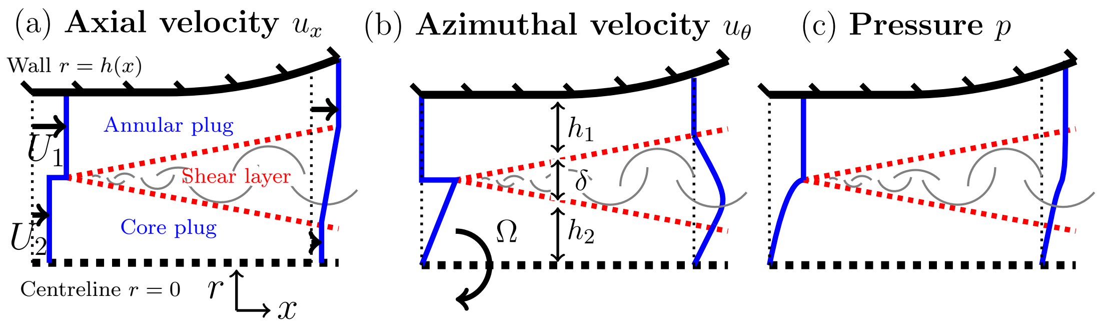

Figure 6.1: Schematic diagram of our simple swirl model for a swirling slower central flow mixing with a non-swirling faster outer flow, showing axial profiles of axial velocity u_x, azimuthal velocity u_θ and pressure p. We indicate the position of the shear layer with red dashed lines.

between $U_1(x)$ and $U_2(x)$. Therefore, the axial velocity profile is approximated by

$$u_x(x,r) = \begin{cases} U_2 & : 0 < r < h_2, \\ U_2 + \varepsilon_r\,(r - h_2) & : h_2 < r < h - h_1, \\ U_1 & : h - h_1 < r < h, \end{cases} \tag{6.1}$$

where $h_1(x)$ and $h_2(x)$ are the widths of the plug regions, $\delta = h - h_1 - h_2$ is the width of the shear layer, and $\varepsilon_r = (U_1 - U_2)/\delta$ is the shear rate.

Similarly to the axial velocity, we approximate the azimuthal velocity profile by decomposing it into a core swirling region and an annular region with no swirl separated by an azimuthal shear layer in which the azimuthal velocity varies quadratically (motivated by CFD calculations which are discussed later). The approximate azimuthal velocity profile is taken to be

$$u_\theta(x,r) = \begin{cases} \Omega r & : 0 < r < h_2, \\ (h - h_1 - r)(\frac{h_2\Omega}{\delta} + \kappa(h_2 - r)) & : h_2 < r < h - h_1, \\ 0 & : h - h_1 < r < h, \end{cases} \tag{6.2}$$

where $\Omega(x)$ is the angular velocity in the core region, and $\kappa(x)$ is the curvature of the velocity profile within the shear layer. From boundary layer theory (see Chapter 2, Section 2.3), conservation of radial momentum indicates that radial pressure gradients must balance the centrifugal force from the swirling flow

$$\frac{\partial p}{\partial r} = \rho \frac{u_\theta^2}{r}. \tag{6.3}$$

Therefore, from (6.2) and (6.3), the approximate pressure profile is

$$p(x,r) = \begin{cases} p_2 + P & : 0 < r < h_2, \\ p_1 + P & : h_2 < r < h - h_1, \\ P & : h - h_1 < r < h, \end{cases} \tag{6.4}$$

where $P(x)$ is the pressure in the non-swirling region of flow and $p_1(x, r)$ and $p_2(x, r)$ are given by

$$
\begin{aligned}
p_1 = \frac{\rho}{12\delta^2} \Bigg(& \delta^2\kappa^2(h_2 - r + \delta)(25h_2^3 + h_2(13r - 5\delta)(r - \delta) \\
& - (r - \delta)^2(3r + \delta) + h_2^2(-23r + 31\delta)) + 4\kappa h_2 \delta\Omega(h_2 - r + \delta)(11h_2^2 \\
& + 2(r - \delta)^2 + h_2(13\delta - 7r)) + 6h_2^2\Omega^2(h_2 - r + \delta)(3h_2 - r + 3\delta) \\
& + 12h_2^2(h_2 + \delta)^2(\kappa\delta + \Omega)^2 \log \frac{r}{h_2 + \delta} \Bigg),
\end{aligned} \tag{6.5}
$$

$$
\begin{aligned}
p_2 = \frac{1}{2}\rho\Omega^2 r^2 + \frac{\rho}{12\delta^2} \Bigg(& \kappa^2\delta^3(2h_2 + \delta)(6h_2^2 + 6h_2\delta - \delta^2) \\
& + 4\kappa h_2 \delta^2\Omega(6h_2^2 + 9h_2\delta + 2\delta^2) + 12\Omega^2 h_2^2 \delta(h_2 + \delta) \\
& + 12h_2^2(h_2 + \delta)^2(\kappa\delta + \Omega)^2 \log \frac{h_2}{h_2 + \delta} \Bigg).
\end{aligned} \tag{6.6}
$$

Equations (6.5) and (6.6) are complicated expressions, but at the pipe inflow, where $\delta = 0$, (6.5) becomes redundant and (6.6) reduces to a simpler form

$$
p_2 = \frac{1}{2}\rho\Omega^2 \left(r^2 - h_2^2\right). \tag{6.7}
$$

Note that $p(x, r)$, given by (6.4), is both continuous and once differentiable with respect to r.

To model the growth of the shear layer, we modify (4.2), from the simple model in Chapter 4, to account for the additional effect of azimuthal shear. Thus, we assume that the shear rate ε_r decays according to[1]

$$
\frac{U_1 + U_2}{2} \frac{\mathrm{d}\varepsilon_r}{\mathrm{d}x} = -S_c \varepsilon_r^2 \frac{|\mathbf{u}_1 - \mathbf{u}_2|}{U_1 - U_2}, \tag{6.8}
$$

where $\mathbf{u}_1 = (U_1, 0)$ and $\mathbf{u}_2 = (U_2, \Omega h_2)$ are the velocities at either side of the layer, and S_c is an empirical spreading parameter which has been recorded to take values $S_c = 0.11 - 0.18$ (as discussed in Chapter 4).

By invoking conservation of mass, axial momentum and angular momentum, we can derive equations describing how U_1, U_2, h_1, h_2, κ and P evolve. Integrated across

[1] Equation (6.8) can be derived using a two-dimensional analogy, similar to the example in Chapter 2, Section 2.6. In the analogy the azimuthal velocity component in the core region is replaced by an out-of-plane velocity component for the two dimensional flow. Therefore, we follow the derivation using the same conservation of mass equations (2.130)-(2.132) except with the rate of entrainment proportional to the magnitude of the velocity difference between the two plug regions $E = S_c|\mathbf{u}_1 - \mathbf{u}_2|$.

the pipe radius, conservation of mass and momentum equations are

$$\frac{\mathrm{d}}{\mathrm{d}x}\int_0^h r u_x \,\mathrm{d}r = 0, \tag{6.9}$$

$$\rho\frac{\mathrm{d}}{\mathrm{d}x}\int_0^h r u_x^2 \,\mathrm{d}r = -\int_0^h r\frac{\partial p}{\partial x}\,\mathrm{d}r + h\tau_{h_r}, \tag{6.10}$$

$$\rho\frac{\mathrm{d}}{\mathrm{d}x}\int_0^h r^2 u_\theta u_x \,\mathrm{d}r = 0, \tag{6.11}$$

where τ_{h_r} is the shear stress in the axial direction at the wall. We assume that the effect of shear stress in the azimuthal direction at the wall is small, so we do not include any stress terms on the right hand side of (6.11) (though we revise this assumption later in Section 6.6). Here, we parameterise the effect of the wall stress in the axial direction using an empirical friction factor f, such that

$$\tau_{h_r} = -\frac{1}{8}f\rho U_1^2. \tag{6.12}$$

Equations (6.9) - (6.11) are derived from the turbulent boundary layer equations in Chapter 2, Section 2.4.3, where $U_x = U_1$ and we set $U_\theta = 0$ because the azimuthal velocity (6.2) is zero at the pipe wall.

By choosing a parabolic profile for the azimuthal velocity (6.2) (instead of a linear profile), there is an additional degree of freedom $\Omega(x)$ which is not determined by (6.11). This is accounted for by imposing conservation of angular momentum within the core region

$$\rho\frac{\mathrm{d}}{\mathrm{d}x}\int_0^{h_2} r^2 u_\theta u_x \,\mathrm{d}r = \rho\Omega h_2^2\frac{\mathrm{d}}{\mathrm{d}x}\int_0^{h_2} r u_x \,\mathrm{d}r. \tag{6.13}$$

Equation (6.13) can be derived by following Chapter 2, Section 2.4.3, where we use Equations (2.97) and (2.99) with $a = 0$ and $b = h_2(x)$. For this case both the stress terms at $r = 0$ and $r = h_2$ vanish due to the fact that $\partial u_\theta/\partial r = u_\theta/r$ for $u_\theta = \Omega r$.

Finally, we neglect energy dissipation within the plug regions, since it is small compared with that near the walls and in the shear layer. Therefore, we impose Bernoulli's equation along streamlines in the annular plug region, and for the core region, since pressure varies radially, we only impose Bernoulli's equation along the central non-swirling streamline, such that

$$\text{either}\quad \frac{\mathrm{d}}{\mathrm{d}x}\left(P + \frac{1}{2}\rho U_1^2\right) = 0, \qquad \text{or}\quad h_1 = 0, \tag{6.14}$$

$$\text{either}\quad \frac{\mathrm{d}}{\mathrm{d}x}\left(P + p_2(x,0) + \frac{1}{2}\rho U_2^2\right) = 0, \quad \text{or}\quad h_2 = 0, \quad \text{or}\quad U_2 = 0, \tag{6.15}$$

where we ignore radial velocity components since they are small. Equations (6.14) and (6.15) are written in this form so that if either plug region is entrained by the shear layer ($h_1 = 0$ or $h_2 = 0$), or if the core region slows to zero velocity ($U_2 = 0$), then the respective Bernoulli's equation no longer holds downstream of that point (similarly to the model in Chapter 4). The latter modelling assumption is based on the observation that if the swirl intensity in the core region is sufficiently large, a slow-moving recirculation region can form along the pipe axis, as shown by [57]. A similar recirculation region has been observed for non-swirling flows if the flow is very non-uniform, or if the pipe expansion angle is too large (See Chapter 4, Section 4.5). In our model, we do not attempt to resolve the recirculation within such a region, but approximate it as a stagnant zone with zero axial velocity $U_2 = 0$ (see Figure 4.2). Later, in Section 6.4, we show that this approximation shows good agreement with CFD calculations.

Note that, by only imposing Bernoulli's equation (6.15) along the central streamline in the core region, the velocity and pressure in our model do not satisfy Bernoulli's equation along other streamlines in the core region. However, in reality we expect there to be very little energy loss in the core region, since it has a plug flow profile. In Appendix C we compare the streamlines calculated using our simple swirl model to those calculated using a k-ε model in a straight pipe example. We find that, according to the k-ε model, Bernoulli's equation holds along all streamlines in the core region to a very good approximation. In comparison, according to the simple swirl model, Bernoulli's equation holds to a good approximation on streamlines in the core region. Therefore, we conclude that, although we have only imposed Bernoulli's equation along the central streamline in our simple swirl model, the flow in the rest of the core region is approximately inviscid, which is consistent with CFD calculations.

To summarise, our model describes the development of the axial velocity $u_x(x, r)$, given by (6.1), the azimuthal velocity $u_\theta(x, r)$, given by (6.2), and the pressure $p(x, r)$, given by (6.4), in a cylindrical pipe. Equations (6.8)-(6.15) govern[2] the variables U_1, U_2, Ω, P, δ, h_1, h_2, ε_r and κ, which are all functions of x. We can solve these equations given initial data at $x = 0$, numerical values for f and S_c, and a pipe shape $h(x)$. For all of the examples we consider here, the shear layer forms at $x = 0$, such that initial conditions for δ and ε_r are taken as $\delta(0) = 0$ and $\varepsilon_r(0) = \infty$[3]. Furthermore,

[2]Note there are 9 unknown variables and in total there are 9 governing equations for these variables, which are (6.8)-(6.11), (6.13)-(6.15), and the relations $h_1+h_2+\delta = h$ and $\varepsilon_r = (U_1-U_2)/\delta$.

[3]In practice it is difficult to implement $\varepsilon_r(0) = \infty$ numerically, so instead we solve for the inverse of the shear rate which satisfies $1/\varepsilon_r(0) = 0$. In addition, since $\delta(0) = 0$, we do not require an initial condition for κ.

pressure is measured with respect to the reference pressure in the annular region at the origin $P(0) = 0$, without loss of generality. The other initial conditions form a set of parameters which are displayed in Table 5.1, where we write all dimensional quantities in terms of the velocity and length scalings $U_0 = U_1(0)$ and $h_0 = h(0)$. There is an additional parameter not displayed in Table 5.1, which is the non-dimensional swirl number [38] of the core region S_w. This is defined as the ratio of angular momentum to axial momentum, measured at the inlet, and is given by

$$S_w = \left. \frac{\rho \int_0^{h_2} r^2 u_\theta u_x \, \mathrm{d}r}{h_2 \int_0^{h_2} r \left(\rho u_x^2 + (p - p|_{r=h_2})\right) \, \mathrm{d}r} \right|_{x=0} = \frac{2h_2(0)\Omega(0)U_2(0)}{4U_2(0)^2 - h_2(0)^2\Omega(0)^2}. \tag{6.16}$$

Our primary interest is understanding the effect of this swirl parameter on the flow development, which is discussed in Section 6.5.

We note that (6.16) is only well-defined for relatively small amounts of swirl $\Omega(0) < 2U_2(0)/h_2(0)$. We also note that (6.16) depends on $\Omega(0)$ differently, depending on the choice of reference pressure. Here, we have taken the reference pressure as $p|_{r=h_2} = P(0) = 0$, which is consistent with [38].

6.4 Comparison with a k-ε model

In this section we compare results from our simple swirl model with those from a steady k-ε model [55], using the open-source software package *OpenFoam* [104]. As examples, we first present comparisons of velocity and pressure profiles for co-axial flow in a straight pipe at swirl number $S_w = 0.67$. Then we compare predictions of the recirculation region that forms along the axis of an expanding pipe at the same swirl number. Finally, we compare calculated values for the pressure recovery C_p and the kinetic energy flux profile factor K over a range of swirl numbers.

As an example geometry for our first comparison, we choose a straight axisymmetric pipe with non-dimensional length $L/h_0 = 20$. The computations are performed using an axisymmetric geometry formed of 30000 cells, with 300 elements in the x direction and 100 elements in the r direction. A convergence check was performed and it was found that this mesh resolution was sufficient for capturing the details of the flow. The inflow velocity ratio is $U_2(0)/U_0 = 0.5$, the inflow core region radius is given by $h_1(0) = h_2(0) = h_0/2$, and the swirl number is $S_w = 0.67$. We use the free-stream boundary conditions for the turbulence variables at the inlet, which are $k = I^2 \times 3/2|\mathbf{u}|^2$ and $\varepsilon = 0.09k^{3/2}\ell$, with turbulence intensity $I = 5\%$ and mixing length $\ell = 0.1h_0$. See [55] for a discussion of the other boundary conditions for k and

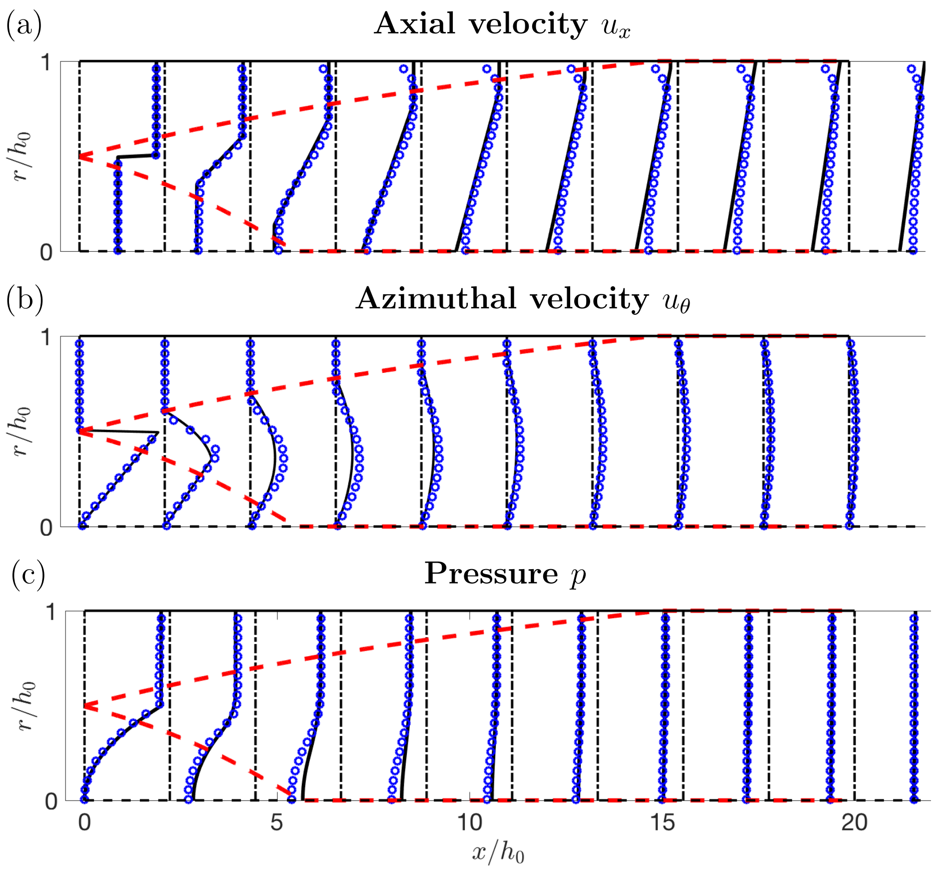

Figure 6.2: Comparison of our simple swirl model (solid black) with a k-ε model (blue circles) for a swirling slower core flow ($S_w = 0.67$, $U_2(0)/U_0 = 0.5$, $h_2(0)/h_0 = 0.5$) mixing with a non-swirling faster outer flow in a straight pipe. Axial profiles are shown at evenly spaced locations for the axial velocity u_x, azimuthal velocity u_θ and pressure p. The position of the shear layer, calculated using our simple swirl model, is overlaid in red dashed lines.

ε, such as on the walls and at the outflow. All of the turbulence parameters in the k-ε model are taken as their standard values, which are given in Chapter 2.

If we take typical length and velocity scales as h_0 and U_0, and we consider the viscosity of water $\nu = 10^{-6}\,\mathrm{m}^2/\mathrm{s}$, then the Reynolds number for the inlet flow is $Re = 10^6$. For comparison with our simple swirl model we estimate the friction factor with the Blasius relationship [11, 66] for flow in smooth pipes

$$f = 0.316Re^{-1/4}, \tag{6.17}$$

giving a value of $f = 0.01$. For the spreading parameter S_c, we find that $S_c = 0.11$ gives the best agreement, which is the same as the axisymmetric examples of the simple model in Chapter 4. We have also compared our simple swirl model to other geometries and at different Reynolds numbers, though we do not display the results here, and in all cases we find that $S_c = 0.11$ gives a good fit using standard turbulence parameter values. This is consistent with the simple model without swirl in Chapter 4.

In Figure 6.2 we compare profiles of axial velocity u_x, azimuthal velocity u_θ and pressure p at evenly spaced locations down the pipe. The position of the shear layer is indicated by red dashed lines. The comparison shows that there is good agreement between our model and the k-ε model. For example, the width of the shear layer, the maximum and minimum velocities and the parabolic swirl profile (and consequently the pressure) in the shear layer match closely. Since our model does not explicitly resolve the development of boundary layers, the comparison is less close near the pipe walls. However, pressure variations in the axial direction, which are controlled by f, agree well (see Figure 6.2 (c)), indicating that the effect of the boundary layers is captured by the simple swirl model using the friction factor parameterisation. Furthermore, we can see that the comparison is also less close downstream, near $r = 0$, since the simple swirl model does not satisfy the symmetry condition, $\partial u_x/\partial r = 0$ at $r = 0$, when the shear layer comes into contact with the pipe axis. In Section 6.6, we discuss two extensions to our model, where we incorporate a boundary layer and a symmetry layer (as in Chapter 4), resulting in an even closer comparison with CFD calculations.

Next, we compare predictions of the stagnation region which can form along the pipe axis. In Figure 6.3 an example of a stagnation region is shown for an expanding pipe with expansion angle 1.4° and non-dimensional length $L/h_0 = 20$. The swirl number is $S_w = 0.67$ and the inlet profile is given by $U_2(0)/U_0 = 0.5$, $h_1(0) = h_2(0) = h_0/2$. Velocity colour plots and streamlines are displayed for both the simple swirl model and the k-ε model, where in the case of the streamlines, the radial velocity is calculated from the axial velocity,

$$u_r = -\frac{1}{r}\int_0^r r\frac{\partial u_x}{\partial x}\,\mathrm{d}r. \tag{6.18}$$

The size and position of the stagnation region show close agreement, indicating that the simple swirl model has good predictive capabilities. Various studies [21, 30, 20, 72] relate this region to the phenomenon of vortex breakdown. In our model, it can be explained by Equations (6.3), (6.8) and (6.15). Due to (6.3), larger amounts of swirl induce a lower pressure along the pipe axis $r = 0$. As the shear layer spreads out due to (6.8), the azimuthal velocity profile (6.2) flattens, causing a rise in pressure along the pipe axis. Hence, from Bernoulli's equation (6.15), this rise in the pressure causes

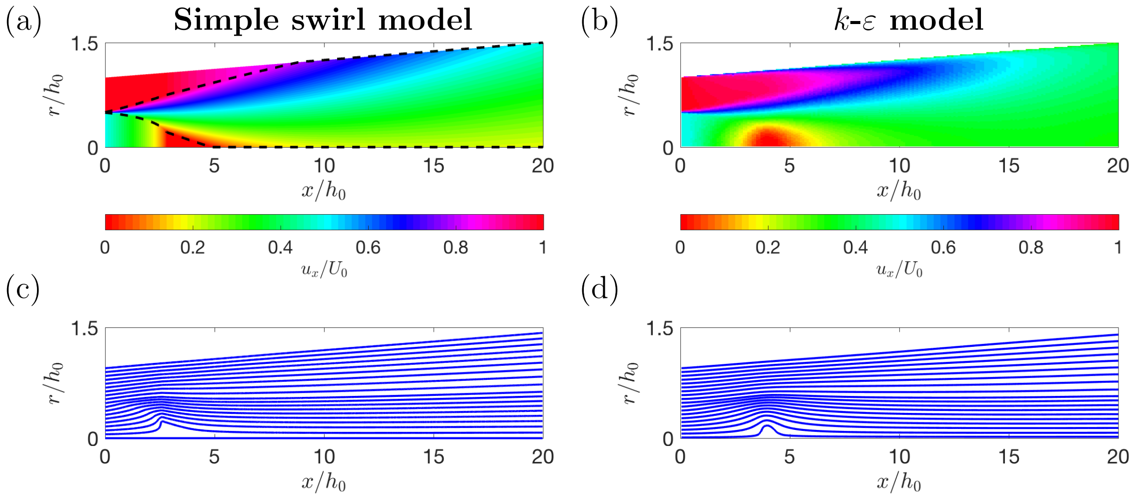

Figure 6.3: Comparison of the stagnation region in an expanding pipe with expansion angle 1.4°, displaying velocity colour plots and streamlines, calculated using our simple swirl model and a k-ε model. The swirl parameter is $S_w = 0.67$ and the inlet profile is given by $U_2(0)/U_0 = 0.5$, $h_2(0)/h_0 = 0.5$.

the speed of the core region to drop. If the effect is sufficiently pronounced then the core region will stagnate completely.

As a final comparison between our simple swirl model and CFD calculations, we make use of two commonly used measures of flow performance: the pressure recovery coefficient C_p and the kinetic energy flux profile factor K [12]. As described in Chapter 1, Section 1.2, the pressure recovery coefficient C_p is a measure of the amount of kinetic energy in a flow which is converted into static pressure. There are various ways to define C_p, but we use the so-called mass-averaged pressure recovery [32], which is defined as

$$C_p = \frac{\int_0^h r u_x p \, \mathrm{d}r|_{x=L} - \int_0^h r u_x p \, \mathrm{d}r|_{x=0}}{\int_0^h \frac{1}{2} \rho r u_x |\mathbf{u}|^2 \, \mathrm{d}r|_{x=0}}, \tag{6.19}$$

and takes values between $-\infty$ and 1, where $C_p = 1$ if all the inlet kinetic energy is converted into static pressure. Note that (6.19) is equal to the definition from Chapter 5 (5.2) except with a modified denominator to account for azimuthal kinetic energy.

The kinetic energy flux profile factor $K(x)$ is a measure of how non-uniform the axial velocity profile of a flow is at a given position x, defined as

$$K(x) = \frac{\frac{2}{h^2} \int_0^h r u_x^3 \, \mathrm{d}r}{\left(\frac{2}{h^2} \int_0^h r u_x \, \mathrm{d}r \right)^3}, \tag{6.20}$$

and takes values between 1 and ∞, where $K = 1$ corresponds to uniform flow.

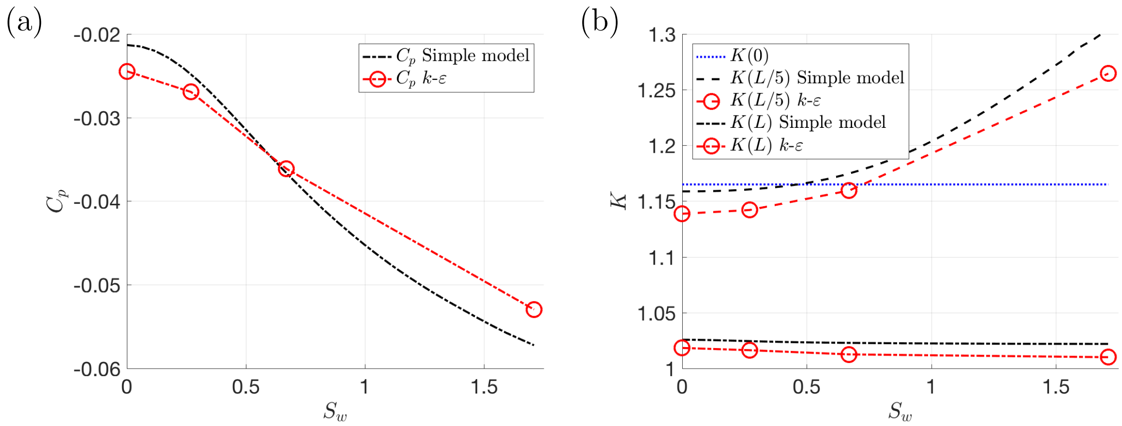

Figure 6.4: Comparison of the pressure recovery coefficient C_p and the kinetic energy flux profile factor K calculated using both our simple swirl model and a k-ε model, where we vary the swirl number S_w defined in (6.16). The kinetic energy flux profile factor is measured at $x = 0$, $L/5$ and L. In these calculations, we consider the same flow geometry as in Figure 6.2.

For the straight pipe example in Figure 6.2 we compare calculations of both C_p and K (measured at $x = 0$, $L/5$ and L) using our simple swirl model and the k-ε model for values of the swirl parameter between $S_w = 0$ and $S_w = 1.71$. The results are plotted in Figure 6.4. Overall, there is good agreement, and both models show that increased swirl has the effect of reducing pressure recovery, whilst making the flow more non-uniform in the near-field (at $x = L/5$), and then more uniform downstream (at $x = L$). Large swirl makes the flow more non-uniform in the near-field due to its distorting effect on the velocity profile [90]. However, it makes the flow more uniform downstream due to increased shear layer growth rates [38] and an overall enhanced mixing effect. These conclusions can be interpreted in the following way: Whilst swirl may produce a more uniform outflow, it distorts the flow in the near-field, resulting in greater energy dissipation, which manifests in a loss of pressure.

Although we do not display the results here, we have also compared our simple swirl model to other turbulence models, such as the k-ω SST model [67], and in other pipe geometries, and we find similar close agreement. Furthermore, in Appendix D we compare our model to some experimental data from other studies of an unconfined swirling jet. These comparisons give us confidence that our simple swirl model has good predictive capabilities, whilst being computationally cheap (e.g. using finite differences with 500 discretisation points, computation time is of the order of 1 s on a laptop computer). Therefore it is useful for examining the effect of swirl in a wide range of flow situations and exploring design spaces.

6.5 Model predictions

In this section we use our simple swirl model to analyse the effect of swirl on different flow situations. First, we look at the effect on the behaviour of the shear layer, determining the distance downstream at which the shear layer has reached across the entire pipe (this information is important for problems involving momentum transfer). Secondly, we establish which swirl numbers and pipe geometries result in a recirculation region forming along the pipe axis. Finally, we use our simple swirl model to optimise the shape of a diffuser for different swirl numbers, using both C_p and $K(L)$ as design objectives.

6.5.1 Shear layer behaviour

As discussed in Chapter 4, Section 4.4, a useful way to characterise the shear layer behaviour when the flow is confined in a pipe is the distance it takes for the shear layer to reach across the pipe. Since the shear layer has an inner and an outer edge, which are not necessarily symmetric, it is useful to consider where each of these edges reaches their respective boundaries. Thus, the outer edge of the shear layer must reach the pipe wall $r = h$ at some distance $x = L_1$, whereas the inner edge of the shear layer reaches the pipe axis $r = 0$ at $x = L_2$ (see Figure 6.5 (a)).

In Figure 6.5 we display colour plots of non-dimensional axial velocity u_x/U_0, and plots of the pressure recovery coefficient C_p, in both a straight pipe and a widening pipe (with expansion angle 1.4°), for different values of the swirl number. For this example we choose a pipe with non-dimensional length $L/h_0 = 20$ and an inflow which is defined by $U_2(0)/U_0 = 0.5$ and $h_1(0) = h_2(0) = h_0/2$. By observation, it is apparent that the shear layer growth rate $\mathrm{d}\delta/\mathrm{d}x$ varies with x, and increases on average with the swirl number. The corresponding values of L_1 and L_2 are plotted in Figure 6.6 (a). We can clearly see that for both the straight pipe and the widening pipe, L_1 and L_2 decrease as the swirl number increases, confirming that shear layer growth rates are enhanced by swirl. We can also see that the values of L_1 and L_2 are smaller for the widening case, indicating that pipe expansion is another mechanism for enhanced shear layer growth rates.

6.5.2 Stagnation region

As is discussed by Lee et al. [57], flows with large swirl numbers have the tendency to form a region of slowly moving recirculation. Here, we use our simple swirl model

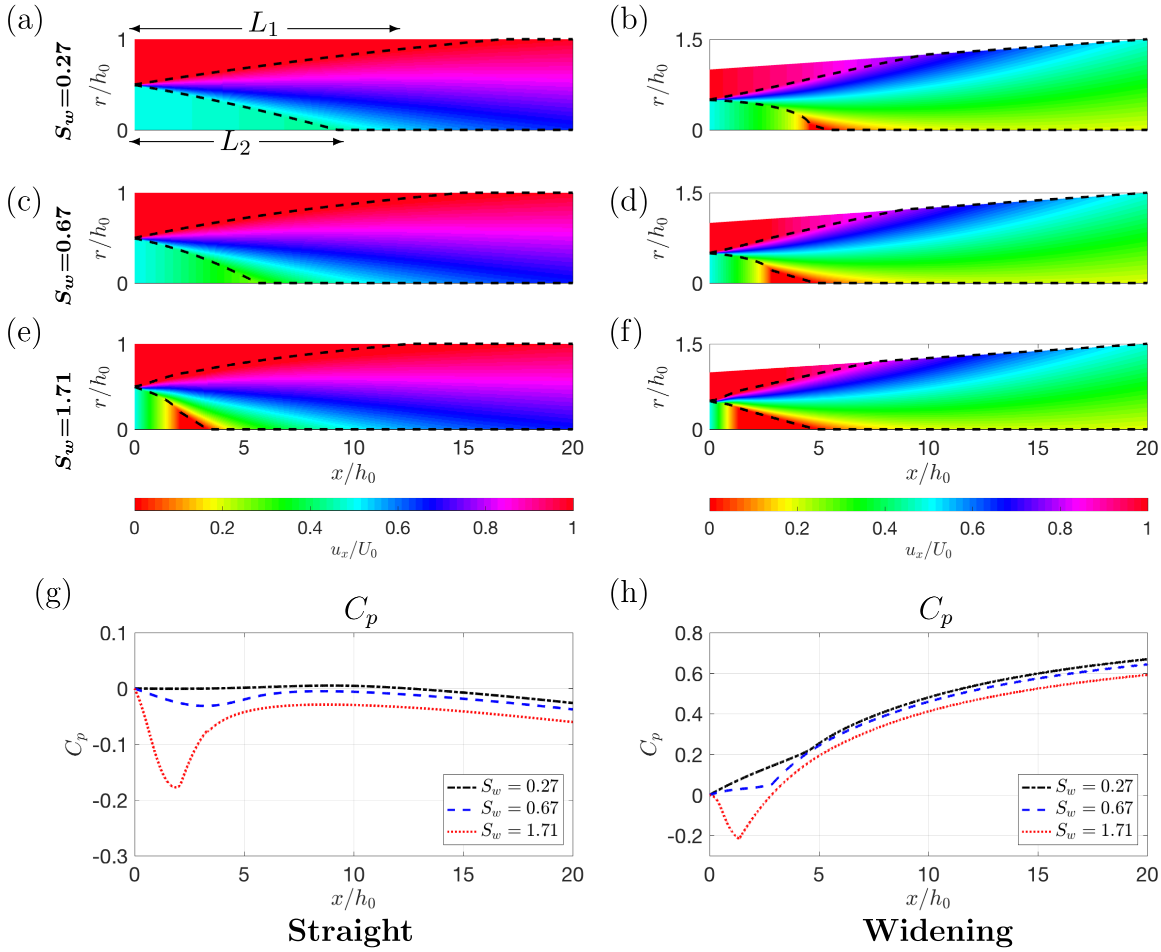

Figure 6.5: The effect of increasing the swirl number S_w between 0.27 and 1.71 on the axial velocity u_x in the case of a straight pipe (a, c, e, g) and a widening pipe (b, d, f, h). The position of the shear layer is indicated in dashed black lines. Pressure recovery C_p, given by (6.19), is plotted as a function of x/h_0 for each case. The distances, L_1 and L_2, at which the annular and core regions are completely entrained by the shear layer, respectively, are illustrated in (a). The inlet profile is given by $U_2(0)/U_0 = 0.5$, $h_2(0)/h_0 = 0.5$.

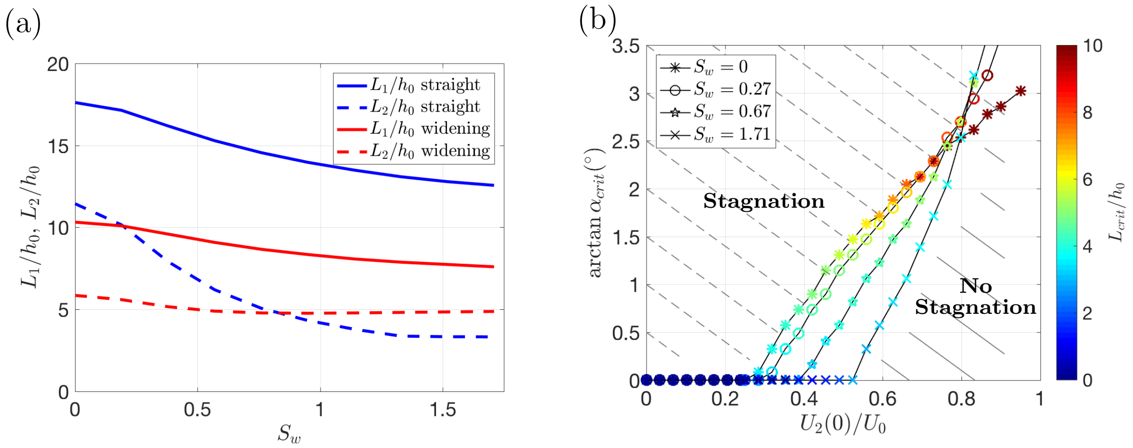

Figure 6.6: Effect of swirl on flow development properties. (a) L_1/h_0 and L_2/h_0 are the non-dimensional distances downstream at which the faster annular and slower core regions are completely entrained by the shear layer (see Figure 6.5 (a)). The inflow for this example is defined by $U_2(0)/U_0 = 0.5$ and $h_2(0)/h_0 = 0.5$. (b) The minimum diffuser angle ($\arctan \alpha_{crit}$) at which flow in a pipe with linearly expanding walls stagnates, for different values of the inlet velocity ratio $U_2(0)/U_0$ and swirl parameter S_w. The non-dimensional distance downstream at which stagnation first occurs L_{crit}/h_0 is indicated by the colour bar (which is saturated above $L_{crit}/h_0 > 10$).

to characterise the onset and size of this region by approximating it as a stagnant zone with zero velocity, as described earlier.

In the examples in Figure 6.5 we can see a stagnation region forming for swirl number $S_w = 1.71$ in the straight pipe case, and for all displayed values of S_w in the widening pipe case. In each case where the stagnation region forms, it then closes again some distance downstream. The results from our model indicate that the size of the stagnation region increases with S_w. Furthermore, it is evident that expanding pipes are more susceptible to stagnation than straight pipes. In the plots of pressure recovery C_p, we see a significant dip in pressure recovery where the flow stagnates. This is due to the fact that as the flow stagnates, the axial velocity profile becomes very non-uniform, resulting in an increase in kinetic energy flux. Therefore, C_p, which is a measure of how much inflow kinetic energy is converted to static pressure, must decrease [12].

In Figure 6.6 (b) we display a plot indicating the criteria for flow stagnation in a pipe of constant expansion angle, for different values of the swirl number. On the x-axis we vary the inlet velocity ratio $U_2(0)/U_0$, whilst on the y-axis we plot the expansion angle ($\arctan \alpha_{crit}$) above which stagnation occurs. In each case the radius of the core region is such that $h_1(0) = h_2(0) = h_0/2$. Regions of the parameter space where a stagnation region appears are indicated by dashed lines. Furthermore, the non-dimensional distance downstream at which the stagnation region forms, which we denote L_{crit}/h_0, is indicated by the colour of the data points that demarcate the boundary between stagnation and no-stagnation. We can see that the flow is less susceptible to stagnation for velocity ratios closer to 1, since the critical expansion angle ($\arctan \alpha_{crit}$) for which stagnation occurs is larger, and the critical distance L_{crit}/h_0 is also larger.

The effect of increasing the swirl number is interesting and possibly counter-intuitive. For velocity ratios less than around $U_2(0)/U_0 \approx 0.7$, increasing S_w causes a reduction in the critical expansion angle, thereby increasing the range of parameter values for which stagnation occurs. This is expected and consistent with the findings of Lee et al. [57]. However, an unexpected result is that for velocity ratios close to 1, increasing S_w reduces the range of parameter values for which stagnation occurs.

6.5.3 Diffuser shape optimisation

As a final investigation using our simple swirl model, we consider a shape optimisation problem in the presence of swirl. In order to illustrate the different effects of swirl, we consider optimising both C_p (6.19) and $K(L)$ (6.20). In the case of pressure recovery we seek to maximise C_p, whereas in the case of kinetic energy flux profile factor we seek to minimise $K(L)$. In Chapter 5 we used a similar approach to maximise pressure recovery in a flow diffuser (in the absence of swirl) by manipulating the channel shape. In that study, a low-dimensional parameterisation of the shape was proposed, which consists of piecewise linear sections. Here, we make use the same parameterisation, such that the diffuser shape takes the form

$$h(x) = \begin{cases} h_0 : & 0 < x < x_1, \\ h_0 + \alpha\,(x - x_1) : & x_1 < x < x_2, \\ h_L : & x_2 < x < L, \end{cases} \tag{6.21}$$

where x_1, x_2 are the shape division points, L is the diffuser length, h_0, h_L are the inlet and outlet radii, and $\alpha = (h_L - h_0)/(x_2 - x_1)$ is the expansion angle. We consider h_0, h_L, and L fixed, whilst we consider x_1 and x_2 as decision variables. For this class of shapes, we use our model to calculate both C_p (6.19) and $K(L)$ (6.20) for all possible values of x_1 and x_2. The question of interest here is to what extent the addition of swirl to the inlet flow is beneficial for achieving mixing and pressure recovery within such a diffuser. In each case, we choose a pipe which has non-dimensional length $L/h_0 = 30$ and expansion ratio $h_L/h_0 = 1.5$. The inflow is defined by $U_2(0)/U_0 = 0.5$

and $h_1(0) = h_2(0) = h_0/2$. We exclude values of x_1 and x_2 which produce a pipe shape with an expansion angle $\alpha > \tan 3.5°$ because it is expected that boundary layer separation can occur in such situations (see Chapter 2), which is not captured by our model. Hence, the plots are only shown in a triangular region. Note that the diffusers we consider here are representative of the mixer/diffuser section in Venturi-enhanced hydropower, since the inflow is non-uniform.

In Figure 6.7 (a, b, d, e) we display contour plots of pressure recovery C_p as a function of x_1 and x_2, for different values of the swirl parameter $S_w = 0$, 0.27, 0.67, 1.71. For each value of S_w, we illustrate the optimum point with a black asterisk, and in Table 6.1 we display a table of the optimum points. As swirl increases, the optimum point changes slightly, with x_1 increasing and x_2 decreasing. This indicates that diffusers with swirling core flows should be designed with a longer initial straight section and a shorter expanding section (with a wider expansion angle) than for non-swirling flows. This is a surprising result, since our original motivation for the addition of swirl was to enhance mixing so that the initial straight section need not be so long. Whilst swirl does increase shear layer growth rates, it creates a more non-uniform flow in the near-field, as seen in Figure 6.4 (b). Therefore, a longer initial straight section is required to allow the flow to become more uniform before expanding, since expansion tends to accentuate non-uniform flows, resulting in poor performance (as discussed in Chapter 5).

In addition we note that the value of C_p at the optimum point decreases with S_w (see Table 6.1), suggesting that a swirling core is always detrimental to pressure recovery, which is consistent with the results from Figure 6.4 (a). We have also calculated C_p for other values of S_w and the maximum value indeed occurs at $S_w = 0$ (see Figure 6.7 (c)). Therefore, whilst swirl may improve pressure recovery when the flow is uniform, by reducing boundary layer separation [34, 46], it has the opposite effect on diffuser performance for non-uniform flow. It should be noted that our simple swirl model does not account for boundary layer separation and, therefore, it cannot capture the positive effect of swirl on diffuser performance that is reported in the literature. However, since we restrict our attention to diffusers with small expansion angles, $\alpha < \tan 3.5°$, there is little risk of boundary layer separation [12].

Similarly, in (f, g, i, j) we display the corresponding contour plots of $K(L)$ as a function of x_1 and x_2 for different values of S_w. In (f) we display the minimum value of $K(L)$ for each value of S_w, and a table of the optimum points is given in Table 6.1. We find that the optimum shape is independent of swirl, having no initial straight section ($x_1 = 0$) and a very short widening section (with a large expansion

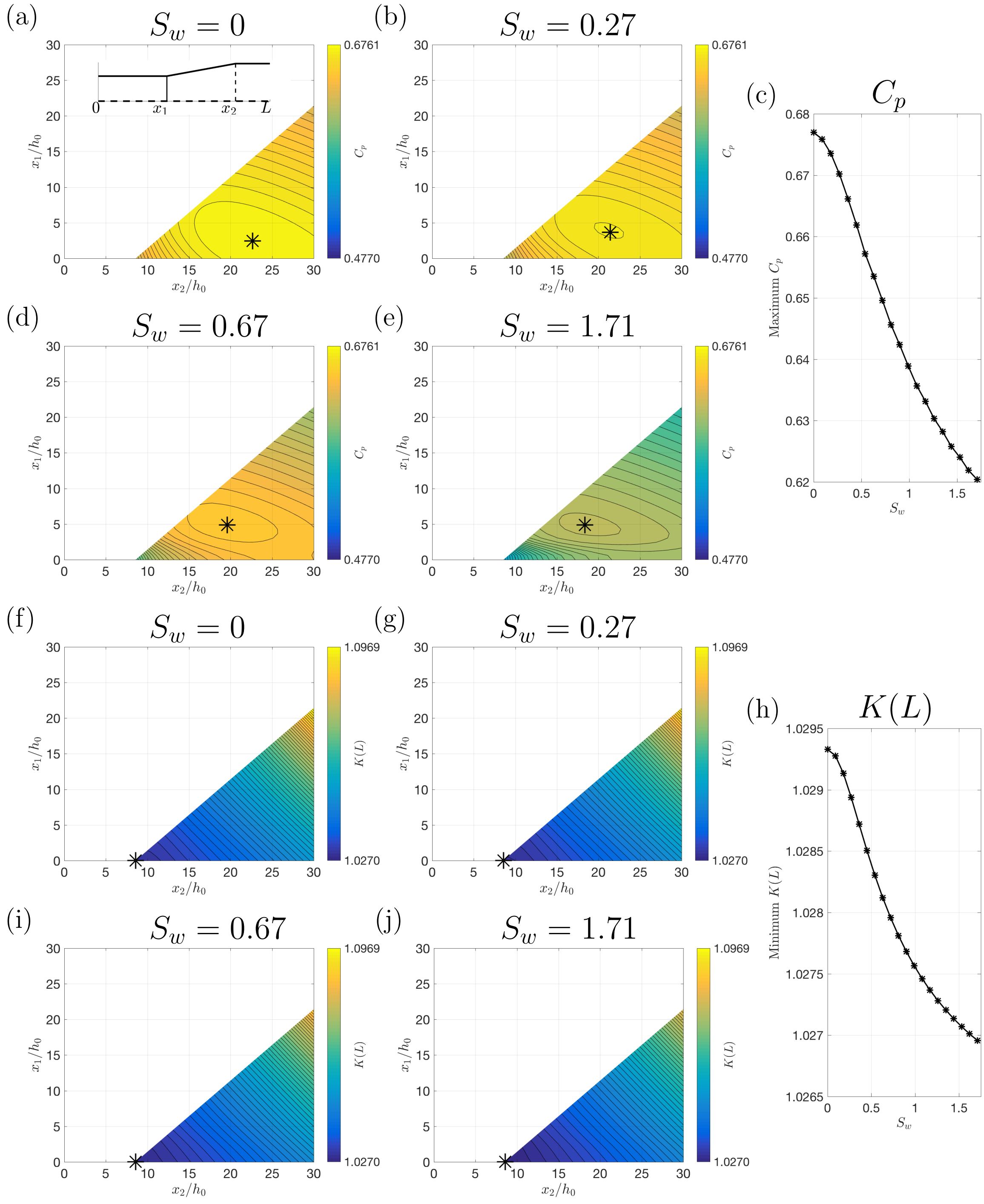

Figure 6.7: (a, b, d, e) Contour plots of pressure recovery coefficient C_p (6.19) for all permissible values of x_1 and x_2, a low-dimensional parameterisation of a diffuser shape which is divided into two straight sections separated by a widening section. Four different swirl number values are used and each contour plot has the same colour scale. Optimal shapes are indicated with a black asterisk. The optimum C_p values for these and other swirl numbers are displayed in (c). (f, g, i, j) Corresponding contour plots for the outlet kinetic energy flux profile factor $K(L)$ (6.20), where the optimum values are displayed in (h). In all cases the inlet profile is given by $U_2(0)/U_0 = 0.5$, $h_2(0)/h_0 = 0.5$.

S_w	x_1	x_2	C_p	x_1	x_2	$K(L)$
0	2.4490	22.6531	0.6761	0	8.5714	1.0293
0.27	3.6735	21.4286	0.6695	0	8.5714	1.0289
0.67	4.8980	19.5918	0.6511	0	8.5714	1.0280
1.71	4.8980	18.3673	0.6196	0	8.5714	1.0270

Table 6.1: List of optimum shape configurations for different swirl numbers. The left hand table corresponds to the maximisation of the pressure recovery C_p, whereas the right hand table corresponds to the minimisation of the outlet kinetic energy flux profile factor $K(L)$.

angle). Although we do not display the results here, we have also calculated $K(L)$ for each value of x_1 and x_2 using the k-ε model, and we find a similar optimum shape. From Table 6.1, we see that as S_w increases the minimum value of $K(L)$ decreases, indicating that swirl enables the optimal shape to produce a more uniform outflow, which is consistent with the results from Figure 6.4 (b). These results support our conclusions from Section 6.4 that whilst swirl makes the outflow more uniform, it produces greater pressure losses in doing so.

6.6 Inclusion of a boundary layer and a symmetry layer

We have already compared our simple swirl model to a k-ε model in Section 6.4 and we found that there was close agreement. However, the agreement was less close near the pipe walls, due to the fact that our model does not account for boundary layer development. Furthermore, the velocity profile given by (6.1) does not satisfy the symmetry condition $\partial u_x/\partial r = 0$ at $r = 0$ when the core region is entrained by the shear layer ($h_2 = 0$). Therefore, in this section we apply the two extensions from Chapter 4, Section 4.7 to our model, which address these discrepancies. These extensions, although they are not necessary to draw the conclusions we have made previously, are especially useful for more detailed predictions of the effect of swirl. By including these extensions we introduce several new variables, which we model using integrated conservation of axial and angular momentum.

Following Chapter 4, Section 4.7, we incorporate a turbulent boundary layer of width $h_b(x)$ into our model using a 1/7 power law velocity profile, given by (4.17) with y replaced by r, such that

$$u_x = U\left(\frac{h-r}{h_b}\right)^{1/7}, \tag{6.22}$$

within the boundary layer $h - h_b < r < h$. The width of the boundary layer h_b is determined by Equation (4.22), which is

$$\rho \frac{\mathrm{d}}{\mathrm{d}x} \int_{h-h_b}^{h} r u_x^2 \,\mathrm{d}r - \rho U_1 \frac{\mathrm{d}}{\mathrm{d}x} \int_{h-h_b}^{h} r u_x \,\mathrm{d}r = -\frac{1}{2}\left(h^2 - (h-h_b)^2\right) \frac{\mathrm{d}p}{\mathrm{d}x} + h\tau_{h_r}. \quad (6.23)$$

This derives from conservation of axial momentum, integrated across the boundary layer width, as described in Chapter 2. Unlike the model in Chapter 4, here we must account for situations where the boundary layer comes into contact with swirling flow. This occurs when the shear layer meets the edge of the boundary layer (i.e. $h_1 = 0$). Therefore, in such situations we propose that there will be an additional swirl boundary layer of a similar form to (6.22). In order to calculate an analytical expression for the pressure in the boundary layer from (6.3), we choose a $1/2$ exponent, instead of a $1/7$ exponent, for the boundary layer profile. Therefore, if we denote the azimuthal velocity at the edge of the boundary layer $U_\theta(x)$, then the the azimuthal velocity within the boundary layer takes the form

$$u_\theta = U_\theta \left(\frac{h-r}{h_b}\right)^{1/2}. \quad (6.24)$$

Choosing a different exponent for the profile (6.24) is an ad hoc approach, but we do not think this has a significant effect on the solution.

The azimuthal velocity at the edge of the boundary layer $U_\theta(x)$ is zero until the boundary layer comes into contact with the swirling shear layer (i.e. $h_1 = 0$). Downstream of this point the azimuthal velocities at the edges of the boundary layer and the shear layer are equal to each other and given by $U_\theta(x)$. The value of $U_\theta(x)$ is then determined by conservation of angular momentum integrated across the boundary layer

$$\rho \frac{\mathrm{d}}{\mathrm{d}x} \int_{h-h_b}^{h} r^2 u_\theta u_x \,\mathrm{d}r = \rho U_{\theta_1}(h-h_b) \frac{\mathrm{d}}{\mathrm{d}x} \int_{h-h_b}^{h} r u_x \,\mathrm{d}r + h^2\tau_{h_\theta} - (h-h_b)^2 \tau_{(h-h_b)_\theta}. \quad (6.25)$$

Equation (6.25) can be derived by following Chapter 2, Section 2.4.3, with $a = h - h_b$ and $b = h$. In this case, we model both the radial and azimuthal wall stress terms in (6.10) and (6.25) using (2.109) and (2.110) with $U_x = U_1$, such that

$$h\tau_{h_r} = -\frac{1}{8} f \rho U_1 h \sqrt{U_1^2 + U_\theta^2}, \quad (6.26)$$

$$h^2\tau_{h_\theta} = -\frac{1}{8} f \rho U_\theta h^2 \sqrt{U_1^2 + U_\theta^2}. \quad (6.27)$$

Furthermore, since U_θ and τ_{h_θ} are not necessarily zero, the right hand side of (6.11) must include a stress term ($h^2\tau_{h_\theta}$), just as in (2.108). Note that in the original simple swirl model this term was ignored, but here we keep it to make the extended model more generalised (i.e. to account for situations where (6.27) is not small).

The azimuthal shear stress at the edge of the boundary layer $\tau_{(h-h_b)_\theta}$ is treated with a Prandtl mixing length model [87], similarly to Chapter 2, Section 2.4.1.1, using a mixing length proportional to the shear layer width, $\ell = C\delta$, and approximating the velocity gradient $\partial u_x/\partial r \approx (U_1 - U_2)/\delta$, such that ν_t is given by (2.122), which is

$$\nu_t = C^2 \delta (U_1 - U_2). \tag{6.28}$$

The constant C is related to the turbulent Reynolds number, and must be determined by fitting to experimental data or CFD calculations. Thus, assuming $\nu \ll \nu_t$, we have

$$\tau_{(h-h_b)_\theta} = \left[\rho \left(\nu + \nu_t \right) \left(\frac{\partial u_\theta}{\partial r} - \frac{u_\theta}{r} \right) \right]_{r=h-h_b} \approx \rho C^2 (U_1 - U_2) \left(\kappa \delta^2 - h_2 \Omega \right). \tag{6.29}$$

Next we incorporate a turbulent symmetry layer into our model. If the core region is entrained by the shear layer, such that $h_2 = 0$, then we introduce a layer along the pipe axis of width $h_s(x)$, which satisfies the symmetry condition $\partial u_x/\partial r = 0$ at $r = 0$. Following Chapter 4, Section 4.7, we use a quadratic velocity profile within the symmetry layer, given by (4.19) with y replaced by r, such that

$$u_x = U_2 + \frac{(U_1 - U_2)}{2 h_s \delta} \left(r^2 - h_s^2 \right), \tag{6.30}$$

within the symmetry layer. The width of the symmetry layer h_s is governed by Equation (4.23), which is

$$\rho \frac{\mathrm{d}}{\mathrm{d}x} \int_0^{h_s} r u_x^2 \, \mathrm{d}r - \rho U_2 \frac{\mathrm{d}}{\mathrm{d}x} \int_0^{h_s} r u_x \, \mathrm{d}r = -\frac{1}{2} h_s^2 \frac{\mathrm{d}p}{\mathrm{d}x} + h_s \tau_{(h_s)_r}. \tag{6.31}$$

This derives from conservation of axial momentum, integrated across the width of the layer, as described in Chapter 2. The radial stress at the edge of the symmetry layer $\tau_{(h_s)_r}$ is modelled using the same Prandtl mixing length argument as above, and is therefore given by (4.21), which is

$$\tau_{(h_s)_r} = \rho C^2 (U_1 - U_2)^2. \tag{6.32}$$

To summarise, we have incorporated two additional layers into our simple swirl model: a boundary layer near the pipe wall satisfying the no-slip condition, and a symmetry layer near the pipe axis satisfying the symmetry condition. We have introduced three new variables h_b, h_s, and U_θ, which are all functions of x. These variables are governed by (6.23), (6.25) and (6.31), in which we have used Prandtl

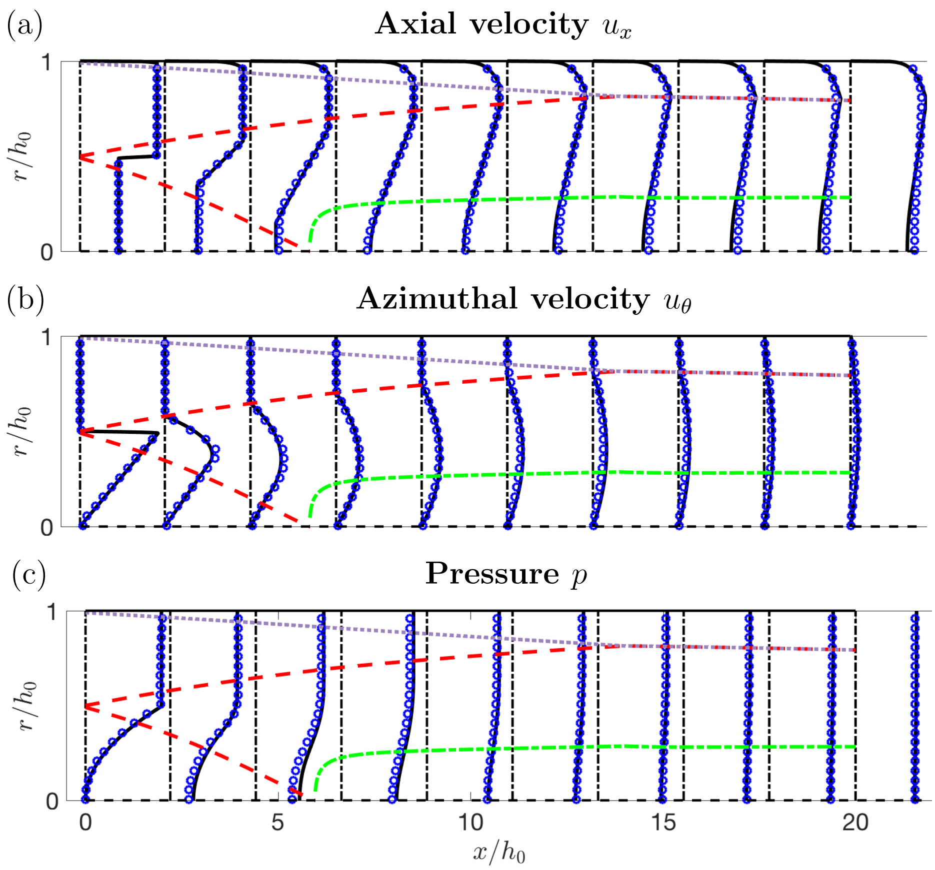

Figure 6.8: Comparison of our extended swirl model (solid black) with a k-ε model (blue circles) using the same parameter values as in Figure 6.2. Axial profiles are shown at evenly spaced locations for the axial velocity u_x, azimuthal velocity u_θ and pressure p. The position of the shear layer, the boundary layer and the symmetry layer are overlaid in red dashed, purple dotted and green dash-dotted lines, respectively. The swirl number is $S_w = 0.67$ and the inlet profile is given by $U_2(0)/U_0 = 0.5$, $h_2(0)/h_0 = 0.5$.

mixing length arguments to model internal shear stress terms and a friction factor parameterisation to model the wall stress terms.

A comparison of our extended swirl model to a k-ε model is displayed in Figure 6.8, in which we plot profiles of axial velocity u_x, azimuthal velocity u_θ and pressure p at evenly spaced locations down a straight cylindrical pipe. For this example we use the same k-ε calculations as in Figure 6.2. For comparison with our extended swirl model we use the same values for the spreading parameter $S_c = 0.11$ and the friction factor $f = 0.01$ as in Figure 6.2. For the mixing length constant C, we find that $C = 0.13$ gives the best fit with the data. We can see that the comparison here is much closer than in Figure 6.2. In particular, the development of the boundary layer near the pipe wall (indicated by a purple dotted line) shows good agreement. The symmetry layer near the pipe axis (indicated by a green dot-dashed line) is also captured well. In fact, the average discrepancy between the extended swirl model and the k-ε model is 6%, compared to 11% for the original simple swirl model in Figure 6.2.

The extended model has approximately the same computational cost[4] as the original swirl model, though it contains more variables and equations, and it is perhaps more difficult to implement. Therefore, the original model serves as a convenient tool for benchmark predictions, whilst the extended model is appropriate for more detailed and accurate calculations of flow development which take longer to implement.

6.7 Discussion and conclusions

We have developed a simple model for confined co-axial flow with a core swirling region, which shows good agreement with CFD, whilst being computationally cheap. The model depends on two parameters, the friction factor f, which was well approximated with the Blasius relationship (6.17), and the spreading parameter S_c, which was fitted to CFD calculations, giving a value $S_c = 0.11$, which is the same as for the axisymmetric examples of the simple model in Chapter 4.

The simple swirl model is useful for predicting essential aspects of the flow behaviour, such as the shear layer growth and pressure recovery. We showed that, whilst adding swirl to the core region is a good mechanism for increasing shear layer growth rates, it also increases pressure losses. The original motivation for this study was to

[4]The computational cost of the extended model is slightly larger than that of the original simple swirl model due to having three extra variables. However, the computational cost for each of the models is of the order of 1 second on a laptop computer. Therefore, we do not consider the difference in cost significant.

investigate the use of swirl to enhance mixing between the secondary and primary flows in Venturi-enhanced hydropower. Our results indicate that the increased shear layer growth rates would enhance mixing between the flows, but the increased pressure losses would have a detrimental effect on pressure recovery, and hence the amount of generated power. Therefore, swirl is not appropriate for Venturi-enhanced hydropower and should be reduced/avoided as much as possible. However, should there be some swirl present in the flow, we showed how this affects the optimum diffuser shape. We also used our model to characterise the criteria for which a recirculation region appears along the pipe axis, so that it may be avoided.

We showed that an extended version of the model, which includes a boundary layer at the pipe wall and a symmetry layer at the pipe axis, gives even better agreement with CFD calculations than the simple swirl model. Whilst unnecessary for the conclusions made using the simple swirl model, the extended swirl model provides more detailed and realistic flow predictions.

For future work, the effect of different swirl distributions for the core flow, such as a q vortex [38], could be investigated. Furthermore, this work could be extended to situations in which the outer annular flow is also rotating, not necessarily in the same direction as the core flow. In such cases (where the annular region has swirl) we would need to use more complex profiles for the azimuthal velocity than (6.2). In the same way we introduced the variables $\Omega(x)$ and $\kappa(x)$ to describe the swirl in the core and shear layer regions in (6.2), we would need to introduce more variables to describe the swirl in the annular region. Similarly to before, we could describe the evolution of these variables using equations which derive from integrating conservation of angular momentum. When extending our simple swirl model to account for such situations, Bernoulli's equation (6.14) becomes difficult to impose along streamlines in the annular region, since pressure varies radially. One possible approach to deal with this difficulty is by integrating Bernoulli's equation across the annular region, and imposing this integrated equation instead, which does not vary radially. It would be interesting to see whether such an approach would yield realistic flow behaviour.

Chapter 7

A case study of Venturi-enhanced hydropower

7.1 Introduction

In the introduction to this thesis, we explained the operating principles of Venturi-enhanced hydropower. We discussed how the hydrodynamic efficiency depends on the mixing together of the primary and secondary flows within a closed channel. Chapters 3 - 6 focused on modelling and optimising the flow in the mixer/diffuser section, which is between where the primary and secondary flows first meet and the diffuser outflow (see Figure 1.2). However, outside the mixer/diffuser section, there is more to the story which we have not yet discussed. Therefore, in this chapter we extend our modelling and optimisation work to account for the whole of the Venturi-enhanced hydropower, from the river intake upstream to the river outflow downstream, and we reformulate the optimisation problem to account for the balance between the generated power and the turbine cost.

In the optimisation problem in Chapter 5 we set the pressure recovery as the optimisation objective. In reality, the objective is a balance between generated power and cost. The principle of Venturi-enhanced hydropower is to generate cost-effective low head hydropower by exploiting the Venturi effect. In Chapter 1 we discussed how, for a given head drop across a river, the maximum possible generated power is obtained when the turbine (secondary flow) receives 100% of the total flow, such that there is no primary flow and no Venturi. However, this is also the most expensive configuration. By passing only a fraction $\mathcal{F}$ of the flow through the turbine, the cost of the turbine is reduced (because it is smaller), at the expense of losing some of the power (see Section 1.1.2). Therefore, a more complete optimisation must include a model for the power generated and the cost of the turbine.

The power available to the Venturi-enhanced hydropower is equal to the total flow rate through it Q_{total} multiplied by the pressure drop[1] across it Δp_{total}. It is assumed that the pressure drop across the Venturi Δp_{total} is fixed and determined by the river. The total flow rate Q_{total} is determined by the overall energy loss associated with the Venturi geometry (predominantly wall drag and mixing losses). By scaling the geometry, it is possible to achieve a desired flow rate. To calculate the appropriate scaling, which we denote $\mathcal{L}$, we require a model for the relationship between Q_{total} and Δp_{total} of the form

$$Q_{total} = q(\Delta p_{total}, \mathcal{L}), \tag{7.1}$$

where q is some function that needs to be determined. Since the flow rate through the turbine is $Q_s = \mathcal{F} \times Q_{total}$, the generated power also depends on the relationship between Q_{total} and Δp_{total}. Therefore, we begin this chapter by modelling Equation (7.1), accounting for the whole of the Venturi-enhanced hydropower, which includes the river intake upstream, the converger, the mixer/diffuser, and the river outflow downstream. The entire configuration, from the inflow to the outflow, is illustrated in Figure 7.1, where we define the stations 0 - 4 which are useful for modelling terminology.

After deriving the complete model, we then formulate a multi-objective optimisation problem which balances maximising power with minimising cost. The power optimisation problem is formulated by calculating the hydrodynamic efficiency η (1.3). The cost minimisation problem is formulated by making an argument for the relative size of a Venturi-enhanced hydropower turbine compared to a conventional hydropower turbine. Following this, we investigate a case study of a river which provides a flow rate of $Q_{total} = 4\,\mathrm{m}^3\,\mathrm{s}^{-1}$ to the Venturi-enhanced hydropower[2] and a head drop of $\Delta p_{total} = 3\,\mathrm{m}$. We use the simple model of Chapter 4 (together with (7.1)) to describe the flow, and the techniques of Chapter 5 to perform the optimisation.

The main conclusion from Chapter 6 was that introducing swirl to the secondary flow would have a detrimental effect on pressure recovery, and hence generated power. Therefore, we do not include swirl in the majority of the analysis of this chapter, since it should be removed/avoided as much as possible. However, as discussed in Chapter 6, it is quite likely that a small amount of swirl may be present in the secondary flow

[1]Note that Δp_{total} here refers to the overall drop in static pressure, rather than the drop in 'total pressure', which is sometimes used in the literature to refer to the sum of the static pressure and the dynamic pressure (kinetic energy per unit volume).

[2]Typically, the total flow rate through the Venturi Q_{total} will be less than the total flow rate of the river. This is because environmental regulations require rivers to have a minimum natural flow rate that bypasses the turbine.

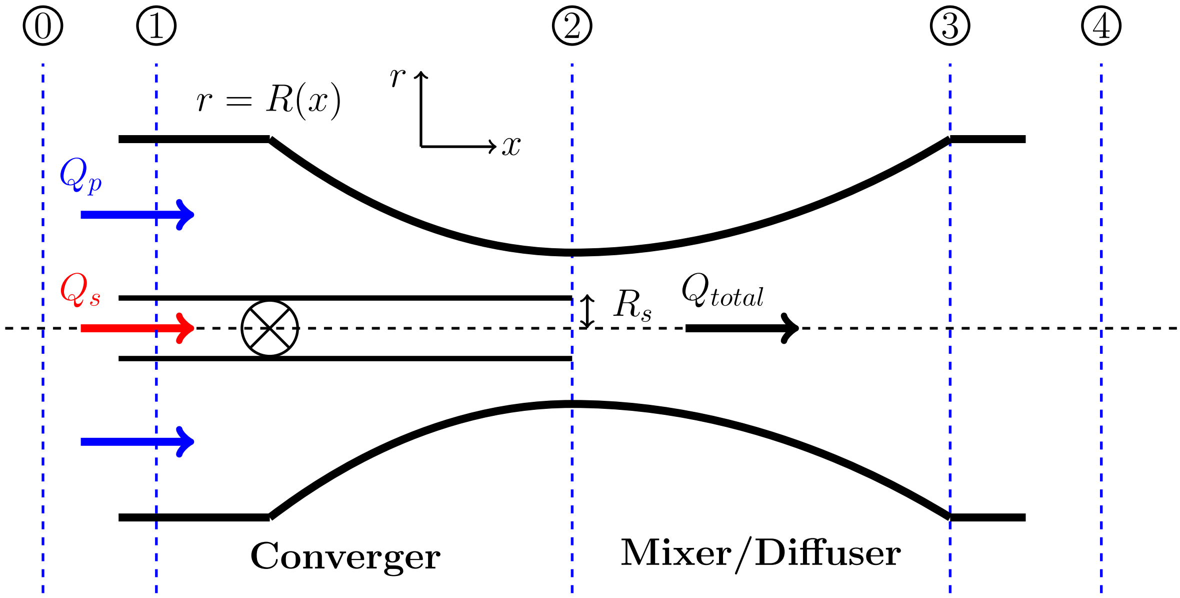

Figure 7.1: Schematic diagram showing a cylindrical cross-section of Venturi-enhanced hydropower, which is composed of a converger and a mixer/diffuser. Primary and secondary flows are indicated by blue and red arrows, respectively. The station numbers 0 - 4 are discussed in the main text.

due to the turbine. Therefore, we use the results from Chapter 6 to briefly discuss the possible effects that this swirl may have on our optimisation problem.

7.2 A complete model for Venturi-enhanced hydropower

In Figure 7.1 we illustrate the stages of Venturi-enhanced hydropower with stations 0 - 4, where the number ordering increases with the direction of the flow. The work in Chapters 3 - 6 focused on the flow between stations 2 and 3, in the mixer/diffuser. Therefore, in order to create a model for the whole of the Venturi-enhanced hydropower, we only need to extend our model to the sections between stations 0 - 2 and 3 - 4. We do so by moving through the stations, one by one, and applying Bernoulli's equation and conservation of mass and momentum arguments. Throughout this Chapter we use the notation R for the channel shape, instead of h, as used previously in this thesis. This is to avoid confusion between subscripts $1, 2, \ldots$ and the variables h_1 and h_2 which were used in Chapters 4 - 6.

Firstly, we consider the interval between stations 0 and 1. The flow upstream at station 0 is assumed to be static (like upstream of a weir) with hydrostatic head $H_0 = p_0/\rho g$. As the flow enters the geometry, it is divided into two streams: a primary flow with flow rate Q_p and a secondary flow with flow rate Q_s. We assume that both flows lose no energy between these stations so that we can apply Bernoulli's equation to each of them

$$p_0 = p_{p_1} + \frac{1}{2}\rho U_{p_1}^2, \tag{7.2}$$

$$p_0 = p_{s_1} + \frac{1}{2}\rho U_{s_1}^2, \tag{7.3}$$

where we assume that both the primary and secondary flow speeds at station 1, U_{p_1} and U_{s_1}, are uniform across their respective cross-sections (subscript numbering is used to indicate the stations). Moving from station 1 to 2, the secondary flow does not change cross-sectional area, whereas the primary flow contracts. We assume that, between station 1 and 2, each of these flows maintains uniform velocity across their respective cross-sections, such that in the case of the secondary flow $U_{s_1} = U_{s_2} = U_s$. In addition, we assume that some energy is lost in the converging section of the primary flow due to wall drag. This loss is represented with a loss coefficient K_c (which we calculate later) in Bernoulli's equation, such that

$$p_{p_1} + \frac{1}{2}\rho U_{p_1}^2 = p_2 + \frac{1}{2}\rho U_{p_2}^2(1 + K_c). \tag{7.4}$$

In the secondary flow, the turbine power P_V is related to the pressures at stations 1 and 2 according to

$$P_V = \left(p_{s_1} - p_{s_2} - \frac{1}{4}f\rho U_s^2 \frac{L_s}{R_s}\right) Q_s, \tag{7.5}$$

where we have parameterised the drag inside the secondary pipe using a friction factor f, and L_s, R_s are the length and radius of the secondary channel, respectively. At station 2, where the primary and secondary flows first meet, we make the key assumption that the pressure is uniform across both the primary and secondary flows,

$$p_{s_2} = p_{p_2} = p_2. \tag{7.6}$$

The motivation behind this assumption was discussed in Chapter 1. In Chapter 5 we defined the pressure recovery coefficient C_p for axisymmetric flow (5.2), which relates the pressure between stations 2 and 3 to the kinetic energy flux at station 2. As discussed in Chapters 4 and 5, we make the assumption that the pressure $p(x)$ is uniform across the diffuser cross-section between stations 2 and 3, whereas the velocity $u(x, r)$ is non-uniform. In this chapter we use the simple model from Chapter 4 to calculate the flow and pressure within the mixer/diffuser, for a given shape $R(x)$ and other parameters. Rearranging the definition (5.2), we find

$$p_3 = p_2 + C_p \frac{1}{2}\rho \frac{Q_p U_{p_2}^2 + Q_s U_s^2}{Q_{total}}, \tag{7.7}$$

which simplifies to

$$p_3 = p_2 + C_p \frac{1}{2}\rho U_{p_2}^2 \left(1 - (1-\beta^2)\mathcal{F}\right), \tag{7.8}$$

where we use the same notation as in Chapter 1 for the velocity ratio $\beta = U_s/U_{p_2}$ and the flow rate fraction $\mathcal{F} = Q_s/Q_{total}$. Finally, going from station 3 to 4 we note that, like the upstream flow, the downstream flow at station 4 is assumed to be static, with hydrostatic head $H_4 = p_4/\rho g$. We assume that none of the kinetic energy at station 3 is recovered to static pressure (i.e. it is all lost in the form of turbulent eddies), such that

$$p_3 = p_4. \tag{7.9}$$

Therefore, combining (7.2), (7.4), (7.8) and (7.9), we find an expression for the pressure drop $\Delta p_{total} = p_0 - p_4$ in terms of the primary flow speed at station 2 without loss of generality (we could choose the flow speed at any station) and non-dimensional parameters, such that

$$\Delta p_{total} = \frac{1}{2}\rho U_{p_2}^2 \left(1 + K_c - C_p \left(1 - \left(1-\beta^2\right)\mathcal{F}\right)\right). \tag{7.10}$$

We write (7.10) in terms of the total flow rate Q_{total} by noting that

$$Q_p = \pi(R_2^2 - R_s^2)U_{p_2} = Q_{total}(1-\mathcal{F}). \tag{7.11}$$

Rearranging (7.11), we get

$$\pi R_2^2 U_{p_2} = Q_{total}\left(1 + \mathcal{F}\left(\beta^{-1} - 1\right)\right). \tag{7.12}$$

Therefore, combining (7.10) and (7.12) we finally arrive at an expression relating the total flow rate to the pressure drop

$$Q_{total} = \sqrt{\frac{R_2^4 \Delta p_{total}}{\gamma\rho}}, \tag{7.13}$$

where we have introduced the non-dimensional number

$$\gamma = \left(1 + \mathcal{F}\left(\beta^{-1} - 1\right)\right)^2 \left(1 + K_c - C_p\left(1 - \left(1-\beta^2\right)\mathcal{F}\right)\right). \tag{7.14}$$

Equation (7.13) is of the same form as (7.1) with $\mathcal{L} = R_2$. Hence, we can design the geometry to take a given total flow rate Q_{total} at a given pressure drop Δp_{total} by choosing the length scale

$$R_2 = \left(\frac{\gamma\rho Q_{total}^2}{\Delta p_{total}}\right)^{1/4}. \tag{7.15}$$

It is useful to refer to other length scales in non-dimensional form, with reference to (7.15). In this way, by scaling R_2 appropriately, all other length scales are changed by the same factor (i.e. the aspect ratio is respected).

Before going any further, it is useful to discuss the different non-dimensional parameters in (7.13) ($\mathcal{F}$, β, K_c and C_p), noting which of them can be controlled, and how they can be calculated. The two parameters which cannot be controlled easily are K_c and C_p. The loss coefficient of the converger K_c is associated with wall drag, and is mostly determined by the shape of the converger and its surface roughness. For a given converger shape the value of K_c can be estimated by consulting experimental data [12] or creating a simple model, as we do in the next section. The pressure recovery coefficient of the mixer/diffuser C_p is a function of the channel shape as well as other parameters, such as β. The main focus of Chapter 5 was to study how C_p depends on the shape of the mixer/diffuser and the inflow conditions (which relate to β). For a given mixer/diffuser geometry and a given value of β, C_p can be estimated using the simple model of Chapter 4.

The two parameters which can be controlled easily are β and $\mathcal{F}$. The flow rate fraction $\mathcal{F}$ is controlled by the design of the turbine. The turbine is manufactured to yield a particular flow rate at a given pressure drop. In the case of Venturi-enhanced hydropower, once a geometry is chosen and scaled according to (7.15), the pressure and velocities at each stage are fixed. Then the turbine is designed to allow a flow rate $Q_s = \mathcal{F} \times Q_{total}$ across a pressure drop $p_{s_1} - p_{s_2}$. If the loss coefficient K_c and the pressure recovery coefficient C_p have been miscalculated, such that the scaling (7.15) does not result in a total flow rate Q_{total}, then the pressure drop across the turbine $p_{s_1} - p_{s_2}$ will also be affected. In such situations, the turbine will be operating 'off design point', at a different flow rate fraction than designed for. So long as this discrepancy is small, it is possible to return $\mathcal{F}$ to the desired value by manipulating the electrical load on the turbine. Hence, the flow rate fraction is only controllable if we have a fairly good estimate of K_c and C_p. Finally, the velocity ratio β is controllable by fixing the cross-sectional areas of the primary and secondary flows (for a given $\mathcal{F}$).

7.2.1 Converger losses

In (7.4) we modelled the energy loss in the converging section of the primary flow with a loss coefficient K_c. Here, we calculate this loss coefficient using a simple model for the primary flow in the annulus between stations 1 and 2. To derive this model we follow the cylindrical channel example from Chapter 2, Section 2.4.3, with $a = R_s$ and $b = R$. Therefore, the converger section is defined for $R_s < r < R$ and $0 < x < L_c$,

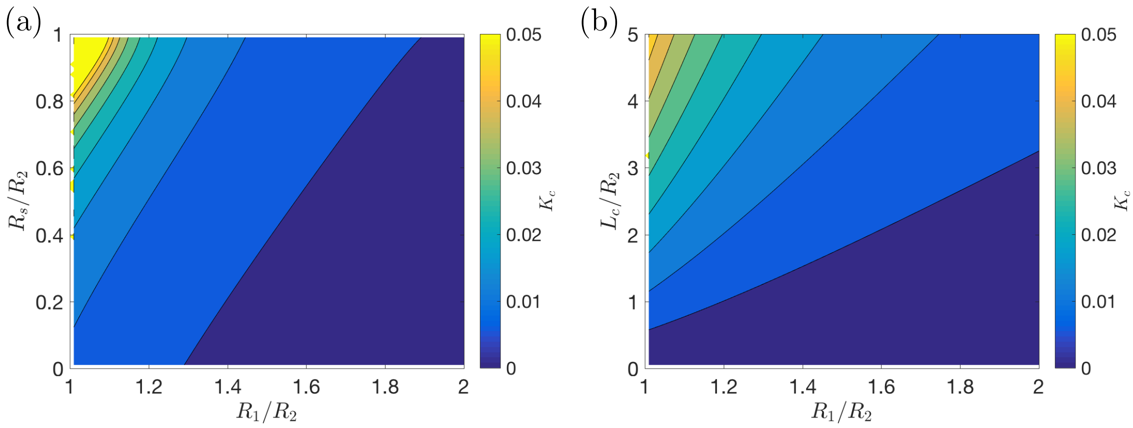

Figure 7.2: Plot of converger loss coefficient K_c given by (7.21). (a) K_c as function of R_1/R_2 and R_s/R_2 with $f = 0.01$ and $L_c/R_2 = 2$. (b) K_c as function of R_1/R_2 and L_c/R_2 with $f = 0.01$ and $R_s/R_2 = 0.5$.

where $x = 0$ corresponds to station 1 and $x = L_c$ corresponds to station 2 (note that the lengths of the converger and secondary tube, L_c and L_s, are not necessarily equal). We assume that the primary flow has uniform velocity $U_p(x)$ and uniform pressure $p_p(x)$ across the converger cross-section. The conservation of mass and momentum equations, (2.97) and (2.98), provide the governing equations for the flow

$$\frac{\mathrm{d}}{\mathrm{d}x}\left(U_p(R^2 - R_s^2)\right) = 0, \tag{7.16}$$

$$\rho\frac{\mathrm{d}}{\mathrm{d}x}\left(U_p^2(R^2 - R_s^2)\right) = -(R^2 - R_s^2)\frac{\mathrm{d}p_p}{\mathrm{d}x} - \frac{1}{4}f\rho U_p^2(R + R_s), \tag{7.17}$$

where U_p and p_p have the initial conditions

$$p_p(0) = p_{p_1}, \tag{7.18}$$

$$U_p(0) = U_{p_1}. \tag{7.19}$$

We can solve (7.16)-(7.19) for a given converger shape $R(x)$ with $R(0) = R_1$ and $R(L_c) = R_2$, and given values for R_s and f. The pressure at the end of the converger is $p_p(L_c) = p_{p_2}$. Hence, considering (7.2) and (7.4), the loss coefficient K_c is formulated as

$$K_c = \frac{p_{p_1} - p_{p_2}}{\frac{1}{2}\rho U_{p2}^2} - 1 + \left(\frac{U_{p_1}}{U_{p_2}}\right)^2. \tag{7.20}$$

Thus, integrating (7.16)-(7.19) we find

$$K_c = \frac{f}{2}(R_2^2 - R_s^2)^2 \int_0^{L_c} \frac{R_s + R(\hat{x})}{(R(\hat{x})^2 - R_s^2)^3}\, d\hat{x}. \tag{7.21}$$

Upon closer inspection of (7.21) we see that, in addition to the shape $R(x)$, K_c only depends on 4 non-dimensional parameters: R_1/R_2, R_s/R_2, L_c/R_2 and f. In Figure

7.2 we plot K_c as a function of R_1/R_2, R_s/R_2 and, L_c/R_2, where we take $f = 0.01$ (corresponding to a Reynolds number $Re = 10^6$ using the Blasius relationship [11, 66]) and we assume $R(x)$ is a linear function given by

$$R = R_1 + (R_2 - R_1)\frac{x}{L_c}. \tag{7.22}$$

From the colour scale in Figure 7.2 we can see that losses grow if R_1/R_2 or R_s/R_2 are close to 1. This is because the fluid is being squeezed through a small cross section with large drag. Likewise, losses grow if the channel length L_c/R_2 is large.

K_c is clearly minimised by choosing the smallest possible values of R_s/R_2 and L_c/R_2, whilst choosing the largest possible value of R_1/R_2. However, if we make R_s too small then there will be large drag losses in the secondary flow and, hence, less power (see Equation (7.5)). Additionally, we can't make R_1/R_2 too large due to practical constraints. If we make L_c/R_2 too small (for a given R_1/R_2) then the converger has a sharp contraction that can cause flow recirculation and further energy losses. For the duration of this chapter, we do not attempt to optimise the shape of the converger, since its contributions to energy loss are small (see Figure 7.2). Instead, we assume a linear converger shape (7.22) and we model the loss contribution with (7.21).

7.3 A multi-objective cost-power optimisation problem

As discussed in Chapter 1, the goal of Venturi-enhanced hydropower is to strike a balance between maximising power and minimising costs. In this section we formulate both the power maximisation and cost minimisation problems. In each case, we outline the objective functions and the control parameters, whilst also discussing the constraints.

First we consider the power generated by the turbine, which is given by (7.5), or in terms of the hydrodynamic efficiency η (1.3),

$$P_V = \eta Q_{total} \Delta p_{total}. \tag{7.23}$$

Therefore, if we consider that the pressure drop Δp_{total} and total flow rate Q_{total} are fixed, then the only way of increasing generated power is by increasing efficiency η. Using (7.3), (7.5) and (7.6), we see that the power generated by the turbine can be written as

$$P_V = \frac{1}{2}\rho U_{p_2}^2 Q_s \left(1 + K_c - \beta^2\left(1 + \frac{fL_s}{4R_s}\right)\right). \tag{7.24}$$

Thus, combining (7.10), (7.23) and (7.24), the hydrodynamic efficiency is

$$\eta = \frac{\mathcal{F}\left(1 + K_c - \beta^2(1 + fL_s/(4R_s))\right)}{1 + K_c - C_p\left(1 - (1 - \beta^2)\,\mathcal{F}\right)}, \tag{7.25}$$

which we choose as the objective for the power maximisation problem. Considering (7.25), we see that efficiency is a function of a number of parameters

$$\eta = \eta\left(\mathcal{F}, \beta, K_c, C_p, f, \frac{L_s}{R_2}, \frac{R_s}{R_2}\right), \tag{7.26}$$

where we have written L_s and R_s in terms of R_2 for consistency. Note that if we fix all the parameters in (7.26) except C_p, then η is maximised by maximising C_p. This was the approach taken in Chapter 5. However, if we keep all the parameters as free variables, then this is not necessarily the case. In fact, C_p itself is a function of the channel shape $R(x)$ and other parameters (see Chapters 4 and 5),

$$C_p = C_p\left(R(x), \beta, \frac{R_s}{R_2}, \frac{L_d}{R_2}, \frac{R_3}{R_2}, f, S_c\right), \tag{7.27}$$

where L_d is the length of the diffuser section and S_c is the spreading parameter.

For the purpose of this analysis, we restrict our attention to the case where the parameters L_s/R_2, L_c/R_2, R_1/R_2, f and S_c are fixed (i.e. they are not considered decision variables). Furthermore, the parameter R_s/R_2 is given in terms of β and $\mathcal{F}$ via the relationship

$$\left(\frac{R_s}{R_2}\right)^2 = \frac{\mathcal{F}}{\mathcal{F}(1-\beta) + \beta}. \tag{7.28}$$

The loss coefficient K_c is given in terms of the above parameters by (7.21). Therefore, the efficiency η depends on only 5 decision variables. Hence, the power maximisation problem is written as

$$\text{Power maximisation}: \qquad \max_{\{R(x), \beta, \mathcal{F}, \frac{L_d}{R_2}, \frac{R_3}{R_2}\}} \eta. \tag{7.29}$$

Next we consider the cost minimisation problem. We make the assumption that the cost of the hydropower is dominated by the turbine cost and that the turbine cost is proportional to its volume V_{T_V}. In Appendix E we compare a Venturi-enhanced hydropower turbine to a conventional hydropower turbine, and we show that the volume ratio of these two turbines is

$$\frac{V_{T_V}}{V_{T_C}} = \left(\frac{\mathcal{F}^3}{\eta}\right)^{3/4}, \tag{7.30}$$

Note that the Venturi-enhanced hydropower turbine volume is only smaller (and therefore cheaper) than the standard hydropower turbine if $\eta > \mathcal{F}^3$ (this is certainly the case if $\mathcal{F} \approx 0.2$, which is a typical value). Therefore the cost minimisation problem is formulated as

$$\text{Cost minimisation}: \quad \min_{\{R(x), \beta, \mathcal{F}, \frac{L_d}{R_2}, \frac{R_3}{R_2}\}} \quad \left(\frac{\mathcal{F}^3}{\eta}\right)^{3/4}. \tag{7.31}$$

From (7.30) we see that as $\mathcal{F}$ decreases the cost decreases, as expected. However, we also expect the efficiency to decrease as $\mathcal{F}$ decreases, because the diffuser inflow becomes more non-uniform and this results in greater mixing losses (see Chapter 1). Therefore, it is not obvious that the cost is minimised by choosing the smallest possible value of $\mathcal{F}$.

Next we formulate a Pareto-type [24] multi-objective optimisation problem for both the cost and power

$$\max_{\{R(x), \beta, \mathcal{F}, \frac{L_d}{R_2}, \frac{R_3}{R_2}\}} \quad \left(\eta - \lambda \left(\frac{\mathcal{F}^3}{\eta}\right)^{3/4}\right), \tag{7.32}$$

where $\lambda \geq 0$ is a control parameter which determines the relative importance of each objective. The parameter λ can also be related to the expected return on the investment (which is related to the efficiency) over the lifetime of the project. Having formulated the objective and decision variables of the optimisation problem, we now discuss the constraints.

For any real hydropower installation there will be some practical constraints which we must take into consideration in the optimisation problem. The most obvious constraints relate to size. In particular, it is expected that the total length and diameter of the geometry are limited by critical values L_{max} and $2R_{max}$. Therefore, if we assume that the converger and secondary tube are the same length, $L_c = L_s$, then we have

$$L_d + L_c \leq L_{max}, \tag{7.33}$$

$$R_3 \leq R_{max}, \tag{7.34}$$

where the length scales R_3, L_c, and L_d are determined from their non-dimensional values in relation to the length scale R_2, which is given by (7.15). There is also the constraint that R_3 (and R_1) must be bounded below by R_2 to ensure a contracting Venturi, and the constraint that L_d must be positive

$$R_3 \geq R_2, \tag{7.35}$$

$$L_d \geq 0. \tag{7.36}$$

The non-dimensional parameters $\mathcal{F}$ and β are also bounded above and below

$$0 \leq \mathcal{F} \leq 1, \tag{7.37}$$

$$0 \leq \beta \leq 1. \tag{7.38}$$

As discussed earlier in Chapter 5, it is necessary to place lower and upper bounds on the derivative of the channel shape $\alpha = \mathrm{d}R/\mathrm{d}x$, such that

$$\alpha_{min} \leq \alpha \leq \alpha_{max}. \tag{7.39}$$

In addition to these box constraints, there are the governing equations which relate the efficiency η to the parameters it depends on (through (7.25) and (7.27)). We represent this dependence with the function

$$\eta = f_\eta \left(R(x),\, \beta,\, \mathcal{F},\, \frac{L_d}{R_2},\, \frac{R_3}{R_2} \right). \tag{7.40}$$

Having outlined all the constraints of the optimisation problem, we summarise it as follows:

$$\max_{\{R(x),\beta,\mathcal{F},\frac{L_d}{R_2},\frac{R_3}{R_2}\}} \quad \left(\eta - \lambda \left(\frac{\mathcal{F}^3}{\eta} \right)^{3/4} \right), \tag{7.41}$$

subject to

$$\eta = f_\eta \left(R(x),\, \beta,\, \mathcal{F},\, \frac{L_d}{R_2},\, \frac{R_3}{R_2} \right), \tag{7.42}$$

$$R_2 = \left(\frac{\gamma \rho Q_{total}^2}{\Delta p_{total}} \right)^{1/4}, \tag{7.43}$$

$$0 \leq L_d/R_2 \leq \left(L_{max} - L_c \right)/R_2, \tag{7.44}$$

$$1 \leq R_3/R_2 \leq R_{max}/R_2, \tag{7.45}$$

$$\alpha_{min} \leq \alpha \leq \alpha_{max}, \tag{7.46}$$

$$0 \leq \beta \leq 1, \tag{7.47}$$

$$0 \leq \mathcal{F} \leq 1. \tag{7.48}$$

Note that we can find an estimate for η (7.25) using the very simple model for mixing in Chapter 1, Section 1.1.2. In this model we neglected wall drag and assumed that the primary and secondary flows mix perfectly in the straight mixer section, resulting in a uniform inflow for the diffuser. Here we extend this very simple model by adding the diffuser to the end of the mixer. We neglect wall drag in the diffuser and assume the flow maintains a uniform profile as it decelerates, such that Bernoulli's equation applies. Under these assumptions, it is straightforward to show that the pressure recovery coefficient is

$$C_p = \frac{(1 - \mathcal{A} + \mathcal{A}\beta)(\mathcal{A}_3^2 - 1 + \mathcal{A}(1-\beta)(2 - \mathcal{A}(1+\mathcal{A}_3^2)(1-\beta) - 2\mathcal{A}_3^2\beta))}{\mathcal{A}_3^2(1 - \mathcal{A} + \mathcal{A}\beta^3)}, \quad (7.49)$$

where $\mathcal{A}_3 = (R_3/R_2)^2$, and $\mathcal{A} = (R_s/R_2)^2$ is related to $\mathcal{F}$ and β by (7.28). The corresponding efficiency is found by inserting (7.49) into (7.25) and setting $f = K_c = 0$ to neglect wall drag in the secondary flow and in the converger (for consistency), such that

$$\eta = \frac{\mathcal{A}_3^2\mathcal{F}(\mathcal{F} + \beta - \mathcal{F}\beta)^2(1-\beta^2)}{\beta^2 + \mathcal{A}_3^2\mathcal{F}(\mathcal{F} + (2 - 3\mathcal{F})\beta^2 - 2(1-\mathcal{F})\beta^3)}. \quad (7.50)$$

Although wall drag has been neglected here, we note that (7.50) is not an upper bound for η. For non-uniform flow the ideal upper limit for C_p (and hence η) is not known. However, (7.50) provides a good estimate for an upper bound and we will use it in the next section to compare with optimised values of η calculated with our simple model from Chapter 4.

7.4 Case study

As a case study, we choose a hypothetical river/dam with a total head drop of 3 m that provides a flow rate of $4\,\mathrm{m}^3\,\mathrm{s}^{-1}$ to the Venturi-enhanced hydropower. We solve the optimisation problem (7.41)-(7.48) numerically, setting the parameter bound values as $R_{max} = 1\,\mathrm{m}$, $L_{max} = 25\,\mathrm{m}$, $\alpha_{min} = 0°$, and $\alpha_{max} = \tan 7°$. We use a friction factor value of $f = 0.01$ and a spreading parameter value of $S_c = 0.11$ (as in Chapters 4 and 5). The converger shape is chosen as a linear profile defined by (7.22), with parameter values $L_c/R_2 = 5$, $R_1/R_2 = 1.7$, and R_s/R_2 is given by (7.28). The loss coefficient K_c is calculated from (7.21). We use the numerical optimisation technique outlined in Chapter 5 to find the optimal shape $R(x)$, but in addition, we include the other parameters β, $\mathcal{F}$, L_d/R_2 and R_3/R_2 as decision variables (these are also dealt with using the interior point method [73]).

The multi-objective optimisation parameter λ is varied between 0.5 and 2 to illustrate the effect of altering the relative importance of cost and power (large λ corresponds to prioritising cost). We plot the Pareto distribution [24] in Figure 7.3 (a). The optimum power ratio (or efficiency) varies between 0.47 and 0.67 (corresponding to a total output power of 55 kW and 79 kW), whilst the cost (or turbine volume) ratio varies between 0.29 and 0.05. In the most expensive limit, the Venturi-enhanced

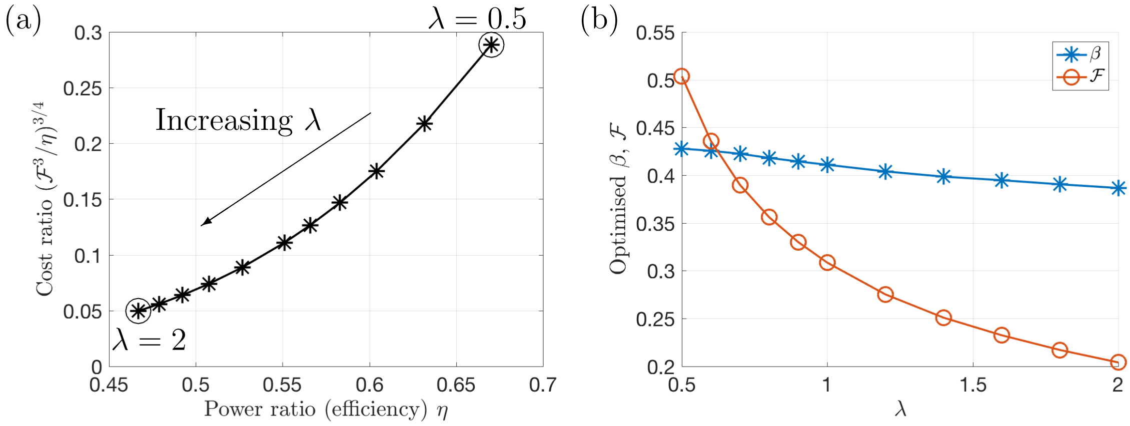

Figure 7.3: Multi-objective optimisation of power and cost (7.41)-(7.48). (a) Pareto distribution obtained by varying $0.5 \leq \lambda \leq 2$. (b) Velocity ratio β and flow rate fraction $\mathcal{F}$, optimised for different values of the multi-objective parameter λ. Large λ corresponds to prioritising cost.

hydropower turbine is 29% of the cost of a conventional hydropower turbine and generates 67% of the power available in the water[3]. In the cheapest limit, it is 5% of the cost, whilst generating 47% of the available power. We compare these values to the estimated upper bound for η, given by (7.50), which are $\eta = 78\%$ and $\eta = 68\%$, respectively. Comparing the optimised values to the estimated upper bound values, we find $67/78 \approx 0.86$ and $47/68 \approx 0.69$, indicating that if we prioritise power in the multi-objective optimisation then η is closer to its estimated upper bound than if we prioritise cost, which is expected.

In Figure 7.3 (b) we plot the optimised values of β and $\mathcal{F}$ as we vary λ. As expected, increasing λ, and hence the importance of cost, results in a lower value of the flow rate fraction. In the most expensive limit the turbine receives 50% of the total flow rate, compared to 20% in the cheapest limit. The optimum value of β does not vary much with λ, but decreases slightly as λ increases. Hence, for all cases we can take $\beta = 0.4$ as a good estimate for the optimum value. The results from Chapter 5 show how β affects the optimum channel shape $R(x)$.

It is interesting to note how the other free parameter values R_3/R_2 and L_d/R_2 vary with λ. The optimum expansion ratio is always the maximum possible, such that $R_3/R_2 = R_{max}/R_2$, which is expected because pressure recovery is maximised when the flow is decelerated as much as possible. The optimum value of $L_d + L_c$ varies between 20.9 m and 22.2 m, compared to the upper bound $L_{max} = 25$ m. Therefore,

[3]Note that in the case where the conventional hydropower turbine is 100% efficient, then the power generated by the conventional hydropower turbine is equal to the power available in the water.

L_{max} is sufficiently large that the upper bound on L_d/R_2 is not active for any value of λ. We do not display the optimum shapes here for confidentiality reasons.

Next, we estimate the possible effect of swirl. In Chapter 6 we discovered that swirl has a detrimental effect on pressure recovery, indicating poor suitability for Venturi-enhanced hydropower. However, as described in Section 6.1, it is likely that the stator blades at the outflow of the turbine will not remove all of the swirl given to it by the entry blades. Therefore, it is important to understand how this swirl could affect our optimisation. To do so, we estimate that the maximum azimuthal velocity (near the outer edge of the secondary flow) is approximately 10% of the secondary flow speed in the axial direction. Using this estimate we calculate the swirl number for the flow, which is given by (6.16), finding $S_w = 0.05$. For such a small value of S_w, we find that swirl has an insignificant effect on the optimum shape and parameters. This is illustrated by Figure 6.7 and Table 6.1, where we optimise the mixer/diffuser shape for different swirl numbers between $S_w = 0$ and $S_w = 1.75$. We can see that the optimum shape is quite similar for $S_w = 0$ and $S_w = 0.27$. Therefore, it is not surprising that the optimum shapes for $S_w = 0$ and $S_w = 0.05$ are nominally the same. Furthermore, we can see in Figure 6.7 (c) that the optimum values of C_p for $S_w = 0$ and $S_w = 0.05$ are also nominally the same. Hence, we conclude that whilst swirl has a detrimental effect on pressure recovery and should be avoided as much as possible, the amount of swirl present here is considered acceptable, and can be ignored for our optimisation.

7.5 Summary and concluding remarks

We have developed a complete model for Venturi-enhanced hydropower, including the intake from the river, the converger, the turbine and the outflow back into the river. This model determines the scaling factor of the geometry for a given total flow rate Q_{total} and pressure drop Δp_{total}. To describe the flow in the converging section, we used a simple model for annular flow, following the example in Chapter 2, Section 2.4.3. Having developed the complete model for Venturi-enhanced hydropower, we reformulated the optimisation problem of Chapter 5 to account for both the generated power and the cost of the turbine. We then applied a multi-objective optimisation approach to investigate the tradeoff between prioritising each of these objectives (power and cost). This reformulated optimisation problem included other parameters, such as $\mathcal{F}$ and β, which we took as fixed in previous chapters, as decision variables. We also used the results of Chapter 6 to discuss the possible effects of swirl that may be present in the secondary flow. It was found that the swirl number of the flow would not be large enough to have a significant effect.

For future work, the effect of a time-varying total head could be studied. This problem is relevant to hydropower generation in tidal sites. In this case, instead of maximising efficiency η, we would maximise an time-integral quantity. For example, we could choose the time-averaged efficiency. Another option is the sum of the time-averaged efficiency and a time-averaged efficiency squared (variance) penalty term. This would correspond to a risk-averse strategy.

Chapter 8

Conclusions

We refer the reader back to the final section of each chapter for a detailed overview of their individual contents. In this chapter we summarise the conclusions of Chapters 4, 5, 6 and 7 and indicate the potential avenues for future work.

8.1 Summary of the results

We have studied the flow behaviour in a novel type of hydropower which uses a Venturi contraction to amplify the pressure drop across a turbine, allowing for cost-effective electricity generation in situations where the head drop is small. The efficiency of Venturi-enhanced hydropower depends on how the secondary flow, which passes through the turbine, mixes with the accelerated primary flow, which is diverted around the turbine, within the confines of a closed geometry. In particular, as the flows mix and expand in the mixer/diffuser section, the kinetic energy of the flow is converted into static pressure. The greater the recovery of pressure in the mixer/diffuser, the larger the pressure amplification across the turbine, and hence the generated power. Therefore, in this thesis we focused our attention on mathematically modelling the mixing process between the primary and secondary flows, and optimising pressure recovery by manipulating the channel shape and inflow conditions.

In Chapter 4 we developed a simple model for turbulent shear layers in confining channels. This model describes the mixing between the primary and secondary flows in the mixer/diffuser section of Venturi-enhanced hydropower. In the model we approximated the flow in the shear layer as a linear profile separating uniform-velocity streams. The model depends on two parameters, the friction factor f, which we found was well estimated by the Blasius relationship [11, 66], and the spreading parameter

S_c, which was fitted to CFD and experimental data. There was some uncertainty regarding the value of the spreading parameter, finding different values when comparing to experimental data in three dimensions ($S_c = 0.18$), and CFD in two dimensions and in the axisymmetric case ($S_c = 0.11$). Hence, appropriate comparisons with experimental data are advised for each particular application.

Using our simple model we showed how the inflow conditions affect the behaviour of the shear layer. In particular, the growth of the shear layer is not necessarily symmetric. For inflows with a velocity ratio $U_2(0)/U_1(0)$ close to 0, or with an inner plug region width ratio $h_2(0)/h(0)$ close to 0, the shear layer is directed towards the centre of the channel. In the opposite cases, the shear layer is directed towards the channel wall. If the inflow is too non-uniform or if the channel expansion angle is too wide, the slower secondary flow can decelerate and form a stagnation region in the centre of the channel. Using our model we calculated the criteria for the existence of such a region. Finally, we showed how the accuracy of our model can be improved by incorporating a boundary layer near the wall that satisfies the no-slip condition, and a symmetry layer near the channel centreline that satisfies the symmetry condition.

In Chapter 5 we developed an optimisation approach which used the simple model from Chapter 4 to find the mixer/diffuser shape that maximises pressure recovery (and hence generated power) for a given non-uniform inflow. By considering a general class of mixer/diffuser shapes, the distinction between mixer and diffuser was blurred. Hence, the mixer/diffuser was simply considered a diffuser which has a non-uniform inflow and a potentially complex shape.

We considered three classes of non-uniform inflow for this diffuser. The first case was a typical inflow from Venturi-enhanced hydropower, consisting of primary and secondary flows with a shear layer in between. The second case was a limiting case where the primary and secondary flows are of similar speed. The third case was a pure shear profile with linear velocity variation between the centre and outer edge of the diffuser. This case corresponds to the downstream limit of the first case, where the shear layer has reached across the width of the diffuser.

We described the evolution of the flow profile using our simple model from Chapter 4. The governing equations of this model formed the dynamics of an optimal control problem where the control was the diffuser shape. A numerical optimisation approach was used to solve the optimal control problem and Pontryagin's Maximum Principle [78] was used to find analytical solutions in the second and third cases.

We showed that some of the optimal diffuser shapes found using our numerical optimisation approach (in the first and third cases), consisted of an initial straight section followed by a widening section, followed by another straight section. This is explained by the balance between two competing physical effects. Wide diffuser angles tend to accentuate non-uniform flow, causing poor pressure recovery, whilst shallow diffuser angles create enhanced wall drag, which is also detrimental to pressure recovery. The optimisation indicated two major distinctions between diffuser design for uniform flow and diffuser design for non-uniform flow. Firstly, in the diffuser industry, diffusers with uniform flow are typically designed to be straight sided, with constant expansion angle, whereas for non-uniform flow we found that the optimum shape has an initial straight section which aids mixing before expansion. Secondly, diffusers with uniform flow are typically designed with an expansion angle that strikes a balance between the effects of wall drag and boundary layer separation, whereas we found that the optimum expansion angle for non-uniform flow is determined by the balance between the effects of mixing and wall drag. Furthermore, we found that the optimum angle for non-uniform flow is less than typically used for uniform flow. Hence, for these flows we showed that the effect of the non-uniform inflow is more important in determining the optimum diffuser shape than the effects of boundary layer separation.

Finally, by approximating the diffuser shape with piecewise linear sections, we made use of a low-dimensional parameterisation, for which more detailed and computationally expensive CFD models could be used to find optimal shapes for more realistic flow behaviour. These CFD models had similar optima to our simple model, indicating that our previous optimisation results were reliable.

Whilst the initial straight section of these optimal shapes is necessary to aid mixing, it also is responsible for large pressure losses due to strong wall drag. Hence, in Chapter 6 we investigated the use of swirl in the secondary flow as a mechanism to promote mixing, thereby potentially allowing for a shorter initial straight section. To describe the effect of swirl in the secondary flow we developed a simple model, which was an extension of the simple model of Chapter 4 for non-swirling flow. In the model we approximated the axial flow profile as a linear shear layer separating uniform-velocity core and annular streams. The azimuthal flow profile was approximated as a solid body rotation within the core region, and a parabolic mixing profile within the shear layer.

We compared the results of this model to CFD calculations, finding good agreement. Then we used the model to study the effect of swirl in the secondary flow. We found that swirl was useful for increasing shear layer growth rates, but it produced large pressure losses in doing so, and for large amounts of swirl a stagnation region formed along the pipe axis. This indicated that the use of swirl would not yield any improvements to the efficiency of Venturi-enhanced hydropower. However, if there is swirl present in the flow, we indicated how this affects the optimum channel shape. We also established the criteria for the development of the stagnation region in terms of the pipe expansion angle and inflow velocity profile, so that it may be avoided.

In Chapter 7 we applied the work from the previous chapters to a case study, where we considered Venturi-enhanced hydropower in a river/dam with a head drop of 3 m and a flow rate of $4\,\mathrm{m^3s^{-1}}$. We extended the simple model from Chapter 4, which describes the flow in the mixer/diffuser section, to account for the flow in the entire Venturi, from the river inflow to the outflow. We used the optimisation techniques of Chapter 5, in conjunction with this model for the entire Venturi, to optimise the shape of the geometry as well as other parameters which we had previously considered fixed. We formulated the optimisation with two objectives, corresponding to the maximisation of power and the minimisation of cost. Using this approach we showed how to design Venturi-enhanced hydropower according to the priority of each of these objectives.

8.2 Future work

Throughout this thesis we have only considered slowly varying geometries, because for rapidly varying geometries with sudden expansions we expect the boundary layers to separate (see Chapter 1), which is not captured by our simple models from Chapters 4 and 6. For future work, our models could be extended to account for boundary layer separation. This could be achieved by considering more generalised boundary layer profiles, other than the self-similar power law we considered in our simple boundary layer models in Chapters 4 and 6. Such an approach would be useful for our optimisation work in Chapter 5, because a model for boundary layer separation would replace the upper bound constraint that we imposed on the expansion angle. For many of the cases we considered in Chapter 5 the optimum expansion angle was less than this upper bound (see Figure 5.2), such that a model for boundary layer separation would be unnecessary. However, this would not be the case for examples such as the small shear limit (see Figure 5.4 (a, c, e)), where the upper bound constraint was active.

In the work in this thesis we have modelled the effect of wall drag with a friction factor and the Blasius relationship [11, 66]. In some cases we incorporated the development of a turbulent boundary layer near the channel walls. The friction factor parameterises the stress at the wall due to the viscous sub-layer that lies within the turbulent boundary layer. Though we have incorporated a turbulent boundary layer into our models in Chapters 4 and 6, we have not attempted to model the viscous sub-layer (or the log-law and buffer layers [87]) explicitly. Future work could incorporate a viscous sub-layer into our models that would replace the friction factor parameterisation. However, for the cases we have considered in this thesis the friction factor parameterisation showed good agreement with experimental data and CFD calculations. Another direction of future work could be the investigation of methods to reduce wall drag. Possible mechanisms to reduce wall drag include the use of smart surfaces [103] and the injection of bubbles into the boundary layers [18]. For future work, such mechanisms could be investigated, and our simple models could be extended to account for more complex wall drag behaviour.

In our investigations on the effect of swirl in Chapter 6, we only considered one type of azimuthal velocity distribution in the secondary flow, which was a solid body rotation. For future work, other distributions could be considered, such as a q vortex [38]. Furthermore, our work could be extended to account for situations where the primary flow is also rotating, not necessarily in the same direction as the secondary flow. It is possible that such swirl distributions could be beneficial to the efficiency of Venturi-enhanced hydropower, even though solid body rotation in the secondary flow was not. However, it would be difficult and costly to produce more complicated swirl distributions, which raises doubts about any possible advantages.

The case study in Chapter 7 could be extended to tidal situations, where the total head drop is varying in time. In such cases, we would need to consider a different form for our power optimisation objective. One option could be the period-averaged generated power. Another option could include a penalty variance term, corresponding to a risk-averse strategy. It would be interesting to see how such extensions would affect the optimal geometry as well as the other optimisation parameters, such as the flow rate fraction.

Appendix A: Further comparisons between the simple model and CFD

In this section we compare the results of the simple model from Chapter 4 to the results of a k-ε model [55] and a k-ω SST model [67] on some other two-dimensional geometries for a variety of Reynolds numbers and inlet conditions. The two channel shapes we select to investigate are a symmetric nozzle shape and a symmetric sinusoidal shape. In each case, due to symmetry, we only consider half of the channel $0 \leq y \leq h(x)$, as in Chapter 4.

The nozzle shape we choose to study is given by a polynomial function

$$h(x) = h(0) + K\left(x^2 - Lx\right), \tag{1}$$

where L is the length of the channel and K is the curvature. In this case, we choose $L = 30\,\mathrm{m}$, $h(0) = 1\,\mathrm{m}$ and $K = 1.2 \times 10^{-3}\,\mathrm{m}^{-1}$. The sinusoidal shape we consider is given by the function

$$h(x) = h(0) + A \sin\frac{n\pi x}{L}, \tag{2}$$

where A and n are the amplitude and frequency of the sine function. In this case, we choose $L = 30\,\mathrm{m}$, $A = -0.25\,\mathrm{m}$ and $n = 2$. In both the nozzle and the sinusoidal case, the inlet profile is taken to be a discontinuous step function (as in Figure 4.3) with $h_2(0) = h_1(0)$. We look at three different values of the inlet velocity ratio $U_2(0)/U_1(0) = 0.25$, 0.5 and 0.75, as well as three different values of the Reynolds number $Re = 10^6$, 10^5 and 10^4.

We use the same k-ε model as in the example in Figure 4.3, with all the standard values for the turbulence parameters, which are given in Chapter 2. We refer the reader to Menter [67] for the details of the k-ω SST model, for which we use the standard values for the turbulence parameters. We use the same mesh and the same software package, *OpenFoam* [104], for the k-ω SST model as for the k-ε model. For comparison with our simple model, we calculate the friction factor using the empirical

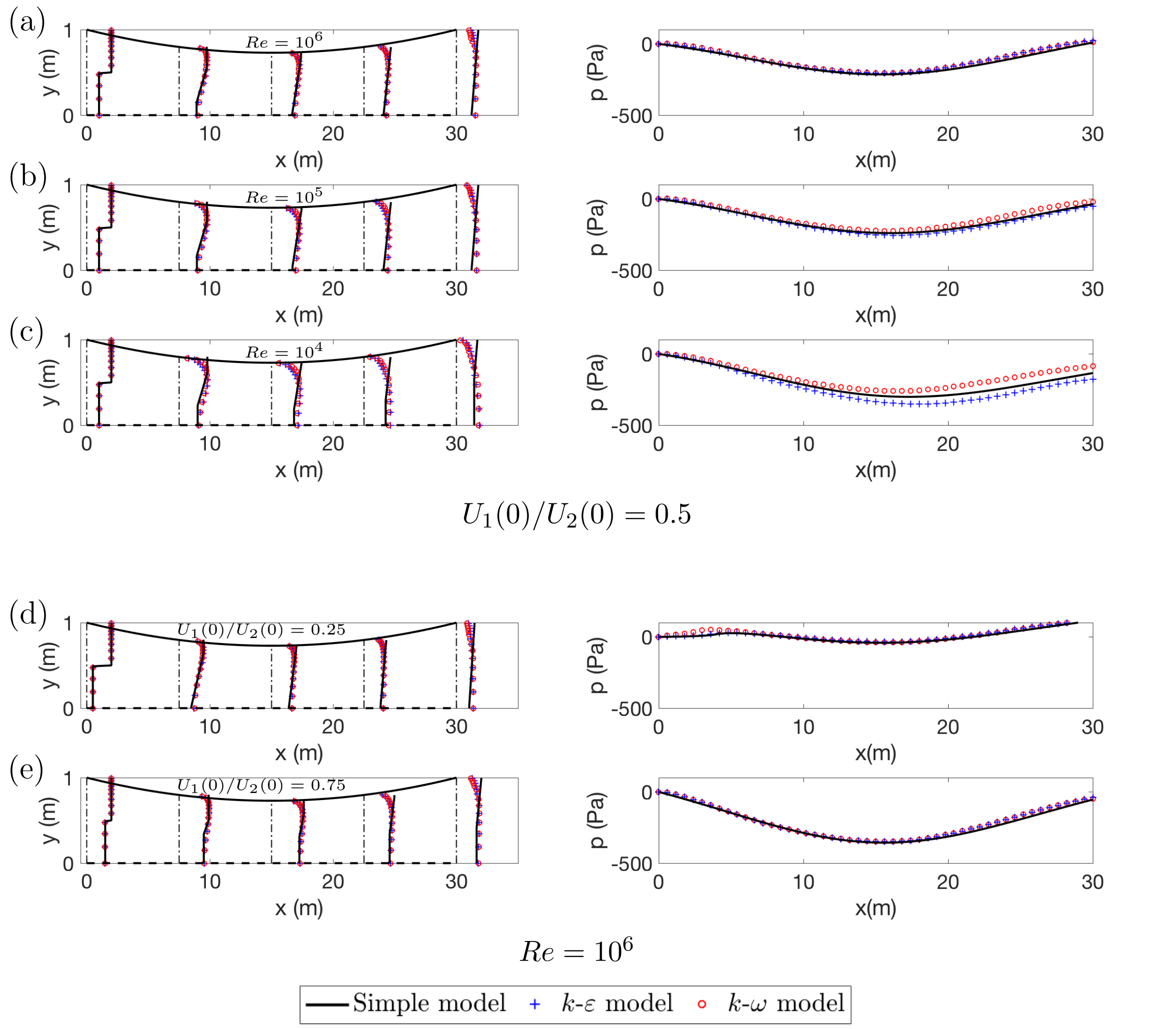

Figure 1: Velocity profiles (left column) and pressure plots (right column) for symmetric nozzle-shaped geometry (half channel shown only).

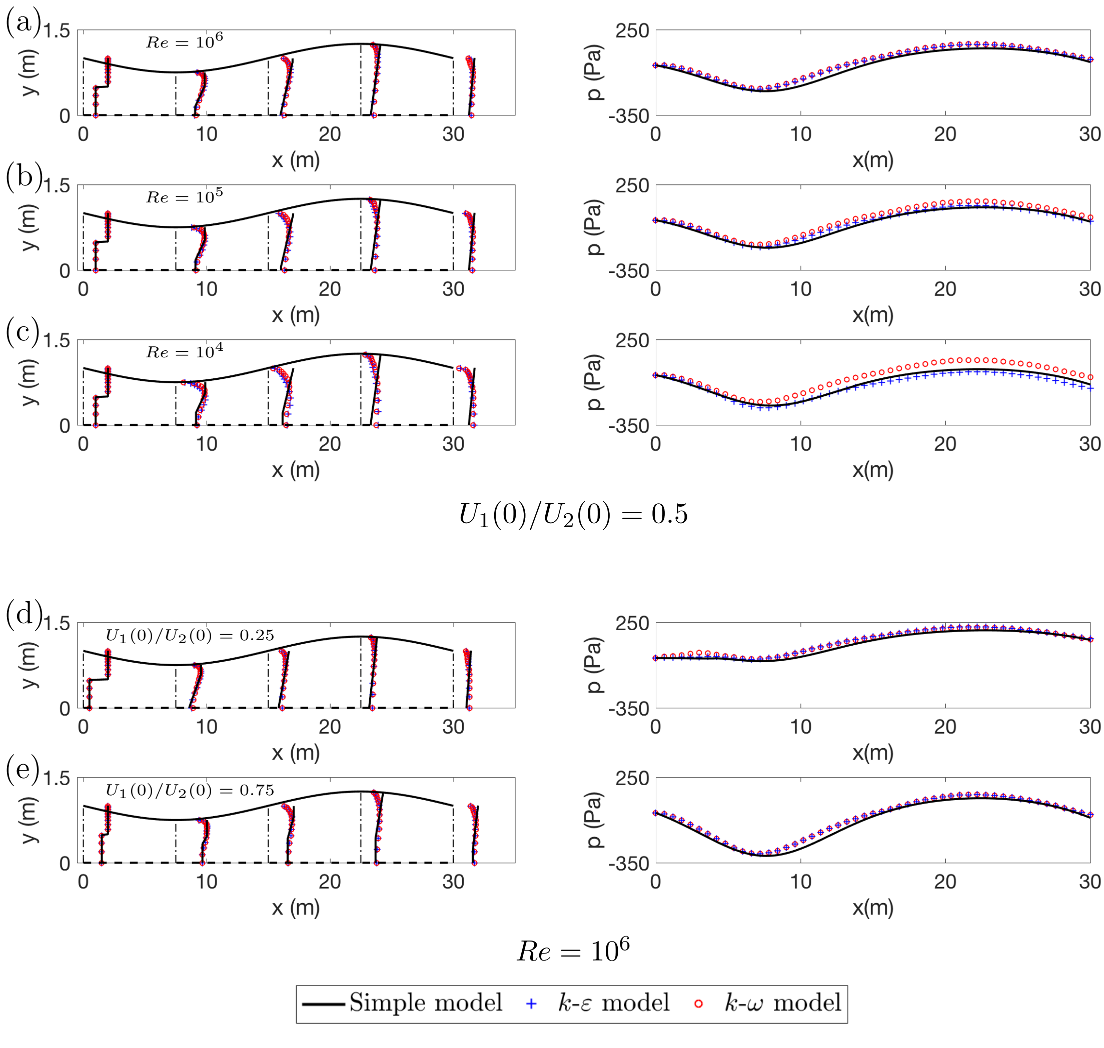

Figure 2: Velocity profiles (left column) and pressure plots (right column) for symmetric sinusoidal-shaped geometry (half channel shown only).

Blasius relationship [66] for flow in smooth pipes $f = 0.316/Re^{1/4}$. We look at three values of the Reynolds number $Re = 10^6$, 10^5 and 10^4, giving friction factor values of $f = 0.010$, 0.018 and 0.032, respectively. For the spreading parameter we find that $S_c = 0.11$ fits best with our data in all cases.

The simple model and both the CFD models show good agreement. The streamwise velocities u and pressure p (relative to the inlet pressure), along the channel centreline, are compared in Figures 1 and 2. Similarly to the comparisons in Chapter 4, the dominant features of the flow profile and pressure variation are captured accurately by the simple model. However, near the wall the simple model is less accurate due to the fact that it does not explicitly resolve the development of boundary layers. For this reason, it is not suitable in situations where there is boundary layer separation. This is illustrated in Figure 1 (b) and (c), where the k-ε and k-ω SST models show some boundary layer separation in the expanding part of the channel and the flow profiles generated by the simple model compare less well in this region. Therefore, the model breaks down for low values of the Reynolds number and/or too rapid widening of the channel, when boundary layer separation is more likely [87]. It is generally accepted that the k-ω SST model is more accurate than the k-ε model for separated flow [67], which is why we see some disagreement between the two CFD models for lower Reynolds numbers. To ensure slowly varying width in the case of the nozzle and sinusoidal geometries given by Equations (1) and (2), we choose small values of K and A.

Appendix B: The constant singular arc solution

In this appendix we go through the details of the constant singular arc solution from Section 5.4.2. The constant singular arc solution is given by (5.99) on an interval $x \in [x_1, x_2]$. Suppose that the diffuser commences on the singular arc α^* such that $x_1 = 0$. In addition, suppose that $H_\alpha < 0$ for $x > x_2$ (just as in Figure 5.7), such that $\alpha = \alpha_{min}$ after the singular arc. In the interval $x \in [0, x_2]$ the solution to Equations (5.82)-(5.95) for constant α^* (and constant $\tilde{U}$) is as follows:

$$p = \frac{\rho Q^2 x (2h_0 + S_c \tilde{U} x)}{48 h_0^2 (h_0 + S_c \tilde{U} x)^2} (-3f(1+\tilde{U})^2 + 8 S_c \tilde{U} (3 + \tilde{U}^2)), \tag{3}$$

$$h = h_0 + S_c \tilde{U} x, \tag{4}$$

$$\lambda_h = \frac{\rho Q^2 (3f(1+\tilde{U})^2 - 8 S_c \tilde{U}(3+\tilde{U}^2))}{24 S_c \tilde{U} (h_0 + S_c \tilde{U} x)^3}, \tag{5}$$

$$\lambda_{\tilde{U}} = \frac{\rho Q^2 (-f(1+\tilde{U}) + 8 S_c \tilde{U}^2)}{16 S_c \tilde{U} (h_0 + S_c \tilde{U} x)^2}, \tag{6}$$

$$\lambda_p = 1. \tag{7}$$

where $\tilde{U}$ satisfies (5.97). Alternatively, $\tilde{U}$ can be written in terms of the inflow velocity ratio $\tilde{U} = (1 - U(0))/(1 + U(0))$, where $U(0)$ satisfies (5.98). As a check to see if $H_\alpha = 0$ on the singular arc, we calculate

$$H_\alpha = \frac{\rho Q^2 (-8 S_c \tilde{U}^3 + 3f(1+\tilde{U}))}{24 S_c \tilde{U} (h_0 + S_c \tilde{U} x)^3}, \tag{8}$$

which is equal to zero due to Equation (5.97). For the second part of the solution, $x \in [x_2, L]$, the control takes the value $\alpha = \alpha_{min}$ since $H_\alpha < 0$. Note, for this part of the solution $\tilde{U}$ is not a constant. For simplicity, let us assume that $\alpha_{min} = 0°$, such that the value of x_2 is given by

$$x_2 = \frac{h_L - h_0}{\alpha^*}. \tag{9}$$

Then the solution to Equations (5.82)-(5.95) for $\alpha = 0°$ and $x \in [x_2, L]$ is as follows:

$$
\begin{aligned}
p &= C_1 + \frac{\rho Q^2}{24h_L^3}\left(\frac{3C_2 f h_L}{2S_c} - 3fx - \frac{8h_L^3}{(C_2h_L - 2S_c x)^2} - \frac{3fh_L^2}{2C_2h_LS_c - 4S_c^2 x}\right. \\
&\quad \left. - \frac{3fh_L}{S_c}\log(C_2h_L - 2S_c x)\right), &(10)\\
h &= h_L, &(11)\\
\tilde{U} &= \frac{h_L}{2S_c x - h_L C_2}, &(12)\\
\lambda_h &= C_3 - 2C_4S_c x + \frac{\rho Q^2}{24h_L^4 S_c(C_2h_L - 2S_c x)^2}\left(h_L^3(3fC_2(C_2-1) - 16S_c)\right. \\
&\quad + 3fh_L^2S_c x(2 - C_2(4+3C_2)) + 12fh_LS_c^2x^2(1+3C_2) - 36fS_c^3x^3 \\
&\quad \left. -6fh_L(C_2h_L - 2S_c x)^2\log(C_2h_L - 2S_c x)\right), &(13)\\
\lambda_{\tilde{U}} &= C_4(C_2h_L - 2S_c x)^2 - \frac{\rho Q^2}{48h_L^3}\left(\frac{32h_L^2}{C_2h_L - 2S_c x} + \frac{3f}{S_c}(h_L - 2C_2h_L + 4S_c x)\right), &(14)\\
\lambda_p &= 1, &(15)
\end{aligned}
$$

where the constants C_1, C_3 and C_4 are found by equating (3), (5), (6) to (10), (13), (14) at $x = x_2$ due to continuity. To calculate the constant C_2, we equate (12) to the solution of (5.97) at $x = x_2$. Now the solution is complete except for one more condition. This final condition is the natural boundary condition for $\lambda_{\tilde{U}}$, which requires

$$\lambda_{\tilde{U}}(L) = 0. \tag{16}$$

However, there are no more constants left to determine. Therefore, this condition forces a relationship between the remaining parameters. If we consider the parameters S_c and f as fixed, then (16) enforces a relationship between the two parameters h_L/h_0 and L/h_0 (it turns out that this relationship is independent of ρ and Q). We do not display the exact relationship between these parameters here because it is long and complicated. However, we note that we can find a simple expression for the approximate relationship by writing the rescaled non-dimensional channel length $L/(S_c h_0)$ in terms of f/S_c and h_L/h_0, and expanding this expression in terms of powers of f/S_c. The result is

$$\frac{L}{S_c h_0} = \left(3^{-1/3}(1+2^{2/3})\frac{h_L}{h_0} - 2\cdot 3^{-1/3}\right)\left(\frac{f}{S_c}\right)^{-1/3} + \frac{1}{3} - \frac{1}{2}\frac{h_L}{h_0} + \dots. \tag{17}$$

There is a particular case which is of special interest, when the value of L coincides with the value of x_2, which is not discussed in Chapter 5. This is the case where the control only takes its singular arc value. Hence, we refer to this case as the *constant* *purely singular arc* case. If we denote the solution to (16) as $\bar{L}$, and we define the function

$$X = \frac{\bar{L}}{S_c h_0} - \frac{x_2}{S_c h_0}, \tag{18}$$

which is a function of only two parameters, f/S_c and h_L/h_0, then the roots of (18) will tell us when there is a constant purely singular arc. Interestingly, we find that the roots of X only depend on f/S_c, and are given by the relationship

$$\frac{f}{S_c} = 18, \tag{19}$$

For realistic values of S_c, the values of f given by (19) are quite high. For example, if $S_c = 0.1$, then the constant singular arc solution would be purely singular only if $f = 1.8$. This friction factor is 180 times larger than the value we used in our optimisation ($f = 0.01$ corresponds to a Reynolds number of $Re = 10^6$ [11, 66]). Therefore, we conclude that such constant purely singular arc solutions only exist for extremely rough pipes.

The pure shear limit example in Figure 5.4 has a singular arc which is approximately constant, with a value very close to the constant singular arc solution (5.99) ($\alpha = \tan 2.76°$) discussed in the first part of this appendix. However, the solution does not start and terminate on the singular arc ($x_1 \neq 0$ and $x_2 \neq L$). Therefore, the constant singular arc analysis is physically relevant, but the constant purely singular arc solution is not.

Appendix C: Bernoulli's equation in the simple swirl model

In this appendix we compare the streamlines calculated using our simple swirl model from Chapter 6 to those calculated using a k-ε model. For the comparison, we use the same straight channel example as in Figure 6.2, where we use the same calculations for the k-ε model. Using both the calculations from the simple swirl model and the k-ε model, we calculate the 'Bernoulli constant' along the streamlines, which is given by

$$C_B = p + \frac{1}{2}\rho\left(u_x^2 + u_r^2 + u_\theta^2\right), \tag{20}$$

where in the case of the simple swirl model u_x, u_θ and p are given by (6.1), (6.2) and (6.4), respectively, and u_r is calculated using (6.18).

In Figure 3 (a, b) we plot the streamlines calculated using both the simple swirl model and the k-ε model, and in (c, d) we plot the Bernoulli constant C_B (20) calculated along each of the streamlines. The colouring of the curves indicates the relevant streamline for each Bernoulli constant. In the case of the simple swirl model, we also show the position of the shear layer, from which we can deduce the size of the plug regions. According to the k-ε model, C_B is approximately constant along the streamlines in both the core and annular plug regions, before they are absorbed by the shear layer. The outermost two streamlines (indicated by the colouring) in the annular region show a drop in C_B when they are absorbed by the boundary layer. In the case of the simple swirl model, C_B is constant along the central non-swirling streamline in the core region, due to (6.15), and C_B is constant along all the streamlines in the annular region, due to (6.14). For the swirling streamlines in the core region, C_B is not quite constant, but does not vary much along the streamline arclength. This indicates that, whilst we do not impose Bernoulli's equation along all the streamlines in the core region in our simple swirl model, the velocities and pressure calculated using our model indicate that this region is nevertheless approximately inviscid, which is consistent with the CFD calculations.

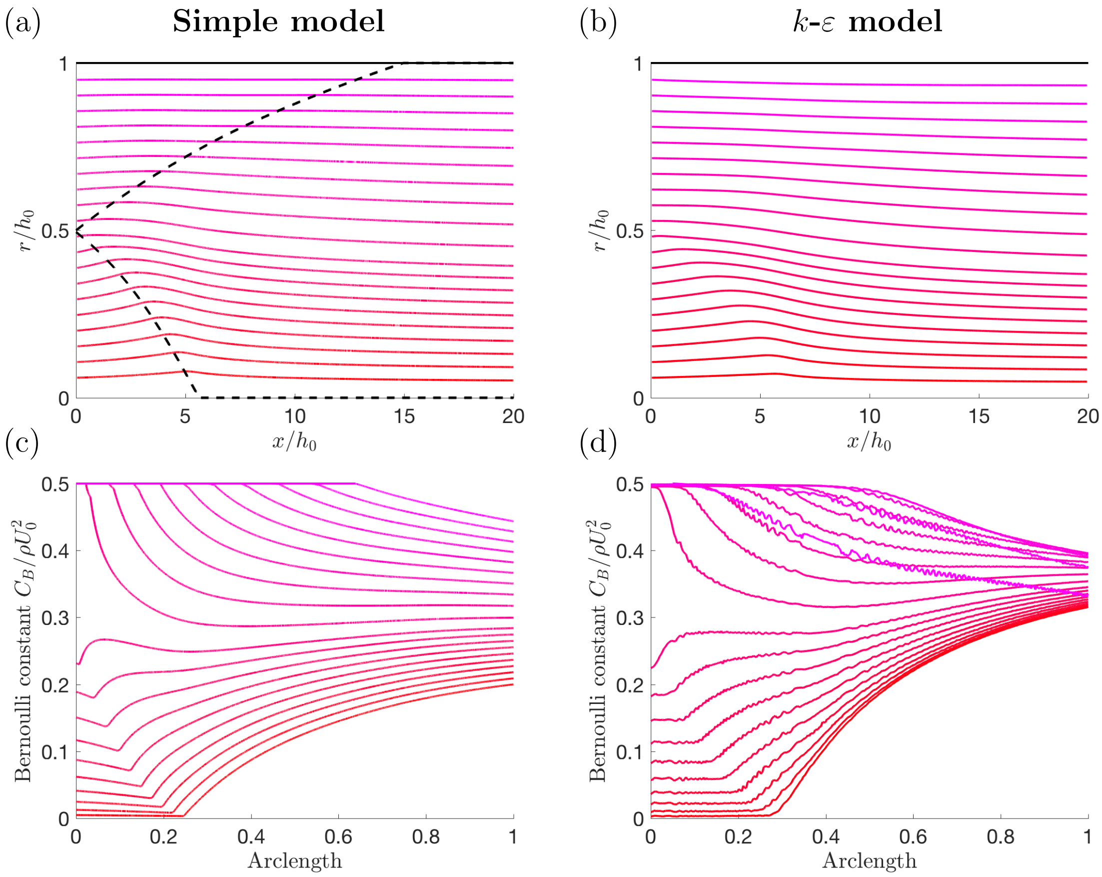

Figure 3: (a, b) Streamlines calculated using our simple swirl model and a k-ε model, for the same example as in Figure 6.2. For the case of the simple swirl model, we also overlay the position of the shear layer in dashed lines. (c, d) The Bernoulli constant C_B (20) calculated along each streamline, measured as a function of the streamline arclength. The colouring of the curves matches the corresponding streamlines in (a, b).

We note that the streamlines for which C_B varies most in our model, are those near the outer edge of the core region, which have the most swirl. In general, as we increase the swirl number, the discrepancy between C_B calculated using the simple swirl model and the k-ε model increases. Therefore, we do not expect our simple swirl model to be accurate for very large swirl numbers.

Appendix D: Comparison between the simple swirl model and experiments

In this appendix we compare our simple model to the experimental results of [38], [21] and [29] for an incompressible swirling jet. Unlike the examples of confined flow we consider in this study, all of these experimental studies are for unconfined flow. Furthermore, they consider a swirling jet entering an ambient fluid, unlike the co-axial annular flow we consider. Therefore, in order to compare with our model, we set $U_1 = 0$ and take the limit as $h(x)$, $h_1(x) \to \infty$. Furthermore, the pressure term $P(x)$ in (6.4) becomes the constant hydrostatic pressure, which we take as $P = 0$, without loss of generality.

As a metric for our comparison, we use the growth rate of the 'jet' width. In terms of our formulation, the half-width of the jet corresponds to the combined width of the core region and the shear layer

$$w = h_2 + \delta. \tag{21}$$

In general, the jet growth rate $w' = \mathrm{d}w/\mathrm{d}x$ is not constant. However, we can estimate w' by taking an average over a particular length scale L_δ, such that

$$\overline{w'} = \frac{w(L_\delta) - w(0)}{L_\delta}, \tag{22}$$

as is done by Gilchrist et al. [38]. In Figure 4 we display a comparison of $\overline{w'}$, normalised with respect to the jet growth rate for non-swirling flow, which we denote $\overline{w_0'}$, calculated using our simple model and the experimental results in the literature (with $L_\delta = 5h_2(0)$). The experimental data is quite scattered and has large error bars, so it is difficult to conclude how good the comparison is. Furthermore, the results of [38] involve two different types of swirl distribution, a solid body rotation and a q vortex, whereas we only consider solid body rotation. However, our model seems

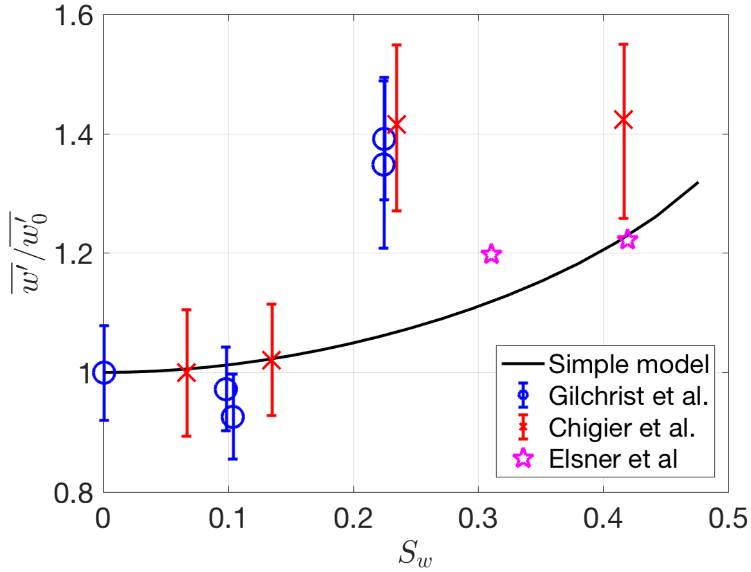

Figure 4: Normalised jet growth rates $\overline{w'}/\overline{w'_0}$ for a swirling jet in an ambient fluid, where we vary the inlet swirl number S_w. Simple swirl model compared against experimental results from the literature.

to agree well with the all the experimental data for small S_w and with the results of [29], which are for a slightly heated jet, for large S_w. Therefore, this gives further affirmation that our simple model has good predictive capabilities for modelling the effect of swirl on shear layer growth.

Appendix E: Estimating the cost of the turbine

In this appendix, we derive a scaling law which determines the volume ratio of the Venturi-enhanced hydropower turbine in relation to that of a conventional hydropower turbine. If we assume that the cost of the turbine is proportional to its volume, and the cost of the hydropower is dominated by the cost of the turbine, then estimating the volume of the turbine is sufficient for estimating the cost. In reality, there are other factors which are important, such as the costs of the generator and the the civil engineering. Here we neglect these details, for the sake of making a simple model for the turbine cost. To derive the scaling law, we assume that the both the Venturi-enhanced hydropower turbine and the conventional hydropower turbine can be described using the same 3 non-dimensional coefficients. This gives us a relationship between the relative diameters of the two turbines, and we assume that the turbine volume (and hence cost) is proportional to the diameter cubed.

We denote Venturi-enhanced hydropower properties with a subscript 1 and conventional hydropower properties with a subscript 2. Furthermore, we assume that the turbines for both cases are geometrically identical such that the following non-dimensional coefficients are the same for each:

$$C_Q = \frac{Q}{ND^3} \quad \text{(flow coefficient)}, \tag{23}$$

$$C_H = \frac{gH}{N^2D^2} \quad \text{(head coefficient)}, \tag{24}$$

$$C_P = \frac{P_V}{\rho N^3 D^5} \quad \text{(power coefficient)}, \tag{25}$$

where Q is the flow rate, $H = \Delta p_{total}/\rho g$ is the head, N is the turbine speed, D is the turbine diameter, and P_V is the power. Firstly, equating the head coefficient C_H

and the flow coefficient C_Q, we get the two relationships

$$\frac{N_2 D_2}{N_1 D_1} = \left(\frac{H_2}{H_1}\right)^{1/2}, \tag{26}$$

$$\frac{N_2 D_2^3}{N_1 D_1^3} = \frac{Q_2}{Q_1}, \tag{27}$$

which we rearrange to get

$$\frac{N_2}{N_1} = \left(\frac{H_2}{H_1}\right)^{3/4} \left(\frac{Q_1}{Q_2}\right)^{1/2}, \tag{28}$$

$$\frac{D_2}{D_1} = \left(\frac{H_1}{H_2}\right)^{1/4} \left(\frac{Q_2}{Q_1}\right)^{1/2}. \tag{29}$$

Note that $Q_1/Q_2 = \mathcal{F}$ by definition. Furthermore, from the definition of the hydrodynamic efficiency (7.23), we have

$$\eta = \frac{H_1}{H_2}\mathcal{F}, \tag{30}$$

which we substitute into (28)-(29) to give

$$\frac{N_2}{N_1} = \left(\frac{\mathcal{F}^5}{\eta^3}\right)^{1/4}, \tag{31}$$

$$\frac{D_2}{D_1} = \left(\frac{\eta}{\mathcal{F}^3}\right)^{1/4}. \tag{32}$$

We assume that the volume of each turbine V_T scales like the cube of the diameter. Therefore, the volume ratio is

$$\frac{V_{T_1}}{V_{T_2}} = \left(\frac{\mathcal{F}^3}{\eta}\right)^{3/4}. \tag{33}$$

As described earlier, we assume that the cost of the turbine is proportional to its volume, such that (33) can also be interpreted as a cost ratio.

Bibliography

[1] MM Alam and JP Meyer. Two interacting cylinders in cross flow. *Physical Review E*, 84:056304, Nov 2011.

[2] FS Alvi, PJ Strykowski, A Krothapalli, and DJ Forliti. Vectoring thrust in multiaxes using confined shear layers. *Journal of Fluids Engineering*, 122(1):3–13, 2000.

[3] W Anderson and M Chamecki. Numerical study of turbulent flow over complex aeolian dune fields: The white sands national monument. *Physical Review E*, 89(1):013005, 2014.

[4] PR Bailey, A Abbá, and D Tordella. Pressure and kinetic energy transport across the cavity mouth in resonating cavities. *Physical Review E*, 87(1):013013, 2013.

[5] GK Batchelor. *An introduction to fluid dynamics*. Cambridge University Press, 2000.

[6] GK Batchelor, HK Moffatt, and MG Worster. *Perspectives in fluid dynamics: a collective introduction to current research*. Cambridge University Press, 2002.

[7] GP Benham, AA Castrejon-Pita, IJ Hewitt, CP Please, RW Style, and PAD Bird. Turbulent shear layers in confining channels. *Journal of Turbulence*, 19(6):431–445, 2018.

[8] J Bezanson, A Edelman, S Karpinski, and VB Shah. Julia: A fresh approach to numerical computing. *SIAM Review*, 59(1):65–98, 2017.

[9] FS Bhinder, MM Al-Mudhafar, and M Ilyas. Further data on the performance of a rectangular diffuser in distorted inlet flows. In *ASME 1984 International Gas Turbine Conference and Exhibit*, pages V001T01A018–V001T01A018. American Society of Mechanical Engineers, 1984.

[10] AJ Bilanin, ME Teske, and G Williamson. Vortex interactions and decay in aircraft wakes. *AIAA Journal*, 15(2):250–260, 1977.

[11] H Blasius. Das ähnlichkeitsgesetz bei reibungsvorgängen in flüssigkeiten. In *Mitteilungen über Forschungsarbeiten auf dem Gebiete des Ingenieurwesens*, pages 1–41. Springer, 1913.

[12] RD Blevins. *Applied fluid dynamics handbook*. New York, Van Nostrand Reinhold Co., 1984.

[13] P-L Bourget and D Marichal. Remarks about variations in the drag coefficient of circular cylinders moving through water. *Ocean Engineering*, 17(6):569–585, 1990.

[14] P Bradshaw and FYF Wong. The reattachment and relaxation of a turbulent shear layer. *Journal of Fluid Mechanics*, 52(01):113–135, 1972.

[15] GL Brown and A Roshko. Turbulent shear layers and wakes. *Journal of Turbulence*, 13(51):1–32, 2012.

[16] JJ Carlson, JP Johnston, and CJ Sagi. Effects of wall shape on flow regimes and performance in straight, two-dimensional diffusers. *Journal of Basic Engineering*, 89(1):151–159, 1967.

[17] IP Castro and A Haque. The structure of a turbulent shear layer bounding a separation region. *Journal of Fluid Mechanics*, 179:439–468, 1987.

[18] SL Ceccio. Friction drag reduction of external flows with bubble and gas injection. *Annual Review of Fluid Mechanics*, 42:183–203, 2010.

[19] LP Chamorro, C Hill, S Morton, C Ellis, REA Arndt, and F Sotiropoulos. On the interaction between a turbulent open channel flow and an axial-flow turbine. *Journal of Fluid Mechanics*, 716:658–670, 2013.

[20] FH Champagne and S Kromat. Experiments on the formation of a recirculation zone in swirling coaxial jets. *Experiments in Fluids*, 29(5):494–504, 2000.

[21] NA Chigier and A Chervinsky. Experimental investigation of swirling vortex motion in jets. *Journal of Applied Mechanics*, 34(2):443–451, 1967.

[22] VH Chu and S Babarutsi. Confinement and bed-friction effects in shallow turbulent mixing layers. *Journal of Hydraulic Engineering*, 114(10):1257–1274, 1988.

[23] SB Dalziel, M Carr, JK Sveen, and PA Davies. Simultaneous synthetic schlieren and piv measurements for internal solitary waves. *Measurement Science and Technology*, 18(3):533, 2007.

[24] I Das and JE Dennis. Normal-boundary intersection: A new method for generating the pareto surface in nonlinear multicriteria optimization problems. *SIAM Journal on Optimization*, 8(3):631–657, 1998.

[25] JF Douglas, JM Gasiorek, and JA Swaffield. Fluid mechanics. *Harlow, Essex, England*, 1986.

[26] W Dubs. Über den einfluß laminarer und turbulenter strömung auf das röntgenbild von wasser und nitrobenzol. *Ein röntgenographischer Beitrag zum Turbulenzproblem. Helv. phys. Acte*, 12:169–228, 1939.

[27] I Dunning, J Huchette, and M Lubin. Jump: A modeling language for mathematical optimization. *SIAM Review*, 59(2):295–320, 2017.

[28] MD Durbin and DR Ballal. Studies of lean blowout in a step swirl combustor. *Journal of Engineering for Gas Turbines and Power*, 118(1):72–77, 1996.

[29] JW Elsner and L Kurzak. Characteristics of turbulent flow in slightly heated free swirling jets. *Journal of Fluid Mechanics*, 180:147–169, 1987.

[30] MP Escudier and J Keller. Recirculation in swirling flow-a manifestation of vortex breakdown. *AIAA Journal*, 23(1):111–116, 1985.

[31] S Farokhi, R Taghavi, and EJ Rice. Effect of initial swirl distribution on the evolution of a turbulent jet. *AIAA Journal*, 27(6):700–706, 1989.

[32] VG Filipenco, S Deniz, JM Johnston, EM Greitzer, and NA Cumpsty. Effects of inlet flow field conditions on the performance of centrifugal compressor diffusers: Part 1 discrete passage diffuser. *Journal of Turbomachinery*, 122:1–10, 1998.

[33] RW Fox and SJ Kline. Flow regimes in curved subsonic diffusers. *Journal of Basic Engineering*, 84(3):303–312, 1962.

[34] RW Fox and AT McDonald. Effects of swirling inlet flow on pressure recovery in conical diffusers. *AIAA Journal*, 9(10):2014–2018, 1971.

[35] SJ Gallimore, JJ Bolger, NA Cumpsty, MJ Taylor, PI Wright, and JMM Place. The use of sweep and dihedral in multistage axial flow compressor blading: part i - university research and methods development. In *ASME Turbo Expo 2002: Power for Land, Sea, and Air*, pages 33–47. American Society of Mechanical Engineers, 2002.

[36] RJ Gathmann, M Si-Ameur, and F Mathey. Numerical simulations of three-dimensional natural transition in the compressible confined shear layer. *Physics of Fluids A: Fluid Dynamics*, 5(11):2946–2968, 1993.

[37] MM Gibson and BA Younis. Calculation of swirling jets with a Reynolds stress closure. *Physics of Fluids*, 29(1):38–48, 1986.

[38] RT Gilchrist and JW Naughton. Experimental study of incompressible jets with different initial swirl distributions: mean results. *AIAA Journal*, 43(4):741–751, 2005.

[39] J Gonzalez-Aguilar, CP Sanjurjo, A Rodriguez-Yunta, and MAG Calderón. A theoretical study of a cutting air plasma torch. *IEEE Transactions on Plasma Science*, 27(1):264–271, 1999.

[40] D Greenblatt and IJ Wygnanski. The control of flow separation by periodic excitation. *Progress in Aerospace Sciences*, 36(7):487–545, 2000.

[41] EM Greitzer and HR Griswol. Compressor-diffuser interaction with circumferential flow distortion. *Journal of Mechanical Engineering Science*, 18(1):25–38, 1976.

[42] MD Griffith, MC Thompson, T Leweke, K Hourigan, and WP Anderson. Wake behaviour and instability of flow through a partially blocked channel. *Journal of Fluid Mechanics*, 582:319–340, 2007.

[43] DW Guillaume and TA Judge. Improving the efficiency of a jet pump using a swirling primary jet. *Review of Scientific Instruments*, 75(2):553–555, 2004.

[44] MD Gunzburger. *Perspectives in flow control and optimization*, volume 5. SIAM, 2003.

[45] AK Gupta, MJ Lewis, and M Daurer. Swirl effects on combustion characteristics of premixed flames. *Journal of Engineering for Gas Turbines and Power*, 123(3):619–626, 2001.

[46] C Hah. Calculation of various diffuser flows with inlet swirl and inlet distortion effects. *AIAA Journal*, 21(8):1127–1133, 1983.

[47] JH Horlock and RI Lewis. Shear flows in straight-sided nozzles and diffusers. *International Journal of Mechanical Sciences*, 2(4):251–266, 1961.

[48] J Jiménez. Turbulence and vortex dynamics. *Notes for the Polytechnique course on turbulence*, 2004.

[49] MA Jones and FT Smith. Fluid motion for car undertrays in ground effect. *Journal of Engineering Mathematics*, 45(3-4):309–334, 2003.

[50] S Kang, X Yang, and F Sotiropoulos. On the onset of wake meandering for an axial flow turbine in a turbulent open channel flow. *Journal of Fluid Mechanics*, 744:376–403, 2014.

[51] CA Kennedy, MH Carpenter, and RM Lewis. Low-storage, explicit runge–kutta schemes for the compressible navier–stokes equations. *Applied Numerical Mathematics*, 35(3):177–219, 2000.

[52] E Kit, I Wygnanski, D Friedman, O Krivonosova, and D Zhilenko. On the periodically excited plane turbulent mixing layer, emanating from a jagged partition. *Journal of Fluid Mechanics*, 589:479–507, 2007.

[53] W Kutta. Lift forces in flowing fluids. *Illustrated Aeronaut. Commun*, 3:133–135, 1902.

[54] DC Lander, CW Letchford, M Amitay, and GA Kopp. Influence of the bluff body shear layers on the wake of a square prism in a turbulent flow. *Physical Review Fluids*, 1:044406, 2016.

[55] BE Launder and DB Spalding. The numerical computation of turbulent flows. *Computer Methods in Applied Mechanics and Engineering*, 3(2):269–289, 1974.

[56] G Lavalle, JP Vila, M Lucquiaud, and P Valluri. Ultraefficient reduced model for countercurrent two-layer flows. *Physical Review Fluids*, 2(1):014001, 2017.

[57] KH Lee, T Setoguchi, S Matsuo, and HD Kim. An experimental study of the under-expanded swirling jet with secondary coaxial stream. *Shock Waves*, 14(1-2):83–92, 2005.

[58] MA Leschziner and W Rodi. Computation of strongly swirling axisymmetric free jets. *AIAA Journal*, 22(12):1742–1747, 1984.

[59] H Liang and T Maxworthy. An experimental investigation of swirling jets. *Journal of Fluid Mechanics*, 525:115–159, 2005.

[60] DG Lilley. Swirl flows in combustion: a review. *AIAA Journal*, 15(8):1063–1078, 1977.

[61] KP Lo, CJ Elkins, and JK Eaton. Separation control in a conical diffuser with an annular inlet: center body wake separation. *Experiments in Fluids*, 53(5):1317–1326, 2012.

[62] S Masuda, I Ariga, and I Watanabe. On the behavior of uniform shear flow in diffusers and its effects on diffuser performance. *Journal of Engineering for Power*, 93(4):377–385, 1971.

[63] Matlab. Matlab user's guide. *Inc., Natick, MA*, 1998.

[64] JP McDanell and WF Powers. Necessary conditions joining optimal singular and nonsingular subarcs. *SIAM Journal on Control*, 9(2):161–173, 1971.

[65] AT McDonald and RW Fox. An experimental investigation of incompressible flow in conical diffusers. *International Journal of Mechanical Sciences*, 8(2):125–139, 1966.

[66] BJ McKeon, MV Zagarola, and AJ Smits. A new friction factor relationship for fully developed pipe flow. *Journal of Fluid Mechanics*, 538:429, 2005.

[67] FR Menter. Two-equation eddy-viscosity turbulence models for engineering applications. *AIAA Journal*, 32(8):1598–1605, 1994.

[68] K Merkle, H Haessler, H Büchner, and N Zarzalis. Effect of co-and counter-swirl on the isothermal flow-and mixture-field of an airblast atomizer nozzle. *International Journal of Heat and Fluid Flow*, 24(4):529–537, 2003.

[69] B Michelsen, S Strobl, EJR Parteli, and T Pöschel. Two-dimensional airflow modeling underpredicts the wind velocity over dunes. *Nature Scientific Reports*, 5, 2015.

[70] BR Morton, GI Taylor, and JS Turner. Turbulent gravitational convection from maintained and instantaneous sources. *Proceedings of the Royal Society of London A: Mathematical, Physical and Engineering Sciences*, 234(1196):1–23, 1956.

[71] JW Naughton, LN Cattafesta III, and GS Settles. An experimental study of compressible turbulent mixing enhancement in swirling jets. *Journal of Fluid Mechanics*, 330:271–305, 1997.

[72] C Nayeri. *Investigation of the three-dimensional shear layer between confined coaxial jets with swirl*. PhD thesis, Technischen Universität Berlin, 2000.

[73] J Nocedal and SJ Wright. *Numerical optimization, second edition*. Springer, 2006.

[74] K Oberleithner, CO Paschereit, and I Wygnanski. On the impact of swirl on the growth of coherent structures. *Journal of Fluid Mechanics*, 741:156–199, 2014.

[75] D Oster and I Wygnanski. The forced mixing layer between parallel streams. *Journal of Fluid Mechanics*, 123:91–130, 1982.

[76] AM Padilla, CJ Elkins, and JK Eaton. The effect of inlet distortion on 3d annular diffusers. In *TSFP Digital Library Online*. Begel House Inc., 2011.

[77] AB Pitcher. *Mathematical modelling and optimal control of constrained systems*. PhD thesis, University of Oxford, 2009.

[78] LS Pontryagin. *Mathematical theory of optimal processes*. CRC Press, 1987.

[79] SB Pope. *Turbulent flows*. Cambridge University Press, 2000.

[80] L Prandtl. Bericht uber untersuchungen zur ausgebildeten turbulenz. *Zs. angew. Math. Mech.*, 5:136–139, 1925.

[81] LR Reneau, JP Johnston, and SJ Kline. Performance and design of straight, two-dimensional diffusers. *Journal of Basic Engineering*, 89(1):141–150, 1967.

[82] O Reynolds. An experimental investigation of the circumstances which determine whether the motion of water shall be direct or sinuous, and of the law of resistance in parallel channels. *Proceedings of the Royal Society of London*, 35(224-226):84–99, 1883.

[83] MM Ribeiro and JH Whitelaw. Coaxial jets with and without swirl. *Journal of Fluid Mechanics*, 96(4):769–795, 1980.

[84] HM Robbins. A generalized Legendre-Clebsch condition for the singular cases of optimal control. *IBM Journal of Research and Development*, 11(4):361–372, 1967.

[85] JC Robinet, JP Dussauge, and G Casalis. Wall effect on the convective–absolute boundary for the compressible shear layer. *Theoretical and Computational Fluid Dynamics*, 15(3):143–163, 2001.

[86] A Sau, RR Hwang, TWH Sheu, and WC Yang. Interaction of trailing vortices in the wake of a wall-mounted rectangular cylinder. *Physical Review E*, 68:056303, Nov 2003.

[87] H Schlichting, K Gersten, E Krause, H Oertel, and K Mayes. *Boundary-layer theory*, volume 7. Springer, 1960.

[88] A Shah, IR Chughtai, and MH Inayat. Experimental study of the characteristics of steam jet pump and effect of mixing section length on direct-contact condensation. *International Journal of Heat and Mass Transfer*, 58(1):62–69, 2013.

[89] S Simone, F Montomoli, F Martelli, KS Chana, I Qureshi, and T Povey. Analysis on the effect of a nonuniform inlet profile on heat transfer and fluid flow in turbine stages. *Journal of Turbomachinery*, 134(1):011012, 2012.

[90] KL So. Vortex phenomena in a conical diffuser. *AIAA Journal*, 5(6):1072–1078, 1967.

[91] P Spalart and S Allmaras. A one-equation turbulence model for aerodynamic flows. In *30th aerospace sciences meeting and exhibit*, page 439. American Institute of Aeronautics and Astronautics, 1992.

[92] S Suresha, RI Sujith, B Emerson, and T Lieuwen. Nonlinear dynamics and intermittency in a turbulent reacting wake with density ratio as bifurcation parameter. *Physical Review E*, 94:042206, Oct 2016.

[93] JK Sveen and SB Dalziel. A dynamic masking technique for combined measurements of piv and synthetic schlieren applied to internal gravity waves. *Measurement Science and Technology*, 16(10):1954, 2005.

[94] CKW Tam and FQ Hu. The instability and acoustic wave modes of supersonic mixing layers inside a rectangular channel. *Journal of Fluid Mechanics*, 203:51–76, 1989.

[95] W Thielicke and E Stamhuis. Pivlab–towards user-friendly, affordable and accurate digital particle image velocimetry in matlab. *Journal of Open Research Software*, 2(1), 2014.

[96] L Ting. On the mixing of two parallel streams. *Studies in Applied Mathematics*, 38(1-4):153–165, 1959.

[97] DJ Tritton. *Physical fluid dynamics*. Springer Science & Business Media, 2012.

[98] TSI. Tsi precision measurement instrumentation. *Inc., 500 Cardigan Road, Shoreview, MN*, 2017.

[99] JG Venditti, CD Rennie, J Bomhof, RW Bradley, M Little, and M Church. Flow in bedrock canyons. *Nature*, 513(7519):534–537, 2014.

[100] HLF von Helmholtz. *über discontinuirliche Flüssigkeits-Bewegungen*. Akademie der Wissenschaften zu Berlin, 1868.

[101] A Wächter and LT Biegler. On the implementation of an interior-point filter line-search algorithm for large-scale nonlinear programming. *Mathematical Programming*, 106(1):25–57, 2006.

[102] BA Waitman, LR Reneau, and SJ Kline. Effects of inlet conditions on performance of two-dimensional subsonic diffusers. *Journal of Basic Engineering*, 83(3):349–360, 1961.

[103] MJ Walsh. Riblets as a viscous drag reduction technique. *AIAA Journal*, 21(4):485–486, 1983.

[104] HG Weller, G Tabor, H Jasak, and C Fureby. A tensorial approach to computational continuum mechanics using object-oriented techniques. *Computers in Physics*, 12(6):620–631, 1998.

[105] CD Winant and FK Browand. Vortex pairing: the mechanism of turbulent mixing-layer growth at moderate reynolds number. *Journal of Fluid Mechanics*, 63(2):237–255, 1974.

[106] S Wolf and JP Johnston. Effects of nonuniform inlet velocity profiles on flow regimes and performance in two-dimensional diffusers. *Journal of Basic Engineering*, 91(3):462–474, 1969.

[107] J Zhang, TL Jackson, J Buckmaster, and F Najjar. Erosion in solid-propellant rocket motor nozzles with unsteady nonuniform inlet conditions. *Journal of Propulsion and Power*, 27(3):642–649, 2011.

[108] T Zierer. Experimental investigation of the flow in diffusers behind an axial flow compressor. *Journal of Turbomachinery*, 117(2):231–239, 1995.